# Jordan Journal of Mechanical and Industrial Engineering (JJMIE)

**Hashemite Kingdom of Jordan**

**Hashemite University**

# Jordan Journal of

# Mechanical and Industrial Engineering

# JJMIE

*An International Peer-Reviewed Scientific Journal*

*Financed by Scientific Research Support Fund*

*Volume 16 Number 3, June 2022*

# Jordan Journal of Mechanical and Industrial Engineering (JJMIE)

**Introduction:** The Editorial Board is very committed to build the Journal as one of the leading international journals in mechanical and industrial engineering sciences in the next few years. With the support of the Ministry of Higher Education and Scientific Research and Jordanian Universities, it is expected that a heavy resource to be channeled into the Journal to establish its international reputation. The Journal's reputation will be enhanced from arrangements with several organizers of international conferences in publishing selected best papers of the conference proceedings.

**Aims and Scope:** *Jordan Journal of Mechanical and Industrial Engineering* (JJMIE) is a refereed international journal to be of interest and use to all those concerned with research in various fields of, or closely related to, mechanical and industrial engineering disciplines. *Jordan Journal of Mechanical and Industrial Engineering* aims to provide a highly readable and valuable addition to the literature which will serve as an indispensable reference tool for years to come. The coverage of the journal includes all new theoretical and experimental findings in the fields of mechanical and industrial engineering or any closely related fields (Materials, Manufacturing, Management, Design, Thermal, Fluid, Energy, Control, Mechatronics, and Biomedical). The journal also encourages the submission of critical review articles covering advances in recent research of such fields as well as technical notes.

## Guide for Authors

**Manuscript Submission:**
High-quality submissions to this new journal are welcome now and manuscripts may be either submitted online or email.

**Online:** For online and email submission upload one copy of the full paper including graphics and all figures at the online, submission site, accessed via http://jjmie.hu.edu.jo. The manuscript must be written in MS Word Format. All correspondence including notification of the Editor's decision and requests for revision, takes place by e-mail and via the Author's homepage, removing the need for a hard-copy paper trail

**Submission address and contact :**
Prof. Ali M. Jawarneh
Editor-in-Chief
*Jordan Journal of Mechanical & Industrial Engineering,* Hashemite University
PO Box 330127, Zarqa, 13115, Jordan
E-mail: jjmie@hu.edu.jo

**Types of contributions***:* Original research papers and Technical reports

**Corresponding author:** Clearly indicate who is responsible for correspondence at all stages of refereeing and publication, including post-publication. Ensure that telephone and fax numbers (with country and area code) are provided in addition to the e-mail address and the complete postal address. Full postal addresses must be given for all co-authors.

**Original material:** Submission of an article implies that the work described has not been published previously (except in the form of itstan abstract or as part of a published lecture or academic thesis), that it is not under consideration for publication elsewhere, tha publication is approved by all authors and that, if accepted, it will not be published elsewhere in the same form, in English or in any other language, without the written consent of the Publisher. Authors found to be deliberately contravening the submission guidelines on originality and exclusivity shall not be considered for future publication in this journal.

**Withdrawing:** If the author chooses to withdraw his article after it has been assessed, he shall reimburse JJMIE with the cost of reviewing the paper.

## Manuscript Preparation:

**General:** Editors reserve the right to adjust style to certain standards of uniformity. Original manuscripts are discarded after publication unless the Publisher is asked to return original material after use. Please use MS Word for the text of your manuscript.

**Structure:** Follow this order when typing manuscripts: Title, Authors, Authors title, Affiliations, Abstract, Keywords, Introduction, Main text, Conclusions, Acknowledgements, Appendix, References, Figure Captions, Figures and then Tables. Please supply figures imported into the text AND also separately as original graphics files. Collate acknowledgements in a separate section at the end of the article and do not include them on the title page, as a footnote to the title or otherwise.

**Text Layout:** Use 1.5 line spacing and wide (3 cm) margins. Ensure that each new paragraph is clearly indicated. Present tables and figure legends on separate pages at the end of the manuscript. If possible, consult a recent issue of the journal to become familiar with layout and conventions. All footnotes (except for table and corresponding author footnotes) should be identified with superscript Arabic numbers. To conserve space, authors are requested to mark the less important parts of the paper (such as records of experimental results) for printing in smaller type. For long papers (more than 4000 words) sections which could be deleted without destroying either the sense or the continuity of the paper should be indicated as a guide for the editor. Nomenclature should conform to that most frequently used in the scientific field concerned. Number all pages consecutively; use 12 or 10 pt font size and standard fonts.

**Corresponding author:** Clearly indicate who is responsible for correspondence at all stages of refereeing and publication, including post-publication. The corresponding author should be identified with an asterisk and footnote. Ensure that telephone and fax numbers (with country and area code) are provided in addition to the e-mail address and the complete postal address. Full postal addresses must be given for all co-authors. Please consult a recent journal paper for style if possible.

**Abstract:** A self-contained abstract outlining in a single paragraph the aims, scope and conclusions of the paper must be supplied.

**Keywords:** Immediately after the abstract, provide a maximum of six keywords (avoid, for example, 'and', 'of'). Be sparing with abbreviations: only abbreviations firmly established in the field may be eligible.

**Symbols:** All Greek letters and unusual symbols should be identified by name in the margin, the first time they are used.

**Units:** Follow internationally accepted rules and conventions: use the international system of units (SI). If other quantities are mentioned, give their equivalent quantities in SI

**Maths:** Number consecutively any equations that have to be displayed separately from the text (if referred to explicitly in the text).

**References:** All publications cited in the text should be presented in a list of references following the text of the manuscript.

*Text:* Indicate references by number(s) in square brackets in line with the text. The actual authors can be referred to, but the reference number(s) must always be given.

*List:* Number the references (numbers in square brackets) in the list in the order in which they appear in the text.

**Examples:**
**Reference to a journal publication:**
[1] M.S. Mohsen, B.A. Akash, "Evaluation of domestic solar water heating system in Jordan using analytic hierarchy process". Energy Conversion & Management, Vol. 38 (1997) No. 9, 1815-1822.

**Reference to a book:**
[2] Strunk Jr W, White EB. The elements of style. 3rd ed. New York: Macmillan; 1979.

**Reference to a conference proceeding:**
[3] B. Akash, S. Odeh, S. Nijmeh, "Modeling of solar-assisted double-tube evaporator heat pump system under local climate conditions". 5th Jordanian International Mechanical Engineering Conference, Amman, Jordan, 2004.

**Reference to a chapter in an edited book:**
[4] Mettam GR, Adams LB. How to prepare an electronic version of your article. In: Jones BS, Smith RZ, editors. Introduction to the electronic age, New York: E-Publishing Inc; 1999, p. 281-304

**Free Online Color :** If, together with your accepted article, you submit usable color and black/white figures then the journal will ensure that these figures will appear in color on the journal website electronic version.

**Tables:** Tables should be numbered consecutively and given suitable captions and each table should begin on a new page. No vertical rules should be used. Tables should not unnecessarily duplicate results presented elsewhere in the manuscript (for example, in graphs). Footnotes to tables should be typed below the table and should be referred to by superscript lowercase letters.

**Notification:** Authors will be notified of the acceptance of their paper by the editor. The Publisher will also send a notification of receipt of the paper in production.

**Copyright:** All authors must sign the Transfer of Copyright agreement before the article can be published. This transfer agreement enables Jordan Journal of Mechanical and Industrial Engineering to protect the copyrighted material for the authors, but does not relinquish the authors' proprietary rights. The copyright transfer covers the exclusive rights to reproduce and distribute the article, including reprints, photographic reproductions, microfilm or any other reproductions of similar nature and translations.

**Proof Reading:** One set of page proofs in MS Word format will be sent by e-mail to the corresponding author, to be checked for typesetting/editing. The corrections should be returned within 48 hours. No changes in, or additions to, the accepted (and subsequently edited) manuscript will be allowed at this stage. Proofreading is solely the author's responsibility. Any queries should be answered in full. Please correct factual errors only, or errors introduced by typesetting. Please note that once your paper has been proofed we publish the identical paper online as in print.

# JJMIE

**Jordan Journal of Mechanical and Industrial Engineering**

# Optimizing PM Intervals for Manufacturing Industries Using Delay-time Analysis and MOGA

## S.K. Tiwari[1*], R.K. Singh[2], B. Kumar[3]

*[1]Birla Institute of Technology, Mesra – Ranchi, JH 835215, India*
*[2]Birla Institute of Technology, Mesra – Ranchi, JH 835215, India*
*[3]Birla Institute of Technology, Mesra – Off-campus Deoghar, Deoghar, JH 814142, India.*

## Abstract

Overall productivity and profitability are directly affected by the adopted maintenance policy for any manufacturing industry. It should maximize the availability of the system and minimize operating costs. This article attempts to develop a preventive maintenance (PM) model based on delay-time analysis to reduce the downtime and cost of maintenance activities. The developed maintenance model is optimized using a multi-objective genetic algorithm (MOGA) to determine the optimal maintenance frequency. Further, sensitivity analysis is performed to verify the consistency of the proposed model. Lastly, the model's applicability is tested by implementing it in a foundry unit, and a drastic reduction in overall maintenance downtime and cost almost by 71.69% is achieved.

## 1. Introduction

Mechanical systems and their components deteriorate with time [1]. Therefore, timely maintenance is required to avoid malfunctioning. However, in most organizations, maintenance is either overlooked or overperformed. In either case, substantial time and money are wasted, which ultimately affects the productivity and revenue of the organization. Moreover, maintenance is attributed to the quality of the products manufactured in any industry. According to a study, solely maintenance operations account for around 28% of entire production costs in any business[2]. Furthermore, maintenance cost has the largest share after energy costs of any operational budget [3, 4]. Therefore, it is required to perform adequate and timely maintenance to reduce the number of failures, thus increasing the reliability of machines and equipment.

Maintenance is the set of activities performed on a system to restore or retain it to a state where it can perform its intended functions [5]. These activities generally involve inspection, cleaning, lubrication, adjustment, alignment, and repair/or replacement of wear-out components/or subcomponents to keep the facility/equipment in working condition and avoid unexpected failure during operation [6]. Two approaches were adopted to perform maintenance in any facility based on this. These are continuous and periodic maintenance [7, 8]. In the first approach, equipment is continuously and rigorously monitored using a sensor-based monitoring system and warns whenever something happens wrong. The latter method involves the empirical and statistical analysis of equipment failure data [7]. But both approaches have certain limitations. Continuous condition monitoring

is quite expensive, and noise can be generated due to imprecise diagnosis. However, periodic maintenance is cost-effective, but has a risk in terms of the possibility of some failure in between two successive maintenance activities [7, 8]. Therefore, the main problem faced by any industry is determining an effective maintenance policy that will improve overall productivity and profitability [9].

Numerous models have been developed to determine an effective maintenance policy [6, 10-16]. Preventive maintenance (PM) is the most studied maintenance policy [10, 11]. An effective PM policy is performed at a planned time interval to prevent potential failures. For any PM program, determining the inspection interval is one of the prime necessities [10]. The inspection interval should be fixed to minimize the cost of performing PM activities [12]. If the inspection interval is too short, it will increase the inspection cost and the facility's downtime, thus affecting the system's overall productivity. Alternatively, if it is too long again, the cost of PM and the system's downtime increases due to the probability of failure [12]. Therefore, it is required to optimize the PM interval to minimize the cost and the downtime due to PM activities [13].

Therefore, this research attempts to develop a PM model that minimizes the total maintenance downtime and the cost associated with maintenance by using a heuristic method. In this regard, mathematical models are developed to find the downtime and cost associated with the maintenance activities using delay-time analysis [14-16]. Further, the optimal maintenance frequency is determined by optimizing the developed models using a multi-

* Corresponding author e-mail: sanjivtiwari@bitmesra.ac.in.

objective genetic algorithm (MOGA) that simultaneously minimizes the downtime and cost. Additionally, sensitivity analysis is performed to verify the consistency of the proposed model. The proposed model is further applied in a foundry unit to optimize the PM policy of one of the most failure-prone equipment.

## 2. Mathematical Model

This study developed the mathematical model based on delay time analysis (DTA) proposed by Christer and Walker in 1984 [17]. According to DTA, every component sounds abnormal before it breakdowns. Figure 1 elaborates on the DTA concept. The line represents the timeline, and the two circles on the timeline represent the initiation of the defect (white circle) and actual failure (black circle). The time between the initiation of the defect and actual failure is known as the delay time (h) [17]. According to the DTA concept, any fault occurring in the time interval $(0, T)$ has a delay time $\Delta h$ within the interval $(h, h+\Delta h)$ with the probability of $f(h)\Delta h$. If the fault arises in the period $(0, T–h)$, it will be repaired as a breakdown repair; otherwise, as an inspection repair, as shown in Figure 2.

The probability of breakdown $b(T)$ due to the occurrence of a fault within a period $(0, T)$ can be expressed as [17]:

$$b(T) = \int_{h=0}^{T} \frac{(T-h)}{T} f(h)dh \qquad (1)$$

The expected downtime per unit time $D(T)$ for a given probability for breakdown failure $b(T)$ is expressed as:

$$D(T) = \frac{D_i + K_f T b(T) D_b}{T + D_i} \qquad (2)$$

where $D_i$ is average inspection downtime incurred in the inspection of the equipment, $D_b$ is average breakdown repair downtime involved in repair/replacement of the equipment failed due to sudden failure, $K_f$ is arrival rate of a defect per unit time, which is the average time a defect arises over a period, $T$ is the time interval between inspections.

Similarly, the expected maintenance cost per unit time $C(T)$ of the equipment with an inspection of period $T$ is expressed as:

$$C(T) = \frac{K_f T C_b b(T) + C_{ir}[1 - b(T)] + C_i}{T + D_i} \qquad (3)$$

where $C_b$ is breakdown repair cost, $C_{ir}$ is inspection and repair cost, $C_i$ is inspection cost.

In this study, the probability distribution function of delay time $f(h)$ follows an exponential distribution. Therefore,

$$f(h) = \frac{1}{\theta} e^{-h/\theta} \qquad (4)$$

where $\theta$ is the mean time between failures (MTBF). It is the mean operating time between subsequent failures of equipment.

From Eq. (1) and (4):

$$b(T) = \int_{h=0}^{T} \left(\frac{T-h}{T}\right) \left(\frac{1}{\theta} e^{-h/\theta}\right) dh \qquad (5)$$

Further putting the value of Eq. (5) in Eq. (2) and (3) and simplifying, we have:

$$D(T) = \frac{D_i + K_f T\{\theta(e^{-T/\theta}-1)+T\}D_b}{T+D_i} \qquad (6)$$

$$C(T) = \frac{K_f T C_b\{\theta(e^{-T/\theta}-1)+T\}+C_{ir}[1-\{\theta(e^{-T/\theta}-1)+T\}]+C_i}{T+D_i} \qquad (7)$$

Therefore, the mathematical model for estimating the optimum maintenance schedule is:

$$Minimize D(T) = \frac{D_i + K_f T\left\{\theta\left(e^{-\frac{T}{\theta}}-1\right)+T\right\}D_b}{T+D_i} \qquad (8)$$

$$C(T) = \frac{K_f T C_b\left\{\theta(e^{-\frac{T}{\theta}}-1)+T\right\}+C_{ir}\left[1-\left\{\theta(e^{-\frac{T}{\theta}}-1)+T\right\}\right]+C_i}{T+D_i}$$

$$s.t. \, t_1 \leq T \leq t_2$$
$$d_{i_1} \leq D_i \leq d_{i_2}$$
$$k_{f_1} \leq K_f \leq k_{f_2}$$
$$\theta_1 \leq \theta \leq \theta_2$$
$$d_{b_1} \leq D_b \leq d_{b_2}$$
$$c_{b_1} \leq C_b \leq c_{b_2}$$
$$c_{ir_1} \leq C_{ir} \leq c_{ir_2}$$
$$c_{i_1} \leq C_i \leq c_{i_2}$$

where $t_1$ and $t_2$ are the lower and upper limit of time interval, $T$; $d_{i1}$ and $d_{i2}$ are the lower and upper limit of average inspection downtime, $D_i$; $d_{b1}$ and $d_{b2}$ are the lower and upper limit of average breakdown repair downtime, $D_b$; $k_{f1}$ and $k_{f2}$ are the lower and upper limit of the arrival rate of a defect per unit time, $K_f$; $\theta_1$ and $\theta_1$ are the lower and upper limit of MTBF, $\theta$; $C_{b1}$ and $C_{b2}$ are the lower and upper limit of the breakdown repair cost; $C_{ir1}$ and $C_{ir2}$ are the lower and upper limit of inspection and repair cost; $C_{i1}$ and $C_{i2}$ are the lower and upper limit of inspection cost.
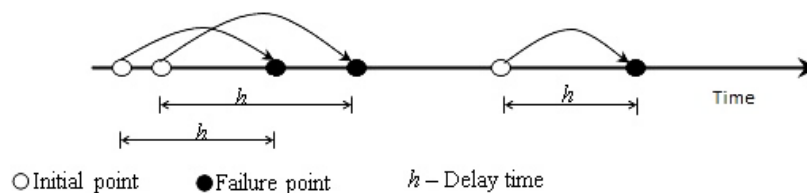


**Figure 1.** Delay time
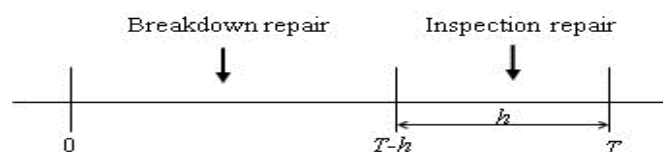


**Figure 2.** Repair type

## 3. Multi-Objective Genetic Algorithm (MOGA)

Holland initially proposed the Genetic Algorithm (GA) in the 1960s [18], and his colleagues and students further refined it at the University of Michigan between the 1960s and 1970s [19]. The concept of GA is based on the evolutionism theory that explains the origin of species [18-20]. Traditionally, GA has been applied to single-objective optimization problems. However, today GA is successfully used to optimize practical issues where two or more objectives [20].

In the last few decades, several variants of GA were introduced to solve different real problems having more than one objective [21-24]. Among them, MOGA was successfully used by various researchers to find the Pareto-based optimal solutions for various real engineering problems. MOGA was first proposed by Fonseca and Fleming, 1993, emphasizing the use of Pareto-based ranking and niching methods to search the true Pareto front without affecting the diversity of the population [25]. In MOGA, every solution linked with each objective can be considered as an elite individual. Therefore, there are *n* elite individuals for any objective. These solutions are preserved to the subsequent generation in genetic algorithms [20]. The pseudo-code of MOGA used in this study is depicted in Figure 3.

## 4. Methodology

The proposed methodology to determine the optimal inspection interval by reducing the downtime and cost associated with preventive maintenance is depicted in Figure 4. The first step involves a thorough analysis of the entire process to understand better and identify the problems. A better understanding of the process is the prime requirement in developing any maintenance model. Insufficient or inadequate knowledge of the process may create confusion in selecting the problem. Moreover, during the problem identification stage, care should be takento classify the occurred breakdown as a maintenance issue, an engineering issue, or an operator issue. After an assortment of the problem, appropriate data shall be collected from the maintenance department or the specific shop itself. Following data are required as defined by the mathematical model:

- Average inspection downtime, $d_i$.
- Average breakdown repair downtime, $d_b$.
- The arrival rate of defect per unit time, $k_f$.
- Mean-time between the failures (MTBF), $\theta$.
- Inspection cost, $C_i$.
- Inspection and repair cost, $C_{ir}$.
- Breakdown repair cost, $C_b$.

After collecting valuable information about the problem, mathematical models are formulated and further optimized using MOGA to estimate the optimum inspection schedule based on minimum downtime and maintenance costs.

## 5. Case Study

The effectiveness of the proposed maintenance model is being investigated through a case study of a leading foundry unit situated in southern India. The proposed model has been implemented to schedule the maintenance activities performed on one of the failure-prone systems, shot blasting machine, which minimizes its cost and downtime. A shot blasting machine is used to clean the surface of the casting after cooling, knock-out, and de-gating. In the existing setup, an overhead rail wheel blasting type shot blasting machine is used in which jets of small metal balls are imposed on the castings to clean their surfaces. It required approximately 10 - 15 minutes to clean 20-30 castings, or 1 ton/hanger (maximum), depending upon the size of castings at a time. The significant parts of the machine are blasting wheels, re-claimer and dust collector, blast system, direct-pressure system, suction (siphon) system.

```
START:
Input: Algorithm control parameters
Output: Pareto Front
Initialize generation counter g=0
Initialize population
Initialize control parameters
Initialize Elite Solution
While g<gmax do
        Perform non-dominated sorting
        Select individual for mating pool
        Perform crossover
        Perform mutation
Perform Elitism
Assign current generation=new generation
Estimate F*=nondominated pareto front of current generation
Assign, {Elite Solution} = {Elite Solution} ∪ F*
Increment the generation g=g+1
End while
Print {Elite Solution}
STOP
```

**Figure 3.** Pseudo-code for MOGA

In the current maintenance plan, each major part is inspected per shift to identify problems, if any, which takes around half an hour (a total of one and a half hours daily). Additionally, regular planned maintenance and any subsequent adjustments or repairs have been carried out per month and take approximately eight hours. Thus, the total downtime of the shot-blasting machine is approximately 53 hours per month ($1.5 \times 30 + 8$ hours) which costs about ₹ 13,250/- per month (@ ₹ 250/hr.). Although, occasional breakdown also occurs due to the sudden failure of one or more of these parts. This increases the total downtime as well as the cost of maintenance. The information related to maintenance downtime and their cost parameters is listed in Table 1.

## 6. Result and Discussion

The MOGA solver in MATLAB 2015a was used to optimize the preventive maintenance frequency in this investigation. The variables were converted to binary coding by generating mathematical models as M-files and then optimized with the "gamultiobj" optimization tool, which uses a multi-objective genetic algorithm. The optimal solutions from the MOGA solver are obtained with the following parameter settings. Population size – 200, Selection function – Tournament, selection size – 2, crossover rate - 0.8, mutation function - constraint dependent, Pareto front population fraction - 0.35,

stopping criteria - 100*No. of variables. The corresponding code is depicted in Figure 5.
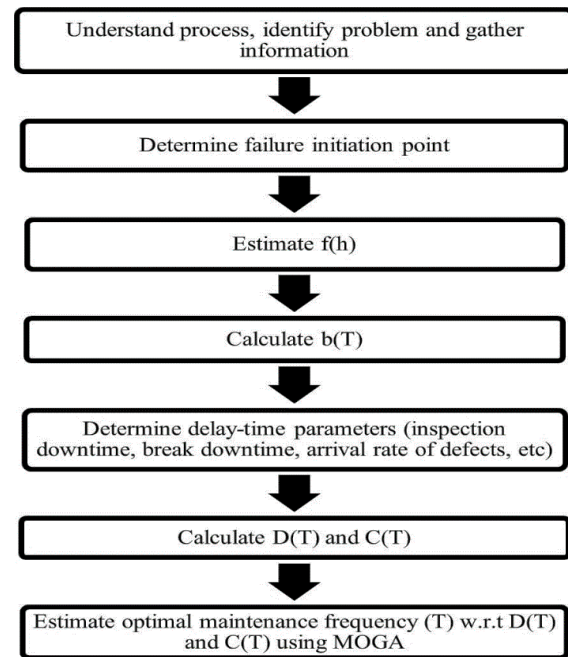


**Figure 4.** Flow chart of the methodology adopted

**Table 1.** Maintenance downtime and cost parameters

| S. No. | Major Parts | $k_f$ | $\theta$ | $d_i$ | $d_b$ | $C_i$ | $C_{ir}$ | $C_b$ |
|---|---|---|---|---|---|---|---|---|
| 1. | Blasting Wheels | 0.26 | 365 | 0.33 | 7 | 500 | 2200 | 22000 |
| 2. | Re-claimer and dust collector | 0.33 | 290 | 0.25 | 3 | 150 | 1300 | 12000 |
| 3. | Blast System | 0.29 | 230 | 0.17 | 3 | 280 | 2200 | 18000 |
| 4. | Direct-pressure systems | 0.41 | 85 | 0.04 | 0.33 | 100 | 1500 | 10000 |
| 5. | Suction (siphon) systems | 0.36 | 30 | 0.04 | 0.33 | 80 | 1200 | 5000 |

```
clear; clc;close all;
fun = @moo_objective_functions;
nvars=8;
A=[]; b=[]; Aeq=[]; beq=[];
lb=[0 0.041 0.26 270 0.33 5000 1200 80]; ub=[120 0.333 0.41 730 7 22000 2200 500];
[x,fval,exitflag,output] = gamultiobj(fun,nvars,A,b,Aeq,beq,lb,ub)
D_T = fval(:,1);
C_T = fval(:,2);
% plot(D_T,C_T,'*-')
T = x(:,1);
D_i = x(:,2);
K_f = x(:,3);
theta=x(:,4);
D_b = x(:,5);
C_b = x(:,6);
C_ir = x(:,7);
C_i=x(:,8);
T1 = table(D_T,C_T,T,D_i,K_f,theta,D_b,C_b,C_ir,C_i)
T_sorted = sortrows(T1,{'D_T'})
D_T_sorted = T_sorted.D_T;
C_T_sorted = T_sorted.C_T;
plot(D_T_sorted,C_T_sorted,'*-')
xlabel('D(T)')
ylabel('C(T)')
title('Pareto Front')
function f = moo_objective_functions (x)
T = x(1); D_i = x(2); K_f = x(3);theta=x(4);
D_b = x(5); C_b = x(6); C_ir = x(7);C_i=x(8);
f(1) = (D_i+K_f*T*(theta*(exp(-T/theta)-1)+T)*D_b)./(T+D_i);
f(2) = (K_f*T*C_b*(theta*(exp(-T/theta)-1)+T)+C_ir*(1-(theta*(exp(-T/theta)-1)+T))+C_i)./(T+D_i);
end
```

**Figure 5.** MOGA code

331

Figure 6 shows the Pareto front for D(T) vs. C(T), in which each point in the Pareto front is a non-dominated solution concerning others. From the detailed study of the graph, it can be concluded that both responses' optimum value is satisfied when the PM frequency is six days. The optimal maintenance downtime is 1.38 hrs./day with a maintenance cost of ₹ 375/- per day. This reduces the total downtime and maintenance cost by approximately 71.69%.

*6.1. Sensitivity Analysis*

Further, sensitivity analysis has been performed to verify the consistency of the model. For this, some critical parameters (such as $k_f$, $\lambda$, $C_i$ and $C_{ir}$) that affect the solution have been varied by 5 and 10%. The results of sensitivity analysis are depicted in Table 2. It can be concluded that the increase and decrease of variables resulted in small changes in the maintenance downtime D(T), maintenance cost C(T), and inspection interval (T). Therefore, the optimum preventive maintenance (PM) schedule for the shot-blasting machine is 6 days, in which both the maintenance downtime and maintenance cost are minimum. Figure 7 shows the graphical representation of the sensitivity analysis.

## 7. Conclusion

This research aimed to use multiple objectives in determining the optimal PM interval. Two criteria, maintenance cost and downtime were selected to assess the PM interval's performance. DTA approach was used to develop the mathematical relationship between the PM intervals and the corresponding criteria. Further, the mathematical models were optimized using MOGA to determine the best PM interval that minimizes the maintenance cost and downtime. The proposed maintenance model was applied in a foundry unit to optimize the PM interval of the shot-blasting machine. The results concluded that the optimum PM interval should be 6 days to satisfy both criteria simultaneously. This reduces the overall maintenance downtime and cost by nearly 71.69%.

Additionally, the sensitivity analysis of the results was carried out to verify the consistency of the proposed model. Furthermore, the developed model can be helpful for any discrete industry. It helps reduce the downtime of the production facility and reduce maintenance and inspection costs. Also, this model enables the maintenance person to decide on periodic maintenance of the production facility to increase productivity.
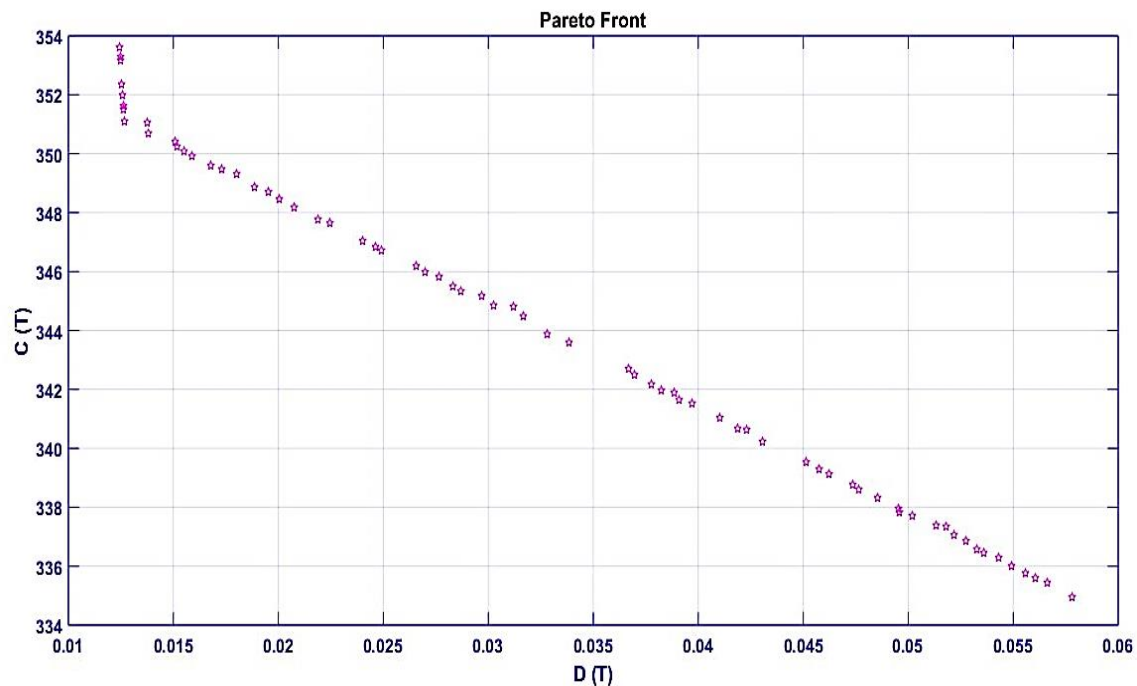


**Figure 6.** Pareto optimal front for D(T) vs. C(T)

**Table 2.** Results of sensitivity analysis

| Case No. | T (Days) | D (T) (Hrs.) | C (T) (₹) |
| --- | --- | --- | --- |
| C1 (Increased by 5%) | 6.65 | 0.0544 | 294.82 |
| C2 (Increased by 10%) | 6.03 | 0.0628 | 265.91 |
| C3 (No Change) | 6.09 | 0.0578 | 334.95 |
| C4 (Decreased by 5%) | 6.69 | 0.0551 | 313.25 |
| C5 (Decreased by 10%) | 6.60 | 0.0543 | 311.03 |
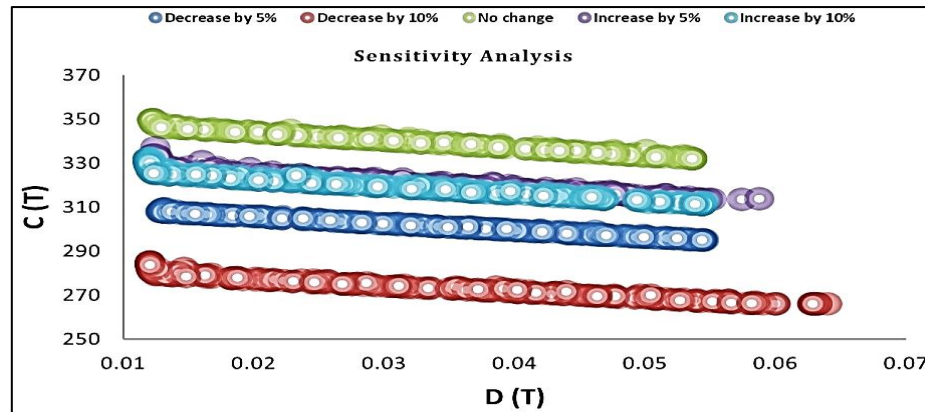
**Figure 7.** Sensitivity analysis

## Acknowledgments

## References

[1] de Jonge, B., Scarf, P.A. A review on maintenance optimization. European Journal of Operational Research, 2020, 285(3): 805-824.

[2] Mobley, R.K. An introduction to predictive maintenance. Elsevier, 2002.

[3] Lofsten, H. Maintenance and reinvestment policies: framework and principles. International Journal of Engineering Management and Economics, 2018, 6(2-3): 207-223.

[4] Park, K.S., Han, S.W. TPM—total productive maintenance: impact on competitiveness and a framework for successful implementation. Human Factors and Ergonomics in Manufacturing & Service Industries, 2001, 11(4): 321-338.

[5] Dhillon, B.S. Engineering maintenance: a modern approach. CRC Press, Florida, 2002.

[6] Basri, E.I., Razak, I.H.A., Ab-Samat, H., Kamaruddin, S. Preventive maintenance (PM) planning: a review. Journal of Quality in Maintenance Engineering, 2017, 23(2): 114-143.

[7] Ebrahimipour, V., Najjarbashi, A., Sheikhalishahi, M. Multi-objective modeling for preventive maintenance scheduling in a multiple production line. Journal of Intelligent Manufacturing, 2015, 26(1): 111-122.

[8] Emovon, I., Norman, R.A., Murphy, A.J. An integration of multi-criteria decision-making techniques with a delay time model for determination of inspection intervals for marine machinery systems. Applied Ocean Research, 2016, 59: 65-82.

[9] Liu, G., Chen, S., Jin, H., Liu, S. Optimum opportunistic maintenance schedule incorporating delay time theory with imperfect maintenance. Reliability Engineering & System Safety, 2021, 213: 107668.

[10] Alaswad, S., Xiang, Y. A review on condition-based maintenance optimization models for stochastically deteriorating system. Reliability engineering & system safety, 2017, 157: 54-63.

[11] Wang, W. A stochastic model for joint spare parts inventory and planned maintenance optimization. European Journal of Operational Research, 2012, 216(1): 127-139.

[12] Keizer, M.C.O., Flapper, S.D.P., Teunter, R.H. Condition-based maintenance policies for systems with multiple dependent components: a review. European Journal of Operational Research, 2017, 261(2): 405-420.

[13] Samhouri, M.S., Al-Ghandoor,A., Fouad, R.H., Alhaj Ali, S.M. An intelligent opportunistic maintenance (OM) system: a genetic algorithm approach. Jordan Journal of Mechanical and Industrial Engineering, 2009, 3(4): 246-251.

[14] de Souza, N.M., de Almeida Filho, A.T. A systematic airport runway maintenance and inspection policy based on a delay time modeling approach. Automation in Construction, 2020, 110: 103039.

[15] Zhao, F., Wang, W., Peng, R. Delay-time-based preventive maintenance modelling for a production plant: a case study in a steel mill. Journal of the Operational Research Society, 2015, 66(12): 2015-2024.

[16] Das Adhikary, D., Bose, G.K., Jana, D.K., Bose, D., Mitra, S. Availability and cost-centered preventive maintenance scheduling of continuous operating series systems using multi-objective genetic algorithm: A case study. Quality Engineering, 2016, 28(3): 352-357.

[17] Christer, A.H., Waller, W.M. Delay time models of industrial inspection maintenance problems. Journal of the Operational Research Society, 1984, 35(5): 401-406.

[18] Rahimi, M., Fazlollahtabar, H. Optimization of a closed loop green supply chain using particle swarm and genetic algorithms. Jordan Journal of Mechanical and Industrial Engineering, 2018, 12(2): 77-91.

[19] Holland, J.H.Adaptation in natural and artificial systems: an introductory analysis with applications to biology, control, and artificial intelligence. MIT press, 1992.

[20] Mansouri, V., Khosravanian, R., Wood, D. A., Aadnoy, B.S. 3-D well path design using a multi objective genetic algorithm. Journal of natural gas science and engineering, 2015, 27: 219-235.

[21] Pati, S., Yadav, D., Verma, O.P. Synergetic fusion of energy optimization and waste heat reutilization using nature-inspired algorithms: a case study of kraft recovery process. Neural Computing and Applications, 2021, 33(17): 10751-10770.

[22] Verma, O.P., Manik, G., Jain, V.K., Jain, D.K., Wang, H. Minimization of energy consumption in multiple stage evaporator using genetic algorithm. Sustainable Computing: Informatics and Systems, 2018, 20: 130-140.

[23] Kazem, B.I., Mahdi, A.I., Oudah, A.T. Motion planning for a robot arm by using genetic algorithm. Jordan Journal of Mechanical and Industrial Engineering, 2008, 2(3): 131-136.

[24] Omran, A., Bayoumi, M., Kassem, A., El-Bayoumi, G. Optimal forward kinematics modeling of Stewart manipulator using genetic algorithms. Jordan Journal of Mechanical and Industrial Engineering, 2009, 3(4): 280-293.

[25] Fonseca, C.M., Fleming, P.J. Genetic algorithms for multi-objective optimization: formulation discussion and generalization. In ICGA, 1993, 93(7): 416-423.

# JJMIE

**Jordan Journal of Mechanical and Industrial Engineering**

# The Effect of Acrylic Reinforcement with Different Types of Composite Material on the Impact Energy

## Raed Naeem Hwayyin[1*] , Ahmed Salman Hammood[2], Azhar Sabah Ameed[3]

*[1]University of Technology/ Petroleum Technology Department, Baghdad-Iraq*
*[2]University of Technology/Factory and Training Center, Baghdad-Iraq*
*[3]University of Technology/ Electromechanical Department, Baghdad-Iraq*

## Abstract

The study investigates the improvement of the impact energy of acrylic such as (Elastic modulus ($E_c$), Impact strength ($G_c$), and Fracture toughness ($K_c$)) by reinforcing with a composite material consisting of different shapes of metal mesh at different diameters of the circular longitudinal holes and different volume fraction by adopting the Charpy test in determining the experimental results. The specimens of acrylic prepared by cutting them according to the standard of Charpy test specimens (ASTM D-256) using laser beam type $CO_2$ by a CNC machine and then drilling them longitudinally with diameters (2, 4, and 6 mm). Increasing the diameter of reinforcement composite material in acrylic at (2 mm, 4 mm, and 6 mm) caused to an increase in the impact energy at ratio (33.3%, 60%, and, 83.3%) respectively for a fiber that has a rectangular shape at (1mm*1mm), while it increased at ratio (44.4%, 50%, and 60%) for rectangular shape with dimensions (2mm*2mm) and increased in a ratio (61.53%, 64.28%, and, 71.42%) for rhombic shape at dimensions (7mm*7mm). The SEM images showed the occurrence of sharp shear in the wire of the metal mesh of fiber without dislocating it from the composite material which indicates the homogeneity of the composite material and the success of achieving the reinforcement to increase the resistance of the impact composite specimens

## Nomenclatures

| | |
|---|---|
| $A_0$ | is impact of pure acrylic material. |
| A | The specimens prepared from metal mesh type rectangular shape size (1mm*1mm) at diameter (2mm), (4mm) and, (6mm). |
| B | The specimens prepared from metal mesh type rectangular shape size (2mm*2mm) at diameter (2mm), (4mm) and, (6mm). |
| C | The specimens prepared from metal mesh type rhombic shape size (7mm*7mm) at diameter (2mm), (4mm) and, (6mm). |
| $W_m$ | Weight of matrix (polyester) ,(g). |
| $W_c$ | Weight of composite specimens, (g). |
| $W_f$ | Weight of fiber (metal mesh) ,(g). |
| $W_{acr.}$ | Weight of acrylic ,(g). |
| $V_f$ | The volume fraction of fiber , (cm$^3$). |
| $V_m$ | The volume fraction of matrix , (cm$^3$). |
| $V_{acr.}$ | The volume fraction of acrylic , (cm$^3$). |
| $\rho_f$ | The density of fiber , (g/cm$^3$). |
| $\rho_m$ | The density of matrix , , (g/cm$^3$). |
| $\rho_{acr.}$ | The density of acrylic , (g/cm$^3$). |
| $\rho_c$ | The density of composite, (g/cm$^3$). |
| $E_c$ | Elastic modulus of composite (GPa). |
| $E_f$ | Elastic modulus of fiber (GPa). |
| $E_m$ | Elastic modulus of matrix (GPa). |
| $E_{acr}$ | Elastic modulus of acrylic (GPa). |
| m | Mass of the pendulum (kg) |

| | |
|---|---|
| g | Acceleration factor of gravity (m/s$^2$) |
| h | Initial height of pendulum (mm) |
| h' | maximum height fracturing the impact specimens. |
| $U_c$ | Impact energy (J). |
| $G_c$ | Impact strength of material (J/m$^2$). |
| $A_r$ | Cross sectional area of specimen (mm$^2$) |
| $K_c$ | Fracture toughness (MPa . m$^{1/2}$) |

## 1. Introduction

Within the past decade, researchers have studied the development of composite structures with the increasing industrial and construction applications and attention to improve the mechanical properties of acrylic and reinforce it with composite materials in order to obtain higher specifications. The researchers studied the behavior of acrylic used in the manufacture of dentures as a base material during impact loading using cast notches versus automatic slitting under different temperatures. The two forms of slitting (forming and shaping) were performed equally across all specimens [1]. The researchers studied strengthening the high-impact acrylic resins (Metrocryl HI) and its effect by adding zirconia powder at two different concentrations on transverse strength, impact strength, surface hardness, solubility and water absorption

* Corresponding author e-mail: 10596@uotechnology.edu.iq.

[2]. The study presented acrylic as a replacement matrix for thermal hardening compounds for its mechanical superiority and ease formation at low temperature and the possibility of recycling, where Charpy test and, low- speed impact study tests were conducted and compared with conventional compounds manufactured using epoxy resins and polyester with respect to impact resistance[3]. The study investigates the improvement of the mechanical properties of the acrylic layer by creating a crack according to polynomial's function using $CO_2$-laser and without additives. The cracks were created by the laser at different powers and different speeds [4]. The use of metal and fiber reinforcements produces beneficial results [5–6]. Metal wires can be placed inside polymers, but fibers have been demonstrated to be more effective [5]. Metal and glass fiber exhibits different mechanical properties. Due to their high modulus of elasticity, lack of resilience, and poor adherence to the acrylic resin matrix, metals demonstrated significantly higher interfacial stresses within the resin matrix [7, 8]. Salted fiberglass has the ability to adhere to an acrylic type resin matrix [9]. It also has a low elastic modulus if compared to metals that achieve a more appropriate stress distribution pattern [7]. Fiber reinforcement and resin matrix together have similar mechanical performance without high-stress concentration at the interface reducing chances of failure [8]. The interaction between glass fibers and acrylic resins achieves success when a flexible material (such as a matrix of acrylic resin) is used and strengthened with a material such as glass fiber together [7, 10-11].The study examined the improvement of mechanical properties by strengthening using organic fibers in epoxy resins through tensile and bending tests [12]. He investigated the sheets' microstructure, wear-resistance, and impact stress of polymeric materials manufactured at different composition ratios and their effect on improving their mechanical properties[13].The study examined the behavior of composite materials when exposed to impact at low and high speeds to determine the design is reliable and effective in the field of application as well as the cost[14]. The study examined the possibility of benefiting from the use of synthetic fibers from Bagasse in strengthening polyester at different rates and its effect on improving the elastic modulus and the amount of elongation in it [15].They studied the interlayer bonding on the mechanical behavior of the laminated glass through a mathematical model to predict the mechanical behavior based on the type and thickness of the material and the thickness of the glass plate[16].The current study aims to investigate the improvment the mechanical properties of acrylic such as (Elastic modulus ($E_c$) , Impact strength ($G_c$) , and Fracture toughness ($K_c$) ) by reinforcing acrylic impact specimens by inserting composite that material consists of polyester (matrix) reinforced with a different type of metal mesh (fiber) in the cylindrical hole has different diameters.

## 2. Methodology

Determining the mechanical properties of composite materials depends on determining the volume or weight fraction of the materials included in the composite material (fiber and matrix) and the effect of the properties of each of them on the composite material. Practical tests are the accurate means of measuring the properties of composite material, whether it consists of two or more materials. The calculated volume fraction of the fiber and matrix of the composite material contributes to determining the

properties of the final composite material. Mathematical calculations based on experimental results provide real data as well as the effect of changing its ratio on the mechanical properties of the composite material.The resin weight is the difference between the composite specimen and fiber weights[17]:

$$W_m = W_C - W_f \tag{1}$$

And for specimes consist of three composite material the equation will be:

$$W_m = W_c - W_f - W_{acr.} \tag{2}$$

The volume of the fibers (metal mesh) in the composite:

$$V_f = \frac{W_f}{\rho_f} \tag{3}$$

The volume ratioof fiber (metal mesh)to matrix (polyester resin) of the composite material which inserted in the acrylic specimens:

$$\frac{V_f}{V_m} = \left(\frac{W_f}{W_m}\right) * \left(\frac{\rho_f}{\rho_m}\right) \tag{4}$$

While the volume ratio of fiber to the volume of the composite specimens (Vc) consists of three material :

$$\frac{V_f}{V_c} = \frac{V_f \rho_f}{V_f \rho_f + V_m \rho_m + V_{acr.} \rho_{acr.}} \tag{5}$$

Or,

$$\frac{V_f}{V_c} = \frac{1}{1 + \left(\frac{W_m \rho_m + W_{acr.} \rho_{acr.}}{W_f \rho_f}\right)} \tag{6}$$

And, the matrix volume ratio is equal to:

$$\frac{V_m}{V_c} = \frac{1}{1 + \left(\frac{W_f \rho_f + W_{acr.} \rho_{acr.}}{W_{m*} \rho_m}\right)} \tag{7}$$

The density of composite material:

$$\rho_c = \rho_f V_f + \rho_m V_m + \rho_{acr.} V_{acr.} \tag{8}$$

The Young modulus (Elastic modulus) of composite material [17,18] :

$$E_c = V_f . E_f + V_m E_m + V_{acr.} E_{acr.} \tag{9}$$

The impact energy in Charpy test, as in the following equation[19]:

$$U_c = m.g.(h-h\text{ }') \tag{10}$$

The calculation of impact strength can be done by the following equation [20]:

$$G_c = U_c / A_r \tag{11}$$

The fracture toughness,which describes the resistance of material containing a crack to fracture, can be expressed as:-

$$K_c = \sqrt{G_c . E_c} \tag{12}$$

## 3. Material and Methods

### 3.1. Materials

The materials tested acrylic layer reinforced with composites which consist of polyester resin as a matrix and a different type of metal mesh as fiber to improve the impact energy absorption of it. The composite material consists of two materials; the first is polyester as a matrix whose specifications [21] are shown in Table 1, the second is a metal mesh of various types as fibers show in Figure 1. The metal mesh specifications [22] are shown in Table 2. The acrylic specimens are prepared by drilling them longitudinally at different diameters to insert the composite material as shown in Figure 2.
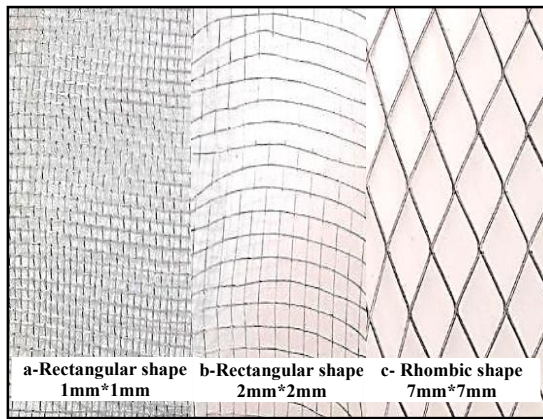
**Figure 1.** a,b and c Types of metal mesh using for reinforced the impact acrylic specimens.
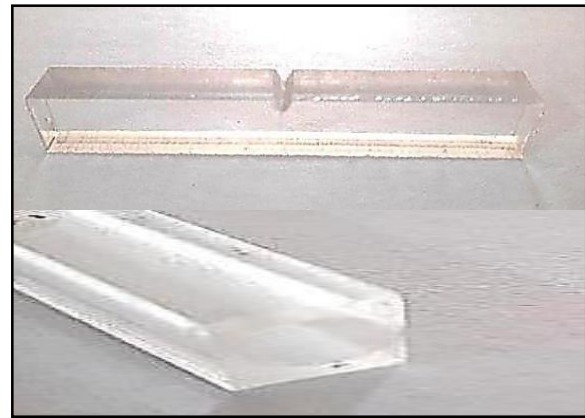


**Figure 2.** The impact acrylic specimens which prepared to insert the composite material in it

**Table 1.** Mechanical Properties of Polyester resin.[21]

| Value | Properties |
|---|---|
| 1.22 | Specific density (at 20 Co) |
| 65 N/mm$^2$ | Tensile stress at break |
| 3.0 % | Elongation at break (50mm gauge length) |
| 3600 N/mm$^2$ | Modulus of elasticity |
| 1268 kg/m$^3$ | Density ( p ) |
| 70 | Rockwell Hardness |

**Table 2.** the properties of metal mesh (fiber) [22].

| Mechanical Property Specification | | | | |
|---|---|---|---|---|
| Grade | Tensile strength (MPa) | Yield Strength (MPa) | Elongation % | Hardness Rockwell (HR B) |
| 904L | 490 | 220 | 35 | 90 |

| Physical Properties | | | | | | | | | |
|---|---|---|---|---|---|---|---|---|---|
| Grade | Density (kg/m$^3$) | Elastic Modulus (GPa) | Mean coefficient of thermal expansion | | | Thermal Conductivity | | Specific Heat (J/kg.K) | Electrical resistivity (nΩ.m) |
| | | | 0-100 C$^o$ | 0-315 C$^o$ | 0-538 C$^o$ | at 20 C$^o$ (W/m.k) | at 500C$^o$ (W/m.k) | | |
| 904L | 8000 | 200 | 15.0 | --- | --- | 13.0 | --- | 0.1846 | 850 |

### 3.1.1. Methods

The study dealt with the variables affecting the reinforcement of the acrylic material represented by changing the cavity diameter of the acrylic impact specimens with diameters (2 mm, 4 mm, 6 mm) by using cylindrical reinforcement on the cavity circumference from a metal mesh having different sizes (1 mm, 2 mm, 7 mm) as in Figure 3, in addition to the ratio of the weight of the materials that make up the composite material on the impact energy.The impact Charpy test is performed for supported acrylic specimens using an impact device of type (XJU-22 Pendulum impact tester) as shown in Figure4-a. The specimens are classified according to their diameter and the type of reinforcing metal mesh (fiber) used in the composite material. The impact tests are prepared by placing the specimen at the base and the notch in the middle and then the pendulum is released to hit the specimen and break it at the notch. The pendulum continues to swing to the maximum height after fracturing the impact specimens that are less than the initial height due to the energy lost in fracturing the specimen which represents the impact energy (U$_c$). The impact specimens are prepared from an acrylic layer, where the laser beam was used for a machine of the type (CNC- Machine ) to cut the impact specimens according to the standard Charpy test specimens (ASTM D-256)[23], which normally measure (55x10x10 mm) as shown in Figure4-b. at impact speed (3.5m/sec).  Impact specimens of acrylic were drilled longitudinally with diameters (2, 4, and 6 mm) for casting the composite material in them.

The casting process of composite material in the longitudinal hole is achieved at room temperature and by adding the hardener with a ratio (0.1) to the polyester.
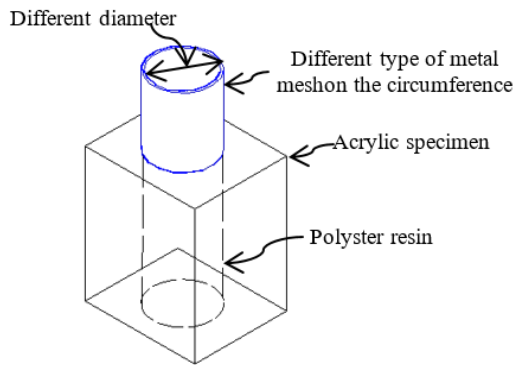
**Figure3.** The reinforcement method of impact acrylic specimens with metal mesh and polyester resin

## 4. Results and Discussion

The purpose of reinforcing acrylic with a composite material in the impact test is to verify the effect of the variable factors on the impact energy and its relationship to the ratio of materials included in the composite material in enhancing the mechanical properties in the impact test such as (volume fraction, type and specifications of the fiber and the matrix so that the method of its arrangement in the composite material).

*4.1. Effect of Young modulus ($E_c$):*

The experimental results of determining the elastic modulus (Young modulus) of the composite material shown in Figure5 present that the specimens type A used a reinforcement with a metal mesh having the characteristics of (metal mesh type rectangular shape size 1mm*1mm) at different diameters (2mm, 4mm, and 6 mm). The specimens type A achieved the highest increase in impact energy with a percentage of (83.3%), while the specimens type (B and C) get maximum increasing with ratio (60 % and 71.4 %) in comparison with the impact energy of pure acrylic specimens (type $A_o$) due to increasing the elastic modulus of a composite material of specimens type (A, B and C) with ratio (85.98%, 81.3% and, 82.58%) respectively.

The specimens type ( A, B, and C) used a metal mesh with specifications of (rectangular shape size 1mm*1mm, rectangular shape size 2mm*2mm, and rhombic shape size 7mm*7mm) respectively. The increase in the elastic modulus represents an increase in the ability of the composite material to absorb the impact energy because it will require higher stress to pass the area of elasticity which gained that increase through reinforcing it with the composite material causing to raise the stress required for fracture.



**a.** Standard specimens      **b.** Charpy impact device

**Figure 4.** a and b The standard impact specimen (ASTM D-256) and the picture of the Charpy impact test
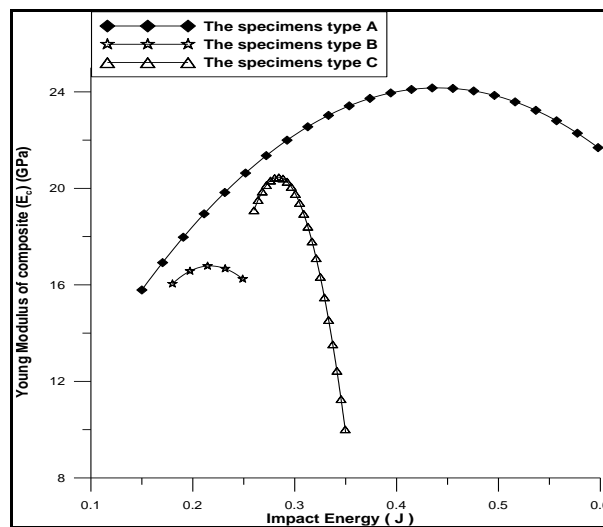


**Figure 5.** The relationship between the Young modulus and Impact Energy of specimens types (A , B and C)

### 4.2. Effect of the impact strength ($G_c$):

The experimental results as shown in Figure 6 reveal that the impact stress has a linear relationship with the impact energy of different types of specimens. The specimens type A showed an increase in impact stress by (83.3%), while the percentage of increase in specimens types (A, and B) was (60% and 71.4%) in comparison to the impact energy of pure acrylic specimens (type $A_o$). The value of the impact stress is related to impact energy because the cross-sectional area of specimens is constant, which represents the distribution of stress on the cross-section area of specimens during the impact test.

### 4.3. Effect of the fracture toughness ($K_c$):

The experimental results shown in Figure7 demonstrate that the strength of the fracture increases for a specific limit in the specimens type (B and C), then the rate of increase gradually begins to decrease as in the specimens of type (B) reinforced with a metal mesh type (rectangular shape size 2mm*2mm), after achieving the maximum increase in the fracture toughness by a ratio (72.65%), while in specimens type (C) reinforced with a metal mesh type (rhombic shape size 7mm*7mm) achieved the highest increase in fracture toughness by (77.69%), then it began to decline. The effective factor on the fracture toughness is the homogeneity of the composite material and the proportion of each of the materials in it. The maximum fracture toughness achieved by specimens type (A) at a ratio(84.71%) reinforced by (rectangular shape size 1mm*1mm).

### 4.4. Effect of the volume fraction Ratio :

The effect of volume fraction ratio is the effect of the ratio of fiber volume (metal mesh), matrix (polyester), and acrylic to the volume of the composite material on the impact energy as shown in Figure8. The increase of the impact energy at ratio (83.3%) due to increasing the volume fraction ratio of the fiber and the matrix with ratio (80.4%, and 21.87%) respectively, while decreasing the volume fraction of acrylic with ratio (8.42%) of specimens type (A). As to the impact energy of specimens prepared according to type (B) increased at ratio (60%) due to increasing the volume fracture ratio of fiber and matrix at (57% and 79.96%) while decreasing the acrylic volume fraction with ratio (23.6%). Meanwhile, the increase of impact energy at ratio (71.42%) of specimens type (C) as a result of increasing the volume fracture ratio of fiber, matrix at (54% and 44.64%)respectively, while decreasing the acrylic volume fraction at ratio (3.96%).The maximum volume fraction ratio to composite volume achieved by acrylic with ratio (86.72 %, 95.17 % and, 95.837%)  than volume ratio of a matrix at (22.51%, 22.05% and, 15.78%) while the volume ratio of fiber at ratio (1.8%, 0.95% and, 1.72%) as shown in Figures9 and 10. of specimens types (A, B and C) respectively.
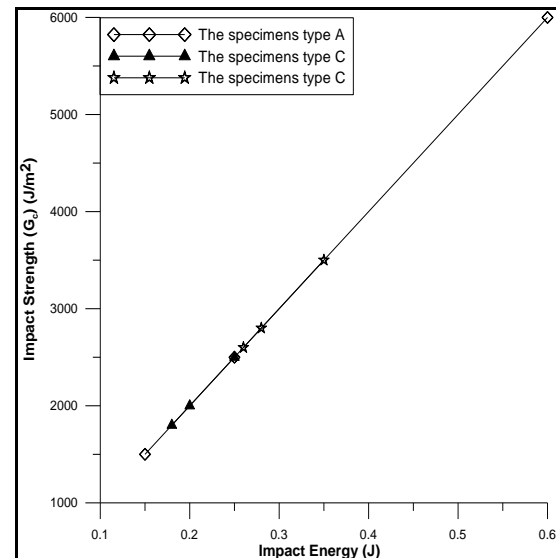


**Figure 6.** The relationship between the impact strength and impact Energy of specimens types (A , B and C)
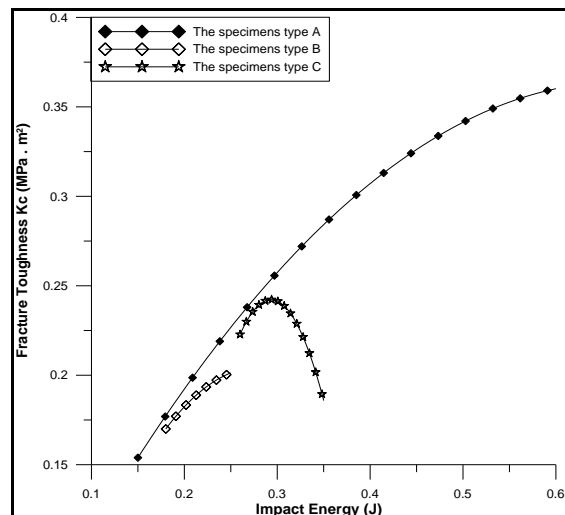


**Figure7.** The relationship between the fracture toughness and impact energy of specimens types (A , B and C)
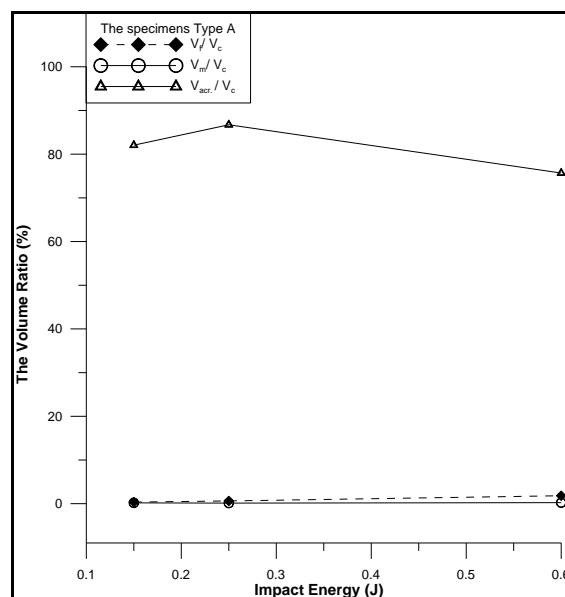


**Figure 8.** The relationship between the volume ratio and impact Energy of specimens types (A)

*4.5. Effect of the weight ratio:*

Determining the mechanical properties of the composite material depends on the weights of those materials that make up the composite material and the ratio of each to the weight of the final composite material. The experimental results showed an increase of power energy at ratio (83.3%) due to an increase in the weight ratio of each of the fibers and the matrix of (78.7% and 15.29%) respectively, while the percentage of acrylic decreased at (17.65%) for the specimens of type A, as shown in Figure(11). The decrease of the weight ratio of acrylic due to the increase in the diameter of the longitudinal cavity of the specimens tangentially causes a decrease in its weight with an increase in the weight ratio of the two other materials of fiber and matrix. The percentage of increased weight ratio of the fibers and the matrix was at (55.18% and, 79.11%) respectively in the specimens type B, while the weight ratio of the acrylic decreased by (28.85%) that caused to increase impact energy at (60%). The weight

ratio of the fibers and the matrix increased at ratio (51.63% and 41.7%) respectively, while the weight ratio decreased at ratio (9.4%) of specimens type C causing to increase impact energy at (71.42%) as shown in Figures 12 and 13.

The experimental tests run on composite specimens of types (a, b, c) and prepared at different diameters and enhanced with different types of fibers and different fractional volumes. It was found that the fracture plane in most of the specimens was at the same fracture plane at V-notch in the Charpy test during the impact test as shown in Figure14 due to the homogeneity of the composite material in the cavity of the acrylic specimens.The fracture zone of the impact specimens is important in clarifying the behavior of the composite spacimens during the impact test which shows the behavior of the composite material without dislocations of the fiber material (metal mesh) reinforcing the composite material from its place through impact test.



**Figure 9.** The relationship between the volume ratio and impact Energy of specimens types (B)



**Figure11.** The relationship between the weight ratio and impact Energy of specimens types (A)



**Figure 10.** The relationship between the volume ratio and impact Energy of specimens types (C)



**Figure12.** The relationship between the eight ratio and impact Energy of specimens types (B)

**Figure13.** The relationship between the weight ratio and impact Energy of specimens types (C)



**Figure 14.** The fracture impact composite specimens type (A, B and C)

due to the cohesion of the composite material consisting of fibers (metal mesh) of small size (1 mm * 1 mm) due to the increase in the number of metal wires in fracture plane which increases the resistance to the movement of dislocations in the composite material during fracture in an impact test.

The increase in impact energy is due to the increase in the percentage of the reinforced composite material that has higher mechanical and physical properties than acrylic. The diameter at (6 mm) achieved the maximum increase in type A specimens by (83.3%), while the percentage increase was (60% and 71.4%) in specimens type (B and C) compared to specimens type (A$_o$) at the same diameter.

The surface of the fracture zone in the impact specimens as shown in Figures.16-a and b by using a Scanning Electron Microscope (SEM). The pictures show the adhesion of the polyester material grains to the fiber (metal mesh) in impact specimens type (A) in the fracture zone after the fracture occurred in the impact test. The continuity of the adhesion of polyester particles on the metal wire after the specimens fracture in the impact test, enhances the homogeneity of composite material which consists of  the polyester and fiber, causing to  improve the mechanical properties of the reinforced acrylic specimens by increase the resistence of impact energy. So that, Figure16-c shows the end of the wires of fiber in the composite material after the impact test. The shear region confirms the successful reinforcement of the composite material inserted in the acrylic specimens and the uniformity of their structure during the impact test. The regions in Figures (16- d, e and f) refer to crack growth path during the impact test process in the wire of fiber which  reinforced the composite material due to the resistance of metal mesh. The fracture surface of impact specimens showed that the wire of fiber was sheared at the same share stress plane of the matrix as a result of homogeneity of the composite material which was inserted in impact specimens.



**Figure 15.** The effect of the hole diameter of composite which inserted in acrylic on the impact energy

*4.6. Effct of diameter of composite material :*

The effect of weight ratio is the effect of the ratio of fiber weight (metal mesh), matrix (polyester), and acrylic to the total weight of the composite material on the impact energy. The experimental results showed the effect of the diameter of the composite material reinforcing the acrylic specimens at diameters (2 mm, 4 mm and, 6 mm), which increased the impact energy by (33.3%, 60% and, 83.3%) respectively in the specimens type (A) so that, it increased with ratio (44.4%, 50% and, 60%) and (61.53%, 64.28% and, 71.42%) for specimens type (B and C) as shown in Figures.15 a and b. The largest increase in impact energy was at the diameter (6) mm in the specimens of type (A)

**Figures 16.** a, b, c, d, e and f   The SEM pictures of fracture surface of composite impact specimens type (A) at different diameter holes (2mm, 4mm, and 6 mm)
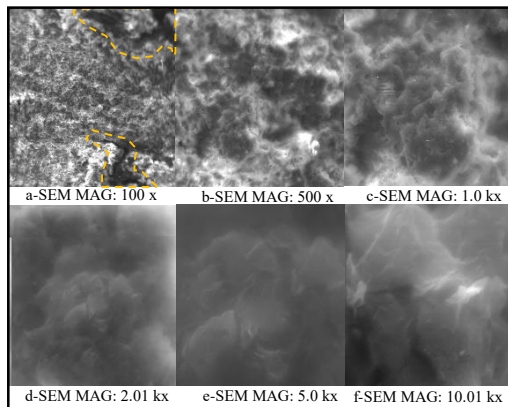


**Figure 18.** The SEM pictures of fracture surface of composite impact specimens type (C)at different diameter holes (2mm, 4mm, and 6 mm)

The SEM picture of the fracture zone of specimens type B at different diameter holes (2mm, 4mm, and 6 mm), shown in Figures 17-a, b, c, d, e and, f show the effect of the concentration of stresses in the regions surrounding the fiber (metal mesh) of the fiber material caused by the impact process of the composite material specimens. The concentration of the stress effect in the matrix surrounding the fiber matrix indicates the occurrence of a high concentration of stresses in the area surrounding the fiber due to the fiber's resistance to impact stress without dislocation the metal wires of the fiber from its place in the composite material. The (SEM) pictures also show that the fiber was sheared sharply at the same plane stress of acrylic plane fracture indicating the effectiveness of the fiber's resistance to shear stress caused by the impact energy of the composite specimens, thus improving their resistance against failure.

The scanning electron microscope (SEM), shown in Figure 18. demonstrates fracture region for impact specimens type C at different diameter holes (2mm, 4mm, and 6 mm) and the growth of the crack in the matrix (polyester) in the composite material caused by the effect of high impact energy on the one hand and the effect of high fiber resistance that explains the presence of more than one crack on the surface of a matrix
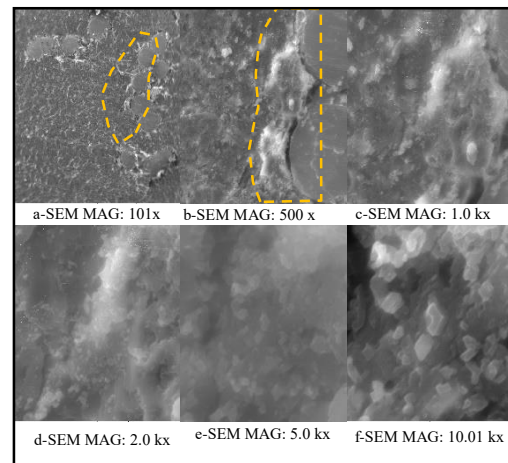


**Figures 17.** a ,b, c, d, e and f  The SEM pictures of fracture surface of composite impact specimens type (B) at different diameter holes (2mm, 4mm, and 6 mm)

(polyester) in the composite specimen. The regularity behavior of the composite material which is inserted in acrylic specimens as one material in resisting the stresses generated by the impact energy without dislocation the fiber enhances its homogeneity in resisting fracture.

## 5. Conclusions

The current study has the following conclusions:
- The maximum increasing in impact energy at a ratio of (83.3%)was achieved with specimens reinforcement with metal mesh and rectangular shape of size dimensions (1 mm * 1 mm) at a diameter (6 mm).
- The increase of the diameter of reinforcement composite material in acrylic at (2 mm, 4 mm, and 6 mm) increased the impact energy at ratio (33.3%, 60%, and 83.3%) respectively in the specimens type (A) while it increased at ratio (44.4%, 50%, and 60%) for specimens type (B) and (61.53%, 64.28%, and 71.42%) for specimens type (C).
- The SEM images showed the occurrence of sharp shear in the wire of the metal mesh without dislocating it from the composite material which indicates the homogeneity of the composite material and the success of achieving enhanced impact resistance of the composite specimens.

### Acknowledgement

### References

[1] Mohamed M. Shehata, Magdy M.M. Mostafa and Amal H. Moubarak, "Effect of Notching on Impact Strength of Thermocyclyed Acrylic Resin Denture Base Material", Volume : 04 ,Issue : 03, Current Science International, ISSN 2077-4435 , 2015, pp.239-244.

[2]  Neveen M. Ayad, Manal F. Badawi, Abdou A. Fatah," Effect of Reinforcement of High-Impact Acrylic Resin with Zirconia on Some Physical and Mechanical Properties", Rev Clín Pesq Odontol. set/dez;4(3): ISSN 1807-5274, 2008, pp.145-151.

[3] G. Kinvi-Dossou, R. Matadi Boumbimba, N. Bonfoh1, S. Garzon-Hernandez, D. Garcia-Gonzalez, P. Gerard and A. Arias, "Innovative Acrylic Thermoplastic Composites Versus Conventional Composites: Improving The Impact Performances",published by Elsevier,Vol.217, 2019, pp.1-13.

[4] R N Hwayyin and A S Hammood, "Improving the Properties of Acrylic by Creating Crack Using Laser Beam",IOP Conf. Series: Materials Science and Engineering 579, 1st International Conference on Petroleum Technology and Petrochemicals, IOP Publishing, ,2019, pp.1-10.

[5] P. K. Vallittu, H. Vojtkova, and V. P. Lassila, "Impact Strength Of Denture Polymethyl Methacrylate Reinforced With Continuous Glass Fibers Or Metal Wire", Acta odontologica Scandinavica, Vol. 53, No. 6,1995, pp. 392–396.

[6] L. E. Bertassoni, G. W. Marshall, E. M. de Souza, and R. Nunes Rached, "Effect Of Pre- And Post Polymerization On Flexural Strength And Elastic Modulus Of Impregnated, Fiber-Reinforced Denture Base Acrylic Resins",Journal of Prosthetic Dentistry,Vol. 100, No. 6, 2008, pp.449–457.

[7] P. Magne, N. Perakis, U. C. Belser, and I. Krejci, "Stress Distribution Of Inlay-Anchored Adhesive Fixed Partial Dentures: A Finite Element Analysis Of The Influence Of Restorative Materials And Abutment Preparation Design",Journal of Prosthetic Dentistry, Vol. 87, No. 5,2002, 516–527.

[8] P. K. Vallittu and C. Sevelius, "Resin-Bonded, Glass Fiber-Reinforced Composite Fixed Partial Dentures: A Clinical Study", Journal of Prosthetic Dentistry, vol. 84, no. 4, 2000, pp.413–418.

[9] G. Basant and Y. G. Reddy, "The Effect Of Incorporation, Orientation And Silane Treatment Of Glass Fibers On The Fracture Resistance Of Interim Fixed Partial Dentures", Journal of Indian Prosthodontist Society, vol. 11, no. 1,2011, pp.45–51.

[10] J. M. Bae, K. N. Kim, M. Hattori et al., "Fatigue Strengths Of Particulate Filler Composites Reinforced With Fibers", Dental Materials Journal, vol. 23, no. 2,2004,pp.166–174.

[11] P. K. Vallittu, "Comparison Of The In Vitro Fatigue Resistance Of An Acrylic Resin Removable Partial Denture Reinforced With Continuous Glass Fibers Or Metal Wires", Journal of Prosthodontics, vol. 5, No. 2,1996, pp.115–121.

[12] Sachin G Ghalme, " Improving Mechanical Properties of Rice Husk and Straw Fiber Reinforced Polymer Composite through Reinforcement Optimization", Jordan Journal of Mechanical and Industrial Engineering, Vol. 15, No. 5, 2021, pp. 411 – 417.

[13] Abdullah M. Al-Huneidei, Issam S. Jalham, " Studying the Properties of Polymer blends Sheets for Decorative Purposes", Jordan Journal of Mechanical and Industrial Engineering, Vol. 7 No.1, 2013, pp. 41 – 48.

[14] S.GHOLIZADEH, "A Review Of Impact Behaviour In Composite Materials", International Journal of Mechanical and Production Engineering,Vol. 7, Issue-3, 2019,pp.35-46.

[15] Fatai Olufemi Aramide, Isiaka Oluwole Oladele, And Davies Oladayo Folorunso," Evaluation of the Effect of Fiber Volume Fraction on the MechanicalProperties of a Polymer Matrix Composite",Leonardo Electronic Journal of Practices and Technologies, Issue 14, 2009, pp.134-141.

[16] O. Alsaed, I. S. Jalham," Polyvinyl Butyral (PVB) and Ethyl Vinyl Acetate (EVA) as a Binding Material for Laminated Glass",Jordan Journal of Mechanical and Industrial Engineering, Vol. 6, No. 2, 2012, pp. 127 – 133.

[17] Reihart T.J. & others, "Engineered Materials Handbook Composites", Vol.1, ASM.International, . 2008.

[18] Abdalla F. H., Megat M. H., Sapuan M. S. and B. B. Sahari, "Determination of Volume Fraction Values of Filament Wound Glass and Carbon Fiber Reinforced Composites", ARPN Journal of Engineering and Applied Sciences, ISSN 1819-6608, VOL.3, NO. 4, 2008, pp.7-11.

[19] H. X. Zhu1 , T. X. Fan & D. Zhang, , "Composite Materials With Enhanced Dimensionless Young's Modulus And Desired Poisson's Ratio", scientific Report Journa, DOI: 10.1038/srep14103, 11 septemper 2015, pp.1-8.

[20] Joshua M. Duell, "Impact Testing of Advanced Composites" ,2004, pp. 97-112.

[21] Raed N. Hwayyin,Azhar Sabah Ameedand Zainab K. Hantoosh," A Study on the Effects of Salt Concentration Environmenton the Mechanical Properties of Polyesterand Composite Materials",Eng. & Tech. Journal, Vol.31, Part (A), No.8, 2013,pp.1459-1473.

[22] Great Steel & Metal company, "ASME SA240 904L Stainless Steel Plate", ISO 9001: Certified Company,2008.

[23] ASTM standard-D256, Published June, Copyright by ASTM, DOI: 10.1520/D0256-10,2010,pp.1-20.

# Research on Robust Control of Automobile Anti-lock Braking System Based on Road Recognition

Gengxin Qi [1, *], Xiaobin Fan[1], Shuaiwei Zhu[1], Xinbo Chen[2], Pan Wang[1], Hao Li[1]

*[1]School of Mechanical and Power Engineering, Henan Polytechnic University, Jiaozuo 454000, P.R. China*

*[2]China North Vehicle Research Institute, Beijing, 100072, China.*

## Abstract

Automobile anti-lock braking system (ABS) is an important component of vehicle active safety control system and is widely used in various automobiles. In the car braking process, the car equipped with ABS can effectively shorten the braking distance, and avoid vehicle side-slip, etc., ensuring the braking performance and driving safety of the vehicle. In order to further improve the performance and robustness of automobile ABS, a robust ABS control method based on road recognition is proposed for the current ABS control method. Based on the fuzzy logic control method, the road surface adhesion coefficient is estimated to realize the road surface recognition, and the optimal slip rate is dynamically obtained. According to the slip rate, a robust controller of ABS is designed. The simulation results show that the robust controller of ABS has good control effect and robustness and can estimate the road adhesion coefficient in real time.

## 1. Introduction

With the development of the automobile industry and the increase of car ownership, the rate of road traffic accidents is also increasing. One of the main factors which causes a lot of traffic accidents and affects traffic safety is driving the car without road information acquisition. To assure the stability of the vehicle under the condition of the critical, anti-lock braking system (ABS), acceleration slip regulation (ASR) and electronic stability program (ESP) have become a necessity for modern car active safety control system [1-2]. ABS can automatically adjust the wheel braking torque to avoid the phenomenon of lock and slip in the braking process. The vehicle is controlled near the optimal slip rate to ensure that the wheel braking has sufficient ground braking force and large lateral force, to improve the directional stability and steering maneuverability of the vehicle, and shorten the braking distance [3].

The control method is the core technology of ABS. Most mature ABS control methods are based on the threshold of speed increment and decrease and the reference slip rate. Although simple and practical, there are some difficulties in debugging and road identification. At present, a variety of ABS control methods with the slip rate as the control target have become the research hotspot. This kind of control method is in the form of continuous quantity control to keep the slip rate optimal and stable during braking. The main control algorithms used in the study of ABS control based on slip rate include logic threshold [4-5], Proportional Integral Derivative (PID) [6-7], fuzzy neural network [8-9], sliding mode control [10-11], optimal control [12-13] and other algorithms. Fu *et al.* [14] took a dangerous goods transport vehicle as the research object and took the slip rate as the control objective, designed the ABS system with three control strategies of Bang-Bang control PID control and adaptive fuzzy PID control, and carried out simulation analysis. Emam *et al.* [15] designed the proportional integral derivative (PID) and fuzzy logic control (FLC) control algorithms based on the optimal slip rate, and carried out simulation tests on rough dry and wet roads, and the results showed that the fuzzy logic algorithm had better control effect. Xu [16] designed a PID control algorithm and a fuzzy PID control algorithm based on the slip rate for anti-lock braking of new energy vehicles. Through MATLAB simulation experiments, it can be proved that the response speed and control precision of the fuzzy PID control algorithm, stability and security can be effectively improved. In order to make full use of the road adhesion ability to improve the braking safety of electric vehicles. On the basis of analyzing the shortcomings of the traditional control algorithm of ABS, He *et al.* [17] proposed a fuzzy immune adaptive PID control algorithm combining the biological immune principle and the adaptive ability of fuzzy logic reasoning. This method had the characteristics of small overshoot, fast response, short braking distance and strong anti-interference ability. Jia *et*

*al*. [18] proposed a kind of ABS adaptive fuzzy PID controller. According to the simulation test, the performance of ABS controlled by adaptive fuzzy PID had been greatly improved compared with the conventional braking system. It had the characteristics of online self-tuning parameters, and had good stability adaptability and robustness. Mao *et al*. [19] proposed an ABS fuzzy immune PID controller. By comparison with traditional PID control through simulation tests, the fuzzy PID free control algorithm had more advantages and higher security in anti-lock braking control. At present, there are more researches on adaptive control or neural control. Yao *et al*. [20] proposed a kind of ADRC of automobile anti-lock braking system, built automobile dynamics model, brake system model, tire model and slip rate model and other major models, designed ABS second-order nonlinear ADRC controller based on slip rate and used MATLAB/Simulink software to control based on active disturbance rejection control (ADRC). Wang *et al*. [21] proposed an electric vehicle anti-lock braking system control method based on radial basis function neural network road recognition. The slip rate was used as the target parameter, and an ABS control strategy combining fuzzy control and predictive control was designed with this, and a braking torque distribution strategy was formulated at the same time. Shen *et al*. [22] established a theoretical model of vehicle anti-lock braking system based on optimal control theory, and compared the effect of ordinary braking and ABS control based on optimal control algorithm through simulation analysis. Wu *et al*. [23] proposed the optimal tracking control of the slip rate for the anti-lock braking system of high-speed vehicles under complex road conditions. Similarly, sliding mode control was also the main control algorithm of ABS due to its robustness, but its chattering cannot be eliminated, which seriously affected its performance. In order to eliminate chattering and enhance its performance, Wang *et al*. [24] proposed an ABS sliding mode variable structure control method based on road surface recognition. This method can recognize the road surface based on the road characteristic coefficient method, dynamically obtain the optimal slip rate of the current vehicle, and then carry out sliding mode variable structure control on the vehicle ABS based on the optimal slip rate. Peri *et al*. [25] proposed a minimum variance control based on digital sliding mode. In the proposed control, the minimum variance enabled the digital sliding mode control to be designed only based on the output measurement of ABS, while the sliding mode control increased the robustness of ABS under certain conditions. Chereji *et al*. [26] proposed an antilock braking system based on sliding mode control algorithm, and introduced two kinds of sliding mode control based on Lyapunov sliding mode Controller (LSMC) and Reach law sliding mode controller (RSMC), and introduced the performance of the algorithm and its application in strongly nonlinear antilock braking system. Wang *et al*. [27] proposed an improved optimal sliding mode control

method for automobile hydraulic anti-lock braking system to achieve robustness and optimal control performance. Wanaskar *et al*. [28] proposed a robust sliding mode controller based on disturbance observer. In order to verify the robustness of the controller, a braking simulation was carried out on a two-axle vehicle model under dry asphalt pavement with snow cover and changing road conditions. Hossein *et al*. [29] proposed a new prediction-based robust controller for antilock braking system, which can guarantee the stability of antilock braking system under uncertainty.

In view of the current ABS control algorithm, in overcoming the high non-linearity, time variability and parameter uncertainty of ABS control, there are problems such as poor anti-interference ability and poor ability to adapt to parameter changes. The most important problem of ABS controller with slip rate as the control target is the stability of the control, that is, the robustness of the system. To improve the robustness of the system, the ABS robust control based on road surface recognition is proposed in this paper. The method realizes road identification by fuzzy logic control algorithm, estimates road adhesion coefficient in real time, and obtains optimal dynamic slip rate. With slip rate as the control objective, ABS robust controller is designed and compared with the traditional PID control method. In this paper, an eight-degree-of-freedom vehicle model is established as the research object, and then the braking experiment and road identification simulation of the control method are carried out through MATLAB/Simulink software to verify its effectiveness.

## 2. Vehicle Dynamics Model

### 2.1. Vehicle Model with Eight Degrees of Freedom

In this paper, the vehicle is simplified as a vehicle model with eight degrees of freedom [30-31]. The vehicle dynamics model is shown in Figure 1, including the transverse motion, longitudinal motion, yaw motion, roll motion, and the rotation motion of four wheels around their respective axes.

The following assumptions are made for the vehicle model:
1. It is assumed that the road surface is relatively smooth, without the vertical and pitching motion of the vehicle in the vertical direction;
2. It is assumed that the origin of the moving coordinate system solidified with the vehicle coincides with the center of mass of the vehicle;
3. Ignore the rolling resistance and air resistance during the movement of tires;
4. It is assumed that each tire has the same mechanical characteristics;
5. It is assumed that the tire angle on the same shaft is the same in the steering process.
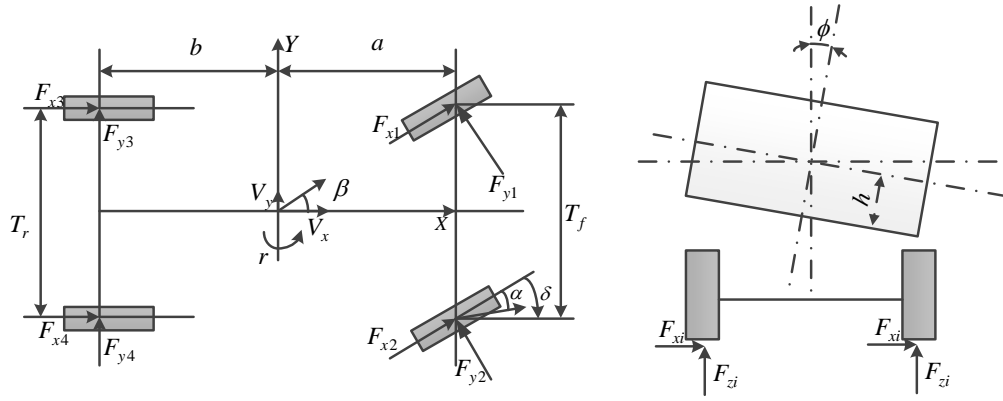
**Figure 1.** Vehicle dynamics model

Lateral motion :

$$m(\dot{v}_y + v_x r) = (F_{x1} + F_{x2})\sin\delta_{df} + (F_{y1} + F_{y2})\cos\delta_{df} + F_{y3} + F_{y4} + m_s h\ddot{\phi} \tag{1}$$

Longitudinal motion :

$$m(\dot{v}_x - v_y r) = (F_{x1} + F_{x2})\cos\delta_{df} - (F_{y1} + F_{y2})\sin\delta_{df} + F_{x3} + F_{x4} - m_s h\dot{\phi}r \tag{2}$$

Horizontal pendulum motion :

$$I_z \dot{r} = I_{xz}\ddot{\phi} + \frac{T_f}{2}(F_{x2} - F_{x1})\cos\delta_{df} + \frac{T_f}{2}(F_{y1} - F_{y2})\sin\delta_{df} + \frac{T_r}{2}(F_{x4} - F_{x3}) +$$
$$a(F_{x1} + F_{x2})\sin\delta_{df} + a(F_{y1} + F_{y2})\cos\delta_{df} - b(F_{y3} + F_{y4}) \tag{3}$$

Rolling motion:

$$I_x \ddot{\phi} = -K_\phi \phi - C_\phi \dot{\phi} + m_s gh\sin\delta_{df} + m_s h(\dot{v}_y + v_x r) \tag{4}$$

Rolling of the wheels :

$$I_{\omega i}\dot{\omega} = T_{di} - F_{xi}R_w - T_{\mu di} \quad (i = 1, 2, 3, 4) \tag{5}$$

In the formula, $m$ is the mass of vehicle reconditioning, $kg$ ; $m_s$ is the sprung mass of the car, $kg$ ; $v_x$ and $v_y$ respectively represent the velocities of vehicles along the $X$ and $Y$ direction, $m/s$ ; $r$ is the angular velocity of the pendulum, $rad/s$ ; $F_{xi}(i = 1,...,4)$ 、 $F_{yi}(i = 1,...,4)$ respectively represent the longitudinal force and transverse force of the tire, $N$ ; $T_{\mu di}(i = 1,...,4)$ is dynamic output braking torque, $N \cdot m$ ; $T_{di}(i = 1,...,4)$ is the wheel driving torque, $N \cdot m$ ; $a$ , $b$ respectively represent the distance from the center of mass to the front and back axis, $m$ ; $h$ is height of the center of mass, $m$ ; $T_f$ and $T_r$ respectively represent the front and rear wheel spacing, $m$ ; $\delta_{df}$ is driver angle input, $rad$ ; $I_x$ , $I_z$ and $I_{xz}$ represent the moment of inertia and product of inertia of the sprung mass around the $X$ and $Z$ axes, respectively, $kg \cdot m^2$ ; $\phi$ , $\dot{\phi}$ and $\ddot{\phi}$ respectively represent the body roll angle, roll angular velocity, and roll angular acceleration, $rad$ , $rad/s$ , and $rad/s^2$ ; $K_\phi$ is the Suspension roll stiffness, $N \cdot m/rad$ ; $C_\phi$ is suspension damping, $N \cdot m \cdot s/rad$ ; $I_{wi}(i = 1,...,4)$ represents rotational inertia of the wheels and their components, $kg \cdot m^2$ ; $R_w$ is wheel radius, $m$ ;

$\omega_i (i = 1,...,4)$ is the angular velocity of the wheel, $rad/s$ .

## 2.2. Brake system model

When braking, the brake hydraulic transmission system can be simplified into a solenoid valve link, a first-order inertia link and an integral link. The simplified model transfer function is shown in formula (6) [3]:

$$G(s) = \frac{K}{s \cdot (T_p s + 1)} \tag{6}$$

In the formula, $s$ is the Laplace operator; $K$ is the system gain; $T_p$ is the time constant.

## 2.3. Tire Model

Considering the nonlinearity in the process of tire motion, the Dugoff model [32] is adopted to analyze the force on the tire.

Longitudinal force of the tire is given as:

$$F_{xi} = C_x \frac{\lambda}{1 + \lambda} f(S_i) \tag{7}$$

Lateral force of the tire is given as:

$$F_{yi} = C_y \frac{\tan\alpha_i}{1 + \lambda} f(S_i) \tag{8}$$

$$S_i = \frac{\mu F_{zi}(1+\lambda)}{2\sqrt{(C_x\lambda)^2 + (C_y\tan\alpha_i)^2}} \quad (9)$$

$$f(S_i) = \begin{cases} (2-S_i)S_i & (S_i \le 1) \\ 1 & (S_i > 1) \end{cases} \quad (10)$$

In the formula, $C_x$ is longitudinal stiffness of tire, $N\cdot m/rad$; $S_i$ is the parameter set in the middle. $\lambda$ is the longitudinal slip of tire; $C_y$ is lateral stiffness of tire, $N\cdot m/rad$; $\alpha_i(i=1,...,4)$ is wheel side slip angle, $rad$. $\mu$ is the longitudinal road adhesion coefficient.

### 2.4. Vertical Load of the Wheel

The vertical load of each wheel is given as:

$$F_{z1} = \frac{mgb}{2(a+b)} - \frac{mh\dot{v}_x}{2(a+b)} - \frac{mh\dot{v}_y b}{(a+b)T_f} - \frac{(K_{\phi f}\phi + C_{\phi f}\dot{\phi})}{T_f} \quad (11)$$

$$F_{z2} = \frac{mgb}{2(a+b)} - \frac{mh\dot{v}_x}{2(a+b)} + \frac{mh\dot{v}_y b}{(a+b)T_f} + \frac{(K_{\phi r}\phi + C_{\phi r}\dot{\phi})}{T_f} \quad (12)$$

$$F_{z3} = \frac{mga}{2(a+b)} + \frac{mh\dot{v}_x}{2(a+b)} - \frac{mh_{cg}\dot{v}a}{(a+b)T_r} - \frac{(K_{\phi r}\phi + C_{\phi r}\dot{\phi})}{T_r} \quad (13)$$

$$F_{z4} = \frac{mga}{2(a+b)} + \frac{mh\dot{v}_x}{2(a+b)} + \frac{mh\dot{v}_y a}{(a+b)T_r} - \frac{(K_{\phi r}\phi + C_{\phi r}\dot{\phi})}{T_r} \quad (14)$$

In the formula, $C_{\phi f}$ is front suspension roll damping, $N\cdot m\cdot s/rad$; $C_{\phi r}$ is rear suspension roll damping, $N\cdot m\cdot s/rad$; $K_{\phi f}$ is front suspension roll stiffness, $N\cdot m/rad$; $K_{\phi r}$ is rear suspension roll stiffness, $N\cdot m/rad$.

### 2.5. Each Wheel Side Slip Angle and Speed of the Wheel Center

Each wheel side slip angle and speed of the wheel center are given as:

$$\alpha_1 = \delta_{df} - arctan\left(\frac{v_y + ar}{v_x - 0.5T_f r}\right) \quad (15)$$

$$\alpha_2 = \delta_{df} - arctan\left(\frac{v_y + ar}{v_x + 0.5T_f r}\right) \quad (16)$$

$$\alpha_3 = -arctan\left(\frac{v_y - br}{v_x - 0.5T_r r}\right) \quad (17)$$

$$\alpha_4 = -arctan\left(\frac{v_y - br}{v_x + 0.5T_r r}\right) \quad (18)$$

$$v_{\omega 1} = (v_x - 0.5T_f r)\cos\delta_{df} + (v_y + ar)\sin\delta_{df} \quad (19)$$

$$v_{\omega 2} = (v_x + 0.5T_f r)\cos\delta_{df} + (v_y + ar)\sin\delta_{df} \quad (20)$$

$$v_{\omega 3} = (v_x - 0.5T_r r) \quad (21)$$

$$v_{\omega 4} = (v_x + 0.5T_r r) \quad (22)$$

### 2.6. Slip Rate Calculation

$$\lambda = \frac{v_x - v_{\omega i}}{v_x} \times 100\% = \left(1 - \frac{\omega_i R_w}{v_x}\right) \times 100\% \quad (i=1,2,3,4) \quad (23)$$

In the formula, $v_{\omega i}(i=1,\cdots,4)$ is the velocity of the wheel center, $m/s$.

## 3. $H_\infty$ Robust Control Design of Automobile Anti-lock Braking System

### 3.1. ABS System Equation

To reduce the complexity of the algorithm, a single-wheel vehicle model is used for algorithm research based on the D'Alembert principle. The model is simplified as two degrees of freedom of the vehicle body in the driving direction and the wheel around the spindle direction. The vehicle dynamics model is shown in Figure 2.
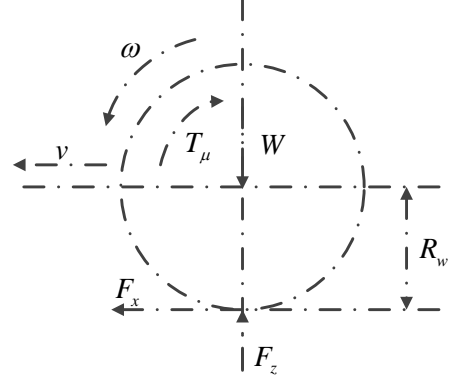


**Figure 2.** Two-degree-of-freedom vehicle dynamics model

$$M\dot{v}_x = -F_{xb} \quad (24)$$

$$I_\omega\dot{\omega} = F_{xb}R_w - T_{\mu d} \quad (25)$$

$$\mu = \frac{F_{xb}}{F_z} \quad (26)$$

In the formula, $M$ is the mass of the car allocated to the wheels, $kg$; $F_{xb}$ is the ground braking force, $N$.

Assuming that the change of vehicle speed is less than that of wheel speed during anti-lock braking, the definition of slip ratio is derived as follows:

$$\dot{\lambda} = -\frac{R_w}{v_x}\dot{\omega} + \frac{\omega R_w}{v_x^2}\dot{v}_x \quad (27)$$

To facilitate the mathematical processing and simulation research in the control process, the brake is assumed to be an ideal component in the calculation, and its nonlinear characteristics are considered weak and the impact of its hysteresis is ignored. Therefore, the brake simplified equation is:

$$T_{\mu d} = C \cdot p \quad (28)$$

In the formula, $C$ is the brake efficiency factor; $p$ is the brake pressure.

Regarding the braking pressure and wheel slip rate of the anti-lock brake system as state variables, the mathematical model of the ABS system is simplified by

referring to the model simplification method of the literature [22]. The state equation of the system is:

$$\begin{bmatrix} \dot{p} \\ \dot{\lambda} \end{bmatrix} = \begin{bmatrix} -\dfrac{1}{T_p} & 0 \\ \dfrac{CR_w}{I_\omega v} & \dfrac{F_x}{Mv} \end{bmatrix} \begin{bmatrix} p \\ \lambda \end{bmatrix} + \begin{bmatrix} \dfrac{1}{T_p} \\ 0 \end{bmatrix} \quad (29)$$

The output equation $Y$ is:

$$Y = \begin{bmatrix} 0 & 1 \end{bmatrix} \begin{bmatrix} p \\ \lambda \end{bmatrix} \quad (30)$$

### 3.2.  $H_\infty$ Robust Control Design

The standard $H_\infty$ control problem is shown in Figure 3. The principle is to design a feedback controller $K(s)$ to optimize the infinite norm of performance indicators. That is，$K(s)$ minimizes the $H_\infty$ norm of the objective function $P$ while stabilizing the controlled object. The performance index is expressed by the transfer function $H_\infty$:

$$J = \inf \|P(s)\|_\infty \quad (31)$$

In the formula, $J$ is performance indicators; $P(s)$ is transfer function matrix including actual objects and weighting functions, etc.
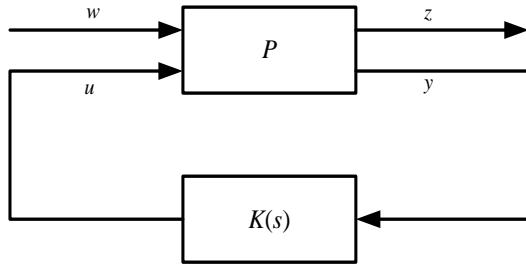


**Figure 3.** Standard $H_\infty$ control problem

In the figure, $P$ is the controlled object; $K(s)$ is the feedback controller; $w$ is the external input signal; $u$ is the control input signal; $z$ is the control quantity; $y$ is the output signal.

Suppose the state space realization of the transfer function $P(s)$ is obtained by formula (32):

$$\dot{x} = Ax + B_1 w + B_2 u$$
$$z = C_1 x + D_{11} w + D_{12} u \quad (32)$$
$$y = C_2 x + D_{21} w + D_{22} u$$

In the formula, $x$ is the state variable.

Formula (32) can also be expressed as:

$$P(s) = \begin{bmatrix} P_{11} & P_{12} \\ P_{21} & P_{22} \end{bmatrix} = \begin{bmatrix} A & B_1 & B_2 \\ C_1 & D_{11} & D_{12} \\ C_2 & D_{21} & D_{22} \end{bmatrix} \quad (33)$$

Block $P(s)$ and $H_\infty$ performance objective function formula (31) are combined as:

$$P(s) = \begin{bmatrix} P_{11} & P_{12} \\ P_{21} & P_{22} \end{bmatrix} = \begin{bmatrix} W_1 & -W_1 G \\ 0 & W_2 G \\ I & -G \end{bmatrix}$$

$$= \begin{bmatrix} A_{W1} & B_{W1}C_G & B_{W1} & 0 \\ 0 & A_G & 0 & B_G \\ C_{W1} & 0 & 0 & 0 \\ 0 & C_{W2} & 0 & I \\ 0 & C_G & I & 0 \end{bmatrix} = \begin{bmatrix} A & B_1 & B_2 \\ C_1 & D_{11} & D_{12} \\ C_2 & D_{21} & D_{22} \end{bmatrix} \quad (34)$$

In the formula, $W_1$ and $W_2$ are weighting functions; $G$ is the state space realization of the transfer function.

The idea of robust control is to transform the performance and stability requirements of the system into the constraints of low frequency and high frequency of the closed loop transfer function. Because it is impossible to simultaneously satisfy the sensitivity index and robust stability in the full frequency domain, it is necessary to coordinate and optimize the two performance index parameters. Therefore, an optimization index with simultaneous weighting of performance and stability is proposed, that is, to seek the infinitesimal norm of controller $K$ to stabilize $G$ to satisfy the inequality. [33]:

$$\left\| \begin{array}{c} W_1 S(s) \\ W_2 (I - S(s)) \end{array} \right\|_\infty \le 1 \quad (35)$$

In the formula, $S(s)$ is the sensitivity function.

Among them, the sensitivity function is:

$$S(s) = (I - (G(s)K(s)))^{-1} \quad (36)$$

The selection principle of weighting function is as follows:

1. Decrease sensitivity in middle and low frequency region. Due to the existence of target input and interference spectrum in the middle and low frequency bands, the sensitivity characteristics are greatly affected, so the sensitivity reduction processing is carried out in the middle and low frequency bands.
2. Increase sensitivity in high frequency region. In the high frequency region, due to the bad model accuracy and sensor noise, the robust stability is greatly affected, and the sensitivity increment is increased to improve the anti-high frequency noise characteristics and stability.

According to the above selection principle, weighting functions $W_1$ and $W_2$ are selected according to the characteristics of ABS control system. The robust control weighting function $W_2$ is the model error bound, so the definition of $W_2$ should be defined according to the error shape. According to the analysis of the wheel dynamics equation, it is concluded that it is a first-order inertial link, and the error transfer function of the model does not decrease in the high frequency region when the parameters have errors. In order to make the parameters change in a certain range, $W_2^{-1} = 10(s/100+1)/(s+1)$ is selected according to the simulation practice. According to the ABS control principle based on slip rate, the ABS control system requires the output slip rate to track the expected slip rate, and the step response of the system error is required to asymptotically approach zero. Therefore, when selecting $W_1$, the sensitivity function is guaranteed to be

as small as possible. In addition, the requirements of $W_1$ and $W_2$ are in conflict, so the relationship between the two functions should be coordinated, and $W_1^{-1}=(s+1)/(s/100+1)$ is selected.

In this paper, the MATLAB robust control box is used to solve the $H_\infty$ robust control, and the mksys () and augtf () functions in the robust control box are used to establish variables describing the system and turn the augmented transfer function model into a standard $H_\infty$ control problem. The optimal $H_\infty$ control problem is solved by using the hinpof () function. This article takes a certain type of car as the research object, and the vehicle structure parameters are shown in Table 1.

According to the above analysis and the state equation of anti-lock system, the $H_\infty$ robust controller is solved by using hinfpof command in MATLAB software, and the result is a fourth-order model.

By building the vehicle model, braking system, and road recognition module in MATLAB/Simulink, the $H_\infty$ robust controller is finally used to control the ABS system. The control principle is shown in Figure 4.

**Table 1.** Vehicle Structure Parameters

| Parameters and symbols | Numerical value/unit |
| --- | --- |
| Vehicle mass $m$ | 1764 $kg$ |
| Sprung mass $m_s$ | 1646 $kg$ |
| The distance from the center of mass to the front axis $a$ | 1.09 $m$ |
| The distance from the center of mass to the back axis $b$ | 1.53 $m$ |
| Vehicle wheelbase of front and rear $T_f$, $T_r$ | 1.535 $m$ |
| Tire radius $R_w$ | 0.35 $m$ |
| Height of the center of mass $h$ | 0.30 $m$ |
| Moment of inertia of sprung mass around $X$ axis $I_x$ | 288 $kg·m^2$ |
| Moment of inertia of wheel and its components $I_\omega$ | 2400 $kg·m^2$ |
| Moment of inertia of sprung mass around the $Z$ axis $I_z$ | 1353 $kg·m^2$ |
| Longitudinal stiffness of tire $C_x$ | 70000 $N·m/rad$ |
| Lateral stiffness of tire $C_y$ | 55000 $N·m/rad$ |
| Suspension roll damping $C_\phi$ | 4000 $N·m·s/rad$ |
| Suspension roll stiffness $K_\phi$ | 50000 $N·m/rad$ |

$$K(s) = \frac{-3.623s^4 + 1.124 \times 10^6 s^3 + 3.975 \times 10^7 s^2 + 1.886 \times 10^8 s + 2.406 \times 10^8}{s^4 + 2.263 \times 10^4 s^3 + 4.92 \times 10^6 s^2 + 7.148 \times 10^7 s + 6.658 \times 10^7} \tag{37}$$
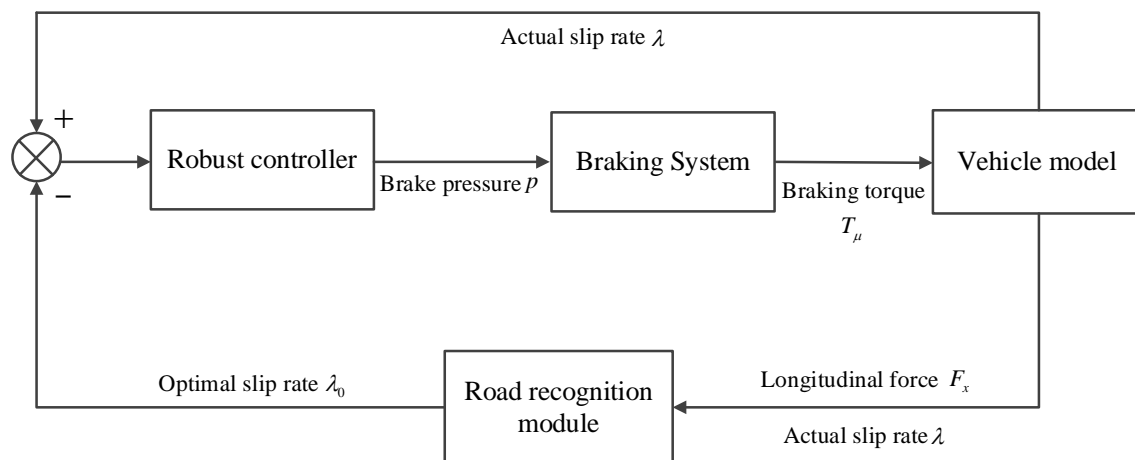


**Figure 4.** Schematic diagram of control system

## 4. Estimation of Road Adhesion Coefficient and Calculation of Optimal Slip Ratio

By analyzing the relationship between tire longitudinal force and slip rate, the adhesion coefficient of the road surface is determined. The Burckhardt tire longitudinal force model is selected as the research object, and various typical road surfaces are fitted through a large number of road tests $\mu-\lambda$ (adhesion coefficient-slip rate) relationship curve. The expression is given as [34]:

$$\mu(\lambda) = c_1\left(1-\exp(-c_2\lambda)\right) - c_3\lambda \qquad (38)$$

In the formula, $c_1$, $c_2$ and $c_3$ are the fitting coefficients obtained from the experiment.

### 4.1. Design Road adhesion coefficient estimation based on fuzzy logic algorithm

Taking a single wheel as the road identification object, the longitudinal force $F_x$ and slip rate $\lambda$ of the tire are obtained by using the above eight-degree-of-freedom vehicle model and the Dugoff tire model. The longitudinal force $F_x$ and slip rate $\lambda$ are used as the input of the road identification module by using the fuzzy logic control to realize the identification of the current road.

1. Parameter fuzzification

It can be seen from Figure 5 that when the wheel slip rate is low, the discrimination of the road surface is low, and it is more difficult to identify the current road surface. When the slip rate is low, the identification of the road surface will not affect the work of the chassis safety system.

As shown in Figure 5, the slip rate is fuzzified into two fuzzy subsets [0,0.01) and (0.01,1]. When the slip rate is greater than 0.16, the membership degree of the fuzzy subset of the large slip rate is 1. According to experience, the tire longitudinal force is normalized and blurred, as shown in Figure 6.
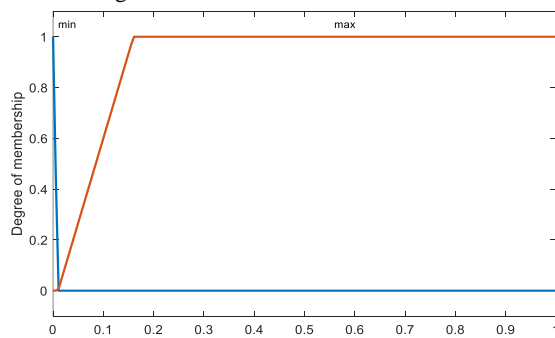


**Figure 5.** The fuzzification of wheel slip rate
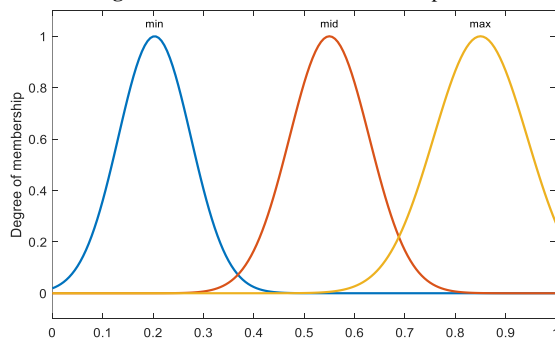


**Figure 6.** The fuzzy normalization of wheel longitudinal force

2. Fuzzy rulemaking

The identification results are continuously adjusted to make them consistent with the actual situation. The fuzzy rules are shown in Table 2. The fuzzy wheel slip rate and the normalized and fuzzy wheel longitudinal force are taken as the input of the fuzzy inference system, and the fuzzy weights coefficients $c_1$, $c_2$ and $c_3$ are outputs.

**Table 2.** Fuzzy rule table

| Rule | Input | | output | | |
|---|---|---|---|---|---|
| | $\lambda$ | $F_x$ | $c_1$ | $c_2$ | $c_3$ |
| 1 | min | none | max | min | max |
| 2 | max | min | min | max | min |
| 3 | max | mid | mid | mid | mid |
| 4 | max | max | max | min | max |

3. Clarification

After the wheel slip rate and longitudinal force are blurred, they need to be cleared to get the desired output. Using the advantages of Gaussian membership function, the output weight coefficient is given better resolution. Combined with Figure 7, the center of gravity method is used to clarify the amount of blur [35].



(a)



(b)



(c)
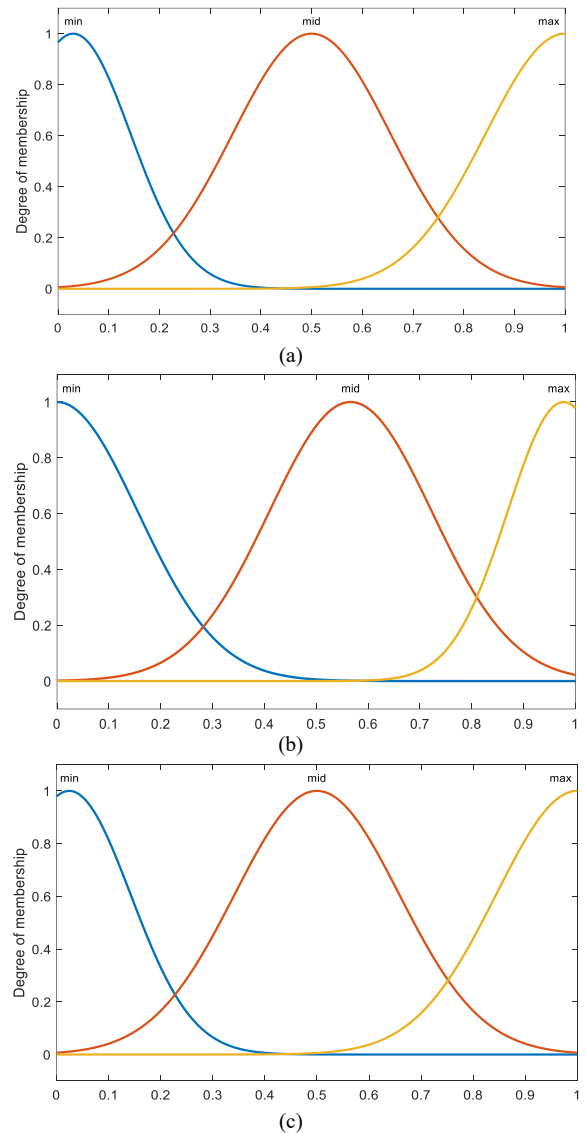
**Figure 7.** Clarifying fuzzy subsets and membership functions

*4.2. Calculation of Optimal Slip Ratio*

According to equation (38), let $\partial\mu/\partial\lambda = 0$, and get the optimal slip rate:

$$\lambda_0 = \frac{1}{c_2}\ln\frac{c_1 c_2}{c_3} \qquad (39)$$

In the formula, $\lambda_0$ is the optimal slip rate; $c_1$, $c_2$ and $c_3$ are the weight coefficients obtained by fuzzy logic algorithm.

## 5. Simulation Results and Analysis

*5.1. Simulation Results and Analysis of Robust Control*

This paper selects a certain type of car as the research object, and the vehicle structure parameters are described in Table **1** above. The test condition selects a road with a road adhesion coefficient of $\mu = 0.8$, and the vehicle speed is set to 80 *km/h*. The simulation model of ABS is established by Matlab / Simulink software platform, and the obtained $K(s)$ is used as the robust controller of ABS to simulate, and the dynamic response of the system is obtained. The simulation results are shown in Figure 8-10.
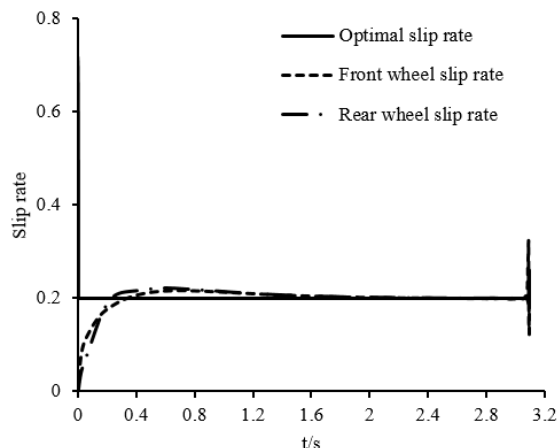


**Figure 8.** Slip rate curve
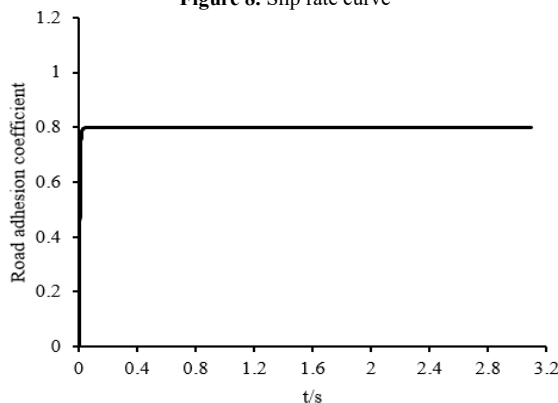


**Figure 9.** Road adhesion coefficient
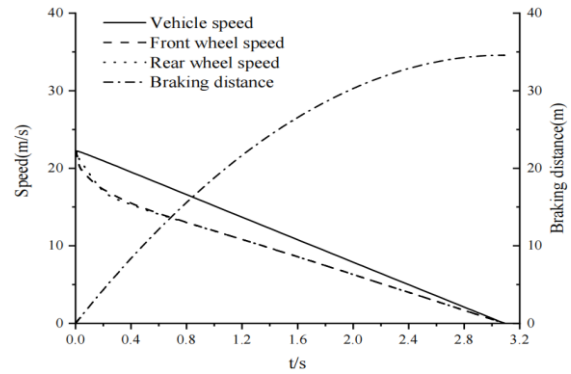


**Figure 10.** Robust control of vehicle speed, wheel speed, and braking distance curve

According to Figure 8, the wheel slip rate basically changes around the optimal slip rate, indicating that the front and rear wheels can make full use of the maximum ground adhesion to improve the braking performance, so that the car can stop within the shortest distance. According to Figure 9, it shows that the road surface recognition module can accurately estimate the current road surface adhesion coefficient and has a better control effect. As shown in Figure 10, after the ABS system is used, the vehicle speed and wheel speed are constantly decreasing, and finally reduced to 0 at the same time, indicating that the wheels are locked when the vehicle brake stops, which improves the handling stability in the braking process. According to the national passenger vehicle braking standard, when the braking speed is $80 km/h$, the braking distance needs to meet $\leq 50.7m$. According to the braking distance curve, when the braking speed is $80\,km/h$, the braking distance is $34.56m \leq 50.7m$, which meets the national standard.

*5.2. Simulation Comparative Analysis of Traditional PID Control and Robust Control*

Traditional PID algorithm is a widely used and mature control method. It does not need to understand the mathematical model of the controlled object, as long as the parameters are adjusted online according to the system situation, and the appropriate proportional, integral and differential coefficients are matched [36]. The simulation model of ABS is established by MATLAB/Simulink software platform. Based on the traditional PID algorithm, the dynamic response of the system is obtained. The simulation results are shown in Figure 11-14.
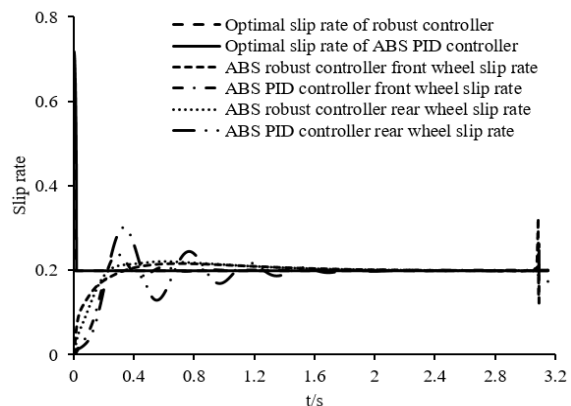


**Figure 11.** Slip rate curve
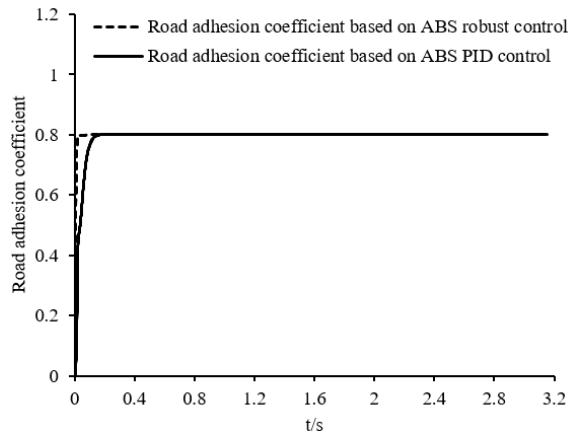
**Figure 12.** Road adhesion coefficient
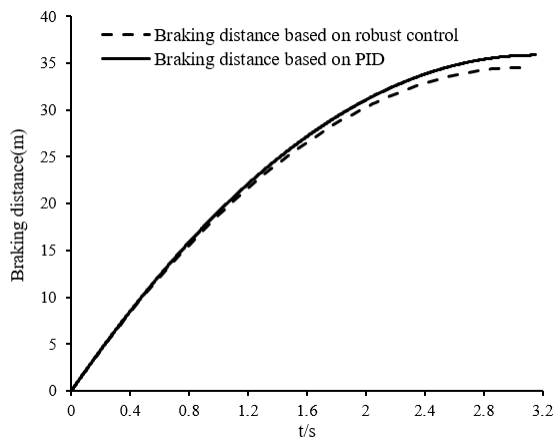


**Figure 13.** Braking distance curve
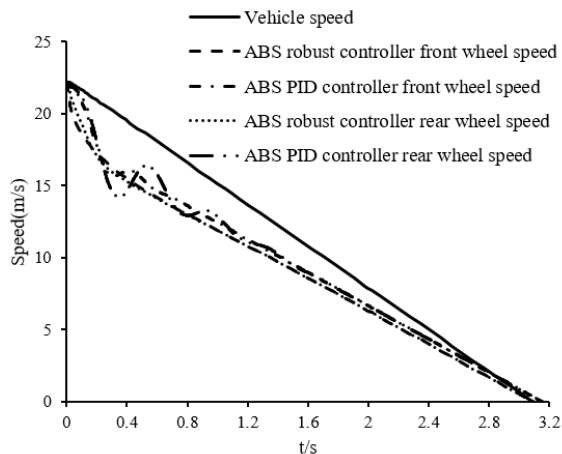


**Figure 14.** Vehicle speed and wheel speed curve

According to the simulation results in Figure 11 and 12, Wheel slip rate of ABS system based on the traditional PID control algorithm basically changes near the optimal slip rate, and the road surface identification module can accurately estimate the road surface adhesion coefficient, which has a good control effect. According to Figure 13, the braking distance satisfies $\leq 50.7m$ and meets the national standard.

**Table 3.** Braking effect

| control arithmetic | Braking time ($s$) | Braking distance ($m$) |
|---|---|---|
| Traditional PID controller | 3.15 | 35.99 |
| Robust controller | 3.09 | 34.56 |

As can be seen from Figure 11-13 and Table 3, when the robust controller works, the car stops at 3.09 $s$ and the braking distance is 34.56 $m$. When the traditional PID controller is used, the car stops at 3.15 $s$ and the braking distance is 35.99 $m$. According to Figure 14, the change curve of speed and wheel speed based on traditional PID control are not as smooth as that of robust control. In terms of control accuracy, response time and robust stability, the robust controller is more superior than the traditional PID controller. The robust controller can ensure that the car completes the braking process with shorter braking distance and less braking time, and the safety factor is higher

## 6. Conclusion

In this paper, the robust ABS controller based on road surface recognition is designed. The adhesion coefficient of road surface is estimated by fuzzy logic control method to realize road surface recognition, and the optimal slip rate is obtained dynamically. According to the obtained dynamic slip rate, the robust controller of ABS is designed. Compared with the traditional PID control ABS system, the ABS system based on robust control can control the wheel slip rate near the optimal slip rate, make full use of the maximum ground adhesion, and obtain sufficient ground brake force. The robust controller can ensure that the car completes the braking process with a shorter braking distance and braking time, with higher safety factor, rapid response, better robustness and stability, and the overall control effect is better than PID control. Therefore, it can provide a theoretical reference for the actual ABS control system.

## Acknowledgements

## References

[1] Wu J, Liu YH, Wang FB, Bao CJ, Sun Q, Zhao YQ. Vehicle active steering control research based on two-DOF robust internal model control. Chinese Journal of Mechanical Engineering,2016, 29(04),739-746.

[2] Chen J, Song J, Li L, Ran X, Jia G, Wu KH. A novel pre-control method of vehicle dynamics stability based on critical stable velocity during transient steering maneuvering. Chinese Journal of Mechanical Engineering, 2016, 29 (03), 475-485.

[3] Zhao ZX, Fan XB, Jin K, Wang F. Simulation study of ABS Fuzzy control based on road surface recognition. Laboratory science,2017,20(05):75-80.

[4] Hu K. Research on Air Pressure ABS Control Algorithm Based on Threshold Logic. MSc Dissertation, Hunan University, Changsha, China, May 2013.

[5] Li G, Wang Y, Zhao DY. Study on Control Strategy and Experiment of Automobile ABS Based on Logical Threshold. Modern Manufacturing Engineering, 2017, (07):12-16.

[6] Wu L, Sun Y, Sun YR. Modeling and Simulation of Automobile ABS System Based on Matlab/Simulink. Sensor Detection and Internet of Things,2014,(5):75-80.

[7] Ammar A. Design of neuro-fuzzy self-tuning PID controller for antilock braking systems. Journal of Babylon University/Engineering Sciences,2014,22(4):775 -787.

[8] Ma ZW, Ni LQ, Chen YK, Zhang HQ, Lin F. Research on ABS Control Strategy Based on Neuro-fuzzy PID. Journal of Chongqing University of Technology (Natural Science), 2018, 32 (09):14-22.

[9] Liu J, Du TH, He LL, Xu DB. Fuzzy Neural Network Model Reference Adaptive Control Strategy in Automobile ABS. Automotive Electrical Appliances,2006,(01):4-7.

[10] Okyay A, Cigeroglu E, Baslama SC. A new sliding-mode controller design methodology with derivative switching function for anti-lock brake system. Journal of Mechanical Engineering Science, 2013,227 (11): 2487-2503.

[11] Leng X. Research on Automobile Anti-lock Braking System Based on Sliding Mode Variable Structure. MSc Dissertation, Harbin University of Science and Technology, Harbin, China, March 2009.

[12] Wang JS, Yang XD. Self-seeking Optimal Control of Automobile Anti-lock Braking System. J Automotive Engineering,2004,(03):299-301.

[13] Li WJ, Fu TL, Chen FL, Wang XD. Self-seeking Optimal Control of Automobile Antilock Braking System. Journal of Harbin University of Science and Technology, 2010, 15 (05):27-30+39.

[14] Fu YM, Liu WY. Design of a special vehicle ABS system based on adaptive fuzzy PID control. Guizhou Science, 2021, 39 (02): 91-97.

[15] Emam, A.S., Mohamed, E.S. Enhancement of Anti-locking Brake System Performance by using Intelligent Control Technique with Different Road Conditions[J]. International Journal of Vehicle Structures and Systems,2021,13(1) 37-45.

[16] Xu YF. Research and optimization of anti-lock braking system for new energy vehicles. Microcomputer Applications,2021,37(03):124-127.

[17] He JD, Zheng YJ, Tan Y, Wu G. Research on Vehicle Anti-braking System Control Algorithm Based on Fuzzy Immune Adaptive PID Control. Third International Conference on Digital Manufacturing & Automation. IEEE Computer Society. Guilin, China (2012)

[18] Jia HN, Yao JX. Research on ABS simulation based on adaptive Fuzzy PID control. Automobile Practical Technology, 2020,(03):147-151.

[19] Mao XW, Li GJ. Research on vehicle anti-lock braking system based on Fuzzy immune PID control. Journal of Jiangsu University of Technology,2020,26(04):95-102.

[20] Yao F, Lin XH, Wu ZB, Li GQ, Jiang F. Research on auto disturbance rejection control of automobile anti-lock braking

system. China Journal of Highway and Transport, 2021, 34(03):235-244.

[21] Wang GW, Yin AD. Research on ABS control of electric vehicles based on neural network road recognition. Journal of Hefei University of Technology (Natural Science Edition) ,2020,43(07):878-883.

[22] Shen C, Hui YL, You YC. Optimal control of automobile anti-lock braking system. Journal of Liaoning Transportation College,2005,(02):59-61.

[23] Wu MX. Optimal Tracking Control of Slip Ratio of Anti-lock Braking System for High-speed Vehicles under Complex Road Conditions. Journal of Shanghai Normal University (Natural Science Edition) ,2019, 48(04):375-382.

[24] Wang F, Fan XB, Zhang YM, Jin K, Yang F. Fuzzy identification based on tire/road adhesion feature. Computer Aided Drafting, Design and Manufacturing,2015,25(01):62-67.

[25] Peri S, Anti D, Miti D, Milojkovi M. Generalized quasi-orthogonal polynomials applied in sliding mode-based minimum variance control of ABS. Acta Polytechnica Hungarica,2020,17(4):165-182.

[26] Chereji E, Radac MB, AI SS. Sliding Mode Control Algorithms for Anti-Lock Braking Systems with Performance Comparisons. Algorithms,2020,14(1):2.

[27] Wang JC, He R. Hydraulic anti-lock braking control strategy of a vehicle based on a modified optimal sliding mode control method. Proceedings of the Institution of Mechanical Engineers, Part D: Journal of Automobile Engineering. 2019, 233 (12): 3185-3198.

[28] Wanaskar V, Shendge P, Phadke S. A disturbance observer-based sliding mode control for anti-lock braking system. 2019 Second International Conference on Advanced Computational and Communication Paradigms (ICACCP), Lanzhou China (2019).

[29] Hossein M. Robust predictive control of wheel slip in anti-lock braking systems based on radial basis function neural network. Applied Soft Computing,2018,70:318-329.

[30] Yu HX. Research on Intelligent Vehicle Collision Avoidance Based on State Estimation. PhD Dissertation, Beijing University of Technology, Beijing, China, June 2015.

[31] Wang B, Sun RY. Research on road surface recognition method based on state characteristic factors. Automotive Engineering,2012,34(06):506-510+522.

[32] Liu XY. Research on Vehicle Stability Based on Direct Yaw Torque Control. PhD Dissertation, Hefei University of Technology, Hefei, China, November 2010.

[33] Chen J. Theory and Practice of Automobile Anti-lock Braking System. 1$^{st}$ed. Beijing Institute of Technology Press: Beijing,1999.

[34] Wang B, Sun RY, Xu YH, Wu LD. Road surface recognition method considering road unevenness. Chinese Journal of Mechanical Engineering,2012,48(24):127-133.

[35] Abdalla M O, Al-Jarrah T M. Fuzzy Logic Control of an Electrical Traction Elevator. Jordan Journal of Mechanical and Industrial Engineering, 2011,5(1):97 -106.

[36] Rajagopal, Kalaivani, Ponnusamy, Lakshmi. Hybrid DEBBO Algorithm for Tuning the Parameters of PID Controller Applied to Vehicle Active Suspension System.Jordan Journal of Mechanical and Industrial Engineering,2015,9(2):85-102.

# An Experimental Investigation of Raw Biogas Combustion in a Small Spark Ignition Engine using Cow Manure in Algeria

## Ibrahim Rahmouni[*], Belkacem Adouane[1]

*Department of Physics, Faculty of Matter Sciences, University of Batna 1, Batna, 05000, Algeria.*
*Laboratory of Applied Energetic Physics (LPEA)*

## Abstract

Biogas from organic waste has a good potential to substitute fossil-based fuels. It is a good example of the circular bioeconomy where low quality waste is turned into a high-quality fuel, while bio-nutrients are recovered at the end of the digestion process. This renewable gas can play a vital role for future energy needs. In this study, an experimental investigation has been carried out on a 5 hp single cylinder Honda GX140 gasoline engine coupled to a TD115 Hydraulic Dynamometer, operating with raw biogas and gasoline. The biogas used to fuel the engine is produced from cow manure at mesophilic conditions. Under two engine loading conditions; 0 and 3.5 N.m, the engine performance characteristics were investigated. A significant increase in the exhaust gases' temperature and fuel mass flow rate was observed for the case of raw biogas. The results also revealed that raw biogas generated higher brake thermal efficiency and brake specific fuel consumption compared to gasoline. This will open the door for biogas to substitute partially fossil-based fuels and give positive societal effects in rural areas.

## 1. Introduction

Globally each year, over 105 billion tons of organic wastes are generated by human activities, in two approaches: directly or indirectly. If they were treated more effectively, 10% of the global greenhouse gas GHG emissions can be removed by 2030. For instance, methane has a contribution of about 20% to the total increase in GHG emissions, and we can cut 25% of all man-made methane emissions by treating them through anaerobic digestion [1].

Under anaerobic digestion, without oxygen, the microorganisms in a series of biological processes degrade the organic material for generating two products. The first is biogas, which is a raw gas that consists of methane $CH_4$ (50-70%), carbon dioxide $CO_2$ (30-50%) and other traces of gases like: $H_2S$, $H_2$, $N_2$, $O_2$, $NH_3$ and $H_2O$. Its density of 1.15 $kg/m^3$ is higher than methane density of 0.75 $kg/m^3$ at normal temperature and pressure because of its $CO_2$ Content [2], and due to the fact that the amount of 1 $m^3$ biogas produces around 5.8 kWh of electrical energy [3]. This renewable energy source can be used for heat and electricity generation, or as traffic fuel. It can also be injected in existing natural gas grids after being upgraded to biomethane. The second product is Digestate which is an excellent fertilizer that consists of useful nutrients, such as nitrogen, phosphorous and potassium [4].

Gaseous fuels for internal combustion engines have long been proposed as a way to keep engine efficiency and performance while lowering emissions [5]. For instance, substituting fossil fuels by biogas for vehicles, can reduce between 75% and 200% of $CO_2$ emissions [6]. Biogas has many advantageous like: high octane number, small flammability limits, high self-ignition temperature and high anti-knock index, which are desirable in SI engines [7].

Many researchers are working on enhancing the use of this alternative fuel in SI engines. Increasing the compression ratio, advancing spark timing, $CO_2$ content variations, biogas upgrading, and blending biogas with gasoline, are all subjects dealt with in the biogas field. In the following paragraphs, we find a number of relevant selected works.

Hotta et al., examined a single cylinder spark ignition engine using gasoline and raw biogas at a compression ratio of 10 under wide open and half throttle settings. When compared to gasoline, they discovered an 18% loss in brake power, a 66% rise in brake specific fuel consumption BSFC, and a 12% drop in brake thermal efficiency BTE when the engine is fuelled with raw biogas [8]. Sudarsono et al., studied the influence of compression ratio on the performance of a 3 kW gen-set fuelled by raw biogas. They found that the optimum compression ratio for the gen-set fueled with raw biogas is 9.5. At the optimum compression ratio, maximum brake power, brake torque,

---

\* Corresponding author e-mail: ibrahim.rahmouni@univ-batna.dz.

BTE and BSFC are 450.37 W, 1.66 Nm, 46.93%, and 0.59 kg/kWh, respectively [9].

Samanta et al., examined the effect of spark timing in spark ignition on a single zone SI engine model. They observed that at 27° before top dead center BTDC, spark timing gives the best performance: BTE is 24% and BSFC is 0.29 $m^3$/kWh [10]. Sendzikiene et al., evaluated experimentally an impact of bio-methane gas with a composition of 65% $CH_4$ and 35% $CO_2$ to Nissan Qashqai HR 16DE SI engine on performance characteristics with the engine throttle 15% open, a constant stoichiometric fuel mixture, and various ignition advance angles compared to petrol. They found that in order to obtain optimal engine thermal efficiency, the ignition angle must be advanced by 4°CA [11].

Kim et al., used a mini co-generation engine system to test biogas fuels of various compositions, and the intake air and fuel flow rates were varied to change the equivalence ratio. The results showed that for a given engine load, the $CO_2$ level increased the ignition delay, fuel consumption, and combustion duration while decreasing the combustion speed. However, using a lean burn strategy improves thermal efficiency, and using biogas with a stoichiometric air/fuel ratio can enhance fuel economy at higher loads [12]. Kriaučiunas et al., tested the effect of different biogas mixtures containing on four-cylinder NISSAN's HR16DE spark ignition engine under two separate spark timings (constant and optimum) at 2000 rpm and with a stoichiometric air and biogas mixture. According to the results, raising the $CO_2$ concentration and using the fixed spark timing increased the mass burned fraction combustion duration by 90%, and reduced in-cylinder pressure and BTE. On the other hand, the authors stated that optimum spark timing selection increases BTE [13].

Simsek et al., performed the impacts of the utilization biogas/gasoline fuel mixtures in different volumetric ratios on a single cylinder Honda GX390 model SI engine, with an increased compression ratio at six different engine loads and constant engine speed, in terms of performance and combustion indicators compared with the gasoline operation. They found that the lowest BTE and the highest BSFC were obtained with 100% biogas. Compared to gasoline, a decrease of 16.04% and an increase of 75.52% were observed, respectively [14]. Awogbemi et al., tested a 5 hp single cylinder Honda GX 140 SI engine using a 20:80 biogas petrol blend at speeds ranging from 1000 to 3500 rpm. The results of the testing revealed that the biogas/petrol mix produced more torque, brake power, indicated power, BTE, and brake mean effective pressure

than petrol, but with lower fuel consumption and exhaust gas temperature [15].

Haryanto et al., evaluated the performance parameters on a 2.5 kVA gasoline generator run with 100% biogas at different loads with an incremental of 100 W. Results showed that the generator set can function with raw biogas with 53 % $CH_4$ content, and it was able to handle a maximum load of 1300 W. With load, output power and biogas consumption increased, on the other hand, biogas specific consumption and engine speed decreased. The maximum thermal efficiency of the generator set was calculated to be 11% [16]. Muhajir et al., investigated on SI generator set performances fueled with gasoline, biogas, and LPG at various electric load. The performances of the generator in terms of brake power and torque are almost similar when fed by gasoline, biogas, or LPG. Brake power and thermal efficiency also enhanced when $O_2$ level in biogas increases [17].

Back to our contribution in this paper, in the light of all results seen in the extended literature review above, we present here the first experiments using a lab-made biogas in a small SI engine. The preliminary results are shown and discussed and they are very encouraging. More advanced work is planned in the near future in order to investigate parameters not covered here. A simulation study is in its way to validate our results and investigate parameters we cannot deal with experimentally.

## 2. The Experimental Investigation and Methodology:

### 2.1. Experimental Raw Biogas Production Set-up

Figure 1, shows the schematic diagram of the experimental raw biogas production setup used in this experiment. The work was conducted in the Applied Energy Physics Laboratory (LPEA), faculty of Matter Sciences at the University of Batna 1.

Raw biogas was generated from cow manure from two digesters of 500 L of each, with a total solid (TS) concentration of 7%, at mesophilic conditions of 35°C, and collected in a storage bag. The raw biogas was analyzed by Biogas 5000 Geotech Analyzer. The raw biogas produced is saturated with moisture, and its composition is shown in Table 1.

**Table.1.** Biogas composition

| Component | Value |
|-----------|-------|
| $CH_4$ | 61.3% |
| $CO_2$ | 32.6% |
| $O_2$ | 1.3% |
| $H_2S$ | 245 ppm |
| BAL | 4.7% |
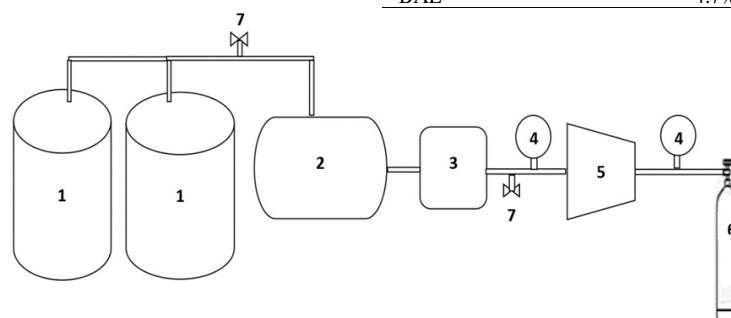


1- Digester of 500 L volume, 2- Storage bag, 3- Biogas analyzer, 4- Manometer, 5- Gas compressor, 6- Bottle, 7- Valve

**Figure 1.** Schematic diagram of the experimental biogas setup

In order to fill-in the produced biogas in bottles, a small compressor, the FN43GY model, was used. Two check valves and two manometers upstream and downstream of the compressor are used for safety reasons. The bottle pressure was maintained at 10 bar, in gaseous phase. This pressure allowed the delivery of the gas to the engine at a constant pressure of about 100 KPa.

### 2.2. Experimental Engine Test Rig

Figure 2, shows the schematic diagram of the experimental engine test rig used in this work. The experiments were carried out in the "Motor Laboratory", at the Department of Mechanical Engineering, University of Batna 2.

The present study was conducted on a 5 hp single cylinder Honda GX140 gasoline engine. This is a four strokes engine with a compression ratio of 8.7:1. The main specifications of the engine are shown in table 2.

The engine was connected to a hydraulic dynamometer, which can adjust the speed and torque using a header tank's water supply. A pulse counting system measures the engine speed electronically. The resulting pulse train is electronically processed to provide a readout of the engine speed. The tachometer optical head is connected to the instrumentation unit through a 5-pin cannon plug/socket.

The engine torque is measured by a rotary potentiometer and transmitted to a torque transducer through a 4-pin cannon plug/socket.

The exhaust gas temperature is measured by a chrome/alumel thermocouple conforming to BS1827. The thermocouple is located into the exhaust pipe close to the cylinder block of the engine. Color-coded leads from the thermocouple are connected to terminals underneath the instrumentation unit. The gasoline consumption is determined by measuring the time (t) taken for the engine to consume 8 ml in the graduated flow pipette.

The raw biogas consumption is also determined by measuring the time (t) taken for the engine to consume $0.01 \, m^3$ of biogas using an (AC-5M) gas meter model.

**Table.2.** Engine specifications [21].

| Item | Specification |
|---|---|
| Type | Four strokes, air cooled, single cylinder, OHV |
| Bore × Stroke | 64 × 45 mm |
| Total Displacement | 144 $cm^3$ |
| Compression Ratio | 8.7:1 |
| Max. Power | 3.6 KW @ 4000 RPM |
| Max. Torque | 9.8 N.m @ 2500 RPM |



1- Engine, 2- Hydraulic dynamometer, 3- Carburetor, 4- Inclined tube manometer, 5- Airbox/viscous flowmeter, 6- Gas meter, 7- Control valve, 8- Biogas flow manometer, 9- Biogas bottle, 10- Gasoline tank, 11-Gasoline tank level, 12- Graduated flow pipette, 13- Tachometer, 14- Torque meter, 15- Exhaust temperature meter, 16- C/A Thermocouple, 17- Rotary potentiometer, 18- Pulse counting system, 19- Thermocouple sockets, 20- 4/5 Pin canon (tachometer/torque transducer).

**Figure 2.** Schematic diagram of the experimental engine test rig

Front Interface

Back Interface

**Figure 3.** Experimental engine test rig.

For the adaption of the biogas fuel for the given engine, the fueling system of the engine was modified. The petrol carburetor was replaced with LPG/CNG gasoline dual fuel carburetor. In this carburetor, the air and raw biogas get mixed in appropriate proportions, before entering the engine cylinder.



**Figure 4.** LPG/CNG gasoline dual fuel carburetor [19].

## 2.3. Experimental Procedure and Mathematical Formulas

The objective of these experiments is to study the variations of the engine performance characteristics, such as exhaust gas temperature, fuel mass flowrate, brake specific fuel consumption and brake thermal efficiency. Under two engine loading conditions, 0 & 3.5 N.m using the hydraulic dynamometer coupled to a single cylinder gasoline engine. The engine was tested with four speed settings: 2000, 2500, 3000 and 3500 rpm. The experiments were conducted for the two fuels, i.e., raw biogas and gasoline.

At each engine speed, the required values such as fuel flowrate, torque and exhaust gas temperature will be recorded to calculate the performance characteristics of the engine. A stop watch and a thermometer were also used for the experiment.

Applying the output value from the experiments and with the help of mathematical formulas, brake power (BP), fuel mass flowrate ($\dot{m}_f$), brake specific fuel consumption (BSFC), and brake thermal efficiency ($\eta_{Bt}$) were measured.

### 2.3.1. Brake power

The brake power is given by:

$$BP = (2 \times \pi \times N \times T) / 60000 \qquad (1)$$

where BP is the brake power (kW), N is the engine speed (Rev/min), and T is the torque (N.m).

With correction to standard condition of pressure and temperature:

$$BPc = BP \times Ps/P \times T/Ts \qquad (2)$$

where BPc is the corrected brake power (kW), Ps and Ts are the pressure and temperature at standard conditions respectively, P and T are the measured pressure and temperature respectively.

### 2.3.2. Fuel mass flowrate

For gasoline, the formula below is used:

$$\dot{m}f = (Sg_f \times V \times 3600) / (t) \qquad (3)$$

where $\dot{m}_f$ is the fuel mass flowrate (Kg/hr), $S_{gf}$ is the specific gravity of fuel, V is volume of fuel ($m^3$), and t is time (sec), where $S_{gf}$ for gasoline: 0.74.

To calculate the mass flowrate of biogas, the following formula is used:

$$\dot{m}f = \rho(\text{actual biogas}) \times V/t \qquad (4)$$

where $\rho$ is the density of the raw biogas($Kg/m^3$).

After pursuing an analytical calculation, the actual density of our biogas is found to be 1.02 Kg/m$^3$.

### 2.3.3. Brake specific fuel consumption

The brake specific fuel consumption is given by:

$$BSFC = \dot{m}_f / BPc \qquad (5)$$

where, BSFC is the brake specific fuel consumption (Kg/kWh).

### 2.3.4. Brake thermal efficiency

The brake thermal efficiency is given by:

$$\eta Bt = (BPc \times 3600) / (\dot{m}_f \times LCV) \times 100 \qquad (6)$$

where, $\eta_{Bt}$ is the brake thermal efficiency (%), and LCV is the lower calorific value (kJ/Kg).

where, the LCV of gasoline is 44000 kJ/Kg, and the LCV of our raw biogas is 20283.09 kJ/Kg.

## 3. Results and Discussion

The engine performance characteristics on gasoline and raw biogas for two different load conditions at various speed were investigated. The results of performance parameters are presented below:

### 3.1. Exhaust Gas Temperature
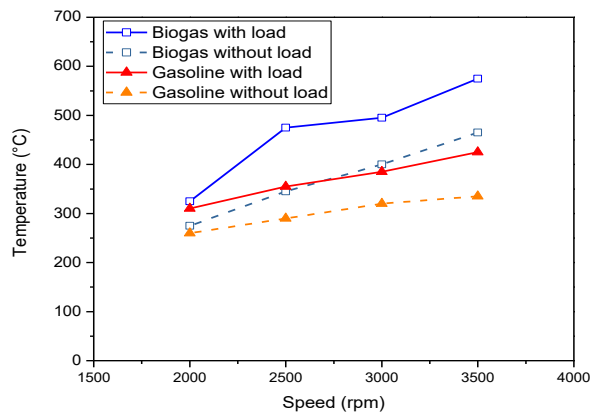


**Figure 5.** Exhaust gas temperature versus engine speed with load and without load for both gasoline and raw biogas.

Figure 5, shows the exhaust gas temperature variation in the two cases (with and without load) fueled with raw biogas and gasoline for different speeds.

It was found that with the increase of speed, the exhaust gas temperature increases gradually for all cases. The case of "load" was usually higher than the case of "without load". This is because the increase of in-cylinder temperature and pressure reaches a maximum of 575°C at 3500 rpm in the case of raw biogas with load compared to 465°C without load. For gasoline, 425°C at 3500 rpm are attained in the case of load compared to 335°C without load.

The reason for the higher exhaust temperature in the case of raw biogas is mainly because of the carburetor used to mix air and biogas, where it is likely that the engine is operating near stoichiometry. Mariani et al., suggested a solution by recycling uncooled exhaust gas (EGR) and mixed with the fresh charge, an air-biogas mixture, to control in-cylinder gas temperature. Depending on the amount of adopted EGR, the intake charge temperature consequently increases [20].

### 3.2. Fuel Mass Flowrate
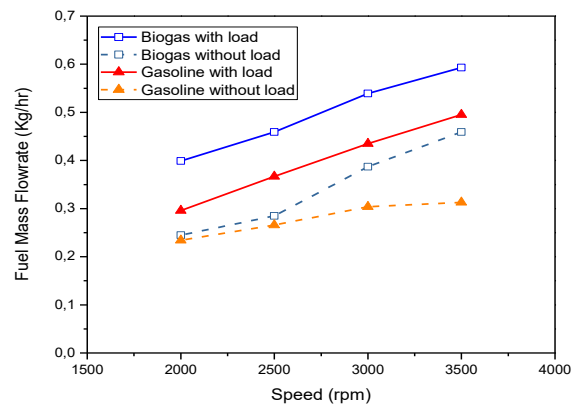


**Figure 6.** Fuel mass flowrate versus engine speed with load and without load for both gasoline and raw biogas.

Figure 6, indicates the variation of fuel mass flowrate in the two cases (with and without load) fueled with raw biogas and gasoline for different speeds.

As expected, it was found that with increasing speed, the fuel mass flowrate increases for all cases. For both fuels, the variation in fuel mass flowrate with load was nearly linear and the cases with load are usually higher than that without load. For the raw biogas, it reached, at a speed of 3500 rpm, 0.593 Kg/hr with load, and 0.459 Kg/hr without load. For gasoline, it reached, at 3500 rpm, 0.495 Kg/hr with load and 0.313 Kg/hr without load.

To create adequate heat input to sustain the load applied to the raw biogas, a larger fuel mass flowrate was required, to compensate for the non-combustible components in the raw biogas, like $CO_2$ and $N_2$, because they have a great impact on the overall performance of the engine. Furthermore, because of the lower density of biogas compared to gasoline, it flows more easily [15].

### 3.3. Brake Specific Fuel Consumption
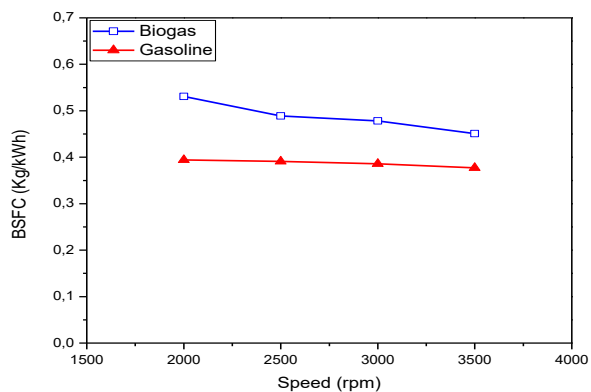


**Figure 7.** Brake specific fuel consumption versus engine speed with load for both gasoline and raw biogas.

From Figure 7, we can see that the BSFC decreases slightly with the speed increase at a constant load. For the case of gasoline, the BSFC is lower than that of the raw biogas, and remains almost constant with speed increasing, with a small decrease at the highest speed. The BSFC falls from 0.531 Kg/kWh to 0.451 Kg/kWh when the speed is raised from 2000 rpm to 3500 rpm for the raw biogas. The BSFC falls from 0.394 Kg/kWh to 0.377 Kg/kWh when the speed is raised from 2000 rpm to 3500 rpm for gasoline.

The lower heating value of biogas compared to gasoline causes the BSFC of biogas to be higher than that of gasoline. It reduces the combustion and flame propagation speed, this means more fuel to achieve the same power. Furthermore, a large amount of $CO_2$ gas present in the raw biogas does significantly increase BSFC values. Using raw biogas with a lower $CO_2$ concentration increases the peak in-cylinder pressure and reduces the BSFC.

The BSFC decrease at higher speeds is very clear for the case of biogas compared to gasoline; this means that approaching the nominal speed, which corresponds to the highest effectiveness of the engine, biogas is more effective in terms of BSFC than gasoline, this is another positive point to be added to biogas. Simsek et al., found also the BSFC value increased with the use of biogas compared to gasoline [14]. Therefore, one can see that to produce the same power output for a certain time lapse, the engine consumes much more raw biogas than gasoline in terms of flowrate only.

### 3.4. Brake Thermal Efficiency
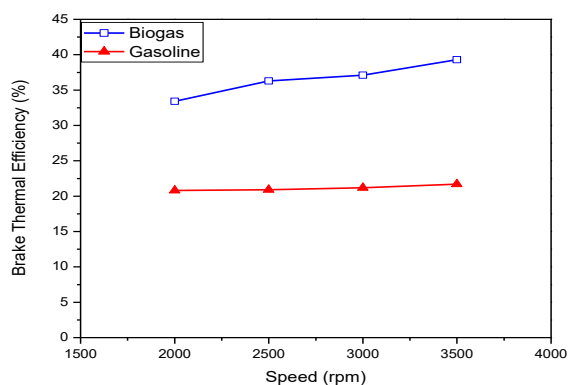


**Figure 8.** Brake thermal efficiency versus engine speed with load for both gasoline and raw biogas.

Figure 8, shows two positive aspects of using biogas as a fuel, first it has a brake thermal efficiency, BTE, higher than that of gasoline, it is almost double at the highest speed of 3500 rpm. Muhajir et al., reported also that the BTE of biogas fueled engine is higher than gasoline fueled engine [17]. On the other hand, the BTE for the case of biogas increases with increasing the engine speed, whereas it is almost constant for gasoline. Aguiar et al., observed that for lower loads, the engine operates with poor efficiency using gasoline [21]. For the raw biogas, with the increase of speed from 2000 rpm to 3500 rpm at a torque of 3.5 N.m, the BTE increases from 33.4% to 39.3%. For gasoline, with the increase of speed from 2000 rpm to 3500 rpm at 3.5 N.m, the BTE increases from 20.8% to 21.7%.

Raw biogas being a gaseous fuel had a better mix with air, improving the combustion process, in addition, a certain proportion of $H_2$ that might be contained in raw biogas can improve the fuel's volumetric burning velocity, which is beneficial to the combustion stability. Zhang et al., concluded that increasing $H_2/CH_4$ ratio in biogas composition increased the engine power output, especially under ultra-lean conditions [22]. Moreover, high resistance to knock permits engines to work at a high compression ratio, producing high thermal efficiency.

### Conclusion

Raw biogas is used to fuel a Honda GX140 engine test rig. The experimental study shows interesting results for raw biogas compared to gasoline. The main conclusions are summarized below:

- The exhaust gas temperature increases by increasing the engine speed and load; for raw biogas, the exhaust gas temperature is higher. At 3500 rpm, the highest temperature was 575°C for raw biogas as a fuel with load, where the minimum temperature was 335°C for gasoline without load.
- The fuel mass flowrate rises sharply with the increase of speed for all cases. For instance, at 3500 rpm with load, the engine consumes 0.593 Kg/hr of raw biogas compared to 0.495 Kg/hr of gasoline.
- At the torque of 3.5 N.m, the BSFC of gasoline is lower than that of raw biogas. For gasoline, between 2000 rpm and 3500 rpm, there is a decrease of around 5%. For raw biogas, between 2000 rpm and 3500 rpm, there is a decrease of around 15%.
- At the torque of 3.5 N.m, the BTE of raw biogas is clearly higher that of gasoline. For raw biogas, between 2000 rpm and 3500 rpm, there is an increase of around 18%. For gasoline, between 2000 rpm and 3500 rpm, there is an increase of around 5%.
- The Brake thermal efficiency BTE of the engine using the two fuels, shows that biogas is performing highly better compared to gasoline; this shows that biogas has all the aspects to play the role of substitute fuel for gasoline and other fossil fuels.
- These preliminary experiments on biogas as a fuel in a small SI engine showed clearly that biogas is a very promising fuel, not only in terms of being $CO_2$ neutral, but also in terms of efficiency and effectiveness. It is clearly proved from the results that the engine is performing better when fueled with biogas.
- The experiments shown above are just an indication of the viability of biogas as a fuel for internal combustion engines, more work is planned to investigate further the impact of this fuel on the engine and its performance.

### Acknowledgment

### References

[1] N. Primmer, "Biogas: Pathways to 2030";2021, World Biogas Association Report.

[2] P.J. Jørgensen, "Green energy"; 2009, Digisource Danmark A/S.

[3] B. Noche, A. Al Mansi, G. De La Torre, "Comparison of Biogas Supply Chains Using the Example of the Conditions of a Municipality". Jordan Journal of Mechanical and Industrial Engineering, Vol. 4, No. 1, 2010, 91-110.

[4] M. Fallde, M. Eklund, "Towards a sustainable socio-technical system of biogas for transport: the case of the city of Linkoping in Sweden". Journal of Cleaner Production, 2014.

[5] R. Ali, S.H. Raheemaha, N.N. Al-Mayyahi. "Numerical Analysis of Combustion Characteristics and Emission of Dual and Tri-Fuel Diesel Engine under Two Engine Speeds".

Jordan Journal of Mechanical and Industrial Engineering, Vol. 14, No. 2, 2020, 205-213.

[6] C.B. Pandya,  R.S. Divyang, M.P. Tushar and P.R. Gaurav, "Performance Analysis of Enriched Biogas Fuelled Stationary Single Cylinder SI Engine". Journal of Mechanical and Civil Engineering (IOSR-JMCE), Vol. 13, No. 2, 2016, 21-27.

[7] K. Ravi, S. Mathew, J.P. Bhasker, E. Porpatham, "Gaseous Alternative fuels for Spark Ignition Engines-A technical review". Journal of Chemical and Pharmaceutical Sciences, Vol. 10, No. 1, 2017, 93–99.

[8] S.K. Hotta, N. Sahoo, K. Mohanty, "Comparative Assessment of a Spark Ignition Engine Fueled with Gasoline and Raw Biogas". Renewable Energy, 2018.

[9] Sudarsono, A.A.P. Susastriawan, I.G. Badrawada, H. Wibowo, D.L. Indrajati, "The Effect of Compression Ratio on Performance of Generator Set Fuelled with Raw Biogas". Journal of Advanced Research in Fluid Mechanics and Thermal Sciences, Vol. 89, No. 01, 2022, 185-195.

[10] A. Samanta, S. Das, P.C. Roy, "Performance Analysis of a Biogas Engine". International Journal of Research in Engineering and Technology, Vol. 05, No. 01, 2018, 67-71.

[11] E. Sendzikiene, A. Rimkus, M. Melaika, V. Makareviciene, S. Pukalskas, "Impact of biomethane gas on energy and emission characteristics of a spark ignition engine fuelled with a stoichiometric mixture at various ignition advance angles".  Fuel, Vol. 162, 2015,194-201.

[12] Y. Kim, N. Kawahara, K. Tsuboi and E. Tomita, "Combustion Characteristics and NOx Emissions of Biogas Fuels with Various $CO_2$ Contents in a Micro Co-Generation Spark Ignition engine". Applied Energy, Vol. 182, 2016, 539-547.

[13] D. Kriaučiunas, S. Pukalskas, A. Rimkus, D. Barta, "Analysis of the influence of $CO_2$ concentration on a spark ignition engine fueled with biogas".  Applied Sciences, Vol. 11, No. 14, 2021, 63-79.

[14] S. Simsek, S. Uslu, H. Simsek, "Experimental study on the ability of different biogas level dual fuel spark ignition engine: Emission mitigation, performance, and combustion analysis".  Oil & Gas Science and Technology - Revue d'IFP Energies Nouvelles, Vol. 76, No. 74, 2021.

[15] O. Awogbemi, Adeyemo, S. Babatunde, "Development and testing of biogas petrol blend as an alternative fuel for spark ignition engine". International journal of scientific and technology research, Vol. 4, No. 09, 2015, 179-186.

[16] A. Haryanto, T.G.T. Nindhia, W. Rahmawati, U. Hasanudin, T.W. Saputra, A.B. Santosa, S. Triyono, "Effect of load on the performance of a family scale biogasfuelled electricity generator". IOP Conference Series: Earth and Environmental Science, Vol. 355, No. 01, 2019.

[17] K. Muhajir, I. G. Badrawada, A. A. P. Susastriawan, "Utilization of biogas for generator set fuel: performance and emission characteristics". Biomass Conversion and Biorefinery, 2019.

[18] Honda Motor Company, L. HONDA GX140. Retrieved from https://www.wersis.net/honda/gx140.html

[19] Kit, GPL.NG. Retrieved from: https://www.slittpeg.com/index.php?main_page=product_info&products_id=267953.

[20] A. Mariani, M. Minale, A. Unich, "Use of biogas containing $CH_4$, $H_2$ and $C0_2$ in controlled auto-ignition engines to reduce NOx emissions". Fuel, Vol. 301, 2021.

[21] P.L. de Aguiar, P.H.S Diniz, L.R. da Costa, R.A. Rattes, A.T. Lopes, R.C. Leitão, W.M. Barcellos, "Performance evaluation of biogas fueled generator set". Journal of the Brazilian Society of Mechanical Sciences and Engineering, Vol. 43:409, 2021.

[22] Y. Zhang, M. Zhu, Z. Zhang, Y.L. Chan, D. Zhang, "Combustion and Emission Characteristics of Simulated Biogas from Two-Phase Anaerobic Digestion (T-PAD) in a Spark Ignition Engine". Applied Thermal Engineering, 2017.

# The Influence of the Layer Orientation on Ultimate Tensile Strength of 3D Printed Poly-lactic Acid

Hussein Alzyod*, Peter Ficzere

*Department of Railway Vehicles and Vehicle System Analysis, Faculty of Transportation Engineering and Vehicle Engineering, Budapest University of Technology and Economics, H-1111 Budapest Műegyetem rkp. 3*

## Abstract

A significant increase in 3D printing technology has been done primarily in the twenty-first century, where there are many research works going on in different fields, such as aerospace, automotive, and medical sectors to improve the 3D printing technology. This paper investigates the effect of printing with four different methods on the tensile strength of the Fused Deposition Modeling printed Polylactic Acid parts. Experimental and statistical analysis found that there is no effect in horizontal printing in both ways, but there is a significant difference in other printing methods.

## 1. Introduction

Additive manufacturing (AM) has evolved tremendously since the patent filing of stereolithography technology (SLA) in the mid-80s [1] into a diverse array available in the market, and founded process categories for polymer processing, which are classified by ISO/ASTM 52900 such as powder bed fusion (PBF), vat photopolymerisation (VP), material extrusion (ME), and material jetting (MJ) [2]. The principle of AM to create final parts directly from CAD models now led to the notion of rapid manufacturing (RM) [1]. According to researchers, RM will significantly impact product development and manufacturing and aid a range of economic and societal effects, and it will be able to create environmentally beneficial designs. [3], [4]. In the coming decade, AM will significantly impact the economy and society [5].In comparison to other techniques, AM has a significant advantage in manufacturing complex-shaped components with multi-material. Moreover, throughout the printing process, a considerable amount of raw materials could be saved. 3D printing products are now widely used in a variety of sectors, such as food [6], aerospace [7], civil engineering [8], automobileindustry [9], [10], AM promotes the implementation of soft and hard tools to assist and reduce the manufacturing process time and enhance mass-replication operations, on the shop floor [11] and produce robust and lightweight parts [7] and spare parts supply chain [12]. The medical field also has a good portionof AM technology [13], [14]. As the Food and Drug Administration confirmed the first 3D printed drug in 2015, there has been an increasing interest in 3D printing of drugs [15].Fused deposition modelling (FDM), as well recognised as fused Filament Fabrication (FFF), is one of the most commonly used in Polymer additive manufacturing (AM)with outstanding mechanical, thermal, and chemical endurance [16], [17]. In comparison to other AM technologies, the FDM approach is significantly simple to set up and use. Several scientific researchers concur that FDM three-dimensional (3D) components are made through heating a fibre thermoplastic polymer filament to near the fusing temperature, then depositing it in an almost molten condition to form the required shape using a heated round spout. When the fibrethermoplastic polymer becomes cold, the material's mechanical properties, like tensile strength and strain, may change. FDM process parameters, such as printing speed, raster angle, layer height, and printing orientation have a significant impact on pattern qualities, and accurate level selection is also critical for component production. The effects of different parameters on responses were investigated in research to evaluate the characteristics of components. Experiments were carried out using a design of experiment (DOE) technique, and the results showed that process parameters, such as air gap, layer height, andraster angle have a significant impact on the responses of FDM-based ABS patterns [18], [19]. An experimental investigation studied the influence of build orientation on strength properties using three distinct AM technologies (3D printer, nano-composite deposition (NCDS), and FDM to produce cylindrical pieces [20]. By conducting various parameters of the FDM process, Anitha et al. used the Taguchi approach to examine the quality attributes of the prototypes [21]. Component orientation and support creation are two important challenges in layer manufacturing. The production of prototypes should be as

* Corresponding author e-mail: Hussein.alzyod@edu.bme.hu.

rapidly as feasible. The most advantageous build orientation of components can shorten lead times and save overall prototype costs. Also, part orientation must be continuously maintained to such a degree that the least amount of support is required. Furthermore, the part must be firmly supported in such a way that the entire contact surface of the support is kept to a minimum during the prototyping process. As a result, the support structure has a limited impact on the prototype's surface properties [22].The pause of printing is needed for some purposes, for example, changing the filament colour, adding an electronic device like sensor or transisitor, and adding a support material with different properties. This replacement takes time before resuming the printing, especially if there is just one extruder [23], [24]. This paper aims to investigate the Ultimate Tensile Strength (UTS) in different printing ways. The null hypothesis was that different printing methods and different printing orientations would have similar UTS. The rest of this article is set out as follows. The used materials, dimensions of the samples, testing machine, and statistical analysis are illustrated in section 2.The resultsof the experimental data and the discussion have also been analysed in section 3. The statistical analysis for the results and the suggested hypothesis is explained in details in section 4. The findings of this article have been explained in the last section.

## 2. Experiment details and methodology

### 2.1. printing machine and printing material

In this work, a FDM 3D printing machine was the Original Prusa i3 MK3S+ 3D, the USA was used (see Table 1 for basic technical details [25]). Parts are created with a Prusament polylactic acid (PLA) filament which is one of the environmentally-safe polymers and can be degradable [26] [27], which is green in colour, 1.75 mm in diameter, and has a tolerance of 0.05 mm, and the properties are shown in Table 2 [28], [29]. A total of twenty specimens were printed in four different ways, with five samples in each mode. The printing ways were continuous horizontal orientation, continuous vertical

orientation, horizontal orientation with a pause, and vertical orientation with a pause. The pause was after 1 mm of printing (after printing the half of specimen), and the printing resumed after the specimen temperature reached room temperature. All samples were produced along the x-axis with a raster angle of +45°/-45° as shown in Figure 1 and the printed parameters were illustrated in Table 3. The experiment began with a 3D modelling design created with solid edge 3D modelling software. Solid Edge 3D is a widely used software in various sectors, such as architecture, electronic parts, manufacturing, and aviation. Solid Edge 3D software has very impressive characteristics, like the range of platforms in its mechanical engineering industry, which allows for creating one-of-a-kind design elements. A three-dimensional design (STL format file) was created according to the standard ISO 527 with 130 mm long, 20 mm in depth, and 2 mm in thickness, shown in Figure 2.
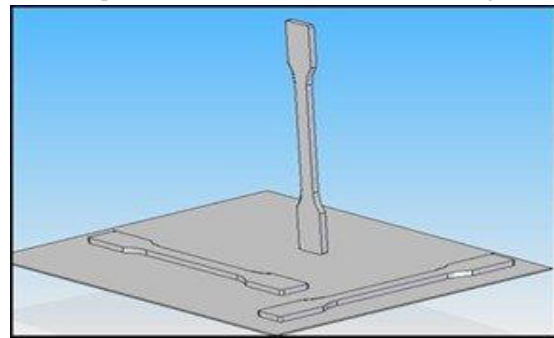


**Figure 2.** Printed Specimen

**Table 1.** Basic technical details for Prusa i3 [25].

| Technical Parameters | Value | Unit |
|---|---|---|
| Build volume | 25 x 21 x 21 | mm |
| Layer height | 0.05 – 0.35 | mm |
| Maximum travel speed | 200 | mm/s |
| Maximum hotend/heatbed temperature | 300 / 120 | °C |
| Filament diameter | 1.75 | mm |
| Nozzle diameter | 0.4 | mm (default) |
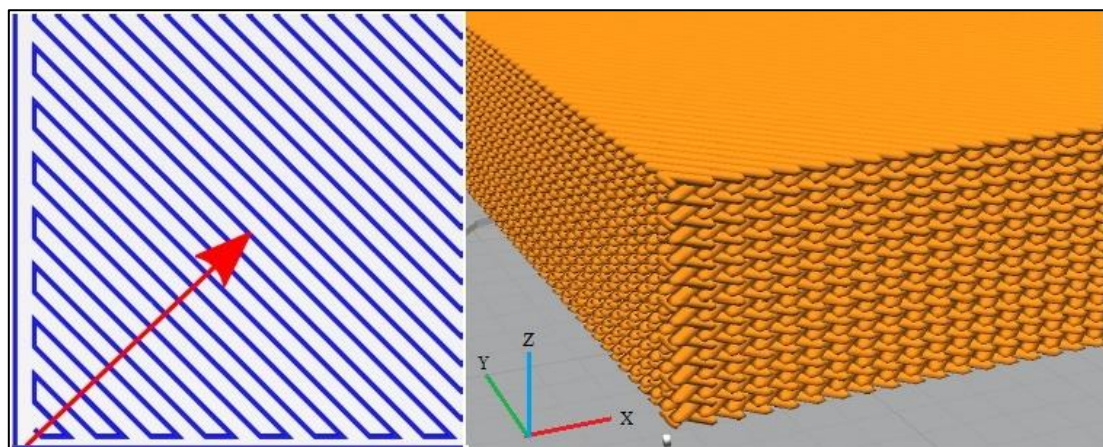


**Figure 1.**Raster angle+45°/-45°.

363

**Table 2** .Property ranges for PLA materials produced using the FDM technique  [28], [29].

| Properties | PLA | Reference |
|---|---|---|
| Tensile strength (MPa) | 15.5–72.2 | [29] |
| Tensile modulus (GPa) | 2.020–3.550 | [29] |
| Elongation at break (%) | 0.5–9.2 | [29] |
| Flexural strength (MPa) | 52–115.1 | [29] |
| Flexural modulus (GPa) | 2.392–4.930 | [29] |
| Printing Temperature (°C) | 190–220 | [28] |
| Printing Speed (mm/s) | 40–90 | [28] |
| Chemical composition | $(C_3H_4O_2)n$ | [30] |

**Table 3.** Printing parameters for all samples.

| Printing parameter | Value | Unit |
|---|---|---|
| Nozzle temperature | 215 | °C |
| Bed temperature | 30 | °C |
| Printing speed | 60 | mm/s |
| Wall speed | 50 | mm/s |
| Wall thickness | 0.4 | mm |
| Layer height | 0.2 | mm |
| Infill density | 100 | % |

The STL file model istransformed into a series of commands for printing layers in the FDM 3D printer, Ultimaker Cura. This software generates a G-Code (G-Programming Language) template providing the whole set of commands and directives to the desired 3D printer, such as printing orientation, speed, nozzle temperature, supports, wall thickness, infill density, and material. This file drives the circular nozzle of the FDM 3D printer and determines the particular routes and paths of printing. The FDM 3D printer uses the G-Code file commands to create the required solid part by extruding the heated PLA filament from the nozzle head and forming a sequence of thin slices upon each other on the bedplate. The circular nozzle moves horizontally along a linear route for each layer. After finishing printing, as shown in Figure , tensile tests are used in this paper to evaluate the mechanical characteristics of PLA materials produced using 3D printing technology. Figure  shows how ZwickiLine was used for small test loads up to 5 kN. The tensile test speed is 5 mm/min, and the laboratory room temperature remains constant at 24 °C during the tensile process. As a result, it can be verified that the test conditions are ambient temperature and semi-equilibrium loading [31].
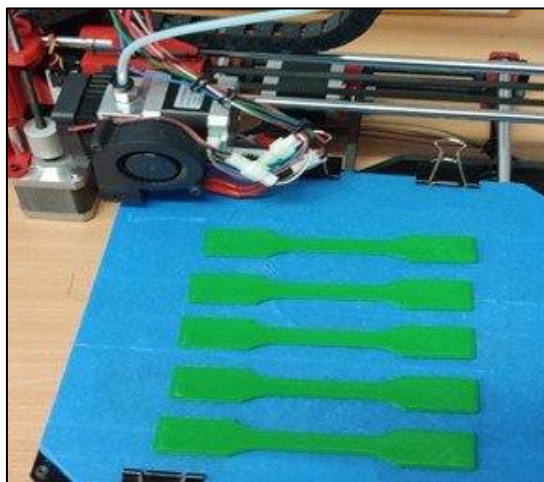


**Figure 3.** Printed specimens.



**Figure 4.** Tensile testing machine.

### 2.2. Statistical analysis

Many statistical tests are used to perform hypothesis testing for mean comparison like Tueky, Bonferroni, Dunn-Sidak, Scheffé, Fisher's Lsd, Holm-Sidak. This paper analysed the data using the Bonferroni method (ANOVA) to analyse the UTS results using OriginLab 2018 software.Before starting the hypothesis testing. Two parameters must be determined, the confidence level and the significant level ($\alpha$). The confidence level denotes the chance that the estimation of a statistical parameter's location in a sample test is also true for the population.Before performing a test, confidence levels should be determined in advance since the error margin, and the test's required scope depends on the confidence level. From 90%-99%, confidence levels are commonly used in testing, and the confidence level $=1 - \alpha$. The significance level ($\alpha$) is the probability of rejecting the null hypothesis when it is true. Theconfidence level and the significant level for the statistical analysis in this paper are 95% and 0.05, respectively.

In statistical analysis, the Bonferroni test is a form of multiple comparison test named after Italian mathematician Carlo Emilio Bonferroni (1892–1960) [32]. When doing a hypothesis test with many comparisons, a result indicating statistical significance in the dependent variable may ultimately arise, even though there is none [33]. According to the Bonferroni test, each test's P-value must be equal to its alpha ($\alpha$) divided by the number of tests executed. The significance level refers to the likelihood that the Bonferroni test would wrongly detect a variation in the sample that does not exist in the population (false positive) means. A 0.05 significance level is a widely used significance level. This study tested 6 comparisons (continuous horizontal vs horizontal with a pause, continuous horizontal vs continuous vertical, horizontal with a pause vs continuous vertical, continuous horizontal vs vertical with a pause, horizontal with a pause vs vertical with a pause, and continuous vertical vs vertical with a pause), there might be up to a 30% likelihood (0.05 + 0.05 + 0.05 + 0.05 + 0.05 + 0.05) that any one of them would demonstrate significant change by chance. By dividing the significance level by the number of tests, the Bonferroni adjustment corrects this. The significance level for a given comparison in this study would be 0.0083, with a chance of incorrectly detecting a difference of no more than 0.05.

## 3. Results and discussion

### 3.1. Experimental results

After printing the five specimens for every printing way, the average curve was drawn to find Young's modulus which represents the slope of the curve based on equation (1) as shown below [34]. The results of the tensile test shown in Table 2 and 5 illustrated that:

$$E = \frac{\sigma}{\varepsilon} \tag{1}$$

**Table 2.** UTS for all printed specimens.

| Printing orientation | UTS | Average UTS | SD |
|---|---|---|---|
| Continuous horizontal | 46.70 | 46.52 | ±0.27 |
| | 46.68 | | |
| | 46.04 | | |
| | 46.60 | | |
| | 46.56 | | |
| Horizontal with a pause | 47.54 | 47.55 | ±0.95 |
| | 47.54 | | |
| | 48.45 | | |
| | 48.22 | | |
| | 46.01 | | |
| Continuous vertical | 26.99 | 24.97 | ±3.70 |
| | 26.48 | | |
| | 18.83 | | |
| | 28.17 | | |
| | 24.37 | | |
| Vertical with a pause | 7.15 | 11.49 | ±4.50 |
| | 18.76 | | |
| | 8.89 | | |
| | 12.40 | | |
| | 10.26 | | |
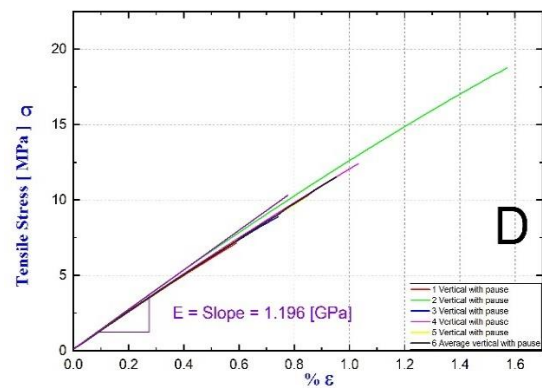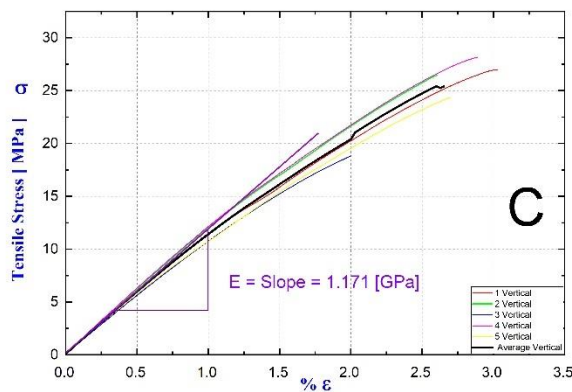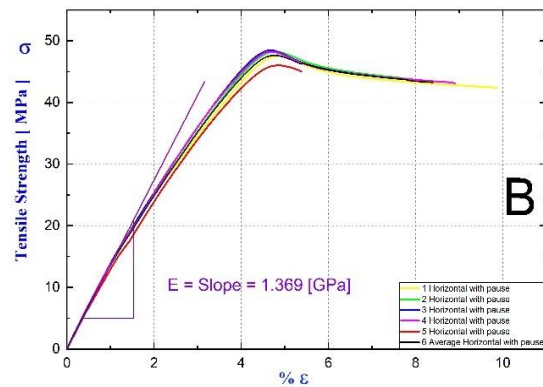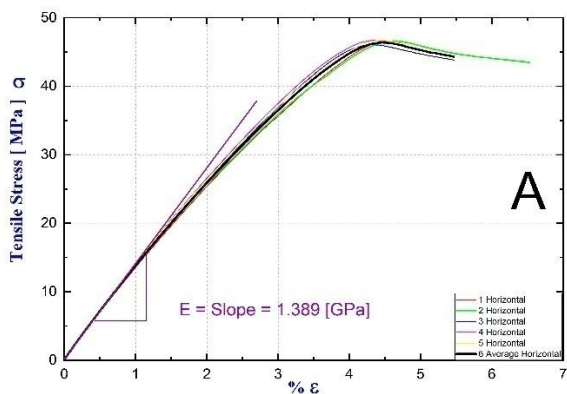


**Figure 5.** Average curves: continuous horizontal orientation (A), horizontal orientation with a pause (B), continuous vertical orientation (C), and vertical orientation with a pause (D).

The two-way horizontal printing showed a significant difference in the tensile strength than the two-way vertical printing. The UTS for continuous horizontal and horizontal witha pause printing was 46.52±0.27MPa and47.55±0.95MPa, respectively, while in the continuous vertical printing,the UTS was almost half of the continuous horizontal printing with UTS 24.97±3.7,and the vertical with a pauseUTS was the lowest with 11.49±4.5. The difference in the UTS between horizontal and vertical orientation is due to the direction of the test being perpendicular to the filament path.This means that in the horizontal orientation, the fracture happened in all layers while in the vertical orientation, the fracture happened just between two layers. Figure shows the box plot of the UTS of the four different ways of printing.

A material's Young's(Elastic) modulus is an essential, fundamental characteristic that defines how the material deforms when stressed [35]. It calculates the strain based on the size of the applied compressive or tensile stress. The greater Young's modulus, the less a material deforms in response to a given stress, making it stiffer. Figure illustratesYoung's modulus for the four printing ways.

### 3.2. Statistical analysis

T-value measures the size of the difference relative to the variation of the sample data. As the t-value increases, the evidence against the null hypothesis increases. The p-value describes how likely is the data randomly occurred by chance.The statistical analyses were done using the Bonferroni method, andTable 3 shows the results.

For horizontal with a pause – continuous horizontal, the t-value is 0.55, and the p-value is 1.0, and according to the Bonferroni test, we failed to reject the null hypothesis. For the rest of the printing methods, we rejected the null hypothesis. Significant equal one denotes that the variation of the means is significant at the 0.05 level and Significant equal zero denotes that the variation of the means is not significant at the 0.05 level.

### 4. Conclusion

The ultimate tensile strength of 3D printed PLA usingthe FDM method has been investigated.The

experimental measurements were done, and the statistical analysis was applied to the results.The null hypothesis was thatdifferent printing methods and orientations might have similar UTS. We found that this hypothesis is true only in continuous horizontal printing and horizontal printing witha pause. The null hypothesis was rejected in continuous vertical printing and vertical printing witha pause. As a result, the pause in horizontal printing will not affect the UTS of the material while there is a significant difference in the UTS in the case of vertical printing.
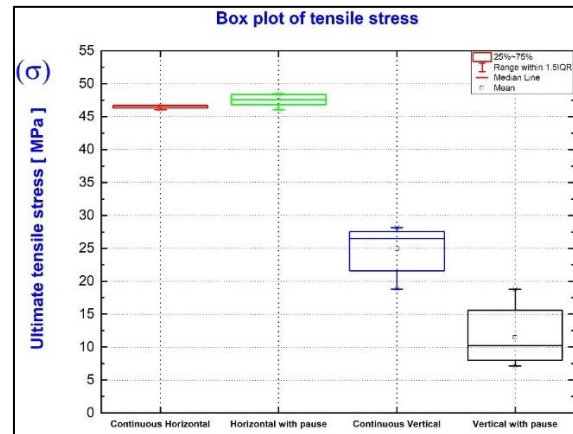

**Figure 6**. Tensile strength
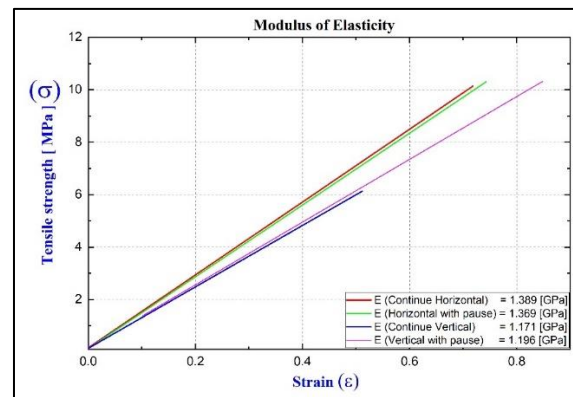

**Figure 7.**Young's modulus.

**Table 3.**Hypothesis test results.

| Printing comparison | Mean difference | t-value | P-value | α | Significant |
|---|---|---|---|---|---|
| Horizontal with a pause – Continuous horizontal | 1.04 | 0.55 | 1 | 0.05 | 0 |
| Continuous vertical – Continuous horizontal | -21.55 | -11.54 | $2.16 \times 10-8$ | 0.05 | 1 |
| Continuous vertical - Horizontal with a pause | -22.58 | -12.10 | $1.10 \times 10-8$ | 0.05 | 1 |
| Vertical with a pause – Continuous horizontal | -35.02 | -18.76 | $1.54 \times 10-11$ | 0.05 | 1 |
| Vertical with a pause – Horizontal with a pause | -36.06 | -19.32 | $9.81 \times 10-12$ | 0.05 | 1 |
| Continuous vertical – Vertical with a pause | -13.47 | -7.22 | $1.23 \times 10-5$ | 0.05 | 1 |

## References

[1] M. Wiese, S. Thiede, and C. Herrmann, " Rapid manufacturing of automotive polymer series parts: A systematic review of processes, materials and challenges," Additive Manufacturing, vol. 36. Elsevier B.V., Dec. 01, 2020. doi: 10.1016/j.addma.2020.101582.

[2] DIN EN ISO/ASTM 52900. BeuthVerlag GmbH, Berlin, 2018.

[3] C. Tuck and R. Hague, "The pivotal role of rapid manufacturing in the production of cost-effective customised products," International Journal of Mass Customisation, vol. 1, no. 2/3, p. 360, 2006, doi: 10. 1504/ IJMASSC. 2006. 008630.

[4] T. A. Campbell and O. S. Ivanova, "Additive manufacturing as a disruptive technology: implications of three-dimensional printing, " Technology & Innovation, vol. 15, no. 1, pp. 67–79, Apr. 2013, doi: 10.3727/194982413X13608676060655.

[5] R. Jiang, R. Kleer, and F. T. Piller, "Predicting the future of additive manufacturing: A Delphi study on economic and societal implications of 3D printing for 2030," Technological Forecasting and Social Change, vol. 117, pp. 84–97, Apr. 2017, doi: 10.1016/J.TECHFORE.2017.01.006.

[6] J. I. Lipton, M. Cutler, F. Nigl, D. Cohen, and H. Lipson, "Additive manufacturing for the food industry," Trends in Food Science & Technology, vol. 43, no. 1, pp. 114–123, May 2015, doi: 10.1016/J.TIFS.2015.02.004.

[7] V. Mohanavel, K. S. Ashraff Ali, K. Ranganathan, J. Allen Jeffrey, M. M. Ravikumar, and S. Rajkumar, "The roles and applications of additive manufacturing in the aerospace and automobile sector," Materials Today: Proceedings, vol. 47, pp. 405–409, 2021, doi: 10.1016/j.matpr.2021.04.596.

[8] N. Labonnote, A. Rønnquist, B. Manum, and P. Rüther, "Additive construction: State-of-the-art, challenges and opportunities," Automation in Construction, vol. 72, pp. 347–366, Dec. 2016, doi: 10.1016/J.AUTCON.2016.08.026.

[9] G. N. H. and G. Dudas. Fedorko, "Design of allocation of new technological equipment within the frame of production process in company Getrag Ford Transmissions Slovakia, sro.," ActaMontanisticaSlovaca, vol. 15, pp. 14–22, 2010.

[10] M. R. Talaganiet al., "Numerical simulation of big area additive manufacturing (3D printing) of a full size car," SAMPE journal, vol. 51, no. 4, pp. 27–36, 2015.

[11] J. C. Vasco, "Additive manufacturing for the automotive industry," Additive Manufacturing, pp. 505–530, Jan. 2021, doi: 10.1016/B978-0-12-818411-0.00010-0.

[12] T. Eggenberger, K. Oettmeier, and E. Hofmann, "Additive Manufacturing in Automotive Spare Parts Supply Chains – A Conceptual Scenario Analysis of Possible Effects," in Industrializing Additive Manufacturing - Proceedings of Additive Manufacturing in Products and Applications - AMPA2017, Springer International Publishing, 2018, pp. 223–237. doi: 10.1007/978-3-319-66866-6_22.

[13] S. Ji and M. Guvendiren, "Recent Advances in Bioink Design for 3D Bioprinting of Tissues and Organs," Frontiers in Bioengineering and Biotechnology, vol. 5, no. APR, Apr. 2017, doi: 10.3389/FBIOE.2017.00023/FULL.

[14] S. Knowlton, B. Yenilmez, and S. Tasoglu, "Towards Single-Step Biofabrication of Organs on a Chip via 3D Printing," Trends in Biotechnology, vol. 34, no. 9, pp. 685–688, Sep. 2016, doi: 10.1016/J.TIBTECH.2016.06.005.

[15] E. Lepowsky and S. Tasoglu, "3D printing for drug manufacturing: A perspective on the future of pharmaceuticals," International Journal of Bioprinting, vol. 4, no. 1, 2018, doi: 10.18063/IJB.V4I1.119.

[16] P. J. Nuñez, A. Rivas, E. García-Plaza, E. Beamud, and A. Sanz-Lobera, "Dimensional and Surface Texture Characterization in Fused Deposition Modelling (FDM) with

ABS plus," in Procedia Engineering, 2015, vol. 132, pp. 856–863. doi: 10.1016/j.proeng.2015.12.570.

[17] I. Gibson, D. Rosen, and B. Stucker, "Additive Manufacturing Technologies 3D Printing, Rapid Prototyping, and Direct Digital Manufacturing Second Edition."

[18] S. H. Ahn, M. Montero, D. Odell, S. Roundy, and P. K. Wright, "Anisotropic material properties of fused deposition modeling ABS," Rapid Prototyping Journal, vol. 8, no. 4, pp. 248–257, 2002, doi: 10.1108/ 13552540210441166/ FULL/ HTML.

[19] B. H. Lee, J. Abdullah, and Z. A. Khan, "Optimization of rapid prototyping parameters for production of flexible ABS object," Journal of Materials Processing Technology, vol. 169, no. 1, pp. 54–61, Oct. 2005, doi: 10.1016/ J.JMATPROTEC. 2005.02.259.

[20] C. S. Lee, S. G. Kim, H. J. Kim, and S. H. Ahn," Measurement of anisotropic compressive strength of rapid prototyping parts," Journal of Materials Processing Technology, vol. 187–188, pp. 627–630, Jun. 2007, doi: 10.1016/J.JMATPROTEC.2006.11.095.

[21] R. Anitha, S. Arunachalam, and P. Radhakrishnan, "Critical parameters influencing the quality of prototypes in fused deposition modelling," Journal of Materials Processing Technology, vol. 118, no. 1–3, pp. 385–388, Dec. 2001, doi: 10.1016/S0924-0136(01)00980-3.

[22] P. K. Venuvinod and W. Ma, Rapid Prototyping. Boston, MA: Springer US, 2004. doi: 10.1007/978-1-4757-6361-4.

[23] R. Singh, R. Kumar, I. Farina, F. Colangelo, L. Feo, and F. Fraternali, "Multi-Material Additive Manufacturing of Sustainable Innovative Materials and Structures," Polymers 2019, Vol. 11, Page 62, vol. 11, no. 1, p. 62, Jan. 2019, doi: 10.3390/POLYM11010062.

[24] H. Kim, E. Park, S. Kim, B. Park, N. Kim, and S. Lee, "Experimental Study on Mechanical Properties of Single- and Dual-material 3D Printed Products," Procedia Manufacturing, vol. 10, pp. 887–897, 2017, doi: 10.1016/J.PROMFG.2017.07.076.

[25] "Original Prusa i3 MK3S kit." https://shop.prusa3d.com/ en/3d-printers/180-original-prusa-i3-mk3s-kit.html?gclid= CjwKCAjwh5qLBhALEiwAioods7nYfRQNcI_r6IDMkGr9 RLWRZsfKAJkZqQBCYtOZcs-KvA8QZsViqBoCG3YQ AvD_BwE (accessed Oct. 13, 2021).

[26] A. Hadny, Q. Ayun, J. Triyono, and E. Pujiyanto, "Optimization of Injection Molding Simulation of Bioabsorbable Bone Screw Using Taguchi Method and Particle Swarm Optimization," Jordan Journal of Mechanical and Industrial Engineering, vol. 16, no. 2, pp. 319–325, 2022.

[27] S. G. Ghalme, "Improving Mechanical Properties of Rice Husk and Straw Fiber Reinforced Polymer Composite through Reinforcement Optimization," Jordan Journal of Mechanical and Industrial Engineering, vol. 15, no. 5, pp. 411–417, 2021.

[28] T. Yao, Z. Deng, K. Zhang, and S. Li, "A method to predict the ultimate tensile strength of 3D printing polylactic acid (PLA) materials with different printing orientations," Composites Part B: Engineering, vol. 163, pp. 393–402, Apr. 2019, doi: 10.1016/J.COMPOSITESB.2019.01.025.

[29] A. Nugroho, R. Ardiansyah, L. Rusita, and I. L. Larasati, "Effect of layer thickness on flexural properties of PLA (PolyLactid Acid) by 3D printing," IOP Conf. Series: Journal of Physics: Conf. Series, vol. 1130, p. 12017, 2018, doi: 10.1088/1742-6596/1130/1/012017.

[30] O. Avinc and A. Khoddami, "Overview of Poly(Lactic Acid) (PLA) Fibre Part I: Production, Properties, Performance, Environmental Impact, and End-use Applications of Poly(lactic acid) Fibres," Fibre Chemistry, vol. 41, no. 6, 2009.

[31] G. Fedorko, V. Molnár, Ž. Ferková, P. Peterka, J. Krešák, and M. Tomašková, "Possibilities of failure analysis for steel

cord conveyor belts using knowledge obtained from non-destructive testing of steel ropes," Engineering Failure Analysis, vol. 67, pp. 33–45, Sep. 2016, doi: 10.1016/J.ENGFAILANAL.2016.05.026.

[32] R. Henry, "Etymologia: Bonferroni Correction - Volume 21, Number 2—February 2015 - Emerging Infectious Diseases journal - CDC," Emerging Infectious Diseases, vol. 21, no. 2, p. 289, 2015, doi: 10.3201/EID2102.ET2102.

[33] G. V. S. S. Sharma, P. S. Rao, and B. Surendra Babu, "Establishing Process Capability Indices in a Sugar Manufacturing Industry-an Industrial Engineering Perspective," Jordan Journal of Mechanical and Industrial Engineering, vol. 15, no. 4, pp. 319–328, 2021.

[34] V. Ivanco, S. Kmet, and G. Fedorko, "Finite element simulation of creep of spiral strands," Engineering Structures, vol. 117, pp. 220–238, Jun. 2016, doi: 10.1016/J.ENGSTRUCT. 2016.02.053.

[35] A. A. Mousa, "The Effects of Content and Surface Modification of Filler on the Mechanical Properties of Selective Laser Sintered Polyamide12 Composites," Jordan Journal of Mechanical and Industrial Engineering, vol. 8, pp. 265–274, 2014.

# Torsional vibration of a Rod Composed of Two Dissimilar Frictionally Welded Parts with and without Crack in a Thermal Environment

Ahmed A. Ahmed[1*], Mohammadtaher M. Saeed Mulapeer [2]

[1]*Chemical and Petrochemical Engineering Department, College of Engineering, Salahaddin University-Erbil, Erbil, 44001, Iraq*

[2]*Mechanical and Mechatronics Department, College of Engineering, Salahaddin University-Erbil, Erbil, 44001, Iraq*

## Abstract

In this study, a three-dimensional thermal environment effect in the form of thermal stresses on linear torsional vibration of non-cracked and cracked rods composed of two dissimilar rods welded by friction welding is investigated. The nonlinear Green strain relation is used to drive the nonlinear strains. Hamilton's principle is used to drive equation of motion and corresponding boundary conditions. To model the crack, a torsional spring is used at the crack location. The crack is assumed to locate at the contact surface of the dissimilar welded rods. Effects of the thermal stresses in the form of the high temperature changes, crack depth ratio, and boundary conditions are examined on the torsional frequencies. Increasing the crack depth ratio at high temperatures results in a high reduction of the torsional frequencies.

## 1. Introduction

Friction welding is one of the most important welding methods which is capable of welding similar and dissimilar parts to each other. In this welding type, one of the bodies, generally with a circular cross-section, turns with a constant rotational velocity, and the other body fixed in one head is pushed toward the turning body to be welded with it through the heat generated due to friction force between two surfaces in contact. The bodies or shafts that are welded by the friction welding method can have the same[1, 2] or different[3] cross-sectional areas in the surfaces which are in contact and must be welded. It has been observed that an interlayer piece such as a plate is used between two rods to increase the quality of the friction welding as performed by Hynes and Velu [4]. The thermal model for heat flow in a friction welding process is investigated by [5]. Generally, the pieces such as shafts or rods which are welded by friction rotary welding, contain some defects such as cracks. The cracks are the most common defects found in such structures which can be generated by mechanical stresses or/and thermal stresses arising from the dissimilarity of thermal expansion coefficients in the contact zone. The cracks are sometimes very dangerous especially if they are open crack types that are capable of propagating through the surface of a body. When a piece such as a shaft, rod, or beam is vibrating, the presence of the crack leads to a fatigue failure and decreases the lifetime. There are several methods to model the crack, such as modelling it with one or more springs, or directly driving the local flexibility induced by the crack to the pieces[6-11].

Several investigations have been devoted to study the torsional, axial, lateral, and coupled vibrations of different parts, such as plates, rods, and beams with and without crack effects. Nacy et al. [12]investigated the vibration analysis of the plates with spot welded stiffeners. Ghadiri et al. [13] studied the free vibration of an axially preloaded laminated composite beam carrying a spring-mass-damper system with a non-ideal support. Kachapi[14] presented the nonlinear vibration and frequency analysis of functionally graded-piezoelectric cylindrical nano-shell with surface elasticity. Abdullah et al. used nonlinear strains to find three-dimensional thermal stress effects on the linear[15]and nonlinear [16] torsional frequencies of the rods with different boundary conditions. Zhu and Li [17] investigated the longitudinal and torsional vibration of size-dependent rods using nonlocal integral elasticity. Li and Hu[18] studied the torsional vibration of bi-directional functionally graded nanotubes based on nonlocal theory. Barretta et al. [19]presented the stress-driven two-phase integral elasticity for torsion of nano-beams.

The crack effect is mostly demonstrated by its position and depth. The crack position and depth can highly impress the different behaviours such as the static and dynamic of the cracked bodies. The crack severity relates to the crack depth. This relation for the transverse crack differs from that of the axial, circumferential, or radial cracks. Dimarogonas and Massouros[20] presented a relation to determine the local flexibility or compliance added by the presence of a circumferential crack. In another investigation devoted to the sensitivity of the

structures such as rotors and shafts to cracks, a different relation was presented by Chondros and Dimarogonas[21] for the dimensionless flexibility of the cracked shaft. For a transverse crack, the relations for the local flexibility and dimensionless flexibility of a cracked beam were presented by Rizos et al.[22]. Loya et al. [23] presented the compatibility relations at the cracked location for a cracked rod in nanoscale for investigating the torsional frequencies. Marin [24] presented the domain of influence in thermoelasticity of bodies with voids. Marin [25] investigated a temporally evolutionary equation in elasticity of micropolar bodies with voids. Amini and Amiri [26] studied the ultrasonic vibration effects on friction stir welding process.

Based on the investigations mentioned above, an absence of studying the torsional vibration of a cracked rod composed of two dissimilar welded rods under the effect of the thermal stresses, is evident. This is the reason that this paper aims to develop a reliable and accurate mathematical model to evoke the behaviour of a frictionally welded rod under a torsional vibration. The equation takes into account the different stiffness of the rod sections and, consequently, a new computability equation at the crack location is obtained. It can be stated that the main purpose of this study is to determine how much the crack and three-dimensional thermal stresses can alter the torsional frequencies of a rod composed of two frictionally-welded parts. To enter the effects of the three-dimensional thermal stresses to the torsional equation of motion of the rod, the nonlinear strains must be obtained using the Green strain relation.

## 2. Theory

For a rod composed of two welded rods, a displacement field given by Eq. (1) can be defined.

$$u_x = 0, u_y = -z\phi(x,t), u_z = y\phi(x,t). \tag{1}$$

The displacement $u_x$, $u_y$, and $u_z$ are, respectively, the displacements in x, y, and z directions. The transverse displacements $u_y$ and $u_z$ relate with the twisting angle $\phi(x,t)$. The nonlinear Green-Lagrange strain relation [27-29] is given by

$$\varepsilon_{ij} = \frac{1}{2}\left(\frac{\partial u_i}{\partial x_j} + \frac{\partial u_j}{\partial x_i} + \frac{\partial u_k}{\partial x_i}\frac{\partial u_k}{\partial x_j}\right). \tag{2}$$

The strains generated by mechanical stresses, can be obtained by substituting Eq. (1) into Eq. (2) as

$$\varepsilon_{xx} = \frac{1}{2}(y^2 + z^2)\left(\frac{\partial \phi}{\partial x}\right)^2 = \frac{1}{2}r^2\left(\frac{\partial \phi}{\partial x}\right)^2, \varepsilon_{yy} =$$
$$\varepsilon_{zz} = \frac{1}{2}\phi^2,$$
$$\varepsilon_{xy} = \varepsilon_{yx} = \frac{1}{2}\left(y\phi\frac{\partial \phi}{\partial x} - z\frac{\partial \phi}{\partial x}\right), \varepsilon_{zx} = \varepsilon_{xz} =$$
$$\frac{1}{2}\left(y\frac{\partial \phi}{\partial x} + z\phi\frac{\partial \phi}{\partial x}\right), \varepsilon_{yz} = \varepsilon_{zy} = 0. \tag{3}$$

In this paper, the stiffness matrix of the isotropic material is used to obtain the stresses from the strains, because both welded segments of a rod are assumed to be isotropic materials. Using the stiffness matrix of the isotropic material and strains presented in Eq. (3), the corresponding stresses are determined as follows. The significance of the component of the stiffness matrix $[C_{ij}]$ is to relate the strains to stresses in one, two, or three dimensional problems. These components or coefficients are given for an isotropic material in Eq. (5).

$$\sigma_{xx} = C_{11}\varepsilon_{xx} + C_{12}\varepsilon_{yy} + C_{13}\varepsilon_{zz} =$$
$$\frac{1}{2}r^2 C_{11}\left(\frac{\partial \phi}{\partial x}\right)^2 + C_{12}\phi^2,$$
$$\sigma_{yy} = C_{21}\varepsilon_{xx} + C_{22}\varepsilon_{yy} + C_{23}\varepsilon_{zz} =$$
$$\frac{1}{2}r^2 C_{12}\left(\frac{\partial \phi}{\partial x}\right)^2 + \frac{1}{2}(C_{22} + C_{23})\phi^2,$$
$$\sigma_{zz} = C_{31}\varepsilon_{xx} + C_{32}\varepsilon_{yy} + C_{33}\varepsilon_{zz} =$$
$$\frac{1}{2}r^2 C_{12}\left(\frac{\partial \phi}{\partial x}\right)^2 + \frac{1}{2}(C_{22} + C_{23})\phi^2, \sigma_{xy} =$$
$$2C_{66}\varepsilon_{xy} = G\gamma_{xy} = G\left(y\phi\frac{\partial \phi}{\partial x} - z\frac{\partial \phi}{\partial x}\right), \sigma_{xz} =$$
$$2C_{55}\varepsilon_{xz} = G\gamma_{xz} = G\left(y\frac{\partial \phi}{\partial x} + z\phi\frac{\partial \phi}{\partial x}\right),$$
$$\sigma_{yz} = 0. \tag{4}$$

A crack can be modelled as a torsional spring whose stiffness is exactly the crack severity. Mathematical modeling of the crack will be more discussed in the incoming subsection. Fig. 1 shows a rod composed of two dissimilar segments with a crack located at the contact zone of the welded segments (distance $b$ from the left end) under $\sigma_{xx}^T$, $\sigma_{yy}^T$, and $\sigma_{zz}^T$ thermal stresses applied, respectively, in x, y, and z directions. Geometries and material properties of each segment of the rod can be similar or different.

Using the stiffness matrix of an isotropic rod $[C_{ij}]$ shown in Eq. (5), the relation between mechanical ($\sigma_{ij}$) and thermal stresses ($\sigma_{ij}^T$) and corresponding strains is written according to [15, 29-31]

$$\begin{Bmatrix} \sigma_{xx} + \sigma_{xx}^T \\ \sigma_{yy} + \sigma_{yy}^T \\ \sigma_{zz} + \sigma_{zz}^T \\ \sigma_{yz} + \sigma_{yz}^T \\ \sigma_{xy} + \sigma_{xy}^T \\ \sigma_{zx} + \sigma_{zx}^T \end{Bmatrix} = \begin{bmatrix} C_{11} & C_{12} & C_{13} & 0 & 0 & 0 \\ C_{21} & C_{22} & C_{23} & 0 & 0 & 0 \\ C_{31} & C_{32} & C_{33} & 0 & 0 & 0 \\ 0 & 0 & 0 & C_{44} & 0 & 0 \\ 0 & 0 & 0 & 0 & C_{55} & 0 \\ 0 & 0 & 0 & 0 & 0 & C_{66} \end{bmatrix} =$$
$$\begin{Bmatrix} \varepsilon_{xx} - \alpha_x\Delta T \\ \varepsilon_{yy} - \alpha_y\Delta T \\ \varepsilon_{zz} - \alpha_z\Delta T \\ 2\varepsilon_{yz} \\ 2\varepsilon_{xy} \\ 2\varepsilon_{zx} \end{Bmatrix}. \tag{5}$$

$$C_{11} = C_{22} = C_{33} = \lambda + 2G, C_{12} = C_{13} = C_{23} = \lambda, C_{44} =$$
$$C_{55} = C_{66} = G, \lambda = \frac{E\nu}{(1+\nu)(1-2\nu)}, G = \frac{E}{2(1+\nu)}, C_{ij} = C_{ji}. \tag{6}$$

$$\sigma_{xx}^T = -(C_{11}\alpha_x\Delta T + C_{12}\alpha_y\Delta T + C_{13}\alpha_z\Delta T),$$
$$\sigma_{yy}^T = -(C_{21}\alpha_x\Delta T + C_{22}\alpha_y\Delta T + C_{23}\alpha_z\Delta T),$$
$$\sigma_{zz}^T = -(C_{31}\alpha_x\Delta T + C_{32}\alpha_y\Delta T + C_{33}\alpha_z\Delta T), \alpha =$$
$$\alpha_x = \alpha_y = \alpha_z, \Delta T = T - T_{room}. \tag{7}$$

For the isotropic materials, the thermal expansion in x, y, and z directions which are, respectively, denoted by $\alpha_x$, $\alpha_y$, and $\alpha_z$ are the same, and all of them are denoted by $\alpha$. Expression $\Delta T$ is temperature changes in which $T_{room}$ is room temperature (stress-free temperature) and is assumed to be $298\,K$ or $25°C$ and $T$ is temperature of the rod.

In this study, boundary conditions and the torsional equation of motion are obtained using Hamilton's principle.

$$\int_0^t \delta(-K_E + U_s + U_T)\,dt = 0. \tag{8}$$

where $K_E$, $U_s$, and $U_T$ are the kinetic energy, strain energy, and potential due to the thermal stresses.

Taking the variations of the $U_s$ and $K_E$, the following relations are obtained.
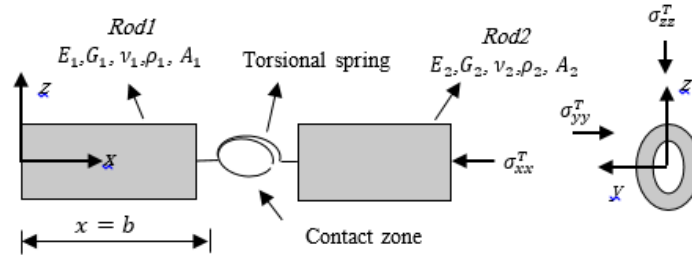
**Figure 1.** A cracked rod composed of two welded different rods under thermal stresses

$$\delta U_s = \delta \int_V \frac{1}{2} (\sigma_{xx}\varepsilon_{xx} + \sigma_{yy}\varepsilon_{yy} + \sigma_{zz}\varepsilon_{zz} + \sigma_{xy}\gamma_{xy} + \sigma_{xz}\gamma_{xz})\, dV = \delta U_1 + \delta U_2 + \delta U_3 + \delta U_4 + \delta U_5 =$$

$$\int_A dA \left\{ \int_0^L \left[ \frac{-3}{2} r^4 C_{11} \left(\frac{\partial \phi}{\partial x}\right)^2 \frac{\partial^2 \phi}{\partial x^2} - r^2 C_{12} \phi \left(\frac{\partial \phi}{\partial x}\right)^2 - r^2 C_{12} \phi^2 \frac{\partial^2 \phi}{\partial x^2} + (C_{22} + C_{23})\phi^3 - G r^2 \frac{\partial^2 \phi}{\partial x^2} - G r^2 \phi \left(\frac{\partial \phi}{\partial x}\right)^2 - \right. \right.$$

$$\left. \left. G r^2 \phi^2 \frac{\partial^2 \phi}{\partial x^2} \right] \delta\phi \, dx + \left[ \left( \frac{1}{2} r^4 C_{11} \left(\frac{\partial \phi}{\partial x}\right)^3 + r^2 C_{12} \phi^2 \frac{\partial \phi}{\partial x} + G r^2 \frac{\partial \phi}{\partial x} + G r^2 \phi^2 \frac{\partial \phi}{\partial x} \right) \delta\phi \right]_0^L \right\},$$

$$\delta U_1 = \delta \int_V \frac{1}{2} (\sigma_{xx}\varepsilon_{xx})\, dV, \qquad \delta U_2 = \delta \int_V \frac{1}{2} (\sigma_{yy}\varepsilon_{yy})\, dV, \qquad \delta U_3 = \delta \int_V \frac{1}{2} (\sigma_{zz}\varepsilon_{zz})\, dV, \qquad \delta U_4 =$$

$$\delta \int_V \frac{1}{2} (\sigma_{xy}\gamma_{xy})\, dV, \qquad \delta U_5 = \delta \int_V \frac{1}{2} (\sigma_{xz}\gamma_{xz})\, dV.$$

$$\delta U_1 = \int_A dA \left\{ \int_0^L \left[ \frac{-3}{2} r^4 C_{11} \left(\frac{\partial \phi}{\partial x}\right)^2 \frac{\partial^2 \phi}{\partial x^2} - \frac{1}{2} r^2 C_{12} \phi \left(\frac{\partial \phi}{\partial x}\right)^2 - \frac{1}{2} r^2 C_{12} \phi^2 \frac{\partial^2 \phi}{\partial x^2} \right] \delta\phi \, dx + \left[ \left( \frac{1}{2} r^4 C_{11} \left(\frac{\partial \phi}{\partial x}\right)^3 + \right. \right. \right.$$

$$\left. \left. \left. \frac{1}{2} r^2 C_{12} \phi^2 \frac{\partial \phi}{\partial x} \right) \delta\phi \right]_0^L \right\}; \tag{9}$$

$$\delta U_2 = \delta U_3 = \int_A dA \left\{ \int_0^L \left[ \frac{-1}{4} r^2 C_{12} \phi \left(\frac{\partial \phi}{\partial x}\right)^2 - \frac{1}{4} r^2 C_{12} \phi^2 \frac{\partial^2 \phi}{\partial x^2} + \frac{1}{2} (C_{22} + C_{22})\phi^3 \right] \delta\phi \, dx + \right.$$

$$\left. \left[ \left( \frac{1}{4} r^2 C_{12} \phi^2 \frac{\partial \phi}{\partial x} \right) \delta\phi \right]_0^L \right\},$$

$$\delta U_4 = \int_A dA \left\{ \int_0^L G \left[ -y^2 \phi \left(\frac{\partial \phi}{\partial x}\right)^2 + yz \left(\frac{\partial \phi}{\partial x}\right)^2 - y^2 \phi^2 \frac{\partial^2 \phi}{\partial x^2} + 2yz \phi \frac{\partial^2 \phi}{\partial x^2} - z^2 \frac{\partial^2 \phi}{\partial x^2} \right] \delta\phi \, dx + \left[ G \left( y^2 \phi^2 \frac{\partial \phi}{\partial x} - \right. \right. \right.$$

$$\left. \left. \left. 2yz \phi \frac{\partial \phi}{\partial x} + z^2 \frac{\partial \phi}{\partial x} \right) \delta\phi \right]_0^L \right\},$$

$$\delta U_5 = \int_A dA \left\{ \int_0^L G \left[ -y^2 \frac{\partial^2 \phi}{\partial x^2} - yz \left(\frac{\partial \phi}{\partial x}\right)^2 - z^2 \phi^2 \frac{\partial^2 \phi}{\partial x^2} - 2yz \phi \frac{\partial^2 \phi}{\partial x^2} - z^2 \phi \left(\frac{\partial \phi}{\partial x}\right)^2 \right] \delta\phi \, dx + \left[ G \left( y^2 \frac{\partial \phi}{\partial x} + \right. \right. \right.$$

$$\left. \left. \left. 2yz \phi \frac{\partial \phi}{\partial x} + z^2 \phi^2 \frac{\partial \phi}{\partial x} \right) \delta\phi \right]_0^L \right\}.$$

$$\delta K_E = \delta \int_V \frac{\rho}{2} \left[ \left(\frac{\partial u_x}{\partial t}\right)^2 + \left(\frac{\partial u_y}{\partial t}\right)^2 + \left(\frac{\partial u_z}{\partial t}\right)^2 \right] dV = \int_0^L \int_0^R 2\rho\pi\, r^3 dr \frac{\partial \phi}{\partial t} \left(\frac{\partial \delta\phi}{\partial t}\right) = \int_0^L S \frac{\partial \phi}{\partial t} \left(\frac{\partial \delta\phi}{\partial t}\right) dx,$$

$$\Rightarrow \int_0^t \delta K_E \, dt = \int_0^t \left[ \int_0^L S \frac{\partial \phi}{\partial t} \left(\frac{\partial \delta\phi}{\partial t}\right) dx \right] dt = \int_0^L \left[ \int_0^t S \frac{\partial \phi}{\partial t} \left(\frac{\partial \delta\phi}{\partial t}\right) dt \right] dx = \int_0^L \left[ \left[ S \frac{\partial \phi}{\partial t} \delta\phi \right]_0^t - \int_0^t S \frac{\partial^2 \phi}{\partial t^2} \delta\phi dt \right] dx =$$

$$\int_0^L \left[ 0 - \int_0^t S \frac{\partial^2 \phi}{\partial t^2} \delta\phi dt \right] dx = \int_0^t \left[ \int_0^L -S \frac{\partial^2 \phi}{\partial t^2} \delta\phi dx \right] dt. \tag{10}$$

Praveen and Reddy [32]stated that the variation of the potential energy due to thermal stresses $\delta U_T$ is given by

$$\delta U_T = \int_V (\sigma_{xx}^T \delta\varepsilon_{xx} + \sigma_{yy}^T \delta\varepsilon_{yy} + \sigma_{zz}^T \delta\varepsilon_{zz})\, dV = \int_0^L \left[ -\sigma_{xx}^T I_P \frac{\partial^2 \phi}{\partial x^2} + (\sigma_{yy}^T + \sigma_{zz}^T) A\phi \right] \delta\phi \, dx +$$

$$\left[ \left( \sigma_{xx}^T I_P \frac{\partial \phi}{\partial x} \right) \delta\phi \right]_0^L. \tag{11}$$

Nonlinear torsional equation of motion and corresponding boundary conditions are obtained by substituting Eqs. (9) - (11) into Eq. (8),

$$\int_0^t \left[ \left( Q_1 \left(\frac{\partial \phi}{\partial x}\right)^3 + (Q_2 + Q_4)\phi^2 \frac{\partial \phi}{\partial x} + (Q_4 + Q_x^T)\frac{\partial \phi}{\partial x} \right) \delta\phi \right]_0^L dt + \int_0^t \int_0^L \left[ -3Q_1 \left(\frac{\partial \phi}{\partial x}\right)^2 \frac{\partial^2 \phi}{\partial x^2} + (-Q_2 - \right.$$

$$\left. Q_4)\phi \left(\frac{\partial \phi}{\partial x}\right)^2 + (-Q_2 - Q_4)\phi^2 \frac{\partial^2 \phi}{\partial x^2} + Q_3\phi^3 + S \frac{\partial^2 \phi}{\partial t^2} - Q_4 \frac{\partial^2 \phi}{\partial x^2} - Q_x^T \frac{\partial^2 \phi}{\partial x^2} + (Q_y^T + Q_z^T)\phi \right] \delta\phi \, dx \, dt = 0. \tag{12}$$

$$\int_A dA = \int_0^R 2\pi r \, dr, r^2 = y^2 + z^2, I_P = \frac{\pi}{2} R^4, Q_1 = \int_A \frac{r^4}{2} C_{11} dA = C_{11} \frac{\pi}{6} R^6, Q_2 = \int_A r^2 C_{12} dA =$$

$$C_{12} I_P, Q_3 = \int_A (C_{22} + C_{23}) dA = (C_{22} + C_{23}) A, Q_4 = \int_A G r^2 dA = G I_P, S = \int_A 2\pi\rho\, r^3 dr = \tag{13}$$

$$\rho I_P, Q_x^T = \int_A r^2 \sigma_{xx}^{Th} dA = \sigma_{xx}^T I_P, Q_y^T = \int_A \sigma_{yy}^{Th} dA = \sigma_{yy}^T A, Q_z^T = \int_A \sigma_{zz}^{Th} dA = \sigma_{zz}^T A.$$

Here, $A$ is the cross-sectional area, $I_P$ is the polar moment of inertia, $R$ is the radius of the rod, and $\rho$ is the density. From Eq. (12) and using the expressions defined in Eq.(13), the equation of motion is obtained as

$$-C_{11} \frac{\pi}{2} R^6 \left(\frac{\partial \phi}{\partial x}\right)^2 \frac{\partial^2 \phi}{\partial x^2} + (-C_{12} I_P - G I_P)\phi \left(\frac{\partial \phi}{\partial x}\right)^2 + (-C_{12} I_P - G I_P)\phi^2 \frac{\partial^2 \phi}{\partial x^2} + (C_{22} + C_{23}) A\phi^3 + \rho I_P \frac{\partial^2 \phi}{\partial t^2} - G I_P \frac{\partial^2 \phi}{\partial x^2} - \sigma_{xx}^T I_P \frac{\partial^2 \phi}{\partial x^2} +$$

$$(\sigma_{yy}^T + \sigma_{zz}^T) A\phi = 0. \tag{14}$$

The torsional equation of motion given by Eq. (14) is a nonlinear equation including linear and nonlinear terms. Because in this study, the linear torsional frequencies will be investigated, the nonlinear terms of the equation of motion and boundary conditions will be neglected and finally, the linear equation of motion and corresponding boundary conditions will be presented in the following form as

$$-GI_P \frac{\partial^2 \phi}{\partial x^2} - \sigma_{xx}^T I_P \frac{\partial^2 \phi}{\partial x^2} + (\sigma_{yy}^T + \sigma_{zz}^T)A\phi - \rho I_P \frac{\partial^2 \phi}{\partial t^2} = 0. \tag{15}$$

$$\left[ \left( GI_P \frac{\partial \phi}{\partial x} + \sigma_{xx}^T I_P \frac{\partial \phi}{\partial x} \right) \delta\phi \right]_0^L = 0. \tag{16}$$

The equation of motion can be written in a more convenient manner as

$$g_1 \frac{\partial^2 \phi}{\partial x^2} + g_2 \phi + g_3 \frac{\partial^2 \phi}{\partial t^2} = 0. \tag{17}$$

$$\frac{\partial^2 \phi}{\partial x^2} + P\phi + F \frac{\partial^2 \phi}{\partial t^2} = 0. \tag{18}$$

$$g_1 = \left( -1 - \frac{\sigma_{xx}^T}{G} \right), \quad g_2 = \left( \frac{\sigma_{yy}^T + \sigma_{zz}^T}{GI_P} \right)A, \quad g_3 = \frac{\rho}{G}, \quad P = \frac{g_2}{g_1}, \quad F = \frac{g_3}{g_1}. \tag{19}$$

### 2.1. racked rod equations

Generally, it is assumed that a crack divides the rod into two segments. If the rod is composed of two dissimilar smaller rods welded by friction welding, there will probably exist a crack or more at the welded or contact zone. So, it is assumed that the crack is located at $x = b = L_1$ which is exactly the end of the first segment as already shown in Fig. 1. It is worth mentioning that the total rod length is $L = L_1 + L_2$ in which $L_1$ is the length of the first segment of the rod and $L_2$ is the second segment length. One of the best methods for modelling the cracks is using the spring model. In this modeling, a spring or more is assumed to behave as a crack at the crack location whose stiffness relates with the crack severity. As the crack depth increases, the crack severity increases, and its effect increases. The crack results in additional flexibility which is known as local flexibility or compliance $C$. Equation of motion can be written according to Eq. (18) for each segment of the cracked rod as following in which $\phi_1(x,t)$, and $\phi_2(x,t)$ are twisting angles of the left and right segments.

$$\frac{\partial^2 \phi_1}{\partial x^2} + P_1 \phi_1 + F_1 \frac{\partial^2 \phi_1}{\partial t^2} = 0. \tag{20}$$

$$\frac{\partial^2 \phi_2}{\partial x^2} + P_2 \phi_2 + F_2 \frac{\partial^2 \phi_2}{\partial t^2} = 0. \tag{21}$$

$$g_{1,1} = \left( -1 - \frac{\sigma_{xx1}^T}{G_1} \right), \quad g_{2,1} = \left( \frac{\sigma_{yy1}^T + \sigma_{zz1}^T}{G_1 I_{P1}} \right)A_1, \quad g_{3,1} = \frac{\rho_1}{G_1}, \quad P_1 = \frac{g_{2,1}}{g_{1,1}}, \quad F_1 = \frac{g_{3,1}}{g_{1,1}} \tag{22}$$

.

$$g_{1,2} = \left( -1 - \frac{\sigma_{xx2}^T}{G_2} \right), \quad g_{2,2} = \left( \frac{\sigma_{yy2}^T + \sigma_{zz2}^T}{G_2 I_{P2}} \right)A_2, \quad g_{3,2} = \frac{\rho_2}{G_2}, \quad P_2 = \frac{g_{2,2}}{g_{1,2}}, \quad F_2 = \frac{g_{3,2}}{g_{1,2}} \tag{23}$$

The separation variable method given by Eq. (24) is used to obtain the closed-form solutions for the rod segments in which $\omega$ is the rod natural frequency.

$$\phi_1(x,t) = \theta_1(x)e^{i\omega t}, \phi_2(x,t) = \theta_2(x)e^{i\omega t}. \tag{24}$$

By substituting Eq. (24) into Eqs. (20) and (21), the equations of motion for both segments of the cracked rod are obtained as

$$\frac{\partial^2 \theta_1}{\partial x^2} + (P_1 - \omega^2 F_1)\theta_1 = 0. \tag{25}$$

$$\frac{\partial^2 \theta_2}{\partial x^2} + (P_2 - \omega^2 F_2)\theta_2 = 0. \tag{26}$$

The closed form solutions for Eqs. (25) and (26) are presented as following.

$$\theta_1(x) = A_1 \sin(\beta_1 x) + A_2 \cos(\beta_1 x). \tag{27}$$

$$\theta_2(x) = A_3 \sin(\beta_2 x) + A_4 \cos(\beta_2 x). \tag{28}$$

$$\beta_1 = \sqrt{(P_1 - \omega^2 F_1)}, \beta_2 = \sqrt{(P_2 - \omega^2 F_2)}. \tag{29}$$

Focusing on the Eqs. (27) and (28), it will be seen that there are four constants to complete the solutions. So, four boundary conditions are required to obtain the torsional natural frequencies but there are only two boundary conditions for a rod. Two other conditions can be derived from the crack location. The conditions are known as compatibility equations and presented as follows[21, 31].

Jump in twisting angle: $\Delta\theta = \theta_2(b) - \theta_1(b) = C_c \frac{\partial\theta_1(x)}{\partial x}\Big|_{x=b}. \tag{30}$

Continuity of the twisting moment:
$$G_1 I_{P1} \frac{\partial\theta_1(b)}{\partial x} = G_2 I_{P2} \frac{\partial\theta_2(b)}{\partial x}. \tag{31}$$

The boundary conditions have already been determined by Eq. (16) for the fixed and free ends of the rod as

Fixed end: $\theta(x) = 0$, $\quad$ Free end: $\frac{\partial\theta(x)}{\partial x} = 0. \tag{32}$

The constant $C_c$ which represents the crack severity can be related to the crack depth ratio and material properties, and it can be determined as[20, 21]

$$C_c = C \times G \times I_P, C = \frac{4}{\pi R^3 G} \times I(a/R). \tag{33}$$

The expression $C$ which is the local flexibility or compliance relates with dimensionless compliance $I(a/R)$ as shown in Eq. (27). The dimensionless compliance $I(a/R)$ can be obtained using crack depth $a$ and rod radius $R$ by the following relation in which $\xi = (1 - a/R)$[20].

$$I(a/R) = 0.035\xi^{-4} + 0.01\xi + 0.029\xi^2 + 0.0086\xi^3 + 0.0044\xi^4 + 0.0025\xi^6 + 0.0017\xi^7 + 0.008\xi^8 - 0.029. \tag{34}$$

Finally, the frequency ratio (FR) between the cracked ($\omega_{cr}$) and non-cracked ($\omega_{non}$) torsional frequencies of a cracked rod can be obtained as

$$FR = \frac{\omega_{cr}}{\omega_{non}}. \tag{35}$$

### 3. Results and discussions

#### 3.1. Material properties

The material properties of the dissimilar rods that have been welded by the friction welding method are tabulated in Table 1. The first rod material shown in Fig. 1 (left rod), is chosen to be duplex stainless steel SAF 2507 and the second rod (right rod) is made up of AISI type 304 stainless steel.

### 3.2. Benchmark results

In the friction rotary welding, the weld remains in the solid-state, avoiding many of the defects associated with melting and solidification during fusion welding, such as pores and solidification cracks. The distortion of the welded component is also reduced. Friction rotary welding is widely implemented across the manufacturing sector and has been used for numerous applications, including turbine shafts, automotive parts including steel truck axels and casings, monel-to-steel marine fittings, piston rods, copper-aluminium electrical connections, and cutting tools.

The process is easily automated, and  it is not dependent on human influence, which results in very low defect rates such as cracks. But, it does not mean that the cracks cannot be generated on the rods. So, a crack or more can be generated on the rod especially at the contact zone, during or after the welding process.If the parts created by friction rotary welding consist of a crack or more, the serious operational problems may occurbecause most of these parts are applied in high temperatures such as piston rod or turbine shafts. In this study, the presence of a crack at the contact zone is considered and its effect is studied. Also, the three-dimensional thermal stresses generated by high temperatures on the rod are considered. The main purpose of this study is to determine how much the crack and three-dimensional thermal stresses can alter the torsional frequencies of a rod composed of two frictionally-welded parts.

In the present study, linear torsional frequencies of a rod composed of two welded rods for cracked and non-cracked cases with clamped-clamped (C-C) and clamped-free (C-F) boundary conditions in a thermal environment are investigated. Thermal stresses are exposed from three mutually directions and consequently, their effect is not negligible. One of the aims of this investigation is to show whether the thermal stresses effects can be neglected or their effect must be taken into account. At the same time, the crack effect on the torsional frequencies must also be examined. Effects of thermal stresses and crack will be significant if they both are simultaneously applied to the rod. For this study, it has been assumed that the geometries of both segments of the rod such as diameter and length are the same so that it can be written that $d = d_1 = d_2 = 2R_1 = 2R_2$ or$A = A_1 = A_2$ and $L_1 = L_2$.

The linear torsional frequencies and frequency ratios of the cracked and non-cracked C-Cand C-Frodsat room temperatureand higher are presented in Table 2 and Table3, respectively. According to the results of Table 2, a decrease in the torsional frequencies of the C-C rod occurs when temperature increases. The crack depth ratio effects ($a$ /$R$) on the frequencies of C-C rods are shown in Table 2.

According to the results of Table3, if the crack depth and temperature highly increase, the C-F cracked rod will extensively be impressed and its frequencies will fall.

The frequency ratio (FR) for the three first modes of the C-C and C-F rods with various crack depth ratios at different high temperatures are tabulated in Tales 2 and 3. As it is obvious, increasing the crack depth ratio and crack severity lead to a decrease in the frequency ratio at any temperature. It means that the frequencies of the cracked rod reduce with increasing the crack depth ratio. Another parameter that alters the frequency ratio is temperature change. The frequency ratio for all modes of the cracked C-C and C-F rods decreases by an increase in temperature for any crack severity. The frequency ratio of the cracked C-F rod is highly impressed by high temperatures and high crack severity values.

**Table 1.** Geometries and properties of duplex stainless steel SAF 2507 and AISI type 304 stainless steel.

| Duplex stainless steel | $\rho_1\ (kg/m^3)$ | $R_1(mm)$ | $L_1(mm)$ | $E_1\ (GPa)$ | $v_1$ | $\alpha_1(1/K)$ |
|---|---|---|---|---|---|---|
| SAF 2507 | 7800 | 6 | 25 | 200 | 0.3 | $14 \times 10^{-6}$ |
| AISI type 304 | $\rho_2\ (kg/m^3)$ | $R_2(mm)$ | $L_2(mm)$ | $E_2\ (GPa)$ | $v_2$ | $\alpha_2\ (1/K)$ |
| stainless steel | 8000 | 6 | 25 | 195 | 0.29 | $17 \times 10^{-6}$ |

**Table 2.** First three torsional frequencies and frequency ratios of a cracked C-C rod with different crack depth ratios $(a/R)$ for different temperature changes. ($L = 50 \; mm$, $d = 12 \; mm$, and $b = L_1 = 25 \; mm$).

| $a/R$ | $\Delta T$ | $\omega_1$(rad/s) | $\omega_2$(rad/s) | $\omega_3$(rad/s) | $FR_1$ | $FR_2$ | $FR_3$ |
|---|---|---|---|---|---|---|---|
| Non | 0 | 195194.52 | 390405.20 | 585583.58 | 1 | 1 | 1 |
| Cracked | 40 | 189039.14 | 387054.89 | 583003.27 | 1 | 1 | 1 |
| | 80 | 182675.64 | 383675.58 | 580411.40 | 1 | 1 | 1 |
| | 120 | 176081.45 | 380266.51 | 577807.79 | 1 | 1 | 1 |
| | 160 | 169229.60 | 376826.85 | 575192.30 | 1 | 1 | 1 |
| | 200 | 162087.41 | 373355.77 | 572564.75 | 1 | 1 | 1 |
| | 300 | 142671.44 | 364534.69 | 565942.05 | 1 | 1 | 1 |
| 1/6 | 0 | 195194.26 | 388621.30 | 585576.71 | 0.9999986 | 0.9954306 | 0.9999882 |
| | 40 | 189038.78 | 385259.52 | 582996.02 | 0.9999981 | 0.9953614 | 0.9999875 |
| | 80 | 182675.15 | 381868.42 | 580403.76 | 0.9999973 | 0.9952898 | 0.9999860 |
| | 120 | 176080.81 | 378447.20 | 577799.75 | 0.9999963 | 0.995215 | 0.9999860 |
| | 160 | 169228.77 | 374995.04 | 575183.84 | 0.9999951 | 0.9951388 | 0.9999852 |
| | 200 | 162086.36 | 371511.09 | 572555.86 | 0.9999935 | 0.9950591 | 0.9999844 |
| | 300 | 142669.63 | 362656.07 | 565932.02 | 0.9999873 | 0.9948465 | 0.9999822 |
| 2/6 | 0 | 195193.08 | 380586.70 | 585544.89 | 0.9999926 | 0.9748504 | 0.9999339 |
| | 40 | 189037.11 | 377171.64 | 582962.46 | 0.9999892 | 0.9744655 | 0.9999300 |
| | 80 | 182672.89 | 373725.71 | 580368.38 | 0.9999849 | 0.9740669 | 0.9999258 |
| | 120 | 176077.83 | 370248.03 | 577762.50 | 0.9999794 | 0.9736540 | 0.9999216 |
| | 160 | 169224.93 | 366737.72 | 575144.66 | 0.9999724 | 0.9732260 | 0.9999171 |
| | 200 | 162081.50 | 363193.83 | 572514.69 | 0.9999635 | 0.9727821 | 0.9999125 |
| | 300 | 142661.25 | 354180.54 | 565885.57 | 0.9999285 | 0.9715962 | 0.9999002 |
| 3/6 | 0 | 195188.17 | 351493.27 | 585412.54 | 0.9999674 | 0.9003293 | 0.9997079 |
| | 40 | 189030.17 | 347860.74 | 582822.84 | 0.9999525 | 0.8987374 | 0.9996905 |
| | 80 | 182663.47 | 344190.45 | 580221.25 | 0.9999333 | 0.8970870 | 0.9996723 |
| | 120 | 176065.42 | 340481.18 | 577607.60 | 0.9999089 | 0.8953751 | 0.9996535 |
| | 160 | 169208.94 | 336731.65 | 574981.74 | 0.9998779 | 0.8935978 | 0.9996339 |
| | 200 | 162061.23 | 332940.50 | 572343.48 | 0.9998384 | 0.8917513 | 0.9996135 |
| | 300 | 142626.33 | 323270.92 | 565692.49 | 0.9996838 | 0.8868042 | 0.9995590 |
| 4/6 | 0 | 195158.30 | 271226.74 | 584633.11 | 0.9998144 | 0.6947313 | 0.9983768 |
| | 40 | 188988.01 | 266712.47 | 582001.89 | 0.9997295 | 0.6890817 | 0.9982823 |
| | 80 | 182606.26 | 262122.61 | 579357.51 | 0.9996202 | 0.6831881 | 0.9981842 |
| | 120 | 175990.06 | 257453.10 | 576699.78 | 0.9994809 | 0.6770333 | 0.9980823 |
| | 160 | 169111.85 | 252699.56 | 574028.52 | 0.9993042 | 0.6705986 | 0.9979767 |
| | 200 | 161938.25 | 247857.15 | 571343.55 | 0.9990797 | 0.6638631 | 0.9978671 |
| | 300 | 142414.65 | 235326.16 | 564569.85 | 0.9982001 | 0.6455521 | 0.9975753 |
| 5/6 | 0 | 194644.39 | 202878.93 | 580480.07 | 0.9971816 | 0.5196624 | 0.9912847 |
| | 40 | 188281.42 | 197147.76 | 577730.41 | 0.9959917 | 0.5093534 | 0.9909556 |
| | 80 | 181674.46 | 191265.16 | 574967.46 | 0.9945193 | 0.4985075 | 0.9906205 |
| | 120 | 174798.66 | 185214.02 | 572191.03 | 0.9927147 | 0.4870637 | 0.9902791 |
| | 160 | 167623.61 | 178974.76 | 569400.93 | 0.9905099 | 0.4749522 | 0.9899314 |
| | 200 | 160111.53 | 172524.70 | 566596.98 | 0.9878097 | 0.4620919 | 0.9895771 |
| | 300 | 139509.25 | 155289.20 | 559525.14 | 0.9778358 | 0.4259929 | 0.9886615 |
| 5.5/6 | 0 | 193342.42 | 197556.84 | 579455.86 | 0.9905115 | 0.5060302 | 0.9895357 |
| | 40 | 186768.97 | 191843.15 | 576700.74 | 0.9879910 | 0.4956484 | 0.9891895 |
| | 80 | 179955.06 | 185954.46 | 573932.41 | 0.9851070 | 0.4846658 | 0.9888372 |
| | 120 | 172872.45 | 179873.43 | 571150.65 | 0.9817754 | 0.4730193 | 0.9884786 |
| | 160 | 165486.73 | 173579.72 | 568355.28 | 0.9778828 | 0.4606352 | 0.9881135 |
| | 200 | 157755.41 | 167049.25 | 565546.09 | 0.9732736 | 0.4474264 | 0.9877417 |
| | 300 | 136524.28 | 149480.62 | 558461.29 | 0.9569138 | 0.4100587 | 0.9867817 |

**Table 3.** First three torsional frequencies and frequency ratios of a cracked C-F rod with different crack depth ratios $(a/R)$ for different temperature changes. ($L = 50\ mm$, $d = 12\ mm$, and $b = L_1 = 25\ mm$).

| $a/R$ | $\Delta T$ | $\omega_1$(rad/s) | $\omega_2$(rad/s) | $\omega_3$(rad/s) | $FR_1$ | $FR_2$ | $FR_3$ |
|---|---|---|---|---|---|---|---|
| Non | 0 | 97479.34 | 292917.64 | 487876.88 | 1 | 1 | 1 |
| Cracked | 40 | 84345.64 | 288733.65 | 484987.23 | 1 | 1 | 1 |
| | 80 | 68745.37 | 284488.23 | 482080.27 | 1 | 1 | 1 |
| | 120 | 48347.09 | 280178.56 | 479155.69 | 1 | 1 | 1 |
| | 160 | … | 275801.64 | 476213.17 | … | 1 | 1 |
| | 200 | … | 271354.21 | 473252.37 | … | 1 | 1 |
| | 300 | … | 259903.24 | 465768.12 | … | 1 | 1 |
| 1/6 | 0 | 97252.12 | 292279.91 | 486664.89 | 0.9976690 | 0.9978228 | 0.9975157 |
| | 40 | 84080.70 | 288090.79 | 483767.44 | 0.9968588 | 0.9977735 | 0.9974849 |
| | 80 | 68417.30 | 283839.93 | 480852.55 | 0.9952277 | 0.9977211 | 0.9974532 |
| | 120 | 47875.51 | 279524.52 | 477919.90 | 0.9902459 | 0.9976656 | 0.9974209 |
| | 160 | … | 275141.52 | 474969.16 | ... | 0.9976065 | 0.9973877 |
| | 200 | … | 270687.63 | 472000.00 | ... | 0.9975435 | 0.9973537 |
| | 300 | … | 259218.68 | 464494.14 | ... | 0.9973661 | 0.9972647 |
| 2/6 | 0 | 96213.86 | 289364.27 | 481157.98 | 0.98701797 | 0.9878690 | 0.9862282 |
| | 40 | 82867.48 | 285151.05 | 478224.94 | 0.98247497 | 0.9875920 | 0.9860567 |
| | 80 | 66908.18 | 280874.72 | 475273.82 | 0.97327544 | 0.9872982 | 0.9858810 |
| | 120 | 45674.52 | 276532.35 | 472304.29 | 0.94472118 | 0.9869861 | 0.9857011 |
| | 160 | … | 272120.79 | 469315.99 | ... | 0.9866540 | 0.9855166 |
| | 200 | … | 267636.61 | 466308.57 | ... | 0.9862998 | 0.9853274 |
| | 300 | … | 256083.21 | 458703.89 | ... | 0.9853021 | 0.9848331 |
| 3/6 | 0 | 92130.39 | 278059.74 | 460980.51 | 0.94512735 | 0.9492761 | 0.9448705 |
| | 40 | 78050.99 | 273742.92 | 457914.98 | 0.92537077 | 0.9480811 | 0.9441794 |
| | 80 | 60792.09 | 269357.03 | 454828.84 | 0.88430814 | 0.9468125 | 0.9434711 |
| | 120 | 36044.05 | 264898.66 | 451721.67 | 0.74552677 | 0.9454637 | 0.9427450 |
| | 160 | … | 260364.08 | 448593.04 | ... | 0.9440265 | 0.9420004 |
| | 200 | … | 255749.22 | 445442.49 | ... | 0.9424921 | 0.9412366 |
| | 300 | … | 243830.75 | 437467.13 | ... | 0.9381597 | 0.9392380 |
| 4/6 | 0 | 74092.12 | 239006.93 | 413101.55 | 0.76008024 | 0.8159526 | 0.8467332 |
| | 40 | 55476.70 | 234182.63 | 409707.60 | 0.6577305 | 0.8110680 | 0.8447801 |
| | 80 | 25798.19 | 229257.04 | 406285.33 | 0.37527167 | 0.8058577 | 0.8427752 |
| | 120 | … | 224223.48 | 402834.03 | ... | 0.8002877 | 0.8407163 |
| | 160 | … | 219074.50 | 399352.94 | ... | 0.7943190 | 0.8386012 |
| | 200 | … | 213801.77 | 395841.28 | ... | 0.7879065 | 0.8364274 |
| | 300 | … | 200013.68 | 386922.91 | ... | 0.7695697 | 0.8307200 |
| 5/6 | 0 | 25815.69 | 200921.88 | 388079.04 | 0.26483243 | 0.6859330 | 0.7954446 |
| | 40 | … | 195301.17 | 384507.16 | ... | 0.6764059 | 0.7928191 |
| | 80 | … | 189513.84 | 380901.79 | ... | 0.6661570 | 0.7901210 |
| | 120 | … | 183544.12 | 377261.96 | ... | 0.6550969 | 0.7873473 |
| | 160 | … | 177373.60 | 373586.68 | ... | 0.6431201 | 0.7844946 |
| | 200 | … | 170980.54 | 369874.87 | ... | 0.6301009 | 0.7815594 |
| | 300 | … | 153839.97 | 360428.16 | ... | 0.5919124 | 0.7738360 |
| 5.5/6 | 0 | 6633.14 | 197544.66 | 386367.72 | 0.06804662 | 0.6744034 | 0.7919369 |
| | 40 | … | 191832.46 | 382783.77 | ... | 0.6643924 | 0.7892656 |
| | 80 | … | 185944.87 | 379165.93 | ... | 0.6536118 | 0.7865203 |
| | 120 | … | 179864.67 | 375513.24 | ... | 0.6419644 | 0.7836977 |
| | 160 | … | 173571.60 | 371824.67 | ... | 0.6293349 | 0.7807946 |
| | 200 | … | 167041.62 | 368099.15 | ... | 0.6155851 | 0.7778073 |
| | 300 | … | 149473.78 | 358616.04 | ... | 0.5751131 | 0.7699454 |

Fig. 2 represents how the torsional frequencies of the C-C and C-F rods with and without crack vary with temperature changes. For the case of the cracked rods, frequencies of all modes are more impressed by temperature changes. Generally, all mode frequencies of the non-cracked rods are higher than the cracked rods at any temperature and with any boundary conditions. An increase in the temperature leads to a decrease in all mode torsional frequencies of the C-C and C-F rods for any crack depth ratio or crack severity.

This is because the structures become softer, weaker, and more ductile at high temperatures which result in lower stiffness and lower frequencies. Therefore, it can be stated that high temperatures cause a reduction in axial rigidity, bending stiffness, and torsional rigidity. Mehta and Kumar [33] have already found that the torsional characteristics, such as torsional rigidity and damping are temperature-dependent.

It is worth mentioning that the effect of the crack with high crack severity (crack severity directly changes with changes of crack depth ratio) becomes very dangerous when the cracked rod is exposed to high temperatures simultaneously. For this reason, such cracked rods must never vibrate at high temperatures because the failure of the rod or structure will soon occur. It is obvious that the

C-F rod is more impressed by the crack and temperature changes than the C-C rod. It implies how the boundary condition can play an important role in the dynamics of structures. Increasing the crack depth ratio causes an increase in the crack severity and additional flexibility of the rods. This leads to a reduction of the torsional frequencies of the C-C and C-F rods at any temperature. As the vibration mode increases, the thermal and crack effects on the rods with any boundary condition increases. It means that the fundamental frequency is more impressed by the crack and thermal changes than the second and third modes. In Fig 2, the case of "Non-Cr" denotes the non-cracked rod case. The lowest torsional frequencies for both C-C and C-F rods at any mode are obtained when the value of crack depth ratio is low and temperature is high and in such cases, the frequencies approach minimum values. As it is seen, the first mode of the C-F does not have a real value, and it has become imaginary. This is due to the extraordinary flexibility induced to the C-F rod by a crack at elevated temperatures. It is worth mentioning that the torsional frequencies increase at temperatures lower than room temperature for any crack severity value and for any boundary condition as already proved by Abdullah et al. [15].
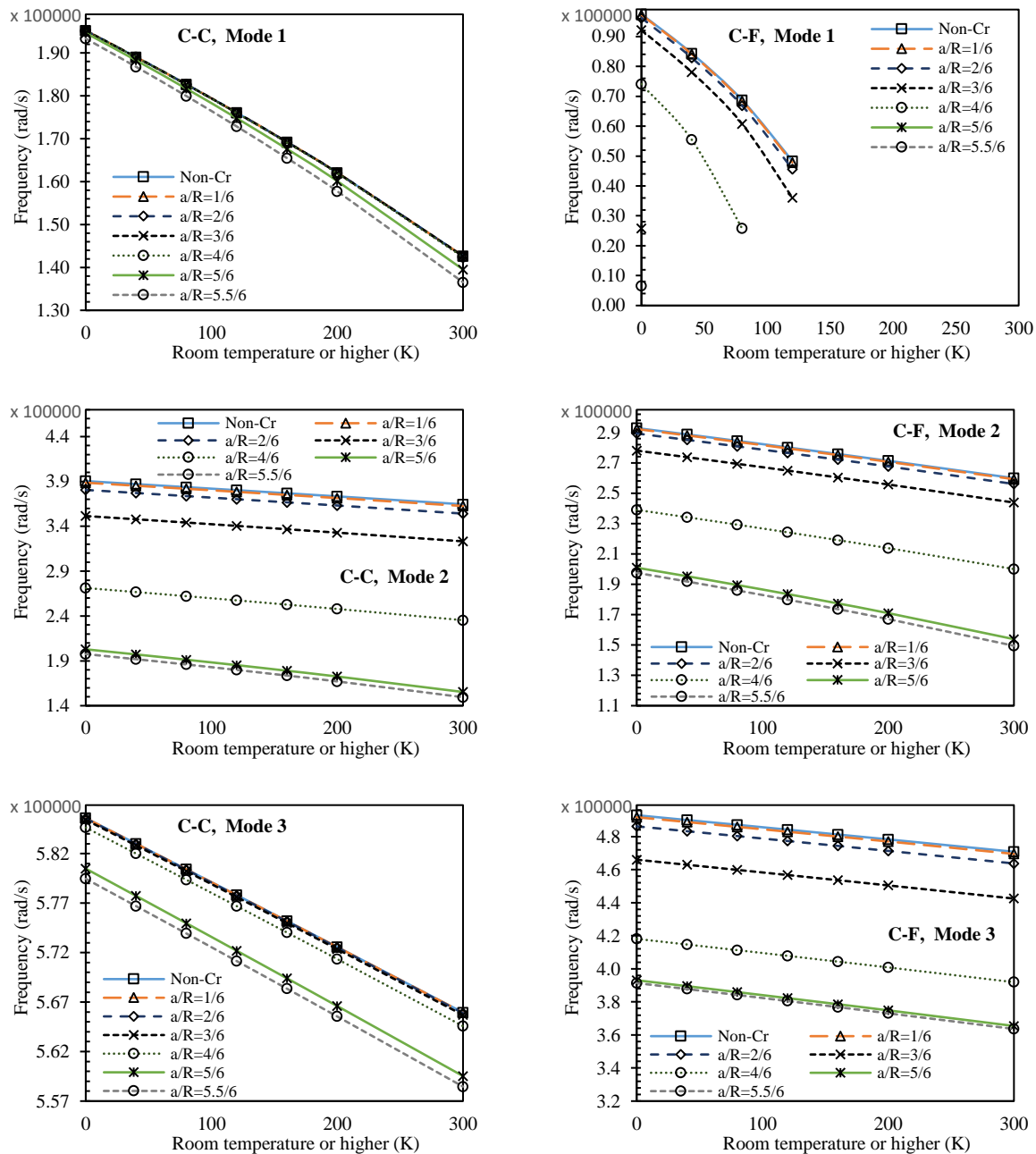


**Figure 2.** Variation of first three frequencies of cracked C-C and C-F rods versus room temperature or higher for different crack depth ratios. ($L = 50\ mm$, $d = 12\ mm$, and $b = L_1 = 25\ mm$).

The comparative parameter that is known as "difference percent" is a very important and usefulparameter to determine what parameters cause the temperature influence on the torsional frequencies to increases or decrease.The value of the difference percent is dependent on the other parameter values$C_c$, $b$,$L$, and $R$.

$$Difference\ percent = \frac{|frequency_T - frequency_{T_{room}}|}{frequency_{T_{room}}} \times 100. \qquad (36)$$

Here, $frequency_T$ is the frequency at temperature$T$, and $frequency_{T_{room}}$ is the frequency at room temperature.

According to Fig. 3,it can be observed that increasing the crack depth ratio $a/R$, consequently increasing the crack severity, leads to an increase in different percent of the rods with any boundary conditions for any vibration mode. This exactly means that the torsional frequencies will be more impressed by temperature changes when the crack is severe or intensive. If the crack severity is low value, all mode frequencies will not be highly sensitive to temperature changes. From the presented curves of Fig. 3, it is seen that the lower modes decrease more than the higher modes due to the temperature changes. As, reduction of the first mode is more than the second and third modes, and the second mode reduction is more than the third mode. It can be noted that the effect of thermal stresses on the torsional frequencies of the cracked rods of C-C and C-F rods cannot be negligible especially at elevated temperatures and high values of the crack severities, and this effect should be taken into account for rod design. The difference percent or effect of temperature changes on the frequencies of the C-F rod is more than the C-C rod because the C-C rod is stiffer than the C-F rod because of possessing two fixed ends.
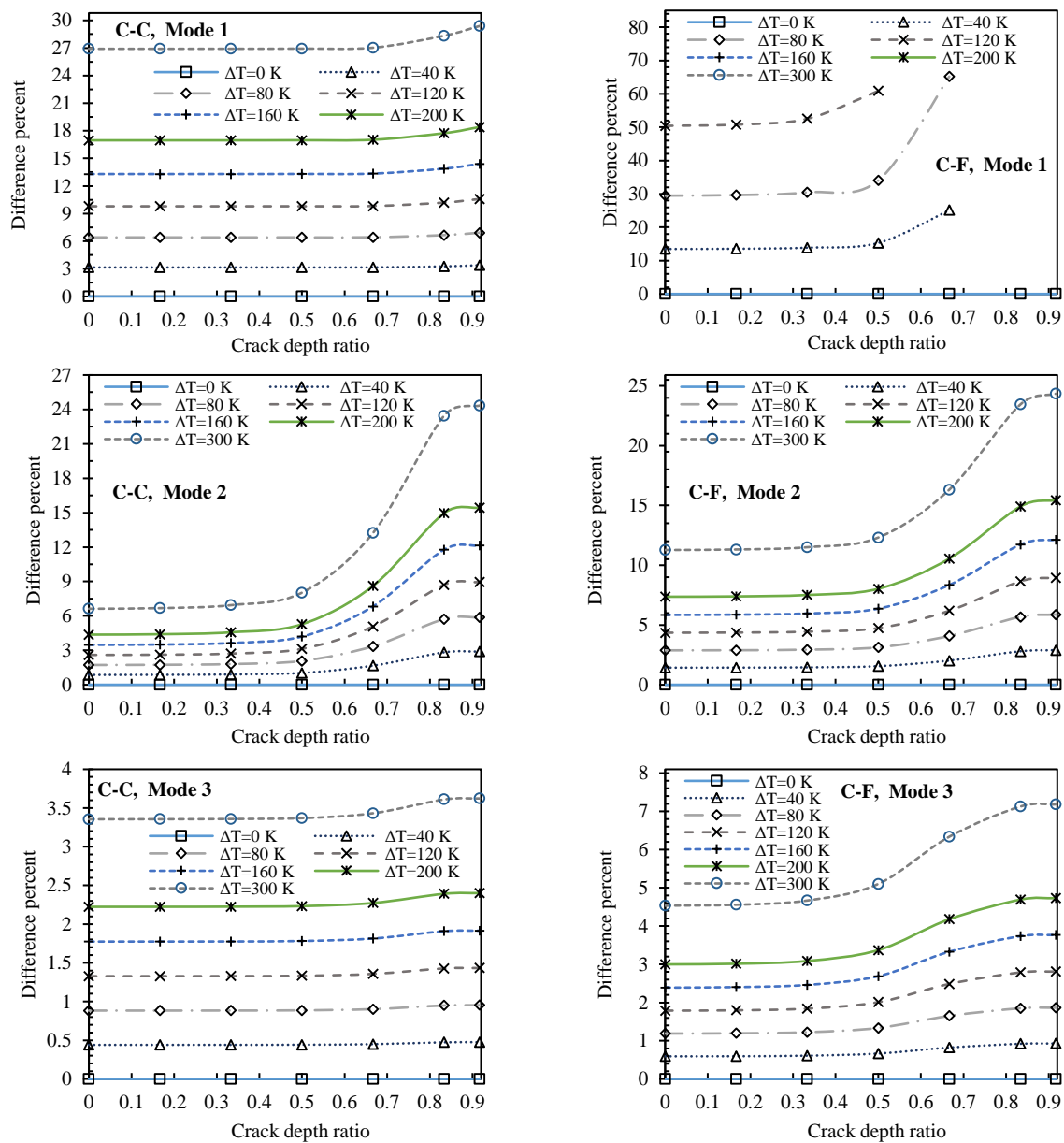


**Figure 3.**Difference percent of first three modes of C-C and C-F rods versus crack depth ratio at room temperature or higher. ($L = 50\ mm$, $d = 12\ mm$, and $b = L_1 = 25\ mm$).

## 4. Conclusions

The following conclusions are made according to the obtained results throughout this study.

- The linear torsional frequencies of non-cracked and cracked rods decline when the temperature is higher than room temperature for any boundary conditions, any crack severity, and any crack depth ratio.
- Increasing the crack depth leads to an increase in the crack severity and a decrease in all torsion frequency modes of the rod composed of two welded parts for any boundary condition at any temperature.
- Lower modes are more impressed by temperature and crack depth changes than higher modes.
- The frequency ratio of the C-C and C-F rods decreases with increasing temperature and crack depth ratio for all vibration modes.
- The difference percent increases with increasing the crack severity. The influence of the temperature on the frequencies becomes low when the crack is not deep. Increasing the difference percent of the C-F rod is much higher than that of the C-C rod for any crack depth especially for the first mode.

## Acknowledgments

## References

[1] C. Rhodes, M. Mahoney, W. Bingel, R. Spurling, C. Bampton, "Effects of friction stir welding on microstructure of 7075 aluminum". Scripta materialia, Vol. 36, No. 1, 1997, 69-75.

[2] H. Seli, M. Awang, A.I.M. Ismail, E. Rachman, Z.A. Ahmad, "Evaluation of properties and FEM model of the friction welded mild steel-Al6061-alumina". Materials Research, Vol. 16, No. 2, 2013, 453-467.

[3] R.S. Mishra, Z. Ma, "Friction stir welding and processing". Materials science and engineering: R: reports, Vol. 50, No. 1-2, 2005, 1-78.

[4] N.R.J. Hynes, P.S. Velu, "Simulation of friction welding of alumina and steel with aluminum interlayer". The International Journal of Advanced Manufacturing Technology, Vol. 93, No. 1, 2017, 121-127.

[5] N.R.J. Hynes, R. Tharmaraj, "Thermal Model for Heat Flow in Friction Stud Welding". J Therm Eng Appl, Vol. 2, No. 2, 2015, 22-27.

[6] G. Irwin, J. Kies, "Fracturing and fracture dynamics". Welding Journal, Vol. 31, No. 2, 1952, 95-100.

[7] J. Loya, J. López-Puente, R. Zaera, J. Fernández-Sáez, "Free transverse vibrations of cracked nanobeams using a nonlocal elasticity model". Journal of Applied Physics, Vol. 105, No. 4, 2009, 044309.

[8] Z.P. Baiant, L. Cedolin, "Finite element modeling of crack band propagation". Journal of Structural Engineering, Vol. 109, No. 1, 1983, 69-92.

[9] T. Chondros, "The continuous crack flexibility model for crack identification". Fatigue & Fracture of Engineering Materials & Structures, Vol. 24, No. 10, 2001, 643-650.

[10] O. Jun, H. Eun, Y.-Y. Earmme, C.-W. Lee, "Modelling and vibration analysis of a simple rotor with a breathing crack". Journal of sound and vibration, Vol. 155, No. 2, 1992, 273-290.

[11] T.G. Chondros, A.D. Dimarogonas, J. Yao, "Vibration of a beam with a breathing crack". Journal of sound and vibration, Vol. 239, No. 1, 2001, 57-67.

[12] S. Nacy, N. Alsahib, F. Mustafa, "Vibration analysis of plates with spot welded stiffeners". Jordan Journal of Mechanical and Industrial Engineering, Vol. 3, No. 4, 2009, 272-279.

[13] M. Ghadiri, K. Malekzadeh, F.A. Ghasemi, "Free Vibration of an Axially Preloaded Laminated Composite Beam Carrying a Spring-Mass-Damper System with a Non-Ideal Support". Jordan Journal of Mechanical and Industrial Engineering, Vol. 9, No. 3, 2015,

[14] S.H.H. Kachapi, "Nonlinear Vibration and Frequency Analysis of Functionally Graded-Piezoelectric Cylindrical Nano-shell with Surface Elasticity". Jordan Journal of Mechanical and Industrial Engineering, Vol. 12, No. 4, 2018,

[15] S.S. Abdullah, S. Hosseini-Hashemi, N.A. Hussein, R. Nazemnezhad, "Temperature change effect on torsional vibration of nanorods embedded in an elastic medium using Rayleigh–Ritz method". Journal of the Brazilian Society of Mechanical Sciences and Engineering, Vol. 42, No. 11, 2020, 1-20.

[16] S.S. Abdullah, S.H. Hashemi, N.A. Hussein, R. Nazemnezhad, "Three-Dimensional Thermal Stress Effects on Nonlinear Torsional Vibration of Carbon Nanotubes Embedded in an Elastic Medium". Nanoscale and Microscale Thermophysical Engineering, Vol. 25, No. 3-4, 2021, 1-28.

[17] X. Zhu, L. Li, "Longitudinal and torsional vibrations of size-dependent rods via nonlocal integral elasticity". International Journal of Mechanical Sciences, Vol. 133, No., 2017, 639-650.

[18] L. Li, Y. Hu, "Torsional vibration of bi-directional functionally graded nanotubes based on nonlocal elasticity theory". Composite Structures, Vol. 172, No., 2017, 242-250.

[19] R. Barretta, S.A. Faghidian, R. Luciano, C. Medaglia, R. Penna, "Stress-driven two-phase integral elasticity for torsion of nano-beams". Composites Part B: Engineering, Vol. 145, No., 2018, 62-69.

[20] A. Dimarogonas, G. Massouros, "Torsional vibration of a shaft with a circumferential crack". Engineering Fracture Mechanics, Vol. 15, No. 3-4, 1981, 439-444.

[21] T. Chondros, A. Dimarogonas, "Dynamic sensitivity of structures to cracks". Journal of Vibration and Acoustics, Vol. 111, No. 3, 1989, 251-256.

[22] P. Rizos, N. Aspragathos, A. Dimarogonas, "Identification of crack location and magnitude in a cantilever beam from the vibration modes". Journal of sound and vibration, Vol. 138, No. 3, 1990, 381-388.

[23] J. Loya, J.a. Aranda-Ruiz, J. Fernández-Sáez, "Torsion of cracked nanorods using a nonlocal elasticity model". Journal of Physics D: Applied Physics, Vol. 47, No. 11, 2014, 115304.

[24] M. Marin, "On the domain of influence in thermoelasticity of bodies with voids". Archivum Mathematicum, Vol. 33, No. 3, 1997, 301-308.

[25] M. Marin, "A temporally evolutionary equation in elasticity of micropolar bodies with voids". Bull Ser Appl Math Phys, Vol. 60, No. 3-4, 1998, 3-12.

[26] S. Amini, M. Amiri, "Study of ultrasonic vibrations' effect on friction stir welding". The International Journal of Advanced Manufacturing Technology, Vol. 73, No. 1, 2014, 127-135.

[27] J. Reddy, P. Mahaffey, "Generalized beam theories accounting for von Kármán nonlinear strains with application to buckling". Journal of Coupled Systems and Multiscale Dynamics, Vol. 1, No. 1, 2013, 120-134.

[28] J. Reddy, S. El-Borgi, J. Romanoff, "Non-linear analysis of functionally graded microbeams using Eringen′s non-local differential model". International Journal of Non-Linear Mechanics, Vol. 67, No., 2014, 308-318.

[29] J.N. Reddy. Mechanics of laminated composite plates and shells: theory and analysis. 2nd ed. New York: CRC press; 2003.

[30] J.R. Vinson, R.L. Sierakowski. The behavior of structures composed of composite materials. 2nd ed. Netherlands: Springer; 2006.

[31] S.S. Abdullah, S.H. Hashemi, N.A. Hussein, R. Nazemnezhad, "Effect of three-dimensional thermal stresses on torsional vibration of cracked nanorods surrounded by an elastic medium". Advances in nano research, Vol. 11, No. 3, 2021, 251-269.

[32] G. Praveen, J. Reddy, "Nonlinear transient thermoelastic analysis of functionally graded ceramic-metal plates". International Journal of Solids and Structures, Vol. 35, No. 33, 1998, 4457-4476.

[33] V. Mehta, S. Kumar, "Temperature dependent torsional properties of high performance fibres and their relevance to compressive strength". Journal of materials science, Vol. 29, No. 14, 1994, 3658-3664.

# Adaptive Neuro Fuzzy Inference System to Predict the Mechanical Properties of Friction Stir Welded AA7075-T651 Joints

Vaibhav S. Gaikwad[1,*], Satish S. Chinchanikar[2]

*[1]Research Scholar, Department of Mechanical Engineering, Vishwakarma Institute of Information Technology, Pune, Maharashtra State, India.*

*[2]Professor,Department of Mechanical Engineering, Vishwakarma Institute of Information Technology, Pune, Maharashtra State, India.*

## Abstract

The soft computing techniques are nowadays widely used in manufacturing industry for the modeling and optimization of processes parameters. The soft computing techniques give excellent predicted values which agree with the experimental results. In the present study, predictive model for the mechanical properties viz. ultimate tensile strength, micro hardness at weld nugget, and surface roughness in weld bead of friction stir weldedAA7075-T651 are developed. The adaptive fuzzy inference system technique is used for the development of the models. The models are developed using triangular, trapezoidal, Gaussian and generalized bell membership functions, and predicted values are compared. The triangular membership function shows minimum testing error of 19.1091, 12.3152, and 1.0018 for ultimate tensile strength, micro hardness at weld nugget, and surface roughness respectively. The validation experiment is performed at tool rotation speed of 1400 rpm and welding speed of 20 mm/min in order to check the predicted adaptive fuzzy inference system output. The observed values obtained after the validation experiment for ultimate tensile strength, micro hardness at weld nugget, and surface roughness are closer to the predicted adaptive fuzzy inference system output. The scanning electron microscopy images with energy dispersive X-ray spectrometer analysis confirmed the homogeneous mixing of material, laminar material flow with the equiaxed grain (size ~260 nm to 3 µm )distribution at the weld nugget. The scanning electron microscopy images of fractured tensile specimen shows the large dimple with the failure of specimen in heat affected zone.

## 1. Introduction

Friction stir welding (FSW) is a solid-state joining process. FSW is environment friendly, energy efficient, and versatile. Particularly, it can be used to join high-strength aerospace aluminum alloys and other metallic alloys that are difficult to weld by conventional fusion welding. FSW is considered to be the most significant development in metal joining in a last two decade [1].

FSW is an ideal solution for joining aluminum alloys; especially for the AA2000 and AA7000 series alloys. High-strength aluminum alloys, such as 7XXX, are commonly used in defense, aerospace, and military applications due to its high strength and light weight. These alloys are difficult to weld using conventional fusion welding as high temperature is involved in the processes, hence it can be joined through FSW. FSW has been successfully used in joining primary structures in the Eclipse 500TMjet [2].

VijayanandRao [3] developed a model to predict the tensile elongation and ultimate tensile strength (UTS) for friction stir welded (FSWed) AA2024 and AA6061 aluminum alloys. The models were developed using response surface methodology and adaptive fuzzy inference system (ANFIS). From this study, it was concluded that ANFIS predicted value has a greater accuracy and robustness in determining the values of dependent variables compared to the response surface methodology models. Eren et al. [4] performed a comprehensive review on the application of artificial intelligence (AI) techniques in FSW. Researchers attempted modeling of FSW using artificial neural network (ANN), machine learning, fuzzy logic, and meta-heuristic techniques and found prediction accuracy close to 95% with the experimental results. Attempts have been also made using ANFIS and machine learning techniques during FSW. Babu et al. [5] developed the model for prediction of mechanical properties of FSWedcryorolled AA2219 alloy using ANN. The genetic algorithm was used to determine the optimum FSW parameters. From

---

\* Corresponding author e-mail: vsgaikwad113@gmail.com.

this study, it was found that ANN modeling can forecast the output responses with high accuracy and the least root mean square error (RMSE) value found from the batch back propagation was 0.0089991.

Teimouri and Baseri[6] developed the prediction model for UTS, % elongation and hardness of FSWed aluminum joints using fuzzy approaches. In this study two approaches were used; the first approach relationships between inputs and outputs based on human expertise were models using manually fuzzy models, then artificial bee colony algorithm (ABC) was used to modify these models. From this study, it was concluded that the combination of fuzzy-ABC system gives more accurate results as compared to manually fuzzy models. Zhao et al. [7] investigated the bobbin pin FSW of AA2219-T87. In this study the empirical models were developed for UTS and % elongation. The calculated R-squared ($R^2$) values for UTS and % elongation were 85 % and 75 % respectively. Choudhary et al. [8] implemented the hybrid particle swarm optimization (PSO) and genetic algorithm (GA) for optimization of submerged arc welding processes parameters. From this study, it was concluded that hybrid PSO-GA approach gives better solution than PSO and GA.

Safeen et al. [9] developed a mathematical model for prediction of mechanical properties which includes impact toughness, UTS, and hardness of the FSWedAA6061-T6 joints. In this study, response surface methodology along with central composite design was used. It was concluded from this study that welding speed of 70 mm/min, rotational speed of 1150 rpm, tool tilt angle of 3° with simple cylindrical pin profile, highest impact toughness, UTS, and hardness were all achieved.

Ahmadnia et al. [10] developed the model to predict the hardness, UTS, and elongation for FSWed AA6061 and AA5010 joints using response surface methodology. In this study, desirability approach was used for the optimization. The obtained optimization results shows that at tool rotational speed of 800 rpm, welding speed of 60 mm/min, and plunge depth of 0.25 mm/min are the optimal conditions which give 174 MPa UTS, 106 Hv hardness, and 33 % elongation. Choudhury et al. [11] used the integrated ANN and teaching learning based optimization (TLBO) soft computing modeling optimization to obtain the optimum processes parameters. In this study, UTS of the Inconel 825 super alloy joints produced using tungsten arc welding were optimized. ANN architecture with seven hidden layerneurons produce an effective error of 0.5% found optimum for predicting the UTS of the joints.

Hayajneh et al. [12] developed the prediction of surface roughness in end milling using two different gene expression programming. In genetic programming 1 and 2 model, the differences are their number of genes, head size, chromosomes, and the linking function. The $R^2$, RMSE and mean absolute percentage error are obtained as 0.923, 0.268 and 0.219 respectively, for all training set in genetic programming 1 model. Farouk et al. [13] perform the optimization of manufacturing tolerance using the goal programming method and the genetic algorithm. The table motion error, tool path error, and tool wear error were optimized using non-dominated sorting genetic algorithm (NSGA). The zero percent rejection was obtained by the optimization using goal programming and NSGA

methodology. Soori et al. [14] performed the review of optimization procedures of machining parameters and applications of the different optimization methods, such as fuzzy logic algorithm, taguchi method, genetic algorithm, artificial intelligence, artificial neural networks and artificial bee colony algorithm, simulated annealing, ant colony optimization, PSO, scatter search technique, and response surface methodology and harmony search algorithm in optimization process of machining parameters.

Ismail [15] et al. used the machine learning techniques to detect fire fighting in power plant industry. One hidden layers and two hidden layers feed forward neural network models were developed for the prediction of occurrence of fire due to the impulsive burning of coal. From this study, it is proposed that two hidden layer feed forward neural network could be best fit for prediction of fire. Ning [16] schedule the resources in automobile part recycling using adaptive technique. Improved reverse PSO technique was used in this study. Using this methodology, the lesser energy consumption, highest recovery resource utilization rate, and the task time of about 200-400s were obtained. Ayun et al. [17] performed the optimization of injection moulding simulation parameters on performance measures viz. shrinkage and warpage of bone screw using PSO. The obtained results show that injection time, melt temperature, and packing time had significant effects on shrinkage and warpage of polylactic acid bone screws. The optimization results show that the shrinkage and warpage value improved to 2.4233% and 0.0928 mm for polylactic acid bone screws and 8.9592% and 0.4646 mm for polyglycolic acid bone screws.

Precup et al. [18] designed the model based fuzzy controllers for network control systems. In this study, Hilbert-Huang transform was applied for variable time delay to smooth the signals. Later on Takafi-Sugeno-Kang Proportional-Integral-Fuzzy design was applied for temperature controlled applications. From this study, it was concluded that the theoretical results were matched in excellent manner with the real-world temperature control applications. Vilela et al. [19] performed the value of information assessment for oil and gas industry by the application of fuzzy inference system (FIS). In this study, the use of a Boolean relationship between project valuation and project decision is replaced by the fuzzy inference system, a fuzzy human thinking approach to make decisions. To integrate more than one criterion into the assessment, the coherent method is used by the FIS as compared with the conventional value of information approach. In value of information approach, if more than criterion is used then the contradictory outcomes will be obtained which conduct to unconvincing assessment. Božanić et al. [20] implemented neuro-fuzzy system in decision making for the selection of construction machine (selection of loader). In this study, the data for neuro-fuzzy system is prepared using multi criteria decision making; logarithm methodology of additive weighs, VIekriterijumsko KOmpromisno Rangiranje, Technique for Order of Preference by Similarity to Ideal Solution. The developed model provides noteworthy support to decision makers for several reasons in selection of loader.

Meyghani et al. [21] performed the finite element modelling of FSW process on complex curved plate. In this study, software tools such as AltairHyperworks and ABAQUS software are employed for the simulation of the processes. The results obtained from the simulation show the significant increase in the heat generation, which results in the enlargement of the shear zone. Due to the enlargement of shear zone, the peak temperature rises to almost 300 °C after 3 seconds. Kavitha et al. [22] performed the optimization of FSW process for joining of AA7079 and AA8050 aluminum alloy using response surface methodology. The UTS of 211.48 MPa obtained at optimum values at tool rotational speed is 1000 rpm, welding speed of 300 mm/min, tool pin diameter of 2.4 mm, and shoulder diameter of 10 mm. Heidarzadeh et al. [23] developed the fuzzy model to predict the UTS and elongation of FSWed pure copper joints. In that study, 20 experiments were performed for the development of fuzzy model. Using fuzzy prediction model, the maximum UTS of 276.1 MPa and elongation of 44.6% was obtained at tool rotational speed of 1136 rpm, welding speed of 46.75 mm/min, and axial force of 3.34 kN.

Jamalian et al. [24] developed the ANN model for FSWed joints of AA5086-H34 plates which are reinforced with nanoparticles of $Al_2O_3$. The multi-pass technique by varying the tool pin was implemented in this study. The optimization results confirm that the highest UTS was obtained using square pin geometry which was of 303 MPa. Terra et al. [25] developed the models for FSW forces in case of square pin profile. In this study, the welding, tangential, transverse, and radial forces are demonstrated as a function of welding speeds, tool rotational speed and the instantaneous angle of rotation. The $R^2$ values acquired are 0.9828, 0.9737, 0.9944, and 0.9881 for tangential, radial welding, and 0.9881 for the transverse force, which confirm the agreement between the models and experiments.

Han et al. [26] developed the ANFIS prediction model for hot deformation processes of Ti600 alloy. In this study, the ANFIS was integrated with back-propagation learning algorithm of neural network. The predicted values of ANFIS for the flow stress of Ti600 titanium alloy has a great accuracy and with absolute relative error less than 17.39%. Guneri et al. [27] implemented the ANFIS for the selection of supplier in the textile industry. The developed ANFIS model is robust with respect to the types of changes in the business. The ANFIS model is compared with the multiple regression model, and it is concluded that the ANFIS model performs better than multiple regression model. Naderloo et al. [28] developed the ANFIS model to predict the crop yield. The study includes higher number of input (eight inputs); two networks were trained. In ANFIS 1, the inputs were fertilizer, diesel fuel, and electricity energies, and in ANFIS 2 inputs were machinery, human labor, water for irrigation, chemicals, and seed energies. The RMSE and $R^2$ values were obtained as 0.013 and 0.996 for ANFIS 1 and 0.018 and 0.992 for ANFIS 2, respectively. Ekici et al. [29] developed the ANFIS model for the prediction of consumption of energy by the building in cold region. It was concluded from the study that ANFIS was efficient in predicting energy consumption of different buildings with a good degree of accuracy reaching 96.5% and 83.9% for heating and cooling respectively.

From the literature reviewed, it has been observed that numerous studies reported on modelling of weld qualities of the FSW process. However, researchers mostly attempted the modelling of processes parameters to predict the weld qualities using statistical techniques [30]. However, very few studies are available on the modelling of the processes parameters of the FSWed AA7075-T651 joints using soft computing techniques in the open literature. AA7075-T651 being low-weight and high-strength has been widely used in aerospace, automotive, and naval applications. However, this alloy showed poor weld ability due to porosity in the fusion zone and poor solidification microstructure. Hence, modelling of the process parameters while FSW of AA7075-T651 is crucial for obtaining a joint with better mechanical properties.

With this view, in the objective of the present study, to model the FSW processes parameters using ANFIS, to predict the weld qualities of FSWed AA7075-T651. In this study ANFIS model is developed using different membership functions. This paper will help the fellow researchers to select the best membership function and give the model to determine the mechanical properties of FSWed AA7075-T651 joints. Experiments were performed using the conical threaded tool varying the welding speed and tool rotation. Microstructural analysis and fracture behavior of FSWed joint is discussed for a better understanding of the process physics.

## 2. Experiment details

In the present study, FSWedAA7075-T651 square butt joints are produced. Experiments were performed on a universal milling machine. Two plates to be welded were initially squared and made free from any burr. The experimental setup is as shown in figure 1(a). A specially designed tool that provides thermo mechanical action along the weld direction due to its rotation and translation was used to get the required joint. A conical threaded tool pin with a constant plunge depth of 5.6 mm as shown in figure 1 (b) is used in the present study. The process parameters were selected based on the literature reviewed and pilot experiments. Experiments were performed under dry conditions and at tool rotations of 1000, 1200, 1400, 1600, 1800 and 2000 rpm, and at welding speeds of 20, 28, and 40 mm/min. A total of eighteen experiments were performed.

In this work, the mechanical behavior of the FSWed of AA7075-T651 joints is investigated in terms of the UTS, microhardness at weld nugget (MWN), and surface roughness (SR) at the center of the weld bead considering the effect of process parameters. The tool material used was H13 type tool steel and its geometry is a conical threaded pin type. The chemical composition of the tool material and workpiece material is depicted in Table 1 and Table 2, respectively. The UTS of base material was obtained as 550 MPa, with peak elongation of 9.1%.

The UTS of FSWed joints was measured using a universal testing machine. The test was performed as per the ASTME8M standard to obtain the transverse UTS of joints. Plate dimensions with positions for extraction of test specimens and tensile test specimens are as shown in figure 2(a) and (b) respectively. The MWN, was measured by Vicker's microhardness tester as per the ISO6507 standard. The diamond indenter with 136º and with a load of 100 grams for a dwell time of 20 seconds was used. The SR at the weld bead was measured by the surface roughness tester at 25 mm from the start of a weld, at the middle of the weld, and 25 mm before the end of the weld. An average of the three values measured at the said locations was noted down. The FSWed joint analysis was performed using field emission scanning electron microscope (FESEM) (Make: FEI Nova Nano SEM 450). The samples of size 5 x 5 mm were cut in transverse direction to weld line by wire electric discharge machining, and then it is observed under FESEM at different magnifications. The elemental analysis of weld nugget (WN) is carried out using Energy-dispersive X-ray spectroscopy (EDS) (Make: BrukerXFlash 6I30 spectrometer) in conjunction with scanning electron microscopy (SEM) images.

## 3. AdaptiveNeuro-Fuzzy Inference Systems Methodology

ANFIS is a model that incorporates both the fuzzy logic qualitative and adaptive neural network approaches and overwhelms their corresponding drawbacks. It is a good estimator and predictor. ANFIS has capability of approximation equal to the neural network; hence, the outputs can be easily constructed with ANFIS [3].

The ANFIS model contains five layers, and each of this layer is connected by numerous nodes. Each input node is extended by the preceding layer. The developed ANFIS models for UTS, MWN, and SR are presented in Figs. 3 (a), (b), and (c) respectively. The models shows that the network includes m inputs (M1, …,Mm), each of these inputs consists of n membership functions. In the present model is constructed by a layer with R fuzzy rules as an output layer. The product of number of membership function (n) and number of inputs (m) gives the total number of layers (N), i.e., ($N=n \cdot m$). The number of nodes in the other layer is related to the number of fuzzy rules (R). The details of each layer is mentioned as follows[3].



(a)  (b)
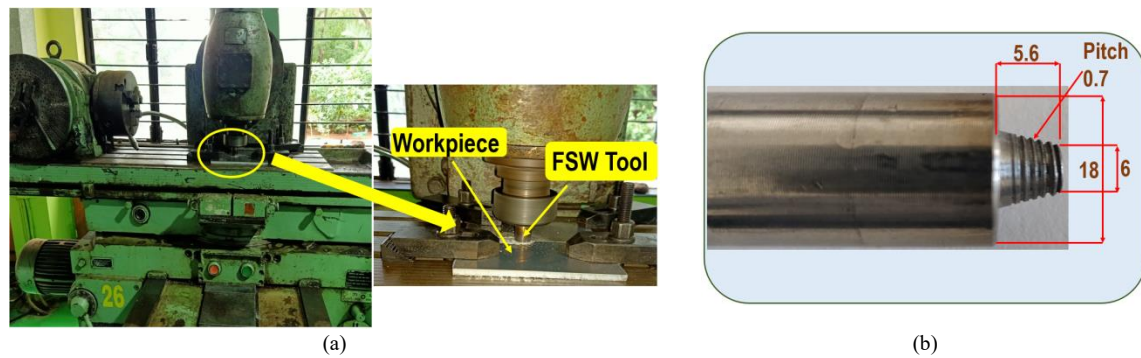
**Figure 1.** Friction stir welding a) Experimental setup, b) Conical threaded tool (all dimensions are in mm)

**Table 1.** The chemical composition (% weight) of H13 FSW tool [31]

| Elements | Cr | Mo | Si | V | C | Ni | Cu | Mn | P | S |
|---|---|---|---|---|---|---|---|---|---|---|
| % | 4.75 | 1.10 | 0.80 | 0.80 | 0.32 | 0.3 | 0.25 | 0.2 | 0.03 | 0.03 |

**Table 2.** Chemical composition (% weight) of AA7075-T651 alloy[31]

| Elements | Si | Fe | Cu | Mn | Mg | Zn | Ni | Pb | Sn | Ti | Cr | Al |
|---|---|---|---|---|---|---|---|---|---|---|---|---|
| % | 0.069 | 0.204 | 1.64 | 0.0060 | 2.33 | 5.28 | 0.012 | 0.012 | <0.0050 | 0.028 | 0.195 | 90.22 |



(a)  (b)
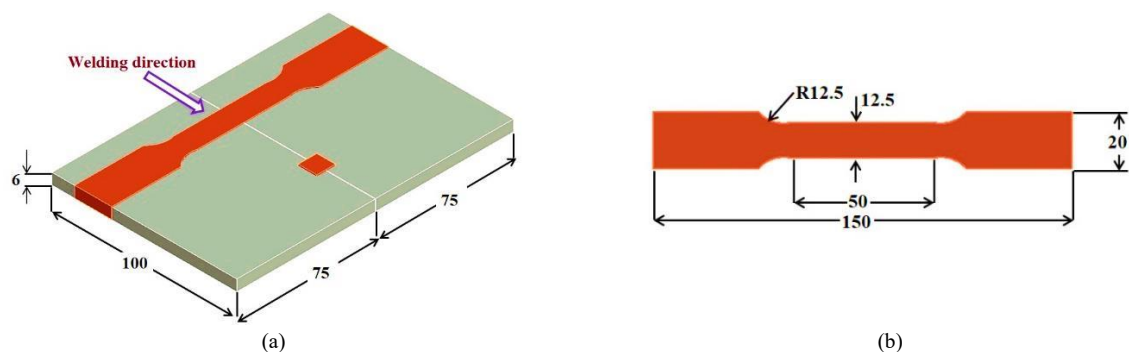
**Figure2.** a) Plate dimensions showing position for extraction of test specimens, b) Tensile test specimen (all the above-mentioned dimensions are in mm)

**Layer 1 (fuzzification):** The crisp inputs are transformed into the linguistic type using membership functions in layer 1. The output of this layer is expressed as,

$$Q_j^i = u_{ij}(X_i), \qquad i = 1 \dots m, \quad j = 1 \dots n \qquad [1]$$

Where $u_{ij}$ is the $j^{th}$ membership function for the input.

**Layer 2 (product layer):** In this layer, each fixed node can be obtained by multiplying the linguistic inputs, which were calculated in the previous layer:

$$Q_k^2 = W_k = u_{1e1}(X_1)u_{2e2}(X_2) \dots u_{me_m}(X_m),$$
$$k=1\dots,R; \ e_1, e_2, \dots\dots, e_m = 1, \dots\dots, n \qquad [2]$$

**Layer 3 (normalized layer):** For the each node the outputs were normalized using weighing factor as mentioned in equation [3].

$$Q_k^3 = \overline{W_k} = \frac{W_k}{W_1+W_2+W_3+\dots+W_R} \qquad [3]$$

**Layer 4 (defuzzification layer):** Takagi-Sugeno fuzzy-type if–then rules were applied in this layer to the output of each node.

$$Q_k^4 = \overline{W_k}f_k \qquad [4]$$

Where, $f_k$ represents the output of $k^{th}$ TSK-type fuzzy rules which is represented as follows:

If $(X_1 \ is \ A_{1 \ e_1})$ and $(X_2 \ is \ A_{2 \ e_2})$ and …….and $(X_m \ is \ A_{m \ e_m})$ then,

$$f_k \textstyle\sum_{i=1}^m p_{ie_i x_i + r_k} \qquad [5]$$

Where, $p_{ie_i, r_k}$ are called as consequent parameters and $e_{1,}e_2, \dots\dots, e_m = 1, \dots., n; k = 1 \dots, R.$

**Layer 5 (Output layer):** The output modeled in the ANFIS is represented in this layer.

$$Q^5 = Y = \textstyle\sum_{k=1}^n \overline{W_k}f_k \qquad [6]$$

To check the performance of the trained ANFIS model, RMSE is evaluated using the equation:

$$\text{RMSE} = \sqrt{\frac{1}{T}\textstyle\sum_{z=1}^T (R_z - A_z)^2} \qquad [7]$$

Where, T is total number of training sample, $R_z$ is the real output, and $A_z$ is ANFIS output in training.
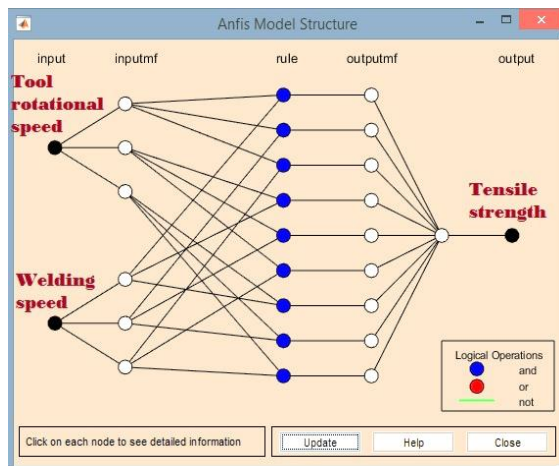


(a)
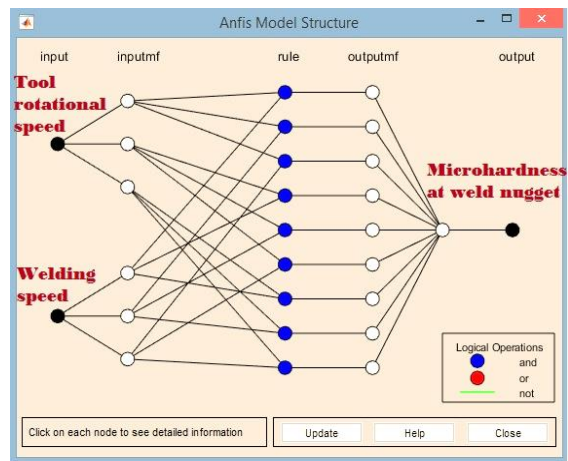


(b)
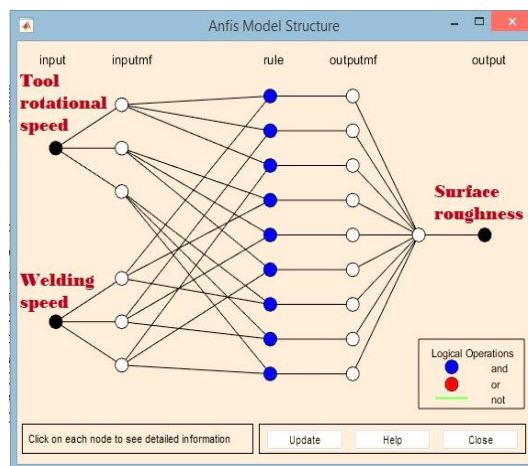


(c)

**Figure 3.** Developed ANFIS models structure for a) UTS b) MWN c) SR

## 4. Results and Discussion

### 4.1. Discussion based on ANFIS

The ANFIS model developed in the present study is using MATLAB R2022a. For predicting the mechanical properties viz. UTS, MWN, and SR of FSW process by ANFIS, the model consists of mainly two phases i.e. training phase and testing phase. The ANFIS model is established using thirteen dataset selected for the training. In the second stage, the trained network has been tested by other five additional data sets. Generally, the testing phase is executed in order to establish the pre-eminent network architecture of the network models.

In the present investigation three responses/outputs (UTS, MWN, and SR) are considered, hence three different models were trained. In ANFIS, the number of membership functions (MFs) and type of fuzzy rules, are considered to be the important factors to predict the accurate model. In the present study Sugenotype fuzzy-based rule has been used for the development of predictive models. The value for the error goal RMSE is set at 0.01

and the number of iterations is 300 epochs. This means, the training epochs are continued, until the RMSE fell below 0.01 or the epochs reach up to 300.

In the present study the number of MFs for input 1 (tool rotational speed) and input 2 (welding speed) are taken as three, and for the output UTS, MWN, and SR model is developed using the type of input MF as triangular (Trimf), trapezoidal (Trapmf), Gaussian (Gaussmf), and generalized bell (Gbellmf) MFs. The type of output MF is taken as a constant. Nine fuzzy rules are used in the present study. The triangular MF for input 1 (tool rotational speed) and input 2 (welding speed), and constant MF for output (UTS) are shown in figure 4 (a)-(c) respectively. Similarly input 1 (tool rotational speed) and input 2 (welding speed), and constant MF for outputs (UTS,MWN, and SR) can be shown using Trapmf, Gaussmf, and Gbellmf. The rules and rule viewer for the developed ANFIS model of UTS using Trimf is shown in figure 5 (a)–(b) respectively. Similarly the rules and rule viewer can be shown for the outputs UTS, MWN, and SR using Trapmf, Gaussmf, and Gbellmf.



(a)

(b)

(c)
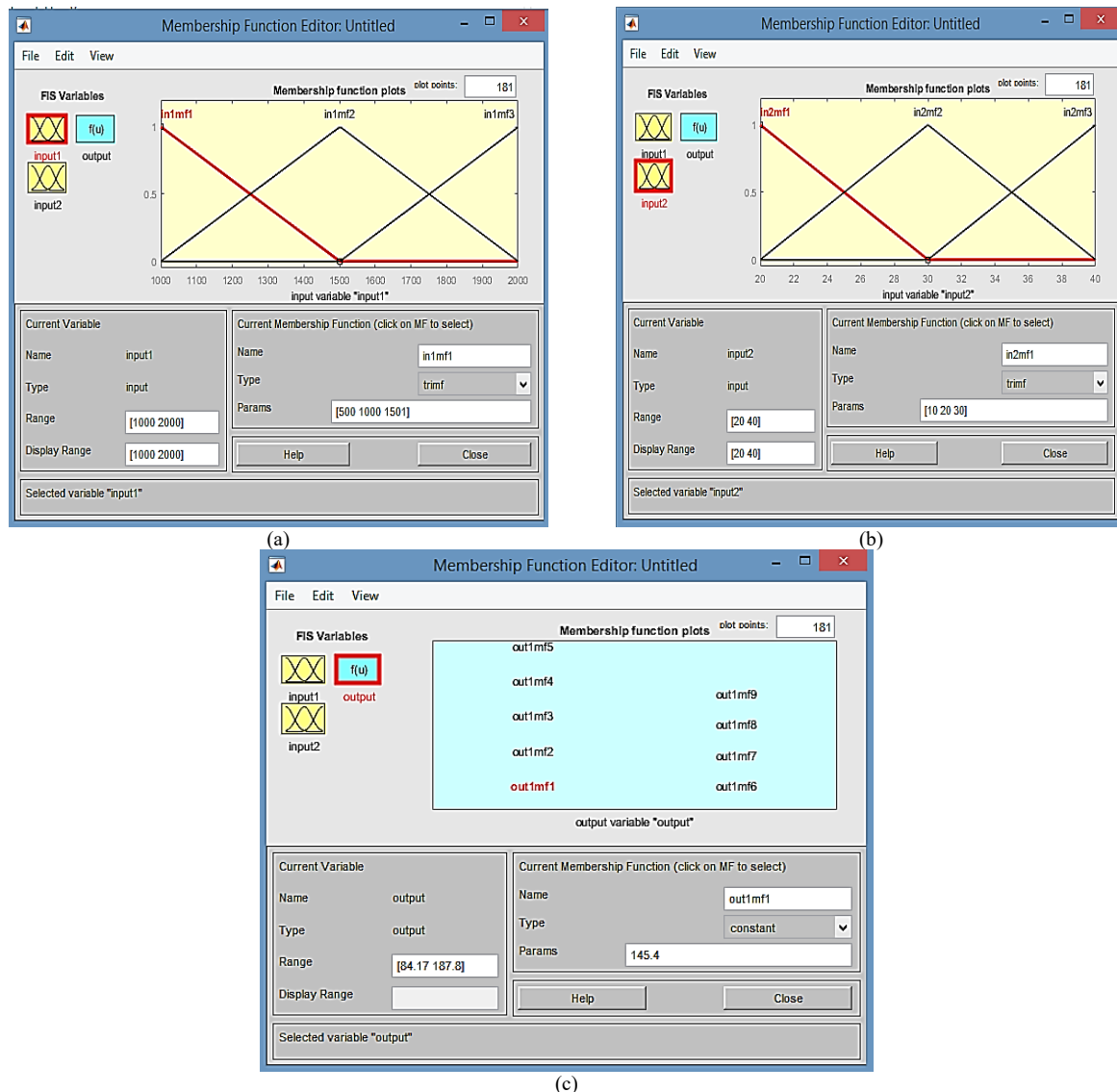
**Figure.** 5 a) triangular MF for input 1 (tool rotational speed) b) for input 2 (welding speed), and c) constant MF for output (UTS)

González et al. [32] developed the empirical model for FSWed Al 6061-T6-Cu C11000 joints. In this study, the correlation between performance measure corrosion resistance and input parameters of FSW such as the welding speed and tool rotational speed was established. The $R^2$for the developed model was obtained to be 0.85.Zhao et al. [33] developed the empirical model for the UTS and tensile elongation of FSWed AA2219-T87 aluminium alloy. The welding factors, such as shoulder pinching gap, tool rotational speed and welding speed are considered as inputs. The $R^2$ values for the UTS and tensile elongation was 0.85 and 0.75 respectively. Yuvaraj et al. [34] performed the optimization and empirical modelling of FSWed AA7075-T651 and AA6061 aluminium alloys. The tool offset, tilt angle, and pin profile were considered as the input parameters and UTS was considered as the output. The $R^2$value of the empirical model was around 0.98.

The predicted values of UTS, MWN, and SR are determined for each of these MFs. The $R^2$ values are determined in the present study for the UTS, MWN, and SR. The $R^2$ values of the output (UTS, MWN, and SR) obtained in the present study using Trimf, Trapmf, Gaussmf, and Gbellmf are greater than and in some cases closer to the $R^2$ values reported in the open literature [32-34]. Also the RMSE, testing error is determined and depicted in table 3.

It can be seen that the developed predictive models with triangular MF gives more accurate prediction of the mechanical properties. The minimum testing error of 19.1091, 12.3152, and 1.0018 is obtained for UTS, MWN, and SR using trimf respectively as compared with the trapmf, gaussmf, and gbellmf. Moreover, the better value of $R^2$ of 0.8639, 0.8178, and 0.9520 are obtained using trimffor UTS, MWN, and SR respectively as compared with the trapmf, gaussmf, and gbellmf.

The maximum testing error of 28.1289, 12.9314, and 1.3791 is obtained for UTS, MWN, and SR respectively using trapmf. Moreover the poor value of $R^2$are obtained as 0.7683, 0.7893, and 0.9321for UTS, MWN, and SR respectively using trapmf as compared with the trimf, gaussmf, and gbellmf.

It is noted that there is the marginal difference in the values of testing error and $R^2$ for gaussmf and gbellmf.

Experiment design matrix with their experimental, predicted ANFIS output using trimf, trapmf, gaussmf, and gbellmf for UTS, MWN, and SR are depicted in table 4.

The performance validation process of ANFIS based on UTS, MWN, and SR are presented graphically in figures7(a) −(c)respectively for trimf. The experimental values and ANFIS predicted values are scattered on both sides and are closer to the45° line, this indicates that the perfect fitness of the developed ANFIS models.
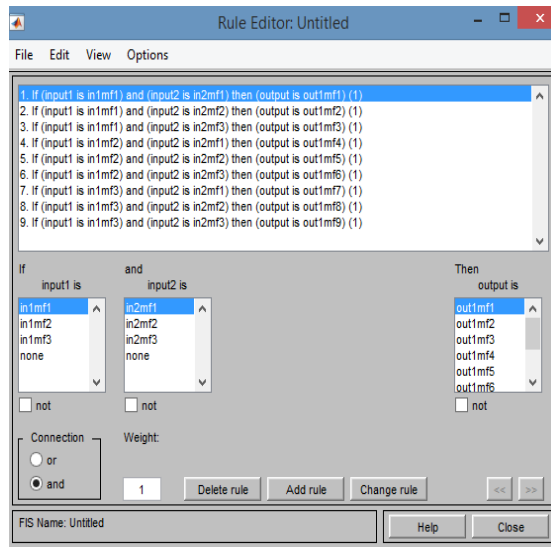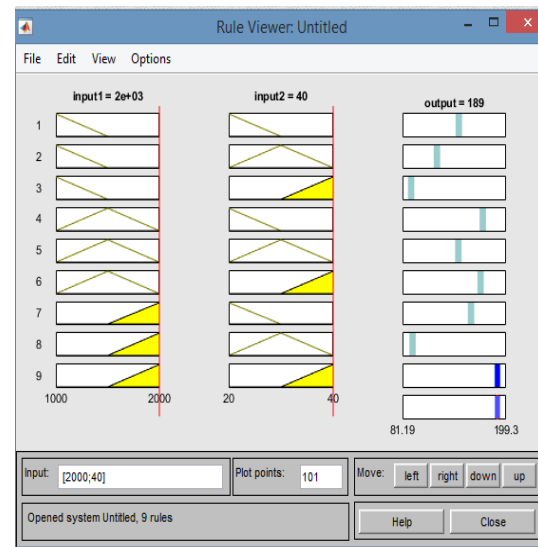


(a)                                                                 (b)

**Figure 6.** a)Rules and b) Rule viewer for the developed ANFIS model of UTS using Trimf

**Table 3**. RMSE, testing error, and determination coefficient ($R^2$) for various MFs

| Type of MFs | UTS | | | MWN | | | SR | | |
|---|---|---|---|---|---|---|---|---|---|
| | Minimal training RMSE | Testing error | $R^2$ | Minimal training RMSE | Testing error | $R^2$ | Minimal training RMSE | Testing error | $R^2$ |
| Trimf | 12.9618 | 19.1091 | 0.8639 | 1.24801 | 12.3152 | 0.8178 | 0.494589 | 1.0018 | 0.9520 |
| Trapmf | 14.5044 | 28.1289 | 0.7683 | 0.902507 | 12.9314 | 0.7893 | 0.415752 | 1.3791 | 0.9321 |
| Gaussmf | 13.6566 | 22.0629 | 0.8302 | 0.968477 | 12.4863 | 0.8073 | 0.462078 | 1.1214 | 0.9477 |
| Gbellmf | 12.0391 | 22.3088 | 0.8525 | 0.777753 | 12.5225 | 0.7962 | 0.398903 | 1.2141 | 0.9482 |

(a)

(b)

(c)
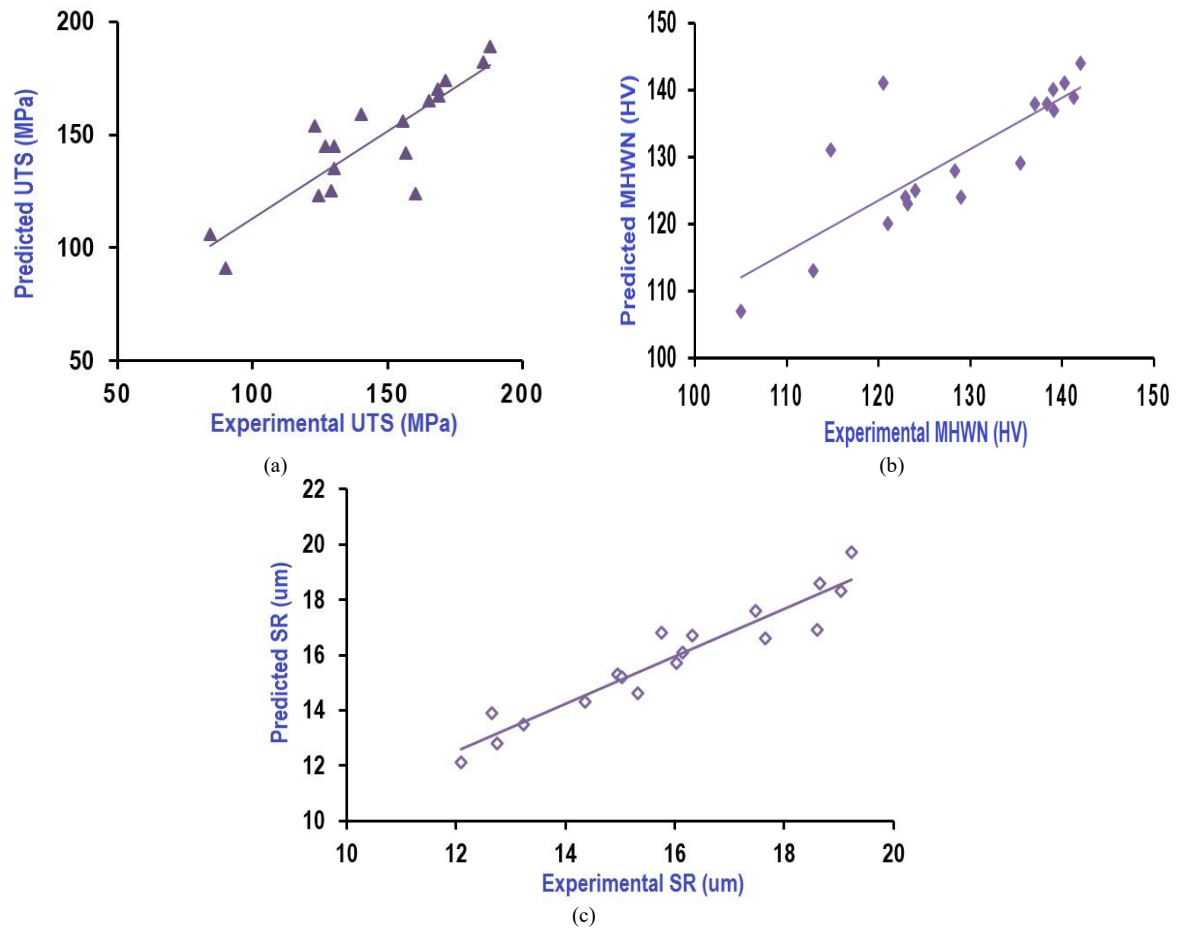
**Figure7**. Performance of predicted ANFIS output using trimf a)UTS, b)MHWN, and c) SR

**Table 4**.Experimental, predicted ANFIS output using trimf, trapmf, gaussmf, and gbellmf for UTS, MWN, and SR

| Run | Tool rotation (rpm) | Tool transverse speed (mm/min) | Experimental values | | | Predicted UTS (MPa) | | | | Predicted MWN (HV) | | | | Predicted SR (μm) | | | |
|---|---|---|---|---|---|---|---|---|---|---|---|---|---|---|---|---|---|
| | | | UTS (MPa) | MWN (HV) | SR (μm) | Trimf | Trapmf | Gaussmf | Gbell mf | Tri mf | Trap mf | Gauss mf | Gbell mf | Tri mf | Trap mf | Gauss mf | Gbell mf |
| 1 | 1000 | 20 | 130.020 | 105 | 12.65 | 145 | 151 | 148 | 149 | 107 | 110 | 109 | 110 | 13.9 | 14.4 | 14.2 | 14.4 |
| 2 | 1000 | 28 | 129.180 | 123.2 | 18.65 | 125 | 129 | 127 | 127 | 123 | 123 | 123 | 123 | 18.6 | 18.6 | 18.6 | 18.6 |
| 3 | 1000 | 40 | 90.070 | 138.4 | 12.1 | 91.1 | 96.2 | 93.3 | 92 | 138 | 138 | 138 | 138 | 12.1 | 12.2 | 12.1 | 12.2 |
| 4 | 1200 | 20 | 155.775 | 112.9304 | 14.9562 | 156 | 156 | 156 | 156 | 113 | 113 | 113 | 113 | 15.3 | 15 | 15.2 | 15 |
| 5 | 1200 | 28 | 130.225 | 128.956 | 17.485 | 135 | 131 | 133 | 133 | 124 | 123 | 124 | 123 | 17.6 | 18.1 | 17.8 | 18.1 |
| 6 | 1200 | 40 | 124.275 | 139.0504 | 12.7582 | 123 | 116 | 119 | 121 | 140 | 139 | 139 | 139 | 12.8 | 12.7 | 12.7 | 12.6 |
| 7 | 1400 | 20 | 168.830 | 121 | 17.65 | 167 | 169 | 168 | 168 | 120 | 122 | 120 | 121 | 16.6 | 16.7 | 16.6 | 16.9 |
| 8 | 1400 | 28 | 127.050 | 124 | 16.32 | 145 | 137 | 143 | 147 | 125 | 124 | 125 | 124 | 16.7 | 16.4 | 16.5 | 16.5 |
| 9 | 1400 | 40 | 123.110 | 120.5 | 13.23 | 154 | 174 | 160 | 164 | 141 | 141 | 141 | 141 | 13.5 | 14.3 | 13.7 | 14 |
| 10 | 1600 | 20 | 168.495 | 122.9704 | 15.7562 | 170 | 169 | 170 | 170 | 124 | 122 | 124 | 123 | 16.8 | 16.7 | 16.8 | 16.7 |
| 11 | 1600 | 28 | 156.705 | 135.476 | 18.605 | 142 | 137 | 140 | 147 | 129 | 124 | 128 | 125 | 16.9 | 16.4 | 16.7 | 16.8 |
| 12 | 1600 | 40 | 171.395 | 140.2904 | 14.3582 | 174 | 174 | 174 | 175 | 141 | 141 | 141 | 141 | 14.3 | 14.3 | 14.3 | 14.3 |
| 13 | 1800 | 20 | 165.255 | 128.3504 | 16.0362 | 165 | 165 | 165 | 165 | 128 | 128 | 128 | 128 | 15.7 | 16 | 15.8 | 15.9 |
| 14 | 1800 | 28 | 160.345 | 139.096 | 19.045 | 124 | 120 | 122 | 126 | 137 | 138 | 137 | 139 | 18.3 | 18.7 | 18.5 | 18.6 |
| 15 | 1800 | 40 | 185.355 | 141.2704 | 15.0382 | 182 | 185 | 183 | 181 | 139 | 139 | 139 | 139 | 15.2 | 15.5 | 15.3 | 15.4 |
| 16 | 2000 | 20 | 140.220 | 114.8 | 15.32 | 159 | 164 | 162 | 160 | 131 | 130 | 131 | 130 | 14.6 | 15.8 | 15.2 | 15.4 |
| 17 | 2000 | 28 | 84.170 | 142 | 19.23 | 106 | 114 | 110 | 100 | 144 | 143 | 143 | 142 | 19.7 | 19.5 | 19.6 | 19.5 |
| 18 | 2000 | 40 | 187.850 | 137 | 16.15 | 189 | 188 | 189 | 190 | 138 | 139 | 138 | 139 | 16.1 | 15.8 | 16 | 15.9 |

*4.2. Discussion based on confirmatory experiment*

In order to check the predictive values of ANFIS model, an additional confirmatory experiment is performed at tool rotation speed of 1400 rpm and welding speed of 20 mm/min. The UTS, microhardness at different zones of weld region, and SR is evaluated. The stress-strain curve, variation of microhardness in weld region, and top surface appearance of FSWed joint produced at 1400 rpm and 20 mm/min are shown in figures 8 (a)-(c) respectively.

The UTS, MWN, and SR obtained are 169.75 MPa, 122 HV, and 16.3 µm respectively at tool rotation speed of 1400 rpm and welding speed of 40 mm/min. It can be seen that the welded joint can sustain the load of 11.632 kN with % peak elongation of 4.9 %. The better tensile strength for FSWed joints can be obtained due to the better stirring of the material. The conical threaded pin increased the amount of material, both in transporting per revolution and extruding backward, resulting in more plastic deformation. It causes the fine grain size at the WN and higher UTS for FSWed joints.

The microhardness values of FSWed AA7075-T651 joints are measured at different points from the weld center on the advancing as well as the retreating side of the joint. The microhardness is measured in different zones of weld such WN, thermo mechanically affected zone (TMAZ), heat affected zone (HAZ), and base material (BM). Severe extrusion and higher plastic deformation during FSW causes variation in the grain size and the microhardness in the welded region. The microhardness of FSWed joints showed variation in the welding zone, mostly followed distribution a letter 'W' shape (fig.8 b) and found maximum at the WN and minimum at the heat affected zone(HAZ).

SR obtained on the weld top surfaces shows process effectiveness and generated surface is important from operational functioning of the welded joint. The figure 8 (c) shows the top surface appearance of confirmatory experiment. The proper mixing of material is observed at the weld line.

The heat generated in FSW results from the frictional effects of the rotating tool on the workpiece. The temperature is higher at highertool rotational speed and vice-a-versa. The temperature considerably increases across the weld samples as the rotating tool speed increases. This is due to greater frictional effects of the rotating tool on the workpiece as the rotational speedincreases leading to a higher amount of heat generation and consequently raising the weld temperature as reported by Abolusoro et al. [35].



(a)



(b)



(c)
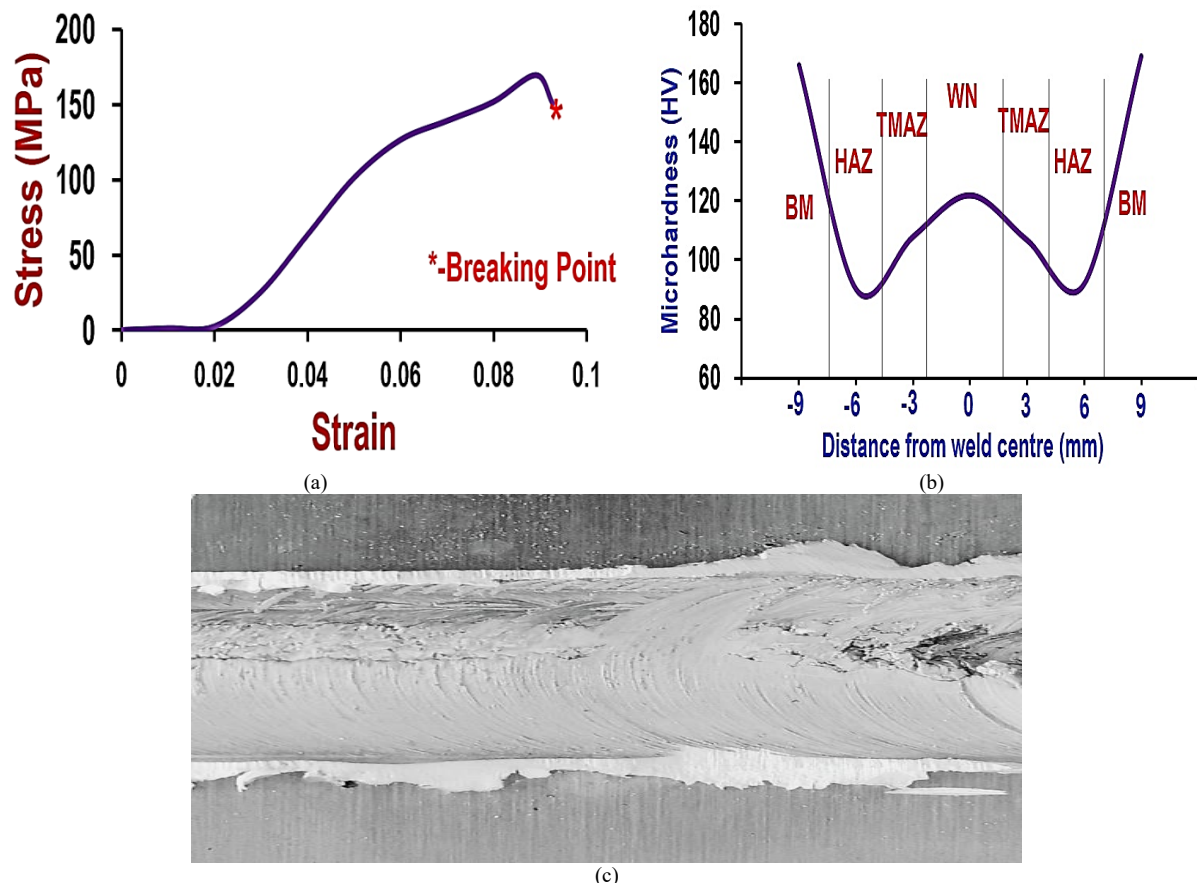
**Figure8**. a)Stress-strain curve b)Microhardness variation at different zones of weld, and c) Top surface appearance of weld

Figures 9 (a)-(c) represents the SEM images of WN, thermo-mechanically affected zone (TMAZ), and HAZ respectively for FSWed joint at tool rotation of 1400 rpm and welding speed of 40 mm/min. Figure 9 (a) depicts uniform grain distribution with ultra-fine grains having sizes in the range of 260 nm to 3 µm can be seen. A tunnel defect can be seen. The circular equiaxed grains are also observed in the WN. It can be seen that the grains in WN are fine as compared to TMAZ and HAZ. It could be attributed to higher heat generated in the WN due to more contact area of the conical threaded pin type tool. Due to higher heat generation in WN causes the dynamic recrystallization of grains resulting in finer grains.

Figure 9 (b) shows the SEM image of TMAZ. The pasty material flow,homogenous mixing of material is observed. The tunnel defect, and teared edge can be seen. The heat transferred from WN to TMAZ was adequate resulted in a homogeneous distribution of grain having a size in the range of 4-10 µm.

Figure 9 (c) depicts the SEM image of HAZ. Homogeneous distribution of grains with a uniform flow of material can be seen. However, the void, the elongated grain with the torn edge can be seen. The heat transferred from WN to HAZ is less (as compared TMAZ), hence teared edge with voids can be seen.

Beygi et al. [36] reported that contact area between tool and material plays an important role for obtaining quality weld. With the increase in the contact area between the tool and the workpiece, the axial load increases and fewer defects are formed due to the higher hydrostatic pressure. Further, the sticking condition increases the shearing contact area between the tool shoulder and material, and therefore, a greater quantity of material enters the shear plastic zone to be transferred around the tool. In the present study, the better results are using the conical threaded tool pin profile. The conical threaded tool pin profile provided more contact area that resulted in obtaining finer grain structure in WN, TMAZ, and HAZ.



(a)



(b)



(c)
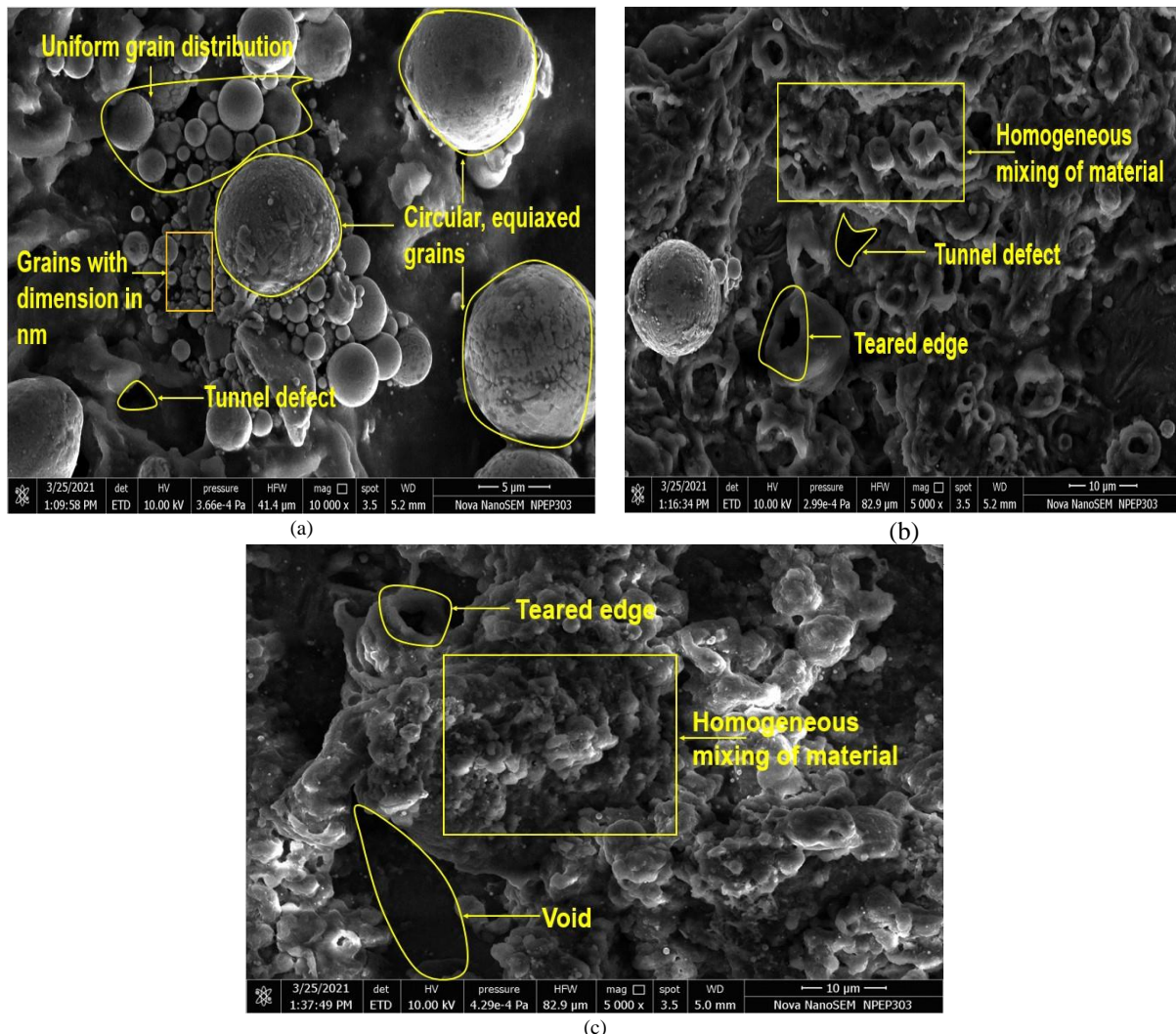
**Figure 9.** SEM images of  a) WN,  b) TMAZ,  c) HAZ

Figures 10 (a) and (b) shows SEM image of the material flow in WN and fracture surface of tensile specimen of FSWed AA7075 joints. The weld quality can be determined considering the flow of pasty material beneath the FSW tool. From the fig. 10 (a), the laminar material flow with homogeneous mixing of material is seen. The larger contact area of conical threaded tool pin profile leads to the proper mixture material. The laminar material flow eliminates the defects and produce the joint with higher strength.

It can be seen from the fig.10 (b), that the large dimples are observed. The dimples shows the failure of specimen is ductile in nature. Moreover, the large size of dimples

shows that the specimen can sustain a large amount of the load. It is seen that the fracture of specimen occurs in the HAZ. The HAZ shows coarser grain distribution, lower microhardness as compared to WN, TMAZ.

In the confirmatory experiment the EDS analysis is performed to check the presence of tool debris. The figure 11 (a) and (b) shows the SEM image captured and its EDS analysis respectively. The EDS analysis showed absence of any debris or any tool material element in the WN. The elements, such as Al, Cu, Mg, and Zn show majority of wt. % . The elements, such as Mn, Sn, and Ti disappear from the WN. The EDS microanalysis showed that the particles in the FSW joint mainly consist of the $\eta(MgZn_2)$ phase.
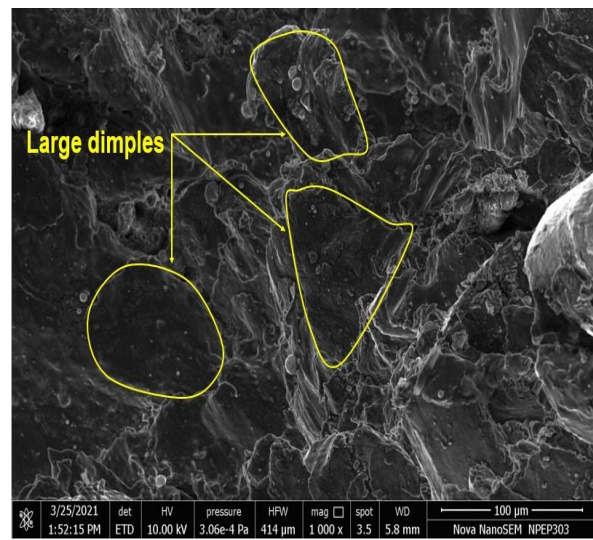


**Figure10.** SEM image of a)Material flow in WN b)Fracture surface of tensile specimen



| El | AN | Series | Unn. C (wt. %) | Norm. C (wt. %) | Atom C (wt. %) | Sigma (wt. %) |
|---|---|---|---|---|---|---|
| Al | 13 | K-series | 57.53 | 72.01 | 83.39 | 2.62 |
| Zn | 30 | L-series | 9.32 | 11.66 | 5.57 | 0.63 |
| Cu | 29 | L-series | 6.12 | 7.66 | 3.77 | 1.09 |
| Fe | 26 | K-series | 3.07 | 3.85 | 2.15 | 0.33 |
| Mg | 12 | K-series | 2.27 | 2.84 | 3.66 | 0.16 |
| Si | 14 | K-series | 0.74 | 0.93 | 1.03 | 0.08 |
| Cr | 24 | K-series | 0.41 | 0.51 | 0.31 | 0.09 |
| Pb | 82 | M-series | 0.35 | 0.44 | 0.07 | 0.06 |
| Ni | 28 | L-series | 0.08 | 0.1 | 0.05 | 0.08 |
| Mn | 25 | K-series | 0 | 0 | 0 | 0 |
| Sn | 50 | L-series | 0 | 0 | 0 | 0 |
| Ti | 22 | K-series | 0 | 0 | 0 | 0 |
| | | Total | 79.89 | 100 | 100 | |
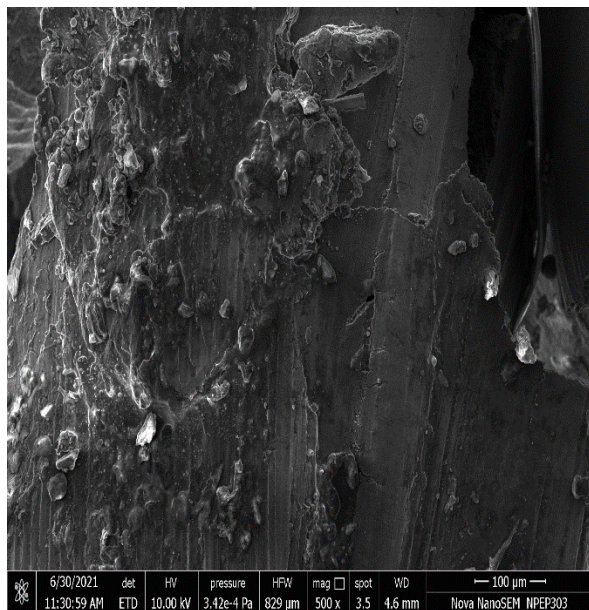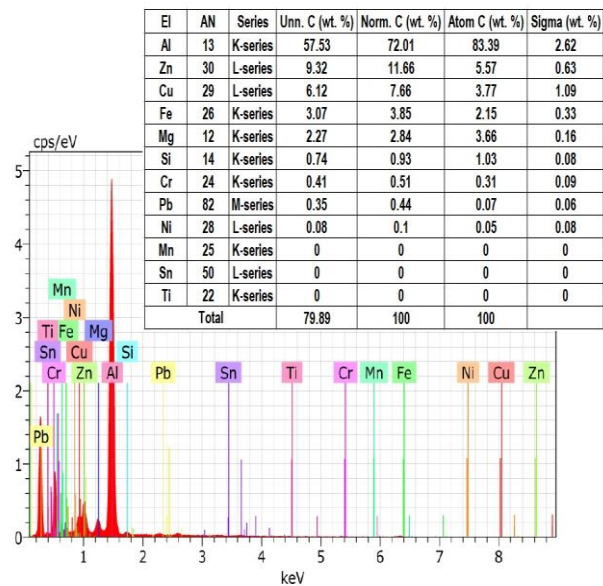
**Figure11.** a) SEM of at center of WN used for EDS b) EDS of WN

## 5. Conclusions

In the present study, the ANFIS model is developed for the mechanical properties viz. UTS, MHWN, and SR. The confirmatory experiment is conducted at tool rotational speed of 1400 rpm and welding speed of 20 mm/min. The microstructure at different regions in weld, material flow in WN, fracture behavior, and EDS analysis of FSWed AA7075 joint is investigated for the confirmatory experiment. The following conclusions could be drawn from the present work.

- The ANFIS model is developed to predict UTS, MHWN, and SR using trimf, trapmf, gaussmf, and gbellmf.
- The trimf shows minimum testing error of 19.1091, 12.3152, and 1.0018 for UTS, MHWN, and SR respectively as compared to trapmf,gaussmf, and gbellmf.
- The trapmf shows maximum testing error of 28.1289, 12.9314, and 1.3791 for UTS, MHWN, and SR respectively as compared to trimf, gaussmf, and gbellmf.
- The $R^2$ values obtained are 0.8639, 0.8178, and 0.9520 respectively for UTS, MHWN, and SR respectively using trimf.
- The SEM images shows the ultrafine grain in WN. The variation of grain size is observed as WN<TMAZ<HAZ<base material.

The overall presentation of the paper is a relatively short and simple in order to help to understand the flow of the paper. The model is not developed using other MFs.

Further study can be carried out to improve the current results using different prediction tools such as ANN. The study can be also extended to the optimization of process parameters using the developed ANFIS model.

## References

[1] J. Zhang, P. Upadhyay, Y. Hovanski, and D. P. Field, "High-Speed Friction Stir Welding of AA7075-T6 Sheet: Microstructure, Mechanical Properties, Micro-texture, and Thermal History".Metallurgical and Materials Transactions A, Vol. 49, No. 1, 2018, 210–222.doi: 10.1007/s11661-017-4411-4.

[2] G. Elatharasan and V. S. S. Kumar, "Corrosion analysis of friction stir-welded aa 7075 aluminium alloy," strojniskivestnik - Journal of Mechanical Engineering, Vol. 60, No. 1, 2014, 29–34.doi: 10.5545/sv-jme.2012.711.

[3] D. Vijayan and V. Seshagiri Rao, "Parametric optimization of friction stir welding process of age hardenablealuminum alloys−ANFIS modeling," Journal of Central South University, Vol. 23, No. 8, 2016, 1847–1857.doi: 10.1007/s11771-016-3239-1.

[4] B. Eren, M. A. Guvenc, and S. Mistikoglu, "Artificial Intelligence Applications for Friction Stir Welding: A Review," Metals and Materials International, Vol. 27, No. 2, 2021, 193–219.doi: 10.1007/s12540-020-00854-y.

[5] K. Kamal Babu,K. Panneerselvam, P. Sathiya, A. NoorulHaq, S. Sundarrajan, P. Mastanaiah, C. V. Srinivasa Murthy, "Parameter optimization of friction stir welding of cryorolled AA2219 alloy using artificial neural network modeling with genetic algorithm," International Journal of Advanced Manufacturing Technology, Vol. 94, No. 9–12, 2018, 3117–3129.doi: 10.1007/s00170-017-0897-6.

[6] R. Teimouri and H. Baseri, "Forward and backward predictions of the friction stir welding parameters using fuzzy-artificial bee colony-imperialist competitive algorithm systems," Journal of Intelligent Manufacturing, Vol. 26, No. 2, 2015, 307–319.doi: 10.1007/s10845-013-0784-4.

[7] S. Zhao, Q. Bi, Y. Wang, and J. Shi, "Empirical modeling for the effects of welding factors on tensile properties of bobbin tool friction stir-welded 2219-T87 aluminum alloy," The International Journal of Advanced Manufacturing Technology, Vol. 90, No. 1–4, 2017, 1105–1118.doi: 10.1007/s00170-016-9450-2.

[8] A. Choudhary, M. Kumar, M. K. Gupta, D. K. Unune, and M. Mia, "Mathematical modeling and intelligent optimization of submerged arc welding process parameters using hybrid PSO-GA evolutionary algorithms," Neural Computing and Applications, Vol. 32, No. 10, 2020, 5761–5774.doi: 10.1007/s00521-019-04404-5.

[9] W. Safeen, S. Hussain, A. Wasim, M. Jahanzaib, H. Aziz, and H. Abdalla, "Predicting the tensile strength, impact toughness, and hardness of friction stir-welded AA6061-T6 using response surface methodology," The International Journal of Advanced Manufacturing Technology, Vol. 87, No. 5–8, 2016,1765–1781.doi: 10.1007/s00170-016-8565-9.

[10]M. Ahmadnia, S. Shahraki, and M. A. Kamarposhti, "Experimental studies on optimized mechanical properties while dissimilar joining AA6061 and AA5010 in a friction stir welding process," The International Journal of Advanced Manufacturing Technology, Vol. 87, No. 5–8, 2016, 2337–2352.doi: 10.1007/s00170-016-8636-y.

[11]B. Choudhury, M. Chandrasekaran, and D. Devarasiddappa, "Development of ANN modelling for estimation of weld strength and integrated optimization for GTAW of Inconel 825 sheets used in aero engine components," Journal of the Brazilian Society of Mechanical Sciences and Engineering, Vol. 42, No. 6, 2020.doi: 10.1007/s40430-020-02390-7.

[12] M. T. Hayajneh , M. Abdellahia, "Prediction performance of end-milling process by gene expression programming".Jordan Journal of Mechanical and Industrial Engineering, Vol. 13, No. 2, 2019, pp. 83–89.

[13] M. Farouk, R. Mohamed, S. Fethi, "Development of A New Technique for Modeling and Optimizing Manufacturing Errors for Cn Machine Tools". Jordan Journal of Mechanical and Industrial Engineering, Vol. 14, No. 4, 2020, pp. 381–386.

[14] M. Soori , M. Asmael, " A Review of the Recent Development in Machining Parameter Optimization". Jordan Journal of Mechanical and Industrial Engineering, Vol. 16, No. 2, 2022 pp. 205–223.

[15] F. B. Ismail, A. Al-Bazi, R. H. Al-Hadeethi, M. Victor, "A Machine Learning Approach for Fire-Fighting Detection in the Power Industry". Jordan Journal of Mechanical and Industrial Engineering, Vol. 15, No. 5, 2021, pp. 475–482.

[16] P. Ning, "An adaptive scheduling method for resources in used automobile parts recycling". Jordan Journal of Mechanical and Industrial Engineering, Vol. 14, No. 1, 2020, pp. 53–60.

[17] A.H.Q. Ayun, J. Triyono , E. Pujiyanto, "Optimization of Injection Molding Simulation of Bioabsorbable Bone Screw Using Taguchi Method and Particle Swarm Optimization".Jordan Journal of Mechanical and Industrial Engineering, Vol. 16, No. 2, 2022, pp. 319–325.

[18] R.E. Precup , S. Preitl , E. M. Petriu, C. A. B. Dragos, A. I. S. Stinean, R.C. Roman, E.L. Hedrea, "Model-based fuzzy control results for networked control systems" Reports in Mechanical Engineering, Vol. 1, No. 1, 2020, pp. 10–25, 2020.

[19] M. Vilela, G. Oluyemi, A. Petrovski, "A fuzzy inference system applied to value of information assessment for oil and

gas industry". Decision Making: Applications in Management and Engineering, Vol. 2, No. 2, 2019, pp. 1–18.

[20] D. Božanić , D. Tešić , D. Marinkovic , A. Milić, "Modeling of neuro-fuzzy system as a support in decision-making processes".Reports in Mechanical Engineering, Vol. 2, No. 1, 2021, pp. 222–234.

[21] B. Meyghani, M. Awang, C. S. Wu, "Finite element modeling of friction stir welding (FSW) on a complex curved plate". Journal of Advanced Joining Processes, Vol. 1, No. January, 2020. doi: 10.1016/j.jajp.2020.100007.

[22] M. Kavitha , V. M. Manickavasagam, T. Sathish , B. Gugulothu , A. S. Kumar, S. Karthikeyan , R. Subbiah, "Parameters Optimization of Dissimilar Friction Stir Welding for AA7079 and AA8050 through RSM". Advances in Materials Science and Engineering, Vol. 2021, 2021.

[23] A. Heidarzadeh, Ö. M. Testik, G. Güleryüz, R. V. Barenji, "Development of a fuzzy logic based model to elucidate the effect of FSW parameters on the ultimate tensile strength and elongation of pure copper joints". Journal of Manufacturing Processes, Vol. 53, No. November 2019, 2020, pp. 250–259.

[24] H. M. Jamalian, M. T. Eskandar, A. Chamanara, R. Karimzadeh, R. Yousefian, "An artificial neural network model for multi-pass tool pin varying FSW of AA5086-H34 plates reinforced with Al2O3 nanoparticles and optimization for tool design insight". CIRP Journal of Manufacturing Science and Technology, Vol. 35, No. 1, 2021, pp. 69–79.

[25] C. S. Terra, J. L. L. Silveira, "Models for FSW forces using a square pin profile tool". Journal of Manufacturing Processes, Vol. 68, No. 1, 2021, pp. 1395–1404.

[26] Y. Han, W. Zeng, Y. Zhao, Y. Qi, Y. Sun, "An ANFIS model for the prediction of flow stress of Ti600 alloy during hot deformation process". Computational Materials Science, Vol. 50, No. 7, 2011, pp. 2273–2279.

[27] A. F. Güneri, T. Ertay, A. Yücel, "An approach based on ANFIS input selection and modeling for supplier selection problem". Expert Systems with Applications, Vol. 38, No. 12, 2011, pp. 14907–14917.

[28] L. Naderloo, R. Alimardani, M. Omid, F. Sarmadia,P.Javadikia, M. Y.Torabi, F. Alimardani, "Application of ANFIS to predict crop yield based on different energy inputs". Measurement, Vol. 45, Vo. 6, 2012, pp. 1406–1413.

[29] B. B. Ekici, U. T. Aksoy, "Prediction of building energy needs in early stage of design by using ANFIS". Expert Systems with Applications, Vol. 38, No. 5, 2011, pp. 5352–5358.

[30] S. Chinchanikar and V. S. Gaikwad, "State of the art in friction stir welding and ultrasonic vibration-assisted friction stir welding of similar/dissimilar aluminum alloys," Journal of Computational and Applied Research in Mechanical Engineering, vol. 11, No. 1, 2021,67–100, 2021, doi: 10.22061/JCARME.2021.7390.1983.

[31] V. S. Gaikwad and S. Chinchanikar, "Mechanical behaviour of friction stir welded AA7075-T651 joints considering the effect of tool geometry and process parameters," Advances in Materials and Processing Technologies, 2021, doi: 10.1080/2374068X.2021.1976554.

[32] F. A. Montes-González, N. A. Rodríguez-Rosales , J. C. Ortiz-Cuellar , C. R. Muñiz-Valdez, J. Gómez-Casas, J. S. Galindo-Valdés, O. Gómez-Casas, "Experimental analysis and mathematical model of fsw parameter effects on the corrosion rate of Al 6061-T6-Cu c11000 joints". Crystals, Vol. 11, No. 3, 2021, pp. 1–19.

[33] S. Zhao, Q. Bi, Y. Wang, J. Shi, "Empirical modeling for the effects of welding factors on tensile properties of bobbin tool friction stir-welded 2219-T87 aluminum alloy". International Journal of Advanced Manufacturing Technology, Vol. 90, No. 1–4, 2017, pp. 1105–1118.

[34] K. P. Yuvaraj, P. AshokaVarthanan, L. Haribabu, R. Madhubalan, K. P. Boopathiraja, "Optimization of FSW tool parameters for joining dissimilar AA7075-T651 and AA6061 aluminium alloys using Taguchi Technique," Materials Today Proceedings, Vol. 45, 2021, pp. 919–925.

[35] O. P. Abolusoro, E. T. Akinlabi, S. V. Kailas,"Tool rotational speed impact on temperature variations, mechanical properties and microstructure of friction stir welding of dissimilar high-strength aluminium alloys". Journal of the Brazilian Society of Mechanical Sciences and Engineering, Vol. 42, 2020, pp.176.

[36] R. Beygi, M. Kazeminezhad, M. Z. Mehrizi, G. Eisaabadi, A. Loureiro, "Friction stir butt welding of Al-Cu bilayer laminated composites: analysis of force, torque, and temperature". International Journal of Manufacturing Technology, Vol.88, 2017, pp.393-400.

# Proposing Multi-item Replenishment model for an Inventory Management System of Malaysia's SMEs

Irfan ur Rahman[1*], Mohd Rizal Salleh[2], Effendi Mohamad[2], Rashid Nawaz[3], Muhamad ArfauzA Rahman[4]

[1]Master student, Faculty of Manufacturing Engineering, UniversitiTeknikal Malaysia Melaka, Malaysia
[2]Professor, Faculty of Manufacturing Engineering, UniversitiTeknikal Malaysia Melaka, Malaysia
[3]Associate Professor, Department of Industrial Engineering, University of Engineering and Technology Peshawar, Pakistan
[4]Lecturer, Queen's University, Belfast, Northern Ireland

## Abstract

The present study describes a modified Economic Order Quantity (EOQ) for multi-item replenishment model with the deterministic demand nature of an inventory management. The function is subjected to the available financial and space constraints in the organization. If the constraints are not satisfied under the given conditions, then Lagrange technique is applied to obtain the optimal order quantity of the multi-items. The purpose of this study is to empower the manufacturing sector of Malaysia's SMEs with the advantages of the inventory model that controls the overproduction and underproduction inventories to meet their customer's demand on the right time. From this study, 90.9% of the optimum quantities of products had been achieved by using the multi-item inventory replenishment model as compared to the EOQ. This model is able to control the total cost of inventory efficiently for the optimum space availability.

## 1. Introduction

Inventory Management (IM) is an important management issue for most organizations as such large, medium-sized and small organizations [1]. IM as a set of policies, includes the physical infrastructure, control form, the planning, the management data engineering as well as the organizational implanting in the inventory system [2]. In addition, IM policy is primarily concerned with two conventional decisions: (i) How much to order (produce or purchase) to replenish an item's inventory, and (ii) When to order[3]. To respond to these two questions, several inventory models have been produced. The prime assumption of classical Economic Order Quantity (EOQ) is the optimal order quantity. However, due to the vast number of unavoidable variables, this assumption may not always be true for most production ergonomics. Pakhira et al. [4], added an inventory modelling manages the amount of inventory that must be kept up to guarantee the continuous production of a product. Therefore, to accomplish the concerned of IM's policy, a model is needed to adjust the cost occurring from carrying an excessive amount of stock against the penalty expenses occurring due to stock deficiency. There is a variety of decisions in product recovery activities[5]. Many inventory models are based on EOQ or Economic

Production Quantity (EPQ), due to its simplicity and robustness[6]. The EOQ model is used to determine an optimal order size by balancing the setup cost and inventory holding cost [7]. While, EPQ model is used to determine the optimal replenishment of lot size to be produced[8]. For several years, the subject of classical EOQ has been discussed in a variety of ways, and several studies have attempted to resolve it. It progresses from a single-item model with demand tied to unit price to multi-item models with a variety of constraints. These two models are fully analytical, requiring a substantial amount of arithmetic to arrive at the best solution[6]. In the case of price competitive environment, planning in sales and marketing are not sufficient to sustain the profit margin. Therefore, it needs to minimize the production cost [9].

In many nations, the retailing industries comprises of a critical number of businesses, particularly in the Small Medium Enterprises (SMEs) sector. For instance, 50% of the SMEs practically come from wholesale and retail enterprises in Malaysia. Out of this part, 80% of the establishments fall into the classification of smallscale enterprises [10]. Table 1 shows the distribution of SMEs in Malaysia by sectors, which represents 89.2% (service), 5.3% (manufacturing), 4.3% (construction) and 1.1%

* Corresponding author e-mail: rizal@utem.edu.my.

(agriculture). The remaining 0.1% is in mining and quarrying sector [11]. Ahmad and Zabri [10]had shown that most of the bigger firms are applying the concepts and strategies of inventory control which have fewer financial restrictions for the adoption of advanced management approach. However, in present, the IM practices implemented by the firms have been designed following to their requirements [12]. Moreover, Ngubane at el. [13], expressed that the absence of IM practices has denied the manufacturing sector of SMEs to become the incredible rivals within the manufacturing organizations. In Malaysia, for instance, the most widely recognized issue facing by SMEs is poor IM strategies that would influence the performance of manufacturing firm [14].

The objective of this study is to introduce a modified EOQ of multi-item replenishment model using the deterministic demandsfor an inventory management system. The proposed model is subjected to determine the optimal quantity of multi-items within the limits of allowable financial and space constraints within the manufacturing sector of Malaysia's SMEs to reduce the total cost of inventory and control the over production as well as underproduction.

**Table 1**: Distribution of SMEs in Malaysia by sector [11]

| Sector | Percentage | Number of SMEs |
|---|---|---|
| Service | 89.2% | 809,126 |
| Manufacturing | 5.3% | 47,698 |
| Construction | 4.3% | 39,158 |
| Agriculture | 1.1% | 10,218 |
| Mining and Quarrying | 0.1% | 865 |

The modified EOQ model will be used to prevent shortages and the required numerical in the model equations are solved manually.

## 2. Literature review

In the last few decades, a number of mathematical models for inventory problems have been created, the first and most basic of which is the EOQ, which was established by Wilson[15]. And today, the establishment of increasingly advanced and complex inventory models has been based on this EOQ model. In terms of demand distributions, certain factors that have been integrated in models including multi-item, quantity discount, deterioration rate, deterministic or probabilistic models[16]. Over the time, the literature on production and inventory models had been modified. Several scholars have contributed to the discussion by modifying inventory model assumptions and incorporating multiple dimensions of inventory management, making it more useful[17]. A mathematical model for controlling a production system for a single item with an unknown deterioration rate has been proposed [18]. A two-level inventory model was established to optimize the cost of inventory management, and a distributed multi-level inventory control strategy for automobile maintenance spare parts[19]. Zhang and Wang [20]have developed a multi-item inventory problem with storage capacity restriction, while a joint inventory model to determine the optimal inventory replenishment product

assortment, shelf space and display area. Kasrhuri et al., [21]developed a fuzzy multi-item inventory model by incorporating storage space and production cost. Furthermore, Zhang and Du [22] conducted the study of multi-product newsboy problem for uncertain demand. Also, Ould-Louly and Dolgui[23]introduced a dynamic single stage multi-item inventory control model with the goal of determining the average holding cost and stockout probability for the components under a certain service level for customer demands and lead time uncertainties. Ertogral, [24] solved a multi-item single source ordering problem using the Lagrange technique, which included transportation costs. Multi item inventory control issues may have the multiple conflicting objectives in addition to a single goal. While, Roy and Maiti[25] proposed a multi-objective inventory model of decaying items with stock-dependent demand with limited storage facility and a total cost budget. Taleizadeh et al., [26]proposed a Pareto and genetic algorithm hybrid method to optimize multi-product, multi-constraint inventory control systems, taking into account both continuous and periodic reviews, as well as fuzzy replenishments and demand. Again, storage capacity and material size limit the number of distinct materials that can be stored in the plant. Pasandideh et al. [27] used a non-dominated sorting genetic algorithm and multi-objective particle swarm optimization to solve a bi-objective economic manufacturing quantity problem for defective items. The problem was stated as a multi-objective nonlinear programming model, with the aim of minimizing both the overall inventory cost and the required warehouse space by determining the order quantities of the product. Balkhi et al., [28] developed a number of inventory models in which demand, output, and deterioration rates are all arbitrary functions of time, and in some of which shortages are permitted but entirely backlogged. Ben-Daya and Raouf[29] proposed a more realistic and general single period solution for multi-item with the restricted budgetary and floor/shelf space constraints, in which, the item demand follows the uniform probability distribution which is subject to space and budget limits.

## 3. Methodology

The methodology adopted in this paper is a quantitative research design. To utilize this model for optimal order quantities of multiple items that need to be replenished, the flow chart of the procedure is shown in Figure 1.

The model requires the necessary data, while solving different equations; in essence the available investment and the space capacity of the organization, demand rate, ordering cost, holding cost, purchase price per unit and the size of individual item.

The optimal order quantities of multiple items have been calculated by EOQ. After calculating the quantities, it is required to solve both the financial and space constraints. Once the constraints have been determined, then its validity check is required. If the left-hand side value of the equations is less than the right-hand side, so constraints are feasible, no further work is needed. However, if the constraints are not feasible, the Lagrange technique should be utilized. These constraints will affect the size of orders quantities for each type of item.

### 3.1. Economic Order Quantity

According to [30], a stock managing method to minimize the overall holding cost and ordering cost is known as Economic Order Quantity (EOQ). EOQ model is concerning the tradeoff between the holding cost and ordering cost by choosing the right quantity for replenishing the inventory of different type of materials. The ordering frequency will be diminished by a colossal order quantity; subsequently there will be decreased in the cost per unit time. Anyway, it prompts the expanding of warehouse holding cost.

In general, the following assumptions are made for the EOQ model.
1. Demand is known and constant.
2. The replenishment is instantaneous and complete.
3. The lead time is known and consistent.
4. Shortage is not allowed.

### 3.2. Equation of EOQ

When perusing the existing study in inventory modeling, one of the noteworthy troubles is the standard arrangement of factors and notations [31].

Figure 3(a) represents the ordering cost of inventory. When the order quantity increases, the cost associated with it will decrease and vice versa. While Figure 3(b) shows the holding cost of inventory. When the order quantity increases, the holding cost will increase due to high number of inventories that are kept in the warehouse. And finally, Figure 3(c) represents the optimal order quantity occurring at the point where the ordering cost and the holding cost curve intersect. Thus, in EOQ model, the optimal order quantity will occur at a point when the total of ordering cost and holding cost are similar. Thus, the optimal order quantity will be the quantity that minimizes the total costs of inventory. Furthermore, a decrease in either ordering cost or holding cost will reduce the total cost curve as of Figure 3(c) [30]. Therefore, the equation $Qt$ of optimal order quantity is derived from Figure 3(c) [30].

$$Qt = \sqrt{\frac{2AD}{h}} \qquad (1)$$

Where:
$D$ = the demand rate per units per year,
$A$ = ordering cost/ per order,
$h$ is inventory holding cost/ per unit andtime = $i \times c$,
$C$ = unit cost of each item,
$i$ = the inventory holding cost percentage.

### 3.3. Description of the Multi-item Inventory Model

The study is concentrated on the deterministic single item inventory model. EOQ equation with the above assumption where the demand and lead-time are constant, replenishment is instantaneous and complete, and shortages are not allowed.

This study will extend the fundamental concept into a multi-item inventory replenishment model for SMEs in Malaysia with the similar supposition but focusing on the existence of financial and space constraints. These constraints will certainly, affect the size of the order quantities for each type of item.



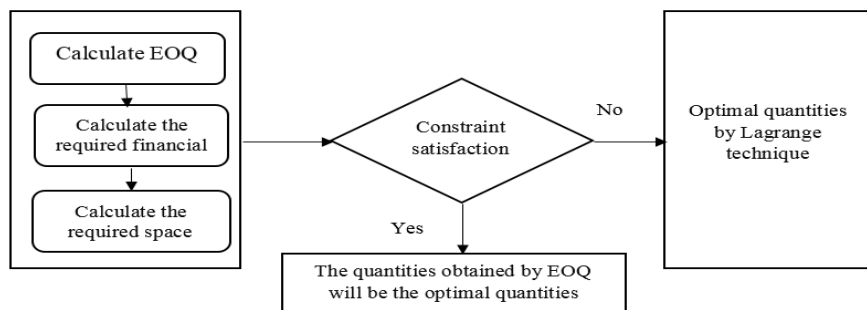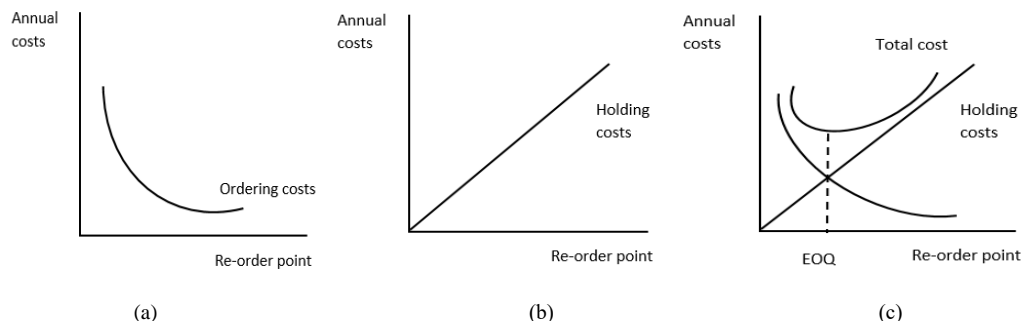**Figure 1**: Flow diagram of multi-item inventory model



**Figure 3**: (a) Ordering cost; (b) Holding cost and (c); Optimal order quantity [30].

The total cost of a multi-item inventory system is determined as the sum of the total cost of every item independently. We assume the shortage of a $n$ item of inventory model is not allowed. Now, the equations for financial and space constraints can be shown as follow [30]:

$$\sum_{n=1}^{m} C_n Q_n \leq F \tag{2}$$

$$\sum_{n=1}^{m} S_n Q_n \leq T.S \tag{3}$$

where:

$Q$ is the number of units per order,

$S_n$ is the required space for every item, $n = 1, 2, 3 \dots m$,

$C_n$ is the capital for every item, $n = 1, 2, 3 \dots m$,

$F$ is maximum allowed financial for inventory,

$T.S$ is maximum storage allowed for each item.

*3.4. Lagrange Technique*

In this study, the nonlinear programming problem has been dealt with by using Lagrange procedure. The Lagrange procedure assumes implicitly that the orders are received simultaneously and does not consider phasing order for the various items.

This technique is initially used to solve the inventory problems by ignoring the financial and space constraints in Equations (2) and (3) respectively. The optimal ordered quantities are obtained by assuming that $Qt = Qt_n$ by Equation (1) [31].

$$Qt_n = \sqrt{\frac{2A_n D_n}{h_n}} \tag{4}$$

This is accomplished by developing a Lagrange expression (LE), which is given by:

$$LE(Q_n, \pi) = \left\{ \left( \sum_{n=1}^{m} \frac{A_n D_n}{Q_n} \right) + \pi \left( \sum_{n=1}^{m} C_n Q_n \right) - F \right\} \tag{5}$$

Where $\pi$ is the Lagrange multiplier. Equation (6) obtained by taking derivative of Equation (5) with respect to $Q_n$. $QLt_n$ represents the optimal quantity obtained by using the Lagrange technique.

$$QLt_n = \left\{ \sum \sqrt{\frac{2A_n D_n}{C_n (i + \pi)}} \right\} \tag{6}$$

Equation (7) obtained by taking derivative of Equation (5) with respect to $\pi$.

$$\pi = \left\{ \frac{1}{2} \left( \frac{1}{F} \sum \sqrt{2A_n D_n C_n} \right)^2 - \frac{i}{2} \right\} \tag{7}$$

Substituting Equation (7) into Equation (6) and rearranging gives;

$$QLt_n = \left( \frac{F}{\sum_{n=1}^{m} C_n Q_n} \right) Qt_n = \left( \frac{F}{E} \right) Qt_n \tag{8}$$

Equation (8) represents the optimal quantity by Lagrange technique and $F$ represents the maximum available financial. Similarly, $E$ represents left hand sides of Equations (2) and (3). Such as; $\sum_{n=1}^{m} C_n Q_n \leq F$ and $\sum_{n=1}^{m} S_n Q_n \leq T.S$.

By repeating the same steps, equation of optimal quantity by Lagrange technique for space constraint and other constraints if available can be obtained. Equation (9) represents the optimal order quantity by Lagrange technique regarding space constraint below;

$$QLt_n = \left( \frac{T.S}{\sum_{n=1}^{m} S_n Q_n} \right) Qt_n = \left( \frac{T.S}{E} \right) Qt_n \tag{9}$$

**4. Result and Discussion**

This study has been carried out in one of the SME in Melaka, Malaysia. The organization is producing several numbers of items. The problem faced by the company is the uncontrollable of over production. It incurred the increment in total cost of inventory. The company also has enough amounts of inventory and space for these items.

The available financial and space measurements have been provided by the company in Table 2.

And on the other hand, because of the economic crises, a company cannot invest all of its capital in one place. So, basically the selected company is in search of an optimal solution to control the inventories within the constraints of available financial and the capacity of space in the warehouse for inventories. The data collection was done by interview technique in the selected company. The interviews were conducted to study the manufacturing operations for the accurate information on the current situation of IM with the supply chain officers. Table 2 represents the collected data of the proposed optimal policy for multi-item inventory replenishment. Based on the company recommendations, the most critical five items have been selected to manage its quantities required per year with the available financial and space on hand.

**Table 2.** Data collected from the interview made at SME

| | | Items | | | | |
|---|---|---|---|---|---|---|
| | | A | B | C | D | E |
| Cost (purchase price/ unit) | $C$ | 12 | 12 | 13 | 15 | 13 |
| Inventory caring cost rate | $i$ | 0.18 | 0.18 | 0.18 | 0.18 | 0.18 |
| Demand rate (unit per year) | $D$ | 261,402 | 65,349 | 914,910 | 676,040 | 518,300 |
| Set up cost | $A$ | 80,000 | 71,000 | 83,000 | 85,000 | 77,000 |
| caring cost per unit per year | $h$ | 2.16 | 2.16 | 2.34 | 2.7 | 2.34 |
| Item size | $S_n$ | 1.33 | 1.33 | 1.33 | 1.33 | 1.33 |
| Available financial (Malaysian ringgit RM) | 32,693,342 | | | | | |
| Available space (cubic meter m³) | 102,500 | | | | | |

Table 3 shows the optimal quantities of five different items which is obtained by the values of $A_n$, $D_n$ and $h_n$ for all five items from Table 2 and putting these values in Equation (4).

**Table 3**: Optimal quantities by EOQ

| Optimal order quantities ($Qt_n$) | |
|---|---|
| $Qt_1$ | 139,151 |
| $Qt_2$ | 65,545 |
| $Qt_3$ | 254,762 |
| $Qt_4$ | 206,314 |
| $Qt_5$ | 184,690 |

### 4.1. Financial Constraint

Financial constraint represents the possible combinations of items and services that a buyer can purchase with the available financial on hand. The overall inventory cost of multi-item has been estimated as the sum of total cost of each item independently. The overall cost of the inventory system for all items is obtained by Equation (2). The feasibility of financial constraint will be checked by putting the values of $C_n$ for all items from Table 2 and the values of $Qt$ for all items from Table 3 in Equation (2).

12 × 139,151 + 12 × 65,545
　　　　+12 × 254,762 + 12 × 206,314
+12 × 184,690 ≤ 32,693,342
10,205,544 ≤ 32,693,342

The total cost of items obtained is RM11,269,941, which is less than the available financial that is RM 32,693,342 in Table 2. So, constraint is not violated and it is feasible. This implies that the quantities of five items obtained in Table 3 are optimum for the available financial to be purchased.

### 4.2. Space Constraint

Space constraint refers to the available space for stock in the organization. The feasibility of space constraint will be checked by putting the values of $S_n$ for all items fromTable 2 and the values of $Qt$ for all items from Table 3 in Equation (3).

1.33 × 139,151 + 1.33 × 65,545
+1.33 × 254,762 + 1.33 ×
206,314 + 1.33 × 184,690 ≤ 102,500
1,131,115 ≤ 102,500

In this manner, the space required for the items to be ordered is 1,131,115 m³. The space is greater than the

available space at the SMEs' warehouse, which is only 102,500 m³ available. Therefore, constraint is not feasible. This implies that the quantities obtained in Table 3 are not the required quantities. The optimal quantities, for which both the constraints will be satisfied, are obtained by Lagrange techniques in Table 4. Table 4 are obtained by putting the optimal quantity $Qt$ for each item from table 3, the value of available space $T.S$ and the value of $E$ in equation (9).

**Table 4**: Optimal quantities by Lagrange technique

| Optimal Order quantities $QLt_n$ | |
|---|---|
| $QLt_1$ | 12,610 |
| $QLt_2$ | 5,940 |
| $QLt_3$ | 23,086 |
| $QLt_4$ | 18,636 |
| $QLt_5$ | 16,736 |

To check whether space constraint is satisfied, the quantities of obtained in Table 4 and the values of $S_n$ for all items from Table 2 put in Equation (3).

1.33 × 12,610 + 1.33 × 5,940
+133 × 23,086 + 1.33 × 18,636
+1.33 × 16,736 ≤ 102,500
102,420.64 ≤ 102,500

The feasibility of space constraint can be seen, because the left-hand side value is less than the right-hand side of equation 3 above. Comparing the values of both Table 3 and 4, there is a substantial difference among the values of optimal quantities determined by EOQ and Lagrange technique. The optimal quantities determined by Lagrange technique in Table 4 are minimum from that of determined by EOQ in Table 3.

It is derived from the results that the optimal order quantities in Table 4 have a positive impact on the financial performance of SMEs in the manufacturing sector. SMEs will control and manage high operating cost by holding excess stocks as well as stock out situation. Larger storage costs, handling charges, and interest from short-term borrowings are the result of more stock in the company than it is required. Stock-outs typically occur when there is a high demand for a product and there is a scarcity of inventory for fast-moving commodities, resulting in lost sales and customer loyalty. Sometimes loss is also incurred, when the products are sold at a lower price than normal[32].The findings show that the Lagrange Technique is used to find the optimal value of an objective function when space and financial limitations are present. In the case of SMEs in Malaysia, collected data is used to

demonstrate the validity of the suggested model. The implications of the multi-item replenishment model are evident from the results, and provide a useful framework for reducing the inventory overall cost and deliver the ability to the organization to take right decision in controlling underproduction and overproduction[33].

## Conclusion

This study has introduced a multi-item inventory replenishment model with the deterministic demand nature to be applied at SMEs in Malaysia. The numeric advantages of utilizing the equations are significant and important, initially, when the quantities cannot surpass the absolute finance and the overall allowed space, the new equation of the EOQ for optimum exploitation of the financial and storage should be removed. The findings show that the optimal quantities of different items were obtained by multi-item inventory replenishment model, within the allowed financial limit and capacity of storage in Table 4, are the optimized one as compared to the quantities obtained by EOQ in Table 3. This model has reduced the value of inventory up to 90.9 %. The result shows that in order to overcome overproduction or to eliminate underproduction, the selected SME needs to order/produce the quantities obtained in Table 4 for five items. The advantages of the proposed model are as follows:(i) Consideration of financial and space constraints make the model realistic as ignorance of these restriction results in infeasible solution, (ii) Providing trade credit strengthens to the supply chain coordination.

There are numerous ways to make the current model more realistic by extending it. And for the future work, it is suggested to find the new EOQ model by introducing constraints other than space and financial for instance, size of order. Additionally, the present study is carried without software, it is suggested for future work to formulate the same model with the application of inventory control software, for instance, application manager, Matrix Laboratory (MATLAB) etc. Furthermore, it is also suggested to utilize the same model with probabilistic demand with shortages and enhance the present work with the determination of total inventory cost.

## Acknowledgments

## References

[1] Haseeb, M.; Lis, M.; Haouas, I.; Mihardjo, L.W.W. The mediating role of business strategies between management control systems package and firms stability: evidence from SMEs in Malaysia, Sustainability, 2019, 11(17): 1-20.

[2] Biswas, S.K.; Karmaker, C.L.; Islam, A.; Hossain, N.; Ahmed, S. Analysis of different inventory control techniques: a case study in a retail shop, Journal of Supply Chain Management System, 2017 (6)3: 35–45.

[3] Aro-Gordon, S.; Guptha, J. Review of modern inventory management techniques, Global Journal of Business and Management, 2016, 1(2): 0–22.

[4] Pakhira, R.; Ghosh, U.; Sarkar, S. Study of memory effect in an inventory model with quadratic type demand rate and salvage value,Applied Mathematical Sciences, 2019, 13(5): 209–223.

[5] García, D.; Palencia, D.; Solano, C.; Mendoza, A. Design of a vendor managed inventory model for impulse purchase products in a two-level supply chain, Jordan Journal of Mechanical and Industrial Engineering, 2020, 14(2): 257-270.

[6] Jonrinaldi, T.R.; Henmaidi, E.W.; Zhang, D.Z. A multiple items epq/eoq model for a vendor and multiple buyers system with considering continuous and discrete demand simultaneously, IOP Conference Series Material Sciemce and Engineering, 2018, 319(1): 0–7.

[7] Di Nardo, M.; Clericuzio, M.; Murino, T.; Sepe, C. An economic order quantity stochastic dynamic optimization model in a logistic 4.0 environment, Sustainibility, 2020, 12(10): 1–25.

[8] Pacheco-Velázquez, E.A.; Cárdenas-Barrón, L.E. An economic production quantity inventory model with backorders considering the raw material costs, Scientia Iranica, 2016, 23(2): 736–746.

[9] Ebrahim, Z.; Anawar, S.; Cheah, A.C.E. Fit manufacturing: mapping product cost requirements using relational database design, Journal of Advance Manufacturing Technology, 2015, 9(1): 65–77.

[10] Ahmad, K.; Zabri, S.M. Inventory management practices among Malaysian micro retailing enterprises, Journal of Business and Retail Management Research, 2016, 11(1): 103–115.

[11] Razak, D,A.; Abdullah, M.A.; Ersoy, A. Small medium enterprises (SMES) in Turkey and Malaysia a comparative discussion on issues and challenges, International Journal of Business Economics and Law, 2018, 15(3): 1–12.

[12] Panigrahi, R.R.; Das, J.R.; Jena, D.; Tanty, G. Advance inventory management practices and its impact on production performance of manufacturing industry, International Journal of Recent Technology and Engineering, 2019, 8(4): 3875–3880.

[13] Ngubane, N.; Mayekiso, S.; Sikota, S.; Fitshane, S.; Matsoso, M.; Bruwer, J.P. Inventory management systems used by manufacturing small medium and micro enterprises in Cape Town, Mediterranean Journal of Social Science, 2015, 6(1): 382–390.

[14] Nur, S.; Mohamed, A.; Hairul, M.S.R. The performance of challenges faced by SME in managing real-time information in the inventory management process, International Journal of Innovative Technology and Exploring Engineering, 2019, 8(12): 5614–5618.

[15] Tersine, R.J. Principles of inventory and material management. 4th ed. New Jersey: Prentice Hall; 1994.

[16] Lesmono, D.; Limansyah, T. A multi item probabilistic inventory model, Journal of Physics: Conference Series, 2017, 893(1): 1-7.

[17] Ahmed, W.; Moazzam, M.; Sarkar, B.; Ur Rehman, S. Synergic effect of reworking for imperfect quality items with the integration of multi-period delay-in-payment and partial backordering in global supply chains. Engineering, 2021, 7(2): 260-271.

[18] Bukhari, F. Adaptive control of a production-inventory model with uncertain deterioration rate, Applied Mathematics, 2011, 2: 1170-74.

[19] Li, J. Distributed multi-level inventory algorithms for automotive maintenance spare parts based on centralized control model, Jordan Journal of Mechanical and Industrial Engineering, 2020, 14(1): 89-99.

[20] Zhang, B.; Wang, X. Optimal policy andsimple algorithm for a deteriorated multi-item EOQ problem, American Journal of Operational Research, 2011, 1: 46-50.

[21] Kasthuri, R.; Vasanthi, P.; Ranganayaki, S.; Seshaiah, C.V. Multi-item Fuzzy inventory model involving three constrains: A Karush-Kuhn-Tucker conditions approach, American Journal of Operational Research, 2011, 1: 155-159.

[22] Zhang, B.; Du, S. Multi-product newsboy problem with limited capacity and outsourcing, European Journal of Operational Research, 2010, 202: 107-113.

[23] Ould-Louly, M.A.; Dolgui, A. A dynamic single-stage multi-item inventory control model. Large Scale Systems: Theory and Applications, 2001, 34(8): 73–78.

[24] Ertogral, K. Multi-item single source ordering problem with transportation cost: A Lagrangian decomposition approach, European Journal of Operational Research, 2008, 191: 156–165.

[25] Roy, T. K.; Maiti, M.; Multi-objective inventory models of deteriorating items with some constraints in a fuzzy environment. Computers & OperationsResearch, 1998, 25 (12): 1085–1095.

[26] Taleizadeh, A.A.; Niaki, S.T.A.; Aryanezhad, M.B. A hybrid method of Pareto, TOPSIS and genetic algorithm to optimize multi-product multi-constraint inventory control systems with random fuzzy replenishments. Mathematical and Computer Modelling, 2009, 49(5–6): 1044–1057.

[27] Pasandideh, S.H.R.; Niaki, S.T.A.; Sharafzadeh, S. Optimizing a bi-objective multi-product EPQ model with defective items, rework and limited orders: NSGA-II and MOPSO algorithms. Journal of Manufacturing Systems, 2013, 32(4): 764–770.

[28] Balkhi, Z. The effects of learning on the optimal production lot size for deteriorating and partially backordered items with time varying demand and deterioration rates. Journal of Applied Mathematical Modeling, 2003, 27: 763-779.

[29] Ben-Daya, M.; Raouf A. On the constrained multi-item single period inventory problem. International Journal of Production Management, 1993, 13: 104-112.

[30] Kumar, R. Economic Order Quantity (Eoq) Model. Journal of Finance and Economic Management, 2016, 5(1): 176–176.

[31] Ghafour, K.M. The role of items quantity constraint to control the optimal economic order quantity. Modern Applied Science, 2017, 11(9): 61.

[32] Pillai, R.N. Inventory management performance in machine tool SMEs: What factors do influence them? Journal of Industrial Engineering and Management, 2010, 3(3): 542-560.

[33] Samak-kulkarni, M.S.M.; Rajhans, N.R. Determination of optimum inventory model for minimizing total inventory cost. Procedia Engineering, 2013, 51: 803–809.

# Simultaneous Scheduling of Machines, Tool Transporter and Tools in a Multi Machine Flexible Manufacturing System Without Tool Delay Using Crow Search Algorithm

Padma Lalitha Mareddy [a],   Sivarami Reddy Narapureddy [b*] ,Venkata Ramamurthy Dwivedula [c],  S.V.  Prayagi [d]

*[a] Professor,Electrical Engg. Dept.,Annamacharya Institute of Technology and Sciences, Rajampet, AP, India. 516125*
*[b] Professor,Mechanical Engg.  Dept., Annamacharya Institute of Technology and Sciences, Rajampet, AP, India. 516125*
*[c] Principal ,Satya Institute of Technology and Management, Vizianagarm, AP, India. 535002*
*[d] Professor,Mechanical Engg.  Dept., Yeshwantrao Chavan College of Engineering YCCE Nagpur, Maharashtra, India.  441110*

## Abstract

This paper deals with machines, tool transporter (TT) and tools simultaneous scheduling in multi machine flexible manufacturing system (FMS) with the lowest possible number of copies of every tool type without tool delay taking into account tool transfer times to minimize makespan (MSN). The tools are stored in a central tool magazine (CTM) that shares with and serves for several machines. The problem is to determine the lowest possible number of copies of every tool variety, allocation of copies of tools to job-operations, job-operations' sequencing on machines and corresponding trip operations of TT, including the dead heading trip and loaded trip times of TT without tool delay for MSN minimization. This paper proposes nonlinear mixed integer programming (MIP) formulation to model this simultaneous scheduling problem and crow search algorithm (CSA) built on the crows' intelligent behavior to solve this problem. The results have been tabulated, analyzed and compared.

## 1. Introduction

Manufacturing companies are expected to handle growing product complexities, shorter market time, new technologies, global competition threats, and quickly changing situation. FMS is setup to deal with manufacturing competition. FMS is an integrated production system consisting of multipurpose machine tools which are computer numerical controlled (CNC), linked to an automated material handling system (MHS) [1]. FMS aims to be flexible in manufacture without undermining the product quality. The flexibility of the FMS relies on the flexibilities of CNC machines, automated MHS, and control software. FMSs have been categorized into distinct kinds as per their workflow patterns, size, or manufacturing type. Four kinds of FMS are described from the planning and control point of perspective: single flexible machines (SFM), flexible manufacturing cells (FMC), multi-machine FMS (MMFMS), and multi-cell FMS (MCFMS) [2]. Advantages, such as reductions in cost, enhanced utilizations, decreased work-in-process, etc have already been proved by existing FMS implementations [3]. Use of resources is improved by scheduling tasks so as to reduce the MSN [4]. One way to achieve high productivity in

FMS is to solve scheduling problems optimally or near optimally.

Tool loading is a complicating issue in scheduling problems since the number of tool copies are limited and may be smaller than the number of machines due to economic restrictions. Job and tool scheduling is an important problem for production systems. Inefficient planning of job scheduling and tool loading may lead to under utilization of capital intensive machines, and high level of machine idle time [5]. Therefore, efficient scheduling of jobs and the tools enables a manufacturing system to increase machines' utilization and decrease their idle times. There are a number of studies on the machines and tools scheduling. Tang and Denardo [6] solved the problem of determining job sequence and tools which are placed before every job is processed on machine for minimization of tool switches. Chandra et al [7] proposed a practical approach for deciding the sequence of jobs and tools for minimization of the total set up and processing times to make sure that jobs are completed before their delivery dates.  Song et al [8] mentioned heuristic algorithm for allocating tools and parts for minimization of tool switches between machines where every part needs to visit only one machine for its complete processing. Roh and Kim [9] examined allotment of part and tool, and scheduling issues for entire tardiness minimization under

* Corresponding author e-mail: siva.narapureddy@gmail.com.

its tool movement plan where every part needs to visit only one machine for its complete processing in FMS. Agnetis et al [1] addressed combined part and tool scheduling in FMC by placing tools in a CTM which are shared by machines using TT to minimize MSN and maximum delay.  When two machines are in need of the same tool, the Tabu search algorithm is applied to address the disagreement. Tsukada and Shin [10] recommended distributed artificial intelligence approach for problems of tool scheduling and borrowing along with an approach to share the tool in FMS to deal the unexpected jobs' introduction in the dynamic situation.  It is demonstrated that sharing of tool among distinct FMS cells helps to reduce tooling costs and improves the tools usage. Jun, Kim and Suh [11]  recommended Greedy Search Algorithm for scheduling and supplying of tools, and determining the amount of additional tools required when FMS setup changes due to  change in the product mix for MSN minimization in FMS. Keung, Ip and Lee [12] investigated machine allocation and job shop scheduling on the parallel machining workstation in tandem with different machines where tools are shared for minimization of tool switching cases and tool switches by means of GA approach. Ecker and Gupta [13] proposed an algorithm to task precedence relationships with the intend of sequencing tasks in order to minimize the overall time required for the tool changes on the SFM equipped with tool magazine, where every job requires one of the tools. Prabhaharan et al [14]  addressed joint scheduling of operation and tool for MSN minimization by using preference dispatching rule and simulated annealing algorithms in the FMC with "m" indistinguishable work cells and the CTM. Karzan and Azizoğlu [15] addressed job sequencing and tool transporter movements problem on SFM with a limited tool magazine capacity.  Branch-Bound algorithm and beam search technique are employed to obtain optimal or near optimal solutions for minimizing tool transporter movements between machine and tool crib area. Suresh Kumar and Sridharan [16]  discussed simulation study conducted to analyze the impact of scheduling rules controlling part launch and tool request selection decisions of FMS. FMS was operating under tool movement along with part movement policy. Simulation study is employed to identify the best possible scheduling rule combinations for part launch and tool request selection to minimize mean flow time, tardiness and conditional mean tardiness. Ant Colony Optimization Algorithm was suggested by Udhay kumar and Kumanan [17]  to produce optimal job and tool sequences to minimize makepan for FMS, and extended GT algorithms were used for active schedule creation. Udhaya Kumar and Kumanan [18]  suggested un-traditional optimization algorithms like SA, ACO, PSO, and GA to produce the optimum jobs and tools sequence for tardiness minimization in FMS, and modified GT algorithms were used to generate efficient schedules.  Aldrin Raj, et al [19] suggested 4 heuristics, including preference shipment rules, revised non-delay schedule generation algorithms with 6 dissimilar rules, revised GTA and Artificial Immune System algorithms for resolving machine and tools combined scheduling in FMS which consists of 4 machines and one CTM to minimize MSN. Özpeynirci [20] introduced a time-indexed mathematical model for machines and tools scheduling in FMS to minimize MSN. Costa, et al [21]  have developed a hybrid GA that implements a local search enhancement scheme to resolve ' p ' parts on ' q ' machines scheduling undertaking tool

change activity triggered by tool wear. Sivarami Reddy et al [22]  presented symbiotic organisms search algorithm (SOSA) to deal with machines and tools joint scheduling to produce best optimal sequences with a copy of every type of tools in a MMFMS that minimize MSN, and it is shown that SOSA outperforms the existing algorithms. Beezao et al [23] modeled and addressed the identical parallel machines problem with tooling constraints for minimizing MSN using an adaptive large neighborhood search metaheuristic(ALNS).  It is demonstrated that ALNS outperformed other existing algorithms. Baykasoğlu and Ozsoydan [24] addressed automatic tool changer (ATC) indexing problem and tool changing problem concurrently in order to reduce non machining times in automatic machining centers using simulated annealing algorithm.  Paiva and Carvalho [25] addressed job ordering and tool changing problem (SSP) to find out the jobs order and the tool loading order so as to minimize the tool changes. A methodology which employs graph representation, heuristic methods and local search methods is used for solving sequencing problem. Such techniques are integrated along with classical tooling approach to solve SSP in an algorithmic local search scheme.  Gökgür et al [26] addressed constraint programming models in environments of parallel machines to solve tools scheduling and allotment problems with prearranged tools quantity in system due to financial limitations to minimize MSN. Job transport times and tool switch times among machines are not taken into account in the references reviewed above.

Sivarami Reddy et al [27] and Sivarami Reddy et al [28] solved machines and tools simultaneous scheduling problems without considering job transfer times and considering tool switch times among machines with a copy of every tool type *(**SMTTATWACT***)* for minimum MSN as an objective and shown that tool transfer times have significant effect on MSN.

Sivarami Reddy et al [29], Sivarami Reddy et al [30],and Sivarami Reddy et al. [31] addressed machines, AGVs and tools simultaneous scheduling with one copy of every tool type considering job transport times among machines, with and without considering tool transfer times among machines respectively to find out optimal sequences for MSN minimization in MMFMS.

Sivarami Reddy et al. [32] and Sivarami Reddy et al. [33] addressed concurrent scheduling of MCs and tools with a replica of each tool kind and alternate machines for minimization of MKSN.

The following are the other scheduling problems addressed in the literature. Al-Refaie et al. [34] devised a mathematical model for concurrent optimal patients' scheduling and sequencing in newly opened operating rooms under emergency events for maximization of patient's assignment over the empty available rooms. Abbas and Hala [35] proposed an optimization model to deal with quay crane assignment and scheduling problem considering multiple objective functions, such as minimization of handling makespan, maximization of number of containers being handled by each quay crane and  maximization of  satisfaction levels on handling completion times.

When operations of different jobs require the same tool at the same time, tool would be allocated for only one operation that causes other operations to wait for the tool in SMTTATWACT. This increases the MSN. Therefore it is important to address machines, TT and tools simultaneous scheduling with the lowest number of copies

of each tool kind which are much less than the number of machines without tool delay (SMATLNTC) by sharing the tools among machines to minimize MKSN in an FMS. As it causes no tool delay which in turn reduces MKSN with few additional copies for few tool types. The novelty of the research is addressing the SMATLNTC for minimization of MKSN first time, presenting nonlinear MIP model. CSA is employed to minimize MKSN of SMATLNTC and demonstrate its difference from other studies.

Automated tool sharing system presents technical solution to tools' high cost where different machines are able to employ same tool by dynamically moving the tool from machine to machine as tooling needs evolve. Because FMS is an interconnected manufacturing facility, it is important to concurrently schedule different components of FMS.

The job shop's scheduling problem [36], and the TT scheduling problem which are analogous to a problem of pick-up and delivery [37] are NP-hard problems. Combining them is a double interlinked NP-hard problem. Determining the lowest possible number of copies of every tool type for no tool delay and allocating them to the operations increases the scheduling problem complexity further, and it is also expected to improve the utilization of machines, TT and tools.

CSA is a metaheuristic developed by Askarzadeh [38]. It attempts to simulate the intelligent behavior of the crows to find the solution of optimization problems. It has been successfully applied to cope with engineering optimization problems [38-40, 27, 41-44, 29]. The advantages of the CSA over most other metaheuristic algorithms are that algorithm operations require two algorithm parameters, simple and easy to implement.

## 2. Problem and model formulation

Setup varies in FMS types and operations. Because having a common configuration is not feasible, the majority research focuses on defined production systems. Specification of the system, assumptions, criteria for objective and the problem addressed in this work are offered in the subsequent sections.

### 2.1. FMS Environment

Using common tool storage is typically followed in several manufacturing systems through one CTM serving multiple machines to cut down tool stocks. During the part's machining, demanded tool is shared from different machines or shipped from CTM by TT. CTM cuts down the tools copies required in system, and therefore cuts down tooling cost. Switching of tools and jobs between the machines will be carried out by TT and AGVs respectively. The FMS in this work is assumed to consist of four CNC machines, CTM with necessary tool types for all the machines and one copy of every type, a TT, two indistinguishable AGVs and each machine with ATC. There are loading and unloading (LU) stations where FMS releases parts for manufacturing and the completed parts are deposited and transported to the final storage facility respectively. To stock up the work-in-progress, an automatic storage and retrieval system (AS/RS) is

available. Figure 1 shows its configuration.
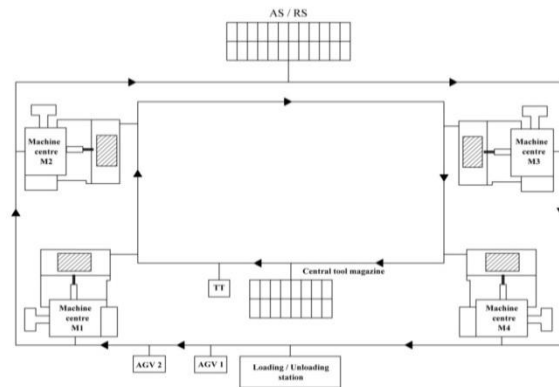


**Figure 1.** FMS environment

### 2.2. Assumptions

The following assumptions are made for the problem being studied

Initially all jobs, machines and TT are available for use.

Tool/ machine can perform one job only at any given time.

Operation's pre-emption on machine is barred.

The necessary machines and tools are identified before scheduling every operation.

Every job has operations' set with its own order and known processing times that also include setup times.

Initially, tools are stored in a CTM.

Transportation time of parts among machines is not taken into account.

At the time of jobs' arrival, the service life given to the tools will be sufficient to perform the operations allocated to the respective tools.

There is only one TT which moves the tools all through the system and tool switch times among machines are taken into account. A flow path layout for TT is given, travel times on each path segment are known and it moves along shortest predetermined paths.

TT starts from CTM initially, returns to CTM after all their assignments have been done and holds a single unit at a time.

The process planning information for determining the sequence of operations for optimizing tolerance stack-up is provided in terms of precedence constraints for each job. Thus, we assume that each job has prearranged operations order that cannot be altered.

### 2.3. Problem definition

Consider an FMS with a job set J of j job types $\{J_1, J_2, J_3 ... , J_j\}$, m machines $\{M_1, M_2, M_3 ... , M_m\}$, and total operations of job set {1,2,3.......N} and k types of tools $\{t_1, t_2, t_3....t_k\}$ with few copies of every type. A job's operations have a predetermined order of processing, and the order is known in advance. At most one operation at a time can be processed by a machine. Until its predecessor operation is complete, an operation cannot begin. The order of operations on a machine determines the setup requirements for a machine. The simultaneous scheduling problem is defined as determining the lowest possible number of copies of every variety of tools, allocation of copies of tools to job-operations and job-operations' sequencing on machines without tool delay, in addition to

determining each job's beginning and finishing times on every machine and tool copy and corresponding trip operations of TT, including the dead heading trip and loaded trip times of TT for MSN minimization in a MMFMS. The problem is stated in crisp, so unambiguous mathematical form is given in section 2.4.

### 2.4. Model formulation

In this section, nonlinear MIP model is introduced to clearly specify the crucial parameters and their effect on the FMS scheduling problem.

#### 2.4.1. Notations

**Decision variables**

$$q_{rs} = \begin{cases} 1 & \begin{array}{l} \text{if } c_r \text{ is less than } c_s, \text{ where } r \text{ and } s \text{ are} \\ \text{operations of different jobs} \end{array} \\ 0 & \text{otherwise} \end{cases}$$

$$y_{hi} = \begin{cases} 1 & \begin{array}{l} \text{if the TT is assigned for dead} \\ \text{heading trip between trip 'h' and} \\ \text{trip 'i' where the demanded tool} \\ \text{is available} \end{array} \\ 0 & \text{otherwise} \end{cases}$$

$$y_{oi} = \begin{cases} 1 & \begin{array}{l} \text{if the TT starts from CTM to} \\ \text{accomplish trip 'i' as its first} \\ \text{assignment} \end{array} \\ 0 & \text{otherwise} \end{cases}$$

$$y_{ho} = \begin{cases} 1 & \begin{array}{l} \text{if TT returns to the CTM after} \\ \text{completing trip 'h' as its last} \\ \text{assignment} \end{array} \\ 0 & \text{otherwise} \end{cases}$$

$$ttw = \begin{cases} tttd_{o,u} & \begin{array}{l} \text{if the TT starts from CTM} \\ \text{to accomplish trip 'i' as its} \\ \text{first accomplishment,} \\ \text{otherwise} \end{array} \\ 0 \end{cases}$$

#### 2.4.2. Mathematical model

In the formulation, machine and tool indices are not employed specifically as each job routing is available; the machine and tool indices are known for each operation index in I. Among operations and loaded trips there is one-to-one association. TT loaded trip for operation $i$ is associated for every operation $i$. The destination of TT loaded trip' $i$' is a machine for which operation $i$ is allocated and its origin is either a machine which is performing the operation using the tool required for operation i or a CTM. The tool needs to follow operations precedence constraints for the operations that belong to the same tool copy and same job i.e. $RT_{kj}$. The objective function for minimization of MSN is

**Subscripts**

| | |
|---|---|
| j | index for a job |
| i, h,r,s | indices for operations |
| k | index for a tool |
| J | job set on hand for processing. |
| $n_j$ | operations in job j. |
| N | $\sum_{j \in J} n_j$, total operations in job set J. |
| I | $\{1,2,\text{------}N\}$, index set for operations. |
| $I_j$ | $\{J_j+1, J_j+2, \text{------}J_j+n_j\}$, the indices' set in 'I' linked with job 'j', where '$J_j$'is jobs' operations listed before job 'j' and $J_1=0$. |
| $IS_i$ | $I-\{h; h \geq i, i, h \in I_j\}$ operations' index set without operation 'i' and same job's following operations to operation 'i'. |
| $IP_h$ | $I-\{i; i \leq h, i, h \in I_j\}$ operations' index set without operation 'h' and same job's preceding operations to operation 'h'. |
| $pt_i$ | operation 'i' processing time. |
| $ct_i$ | operation 'i' completion time. |
| TL | the set of tool types to carry out the jobs' operations |
| TLCopy | set of copies of each tool variety. |
| $R_k$ | indices set in I linked with tool type k in TL, $\forall k \in TL$ |
| $RT_{kj}$ | : $I_j \bigcap R_k$ the index set of operations in I common for tool k and job j $\forall k \in TL, \forall j \in J$ |
| $b_{kci}$ | Set of ready times of copies of tool type `k` at a machine for operation `i`, including tool copies` transfer time from other machines or CTM to this machine. |
| $TLRM_i$ | $\min \{b_{kci}\}, \forall k \in TL, \forall c \in TLCopy, \forall i \in R_k$ |
| $ct_{ick}$ | operation i's completion time using copy c of tool type k, $\forall i \in I$, $\forall c \in TLCopy$, and $\forall k \in R_k$ |
| u | first operation that uses tool k, $u \in R_k, \forall k \in TL$ |
| v | preceding operation of i, $i, v \in R_k, \forall k \in TL$ |
| L | number of TTs |
| $a_j$ | job j ready time |
| $TM_i$ | machine ready time for operation i |
| $tttl_i$ | TT loaded trip 'i' travel time including load and unload times. |
| $tttd_{hi}$ | TT empty trip 'i' travel time, trip commencing at a machine processing operation `h` and concluding at the machine processing operation `i` with the demanded tool. |
| $CTTTL_i$ | TT loaded trip 'i' completion time |
| $Q_i$ | : $\max(ct_{i-1}, TM_i), \forall i \in I$ |

| | |
|---|---|
| $Z = \min(\max(ct_i)), \quad \forall i \in I$ <br> subject to | |
| $Z \geq ct_{N_j + n_j} \quad \forall j \in J$ | (1) |
| $ct_i - ct_{i-1} \geq pt_i + tttl_i, \quad \forall i-1, i \in I_j, \forall j \in J$ | (2a) |
| $ct_{N_j+1} \geq pt_{N_j+1} + tttl_{N_j+1}, \quad \forall j \in J$ | (2b) |
| $ct_{ick} \neq ct_{hck}, i \neq h, \ \forall i, h \in R_k, \ \forall c \in TLCopy, \ and \ \forall k \in TL$ | (2c) |
| $(1 + H\ tagd_{rs})ct_r \geq ct_s + pt_r - H\ q_{rs}$ <br> $(1 + H\ tagd_{rs})ct_s \geq ct_r + pt_s - H(1 - q_{rs})$ $\Big\}$ <br> $\forall r \in I_j, and \ \forall s \in I_l \ where\ j,l \in J, j<l$ | (3) |
| $TM_i < TLRM_i, \ i \in I$ <br> i` is the first scheduled operation on the machine | (4) |
| $Q_i - TLRM_i \geq 0 \quad \forall i \in I$ | (5) |
| $y_{oi} + \sum_h y_{hi} = 1\ h \neq i, \quad i,h \in R_k, \ \forall k \in TL$ | (6) |
| $y_{ho} + \sum_i y_{hi} = 1\ i \neq h, \ i,h \in R_k, \forall k \in TL$ | (7) |
| $\sum_{i \in R_k} y_{oi} \leq L \qquad \forall k \in TL$ | (8) |
| $\sum_{i \in R_k} y_{oi} - \sum_{h \in R_k} y_{ho} = 0, \ \forall k \in TL$ | (9) |
| $CTTTL_i - tttl_i \geq ct_v, \ \forall i,v \in R_k, i \neq u, \ \forall k \in TL$ | (10) |
| $CTTTL_i - tttl_i \geq y_{oi}\ ttw + \sum_{h \in R_k, h \neq i} y_{hi}(CTTTL_h + tttd_{h,v})$ <br> $\forall i \in R_k, \forall k \in TL, \ if\ h,i \in RT_{kj}\ then\ i < h$ | (11) |
| $CTTTL_u - tttl_u \geq \sum_{h,u \in R_k, h \neq u} y_{h,u}(CTTTL_h + tttd_{ho}), \ \forall k \in TL$ | (12) |
| $\max(TM_i, CTTTL_i) \leq ct_i - pt_i, \ \forall i \in I$ | (13) |
| $ct_i \geq 0, \ \forall i \in I$ <br> $y_{hi} = 0,1 \quad i \neq h \quad i,h \in R_k, \forall i \in I$ | |

The 1st constraint specifies that MSN is greater than or equal to the completion time of last operation of all the jobs. The constraint 2a is the operations precedence constraints. The constraint 2b is the constraint for the completion time of first operations of jobs. The constraint 2c is the constraint for the operations that belong to the same tool copy.

H is a large positive integer in the 3rd constraint which ensures that no two operations allocated to the same machine can be concurrently performed. If operations 'r' and 's' that belong to distinct jobs need the same machine, then $tagd_{rs}$ is zero by definition. The 4th constraint defines that the machine ready time should be less than the TLRM$_i$ as the tool is to be shifted either from other machine or CTM if operation 'i' is the first scheduled operation on the machine. The 5th constraint defines that there will not be tool delay for operation i.

The 6th and 7th constraints express that tools are loaded and unloaded once for every operation respectively. The 8th constraint assures that every TT goes into the system at most one time. The 9th constraint keeps total TTs consistent in the system.

The 10th constraint states that TT loaded trip i can begin only when the preceding operation v is completed. The 11th constraint states that TT loaded trip i can begin only after TT dead heading trip is completed, and it is applicable if it is the first loaded trip of TT or TT loaded trips for operations other than the first operation of the tools. The 12thconstraint states that TT loaded trip 'u' i.e. for first operation of a tool can begin only after completion of TT dead heading trip.

The 10th, 11th, and 12th constraints are connected to the starting times of TT loaded trips. Collectively, they declare that the TT loaded trip i cannot commence before the

maximum of dead heading trip to the preceding operation and the finish time of the preceding operation.

The 13th constraint specifies that the operation i cannot begin before maximum of the machine ready time and the TT loaded trip. However, this formulation is intractable due to its size and nonlinearity, thus meta-heuristic algorithm namely CSA is used to obtain near optimal or optimal solutions.

Since the MSN needs to be minimized, calculation of MSN and lowest possible number of tool copies for a given schedule needs to be developed. Flow-chart for such a computation is shown in Figure 2.

*2.4.3. Input data*

Since the FMS configurations differ from one to the other topologically, four different layout configurations shown in Figure 3 are considered as reported in Bilge and Ulusoy [45]. Job sets employed for this problem are the 1st ten job sets

employed by Aldrin Raj et al [19], which are also the standard problems provided by Bilge and Ulusoy [45] but with the additional information, such as tools to carry out the operations. These problems were developed for various levels of travel times to processing times' ratio (t/p). The 82 test problems were designed with 10 job sets, 2 AGVs and 4 layouts, 40 problems with t / p greater than 0.25 and 42 problems with t / p less than 0.25. Four separate layouts (LAOT 1, LAOT 2, LAOT 3 and LAOT 4) with three cases were taken into account for the estimation of the MSN with the growing processing times. The original processing times (OPT), twice the OPT and thrice the OPT had been used in case 1, case 2 and case 3 respectively. Case 1 and case 2 are taken into account for LAOT 1, LAOT 2 and LAOT 3 and all the cases are taken into account for LAOT 4. The three cases are classified into 2 sets with relatively high t / p ratio greater than 0.25(case 1) and relatively small t / p less than 0.25(case 2 and case 3).The above test problems with original travel times of TT are used for this problem.

The following data is offered as an input.

It is assumed that the flow path of tool transporter closely resembles flow path of the AGVs for any given layout, the average speed of tool transporter is 57 m/min, and travel time matrix of tool transporter including load and unload times of tool for various layouts is given in Table 1.

Number of jobs, each job's operations and job's maximum operations in job set.

Machine needed for every job operation (machine matrix),

Time needed to perform every job-operation on the machine (process time matrix), and

Tool for processing every job-operation (Tool matrix)

## 3. CSA

The crow flock behavior has many similarities with the process of optimization [38]. Crows conceal their surplus food in the environment's hiding places and get stored food when necessary. Crows are voracious to get better food sources, and they go after each other. If the crow notices another one is behind it, the crow attempts to deceive that crow by heading to a different location in the vicinity. The crows are searchers from an optimization view point, the environment is a search space. Every hiding place in environment is a corresponding viable solution, the food source's quality is an objective function, and the problem's global solution is the best food source. CSA tries to simulate crows ' behavior to get a solution to the problem of optimization

*3.1. Implementation of CSA.*

In this problem of simultaneous scheduling, CSA is employed to minimize MSN. In the suggested CSA, every parameter of solution vector has to represent job-operation, and the machine and tool that are allocated for job-operation. Therefore, job-operation, machine, and tool encoding is employed. The parameter's first item represents the job number and location in the order in which it happens in vector showing operation number. The parameter's second item indicates the machine allocated to process that operation, selected from machine matrix, and the parameter's third item represents tool allocated to perform the operation selected from tool matrix. Parameters in vector are same as job set's total operations. This coding is useful in checking precedent relationships between job's operations in the vector.
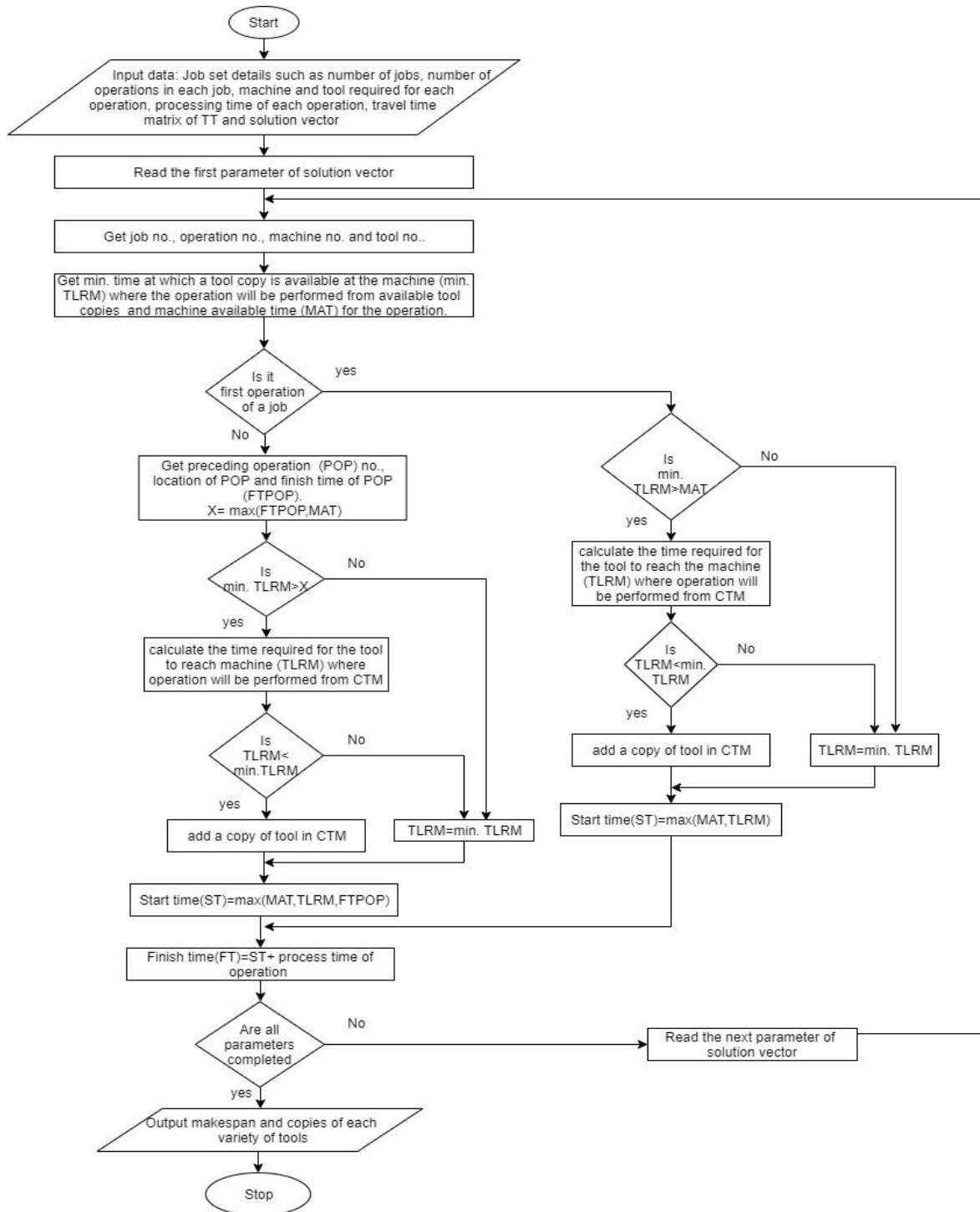
**Figure 2.** Flow chart for calculation of MSN and lowest possible number of tool copies for a given schedule.

**Table 1.** Travel time matrix of TT

| Layout 1 | | | | | | Layout 2 | | | | | |
|---|---|---|---|---|---|---|---|---|---|---|---|
| | To | | | | | | To | | | | |
| From | CTM | M1 | M2 | M3 | M4 | From | CTM | M1 | M2 | M3 | M4 |
| CTM | 0 | 4 | 6 | 7 | 8 | CTM | 0 | 3 | 4 | 6 | 4 |
| M1 | 8 | 0 | 4 | 6 | 7 | M1 | 4 | 0 | 1 | 3 | 1 |
| M2 | 7 | 4 | 0 | 4 | 6 | M2 | 6 | 8 | 0 | 1 | 3 |
| M3 | 6 | 6 | 4 | 0 | 4 | M3 | 4 | 7 | 8 | 0 | 1 |
| M4 | 4 | 7 | 6 | 4 | 0 | M4 | 3 | 6 | 7 | 8 | 0 |
| Layout 3 | | | | | | Layout 4 | | | | | |
| | To | | | | | | To | | | | |
| From | CTM | M1 | M2 | M3 | M4 | From | CTM | M1 | M2 | M3 | M4 |
| CTM | 0 | 1 | 3 | 7 | 8 | CTM | 0 | 3 | 6 | 7 | 10 |
| M1 | 8 | 0 | 1 | 6 | 7 | M1 | 13 | 0 | 3 | 4 | 7 |
| M2 | 7 | 8 | 0 | 4 | 6 | M2 | 14 | 10 | 0 | 6 | 4 |
| M3 | 3 | 4 | 6 | 0 | 1 | M3 | 8 | 6 | 4 | 0 | 4 |
| M4 | 1 | 3 | 4 | 8 | 0 | M4 | 10 | 10 | 8 | 4 | 0 |
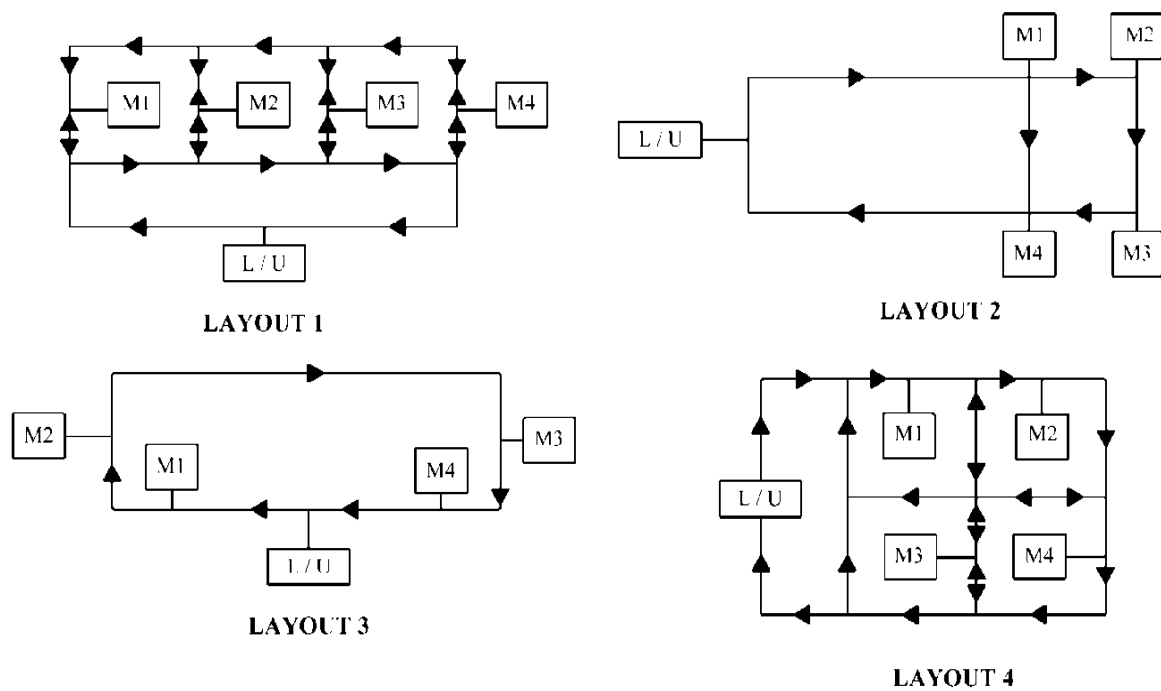


**Figure 3.** The layout configurations

### 3.1.1. Random solution generator (RSG)

RSG is devised to offer solutions for initial population. A solution vector is constructed parameter after parameter by this generator. An operation must be eligible for assigning to a parameter.  An operation is said to be qualified once all of its predecessors are allocated. Qualifying operations are placed in a set for scheduling next. In the beginning, this set is made up by the first operations of each job. At every iteration one among the operations in the set is chosen arbitrarily and put next to the parameter in the vector. Then, machine and tool are picked up from machine matrix and tool matrix for the operation respectively and both are allotted to a parameter to end the vector. The set is kept up to date, and if the solution vector is not yet finished, the process will continue.

### 3.1.2. Limits function

It is used to ensure that the produced operations in a new solution are compatible with the precedence constraints requirement.  If the precedence requirement constraints are not observed, the new solution will be corrected by the limits function so that the operations of the new solution vector will observe the precedence constraints requirement.

CSA's step-by-step implementation procedure is outlined below.

Step1: The problem and adjustable parameters be initialized.

MSN minimization is specified as an objective function. The decision variables are job-operations, machines, tools. The constraints are job-operations precedence requirements, copies of each tool variety and number of TTs.  The CSA parameters, such as flock size (size of population), flight length(fl), probability of awareness (AP) and maximum iterations  (iter$_{max}$) are set.    Initialize iteration no to zero.

Step 2: Initialize positions.

 N crows are arbitrarily situated as group mates in the search space.

This implies that N solutions are produced arbitrarily (located) through the use of RSG in the search space known as initial population.

$$\text{Initial population=} \begin{bmatrix} x_1^{\,1} & x_2^{\,1} & x_3^{\,1} \\ x_1^{\,2} & x_2^{\,2} & x_3^{\,2} \\ - & - & - \\ x_1^{\,N} & x_2^{\,N} & x_3^{\,N} \end{bmatrix}$$

where $x_1^{\,i}$ is sequence of operations  and $x_2^{\,i}$ and $x_3^{\,i}$ are machines and tools allocation  to the corresponding job-operations respectively.

Step 3 : Assess objective function and initialize crows memory.

Each crow's position quality i,e MSN is computed by means of flow chart given in figure 2. The memory of every crow is initialized and crows are believed to have concealed their food in their original positions. That is solutions of the population and associated MSNs   are recorded in memory.

Step 4: Crows make a fresh location in the search space as given below.

Crow i would like to make a new location, then it arbitrarily selects one among the crows, say the crow j, and pursues it to locate hidden food from the crow j. Crow i uses the following equation (14) to obtain new position.

$$x^{i,iter+1} = \begin{cases} x^{i,iter} + r_j\,X\,fl^{i,iter}\,X\left(m^{j,iter} - x^{i,iter}\right) \\ \quad a\ random\ position \end{cases}$$

$$r_j \geq AP^{i,iter} \quad (14)$$

$$otherwise$$

where  $r_j$ is a uniformly distributed random number between 0 and 1.

Fresh solution   (new position) is obtained as per equation (14) for solution   i (present position) in the population.

Step 5: Test if new positions (new solutions) are feasible.

If the new solution is infeasible, the use of limit functions will make it feasible. The crow modifies its location. That is the new solution of i (new location), which is to replace solution of i (present location).

Step 6: Update memory.

If the fresh solution MSN (fresh position of crow) is superior to the old solution MSN recorded in memory (crow's memory), fresh solution along with its MSN replaces the old solution and its MSN.

Repeat steps 4 to 6 for all members of the population.

Step 7: verify termination criterion.

Increment the iteration one by one. Repeat steps 4-6 till iteration no reaches iter$_{max}$. The best MSN position in the memory is identified as the optimization problem's solution when the termination requirement is met.

The initial population is generated arbitrarily by the use of RSG in the proposed methodology. Every vector of the solution consists of parameters equal to the job set operations.  The data mentioned in section 2.4.3 is offered as an input. The code is written in MATLAB and offers a schedule for job-operations together with allocation of machines and tools to the corresponding job-operations for minimum MSN.

At every generation, all candidates of population are selected for replacement. Thus, NP competitions are provided to decide members for next generation.

Example: Job set 5 is considered that has five jobs and operations in job set are 13. Therefore, the solution vector with 13 parameters along with its job-operation, machine and tool based coding is given below.

| 333 | 114 | 141 | 324 | 532 | 322 | 232 | 442 | 433 | 511 |
| 221 | 114 | 233 | | | | | | | |

Randomly generated solution vector for the initial population is shown below.

| 114 | 333 | 522 | 442 | 121 | 232 | 144 | 413 | 231 | 344 |
| 233 | 521 | 312 | | | | | | | |

The generated solutions for initial population observe precedence constraints, therefore, they are feasible solutions.

Assessment: Each vector's MSN value in initial population is calculated and recorded together with vector in memory matrix.

Next generation: First vector in the population is considered as input vector and given below.

333  212  344  114  121  532  511  442  144  423 231  312  223

The above vector MSN is 66 and lowest possible tool copies are [3 2 1 1]

Generated random Value is 0.2059.Since the random value generated is lower than the probability of awareness (0.3), number other than 1 is produced at random and it is 200. The best of the 200th crow recorded in memory is taken and given below to generate new vector.

333  442  344  532  212  511  231  114  121  223  144 312  423

whose MSN is 75 and lowest possible tool copies are [2 2 1 1]

According to equation 14 new solution vector is generated and its feasibility is checked employing the Limit function. The fresh feasible vector generated is given below.

333  442  344  532  212  511  231  114  121  223 423  312  144

The new vector fitness value is assessed, and if it is superior than the input vector best fitness value in memory matrix, then the vector in the memory matrix is substituted by new vector. MSN of this vector is 70 and lowest possible tool copies are [2 2 1 1]

specified generations have been completed, the best sequence until now is given below.

114  532  333  212  344  121  442  521  144  423 231  312  223

whose MSN is 51 and lowest possible tool copies are [2 2 1 1]

First tool copy is represented with A, second tool copy is represented with B and so on. The above vector can be represented in the Job-operation, machine and tool copy form given below.

114A  532A  333A  212A  344A  212A  344A  121A 442B  511A  144A  423A231B  312B  223A

## 4. Results and discussions

The proposed approach has been applied on different population sizes varying from 2 to 12 times of operations in the job set, and it is found that when population size is 10 times of operations, better results are noticed.  Different combinations of probability of awareness (AP) and flight length (fl) are employed, but a combination of 0.3 and 2 provided good results. Good results are obtained between 200 and 250 generations for most of the problems, so 250 generations are taken into account as the stopping criteria. The code written in MATLAB for *SMTTATWLNTC* is run on each job set discussed in section 2.4.3 for 20 times for MSN minimization. The best MSN from 20 runs is

provided for every layout and job set, along with mean and standard deviation (SDV) for various cases in Table 2.

In Table 2, the non zero SDV in case 1 vary for LAOT 1 in the range [ 0.8127, 2.9105], for LAOT 2 in the range [ 0.5501, 2.0417], for LAOT 3 in the range[1.0501, 2.5644] and for LAOT 4  in the range [1.6051, 3.1473]; the non zero SDV in case 2 varies for LAOT 1 in the range [0.2236, 3.2911], for LAOT 2 in the range [1.2085, 3.4622], for LAOT 3 in the range [0.4474, 3.6158] and for LAOT 4 in the range [1.5761, 3.1289] and the non zero SDV in case 3 varies for LAOT  4 in the range [1.2732,  3.5700]. From Table 2 one interesting finding is that the SDV values are extremely small compared with the magnitude of the mean values. In fact, the coefficient of variation for non zero standard deviation varies in the range [0.001746, 0.3445]. Furthermore, the SDV is zero for 13 out of 85 problems. If one looks closer to the final solutions of 20 simulation experiments for these problems, one finds that distinct solutions with the same MSN value exist. It means many optima alternatives are there, and the suggested CSA is able to find them.

### 4.1. Gantt chart

The Gantt chart shows the feasibility of the job set 1 LAOT 2 of case 1 optimal solution for minimum MSN obtained by CSA. Below is given the job set 1 LAOT 2 of case 1 optimal solution vector.

113A  124A  212A  443A  532B  233B  424A 331A  511B  344A  221C  312A  141A

The solution above is given as Table 3 in the table form.

The operations assigned for every tool copy and machines are indicated in Gantt chart together with each operation's start and end times. The Gantt chart also shows empty trips, loaded trips and waiting time of TT. Figure 4 shows the above solution vector's Gantt chart. A five character word represents an operation. For instance, in operation 5132B, the 1st character '4' specifies the job number, the 2nd character '1' denotes the job-operation, the 3rd  character '3' indicates the required machine, the 4th and 5th characters ' 2B ' denotes tool copy i,e tool type 2 and copy 'A' allocated to the job-operation.

In Figure 4,  M4, M3, M2 and M1 denotes machines, T4A, T3A, T3B, T2A, T2B, T1A,T1B and T1C indicate tool copies and TT indicates tool transporter.

LTT xxxxx corresponds to TT loaded trips for operation xxxxx .

ETT xxxxx corresponds to TT empty trips for operation xxxxx.

WT xxxxx denotes TT waiting time to pick up the tool for operation xxxxx from machine.

413

**Table 2.** Best MSN of SMTTATWLNTC with mean and SDV for various job sets, layouts and cases

| Job set number | LAOT 1 | | | LAOT 2 | | | LAOT 3 | | | LAOT 4 | | |
|---|---|---|---|---|---|---|---|---|---|---|---|---|
| | Best MSN | mean | SDV | Best MSN | mean | SDV | Best MSN | mean | SDV | Best MSN | mean | SDV |
| **Case 1** | | | | | | | | | | | | |
| 1 | 110 | 112.35 | 0.8127 | 87 | 87.75 | 0.5501 | 90 | 91.45 | 1.0501 | 123 | 125.75 | 1.2085 |
| 2 | 114 | 118.65 | 1.6944 | 94 | 95.7 | 1.3803 | 98 | 100.15 | 1.5985 | 135 | 137.3 | 1.7199 |
| 3 | 112 | 113.45 | 1.572 | 91 | 94.45 | 1.4318 | 95 | 98.75 | 1.5517 | 125 | 125.55 | 1.7614 |
| 4 | 109 | 111.65 | 1.4965 | 86 | 87.2 | 0.8335 | 85 | 86.95 | 1.4318 | 129 | 133.05 | 1.6051 |
| 5 | 96 | 96.85 | 1.0500 | 74 | 74.95 | 0.2286 | 74 | 75.95 | 2.5644 | 112 | 112.4 | 0.6806 |
| 6 | 107 | 107 | 0.0000 | 99 | 99 | 0.0000 | 100 | 100 | 0.0000 | 117 | 117 | 0.0000 |
| 7 | 107 | 112.95 | 2.6651 | 89 | 91.6 | 1.818 | 89 | 93.7 | 2.1546 | 121 | 128.6 | 4.4296 |
| 8 | 148 | 151.9 | 2.7511 | 135 | 137.25 | 1.2513 | 138 | 140.3 | 1.6575 | 167 | 173.6 | 2.6328 |
| 9 | 107 | 190.45 | 2.9105 | 104 | 106.2 | 1.3611 | 106 | 108.5 | 1.3955 | 135 | 138.3 | 1.6255 |
| 10 | 136 | 164.85 | 2.5808 | 141 | 144.8 | 2.0417 | 143 | 148.55 | 2.1879 | 179 | 183.85 | 2.5397 |
| **case 2** | | | | | | | | | | | | |
| 1 | 149 | 150 | 0.5620 | 132 | 120 | 0.0000 | 135 | 135.4 | 0.5982 | 165 | 166.8 | 1.5761 |
| 2 | 166 | 169.8 | 2.6077 | 145 | 152.25 | 3.3067 | 147 | 153.75 | 3.3541 | 185 | 188.25 | 2.1491 |
| 3 | 162 | 168.95 | 2.9285 | 157 | 159.5 | 1.6702 | 152 | 159.1 | 2.5935 | 172 | 182.85 | 4.4636 |
| 4 | 144 | 146.25 | 1.7733 | 128 | 129.75 | 1.2085 | 128 | 130.35 | 0.8751 | 168 | 170.8 | 2.2804 |
| 5 | 128 | 128.05 | 0.2236 | 96 | 96 | 0.0000 | 105 | 105 | 0.0000 | 141 | 144.2 | 2.7067 |
| 6 | 188 | 188 | 0.0000 | 181 | 181 | 0.0000 | 182 | 182 | 0.0000 | 195 | 195 | 0.0000 |
| 7 | 160 | 163.75 | 2.0474 | 146 | 149.75 | 1.7733 | 132 | 132.2 | 0.4474 | 176 | 182 | 2.9558 |
| 8 | 268 | 266 | 0.0000 | 266 | 262 | 0.0000 | 265 | 265.15 | 0.4894 | 268 | 271 | 2.6557 |
| 9 | 186 | 191.5 | 2.7625 | 180 | 182.9 | 1.9708 | 181 | 183.4 | 1.818 | 200 | 204.3 | 2.3193 |
| 10 | 262 | 269.1 | 3.2911 | 249 | 259.75 | 3.4622 | 252 | 259.6 | 4.6158 | 273 | 284.9 | 5.1289 |
| **case 3** (LAOT 4) | Best MSN | mean | SDV | - | - | - | - | - | - | - | - | - |
| 2 | 241 | 248.3 | 3.57 | - | - | - | - | - | - | - | - | - |
| 3 | 241 | 245.1 | 2.0749 | - | - | - | - | - | - | - | - | - |
| 4 | 208 | 210.1 | 2.2455 | - | - | - | - | - | - | - | - | - |
| 5 | 177 | 177.4 | 1.2732 | - | - | - | - | - | - | - | - | - |
| 7 | 234 | 238.25 | 2.8447 | - | - | - | - | - | - | - | - | - |

**Table 3.** Optimal solution vector for job set 1 LAOT 2 of case 1

| Job-operation | 1-1 | 1-2 | 2-1 | 4-1 | 5-1 | 2-2 | 4-2 | 3-1 | 5-2 | 3-2 | 2-3 | 3-3 | 1-3 |
|---|---|---|---|---|---|---|---|---|---|---|---|---|---|
| Machine number | 1 | 2 | 1 | 4 | 3 | 3 | 2 | 3 | 1 | 4 | 2 | 1 | 4 |
| Tool copy | 3A | 4A | 2A | 3A | 2B | 3B | 4A | 1A | 1B | 4A | 1C | 2A | 1A |

Jaya algorithm reported in Venkata Rao [46] is also applied on the above mentioned problems for various cases and layouts, and the results obtained are recorded along with the results obtained by employing CSA in Tables 4 and 5. When the MSN of both algorithms given in tables 4 and 5 are compared, it is observed that CSA is outperforming the Jaya algorithm.

The best MSN of **SMTTATWLNTC** with the best MSN of simultaneous scheduling of machines and tools with a copy of every tool type considering tool transfer time (**SMTTATWACT**) as reported in Sivarami Reddy et al [27] obtained by CSA and % reduction in MSN of former over later for various cases and layouts are given in Table 6. From Table 6, it is noticed that the % reduction in MSN of **SMTTATWLNTC** over **SMTTATWACT** varies in case1 for LAOT 1 from 0.00 to 20.74, for LAOT 2 from 0.00 to 19.38, for LAOT 3 from 0.00 to 18.46, for LAOT 4 from 0.00 to 4.26; in case 2 for LAOT 1 from 0.00 to 31.72, for LAOT 2 from 0.00 to 26.83, for LAOT 3 from 0.00 to 26.12 and for LAOT 4 from 0.00 to 19.35; and in case 3 for LAOT 4 from 5.85 to 13.

### 4.2. Convergence characterstics

Figure 5 shows CSA convergence characterstics for job set 4 LAOT 2 of case 1. The best value is 86, observed at 214 iteration and time per iteration is 0.429882 seconds.
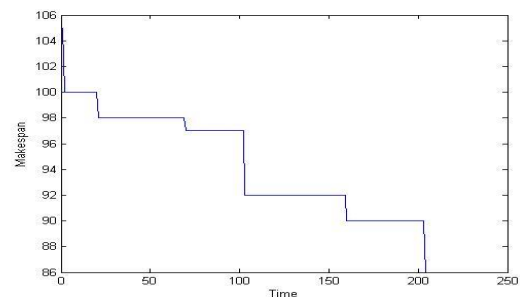


**Figure 5**. Convergence characteristics of CSA for job set 4, LAOT 2 of case 1
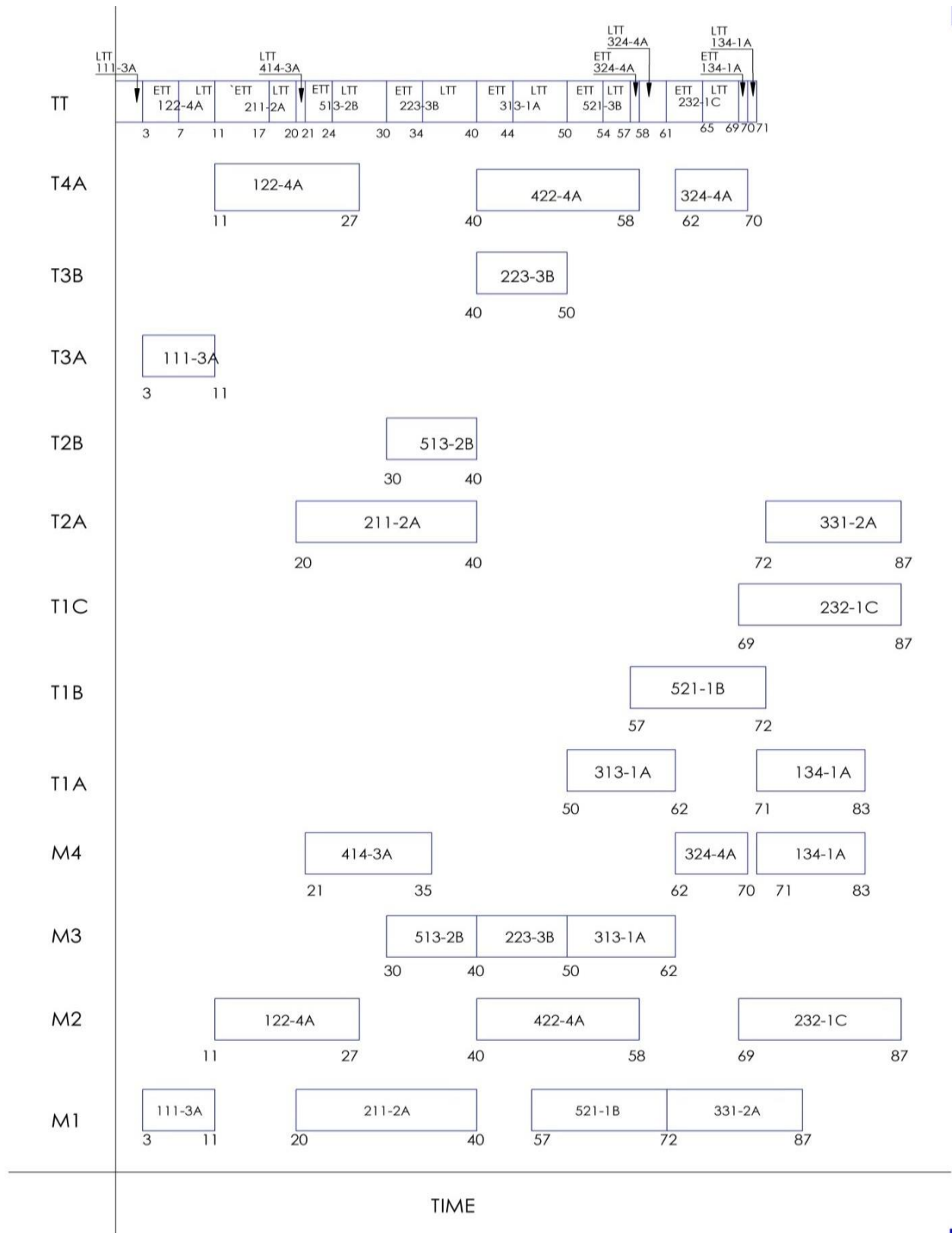
**Figure 4.** Gantt chart for job set 1, LAOT 2 of case1.

**Table 4.** Best MSN of SMTTATWLNTC obtained by CSA and Jaya algorithm for various layouts of case 1

| | case 1 | | | | | | | | | |
|---|---|---|---|---|---|---|---|---|---|---|
| | LAOT 1 | | | | | | | | | |
| Job set number | Best MSN obtained by CSA | Lowest copies for each typeof tool for minimum MSN | | | | Best MSN obtained by Jaya | Lowest copies for each typeof tool for minimum MSN | | | |
| | | T1 | T2 | T3 | T4 | | T1 | T2 | T3 | T4 |
| 1 | 110 | 2 | 1 | 1 | 1 | 113 | 2 | 1 | 1 | 2 |
| 2 | 114 | 2 | 1 | 2 | 1 | 119 | 2 | 2 | 1 | 2 |
| 3 | 112 | 1 | 2 | 2 | 1 | 116 | 1 | 1 | 2 | 2 |
| 4 | 109 | 2 | 2 | 2 | 1 | 112 | 2 | 2 | 2 | 1 |
| 5 | 96 | 1 | 1 | 1 | 1 | 96 | 1 | 1 | 1 | 1 |
| 6 | 107 | 1 | 1 | 1 | 1 | 108 | 1 | 1 | 1 | 1 |
| 7 | 107 | 1 | 1 | 2 | 1 | 113 | 1 | 2 | 1 | 1 |
| 8 | 148 | 1 | 3 | 2 | 1 | 155 | 1 | 3 | 2 | 2 |
| 9 | 107 | 1 | 2 | 2 | 2 | 121 | 1 | 1 | 1 | 2 |
| 10 | 136 | 2 | 2 | 2 | 2 | 164 | 2 | 2 | 2 | 2 |
| | LAOT 2 | | | | | | | | | |
| Job set number | Best MSN obtained by CSA | Lowest copies for each typeof tool for minimum MSN | | | | Best MSN obtained by Jaya | Lowest copies for each typeof tool for minimum MSN | | | |
| | | T1 | T2 | T3 | T4 | | T1 | T2 | T3 | T4 |
| 1 | 87 | 3 | 2 | 2 | 1 | 88 | 2 | 1 | 1 | 2 |
| 2 | 94 | 2 | 2 | 1 | 2 | 97 | 2 | 2 | 2 | 1 |
| 3 | 91 | 2 | 2 | 3 | 2 | 95 | 2 | 2 | 2 | 2 |
| 4 | 86 | 2 | 2 | 2 | 1 | 88 | 2 | 3 | 2 | 1 |
| 5 | 74 | 2 | 1 | 2 | 1 | 75 | 1 | 2 | 2 | 1 |
| 6 | 99 | 1 | 1 | 1 | 1 | 99 | 1 | 1 | 1 | 1 |
| 7 | 89 | 2 | 1 | 3 | 2 | 94 | 1 | 2 | 2 | 2 |
| 8 | 135 | 1 | 2 | 3 | 1 | 137 | 2 | 2 | 3 | 2 |
| 9 | 104 | 2 | 2 | 2 | 3 | 108 | 2 | 3 | 1 | 3 |
| 10 | 141 | 2 | 2 | 3 | 2 | 147 | 1 | 2 | 3 | 2 |
| | LAOT 3 | | | | | | | | | |
| Job set number | Best MSN obtained by CSA | Lowest copies for each typeof tool for minimum MSN | | | | Best MSN obtained by Jaya | Lowest copies for each typeof tool for minimum MSN | | | |
| | | T1 | T2 | T3 | T4 | | T1 | T2 | T3 | T4 |
| 1 | 90 | 3 | 2 | 2 | 1 | 92 | 2 | 1 | 2 | 2 |
| 2 | 98 | 2 | 1 | 2 | 2 | 101 | 3 | 2 | 1 | 2 |
| 3 | 95 | 2 | 2 | 2 | 2 | 100 | 2 | 2 | 2 | 2 |
| 4 | 85 | 2 | 3 | 2 | 1 | 89 | 2 | 3 | 2 | 1 |
| 5 | 74 | 1 | 2 | 2 | 1 | 79 | 1 | 2 | 2 | 1 |
| 6 | 100 | 1 | 1 | 1 | 1 | 100 | 1 | 1 | 1 | 1 |
| 7 | 89 | 1 | 2 | 1 | 2 | 94 | 1 | 2 | 2 | 2 |
| 8 | 138 | 2 | 2 | 3 | 2 | 140 | 1 | 2 | 2 | 1 |
| 9 | 106 | 1 | 2 | 2 | 2 | 109 | 1 | 3 | 1 | 3 |
| 10 | 143 | 1 | 3 | 3 | 2 | 151 | 2 | 2 | 2 | 1 |
| | LAOT 4 | | | | | | | | | |
| Job set number | Best MSN obtained by CSA | Lowest copies for each typeof tool for minimum MSN | | | | Best MSN obtained by Jaya | Lowest copies for each typeof tool for minimum MSN | | | |
| | | T1 | T2 | T3 | T4 | | T1 | T2 | T3 | T4 |
| 1 | 123 | 1 | 1 | 1 | 1 | 128 | 2 | 1 | 1 | 1 |
| 2 | 135 | 2 | 1 | 1 | 1 | 137 | 1 | 1 | 1 | 1 |
| 3 | 125 | 1 | 1 | 1 | 2 | 129 | 1 | 1 | 2 | 1 |
| 4 | 129 | 1 | 2 | 1 | 1 | 134 | 1 | 1 | 2 | 1 |
| 5 | 112 | 1 | 1 | 1 | 1 | 113 | 1 | 1 | 1 | 1 |
| 6 | 117 | 1 | 1 | 1 | 1 | 117 | 1 | 1 | 1 | 1 |
| 7 | 121 | 1 | 1 | 1 | 1 | 130 | 1 | 1 | 1 | 1 |
| 8 | 167 | 1 | 1 | 2 | 1 | 174 | 1 | 2 | 2 | 1 |
| 9 | 135 | 1 | 1 | 1 | 2 | 139 | 1 | 1 | 1 | 2 |
| 10 | 179 | 1 | 1 | 1 | 1 | 183 | 2 | 2 | 2 | 2 |

**Table 5.** Best MSN of SMTTATWLNTC obtained by CSA and Jaya algorithm for various job sets, layouts of case 2 and case 3

| | | case 2 | | | | | | | | |
|---|---|---|---|---|---|---|---|---|---|---|
| | | LAOT 1 | | | | | | | | |
| Job set number | Best MSN obtained by CSA | Lowest copies for each typeof tool for minimum MSN | | | | Best MSN obtained by Jaya | Lowest copies for each typeof tool for minimum MSN | | | |
| | | T1 | T2 | T3 | T4 | | T1 | T2 | T3 | T4 |
| 1 | 149 | 2 | 2 | 1 | 2 | 150 | 3 | 2 | 1 | 2 |
| 2 | 166 | 2 | 2 | 1 | 2 | 170 | 1 | 2 | 1 | 2 |
| 3 | 162 | 1 | 1 | 2 | 2 | 170 | 2 | 2 | 3 | 2 |
| 4 | 144 | 2 | 2 | 2 | 2 | 146 | 2 | 2 | 2 | 2 |
| 5 | 128 | 2 | 2 | 1 | 1 | 128 | 2 | 2 | 1 | 1 |
| 6 | 188 | 1 | 1 | 1 | 1 | 188 | 1 | 1 | 1 | 1 |
| 7 | 160 | 1 | 2 | 3 | 2 | 166 | 1 | 2 | 2 | 2 |
| 8 | 268 | 1 | 2 | 1 | 1 | 270 | 1 | 3 | 3 | 1 |
| 9 | 186 | 1 | 2 | 2 | 2 | 191 | 2 | 2 | 2 | 3 |
| 10 | 262 | 2 | 3 | 3 | 3 | 267 | 2 | 2 | 2 | 2 |
| | | LAOT 2 | | | | | | | | |
| Job set number | Best MSN obtained by CSA | Lowest copies for each typeof tool for minimum MSN | | | | Best MSN obtained by Jaya | Lowest copies for each typeof tool for minimum MSN | | | |
| | | T1 | T2 | T3 | T4 | | T1 | T2 | T3 | T4 |
| 1 | 132 | 2 | 2 | 1 | 2 | 132 | 2 | 2 | 1 | 2 |
| 2 | 145 | 2 | 2 | 2 | 2 | 152 | 2 | 2 | 2 | 2 |
| 3 | 157 | 2 | 2 | 3 | 2 | 158 | 2 | 2 | 3 | 2 |
| 4 | 128 | 2 | 2 | 2 | 2 | 129 | 1 | 2 | 2 | 2 |
| 5 | 96 | 1 | 2 | 1 | 1 | 107 | 1 | 2 | 2 | 1 |
| 6 | 181 | 1 | 1 | 1 | 1 | 181 | 1 | 1 | 1 | 1 |
| 7 | 146 | 2 | 2 | 2 | 3 | 151 | 2 | 2 | 2 | 2 |
| 8 | 266 | 1 | 2 | 2 | 1 | 266 | 1 | 3 | 3 | 2 |
| 9 | 180 | 2 | 2 | 2 | 3 | 184 | 2 | 3 | 2 | 3 |
| 10 | 249 | 2 | 3 | 3 | 2 | 262 | 2 | 3 | 2 | 2 |
| | | LAOT 3 | | | | | | | | |
| Job set number | Best MSN obtained by CSA | Lowest copies for each typeof tool for minimum MSN | | | | Best MSN obtained by Jaya | Lowest copies for each typeof tool for minimum MSN | | | |
| | | T1 | T2 | T3 | T4 | | T1 | T2 | T3 | T4 |
| 1 | 135 | 3 | 2 | 1 | 2 | 135 | 3 | 2 | 1 | 2 |
| 2 | 147 | 2 | 2 | 1 | 2 | 154 | 2 | 2 | 2 | 2 |
| 3 | 152 | 2 | 2 | 3 | 2 | 160 | 2 | 2 | 4 | 2 |
| 4 | 128 | 2 | 3 | 2 | 1 | 130 | 2 | 3 | 2 | 2 |
| 5 | 105 | 1 | 2 | 2 | 1 | 114 | 1 | 2 | 2 | 1 |
| 6 | 182 | 1 | 1 | 1 | 1 | 182 | 1 | 1 | 1 | 1 |
| 7 | 132 | 2 | 2 | 3 | 2 | 151 | 2 | 2 | 3 | 2 |
| 8 | 265 | 1 | 3 | 2 | 2 | 265 | 2 | 2 | 3 | 1 |
| 9 | 181 | 2 | 3 | 1 | 3 | 187 | 2 | 2 | 2 | 3 |
| 10 | 252 | 2 | 3 | 3 | 3 | 264 | 2 | 3 | 3 | 2 |
| | | LAOT 4 | | | | | | | | |
| Job set number | Best MSN obtained by CSA | Lowest copies for each typeof tool for minimum MSN | | | | Best MSN obtained by Jaya | Lowest copies for each typeof tool for minimum MSN | | | |
| | | T1 | T2 | T3 | T4 | | T1 | T2 | T3 | T4 |
| 1 | 165 | 2 | 1 | 1 | 2 | 167 | 2 | 1 | 1 | 2 |
| 2 | 185 | 2 | 2 | 1 | 2 | 187 | 1 | 3 | 2 | 2 |
| 3 | 172 | 1 | 1 | 2 | 2 | 186 | 1 | 1 | 2 | 2 |
| 4 | 168 | 2 | 2 | 1 | 1 | 170 | 1 | 1 | 2 | 1 |
| 5 | 141 | 2 | 1 | 1 | 1 | 146 | 2 | 2 | 1 | 1 |
| 6 | 195 | 1 | 1 | 1 | 1 | 196 | 1 | 1 | 1 | 1 |
| 7 | 176 | 2 | 2 | 1 | 2 | 184 | 1 | 2 | 1 | 1 |
| 8 | 268 | 1 | 2 | 2 | 2 | 272 | 1 | 2 | 3 | 2 |
| 9 | 200 | 2 | 3 | 1 | 2 | 209 | 1 | 2 | 2 | 3 |
| 10 | 273 | 2 | 2 | 2 | 2 | 265 | 2 | 2 | 2 | 2 |
| | | case 3 | | | | | | | | |
| | | LAOT 4 | | | | | | | | |
| Job set number | Best MSN obtained by CSA | Lowest copies for each typeof tool for minimum MSN | | | | Best MSN obtained by Jaya | Lowest copies for each typeof tool for minimum MSN | | | |
| | | T1 | T2 | T3 | T4 | | T1 | T2 | T3 | T4 |
| 2 | 241 | 2 | 2 | 1 | 2 | 249 | 2 | 2 | 1 | 2 |
| 3 | 241 | 1 | 2 | 3 | 2 | 282 | 1 | 1 | 2 | 1 |
| 4 | 208 | 2 | 2 | 1 | 1 | 212 | 1 | 2 | 2 | 2 |
| 5 | 177 | 2 | 2 | 1 | 1 | 182 | 2 | 2 | 1 | 1 |
| 7 | 234 | 1 | 2 | 2 | 2 | 241 | 1 | 2 | 2 | 2 |

**Table 6.** Best MSN values of SMTTATWLNTC, SMTTATWACT and % reduction in MSN of former over later   for various job sets, layouts and cases.

| Job set number | case 1 | | | | | | | | | | | |
| | LAOT 1 | | | LAOT 2 | | | LAOT 3 | | | LAOT 4 | | |
| | MSN of SMTTATWL NTC | MSN of SMTTATW ACT | % reducti on | MSN of SMTTATWL NTC | MSN of SMTTATW ACT | % reducti on | MSN of SMTTATWL NTC | MSN of SMTTATW ACT | % reducti on | MSN of SMTTATWL NTC | MSN of SMTTATW ACT | % reducti on |
|---|---|---|---|---|---|---|---|---|---|---|---|---|
| 1 | 110 | 116 | 5.17 | 87 | 95 | 8.42 | 90 | 95 | 5.26 | 123 | 123 | 0.00 |
| 2 | 114 | 120 | 5.00 | 94 | 100 | 6.00 | 98 | 104 | 5.77 | 135 | 137 | 1.46 |
| 3 | 112 | 118 | 5.08 | 91 | 102 | 10.78 | 95 | 106 | 10.38 | 125 | 131 | 4.58 |
| 4 | 109 | 116 | 6.03 | 86 | 98 | 12.24 | 85 | 99 | 14.14 | 129 | 131 | 1.53 |
| 5 | 96 | 96 | 0.00 | 74 | 77 | 3.90 | 74 | 82 | 9.76 | 112 | 112 | 0.00 |
| 6 | 107 | 107 | 0.00 | 99 | 99 | 0.00 | 100 | 100 | 0.00 | 117 | 117 | 0.00 |
| 7 | 107 | 113 | 5.31 | 89 | 95 | 6.32 | 89 | 99 | 10.10 | 121 | 126 | 3.97 |
| 8 | 148 | 160 | 7.50 | 135 | 151 | 10.60 | 138 | 149 | 7.38 | 167 | 172 | 2.91 |
| 9 | 107 | 135 | 20.74 | 104 | 129 | 19.38 | 106 | 130 | 18.46 | 135 | 141 | 4.26 |
| 10 | 136 | 171 | 20.47 | 141 | 165 | 14.55 | 143 | 166 | 13.86 | 179 | 182 | 1.65 |
| Job set number | case 2 | | | | | | | | | | | |
| | LAOT 1 | | | LAOT 2 | | | LAOT 3 | | | LAOT 4 | | |
| | MSN of SMTTATWL NTC | MSN of SMTTATW ACT | % reducti on | MSN of SMTTATWL NTC | MSN of SMTTATW ACT | % reducti on | MSN of SMTTATWL NTC | MSN of SMTTATW ACT | % reducti on | MSN of SMTTATWL NTC | MSN of SMTTATW ACT | % reducti on |
| 1 | 149 | 170 | 14.09 | 132 | 159 | 16.98 | 135 | 158 | 14.56 | 165 | 175 | 5.71 |
| 2 | 166 | 185 | 11.45 | 145 | 174 | 16.67 | 147 | 180 | 18.33 | 185 | 192 | 3.65 |
| 3 | 162 | 188 | 16.05 | 157 | 178 | 11.80 | 152 | 180 | 15.56 | 172 | 189 | 8.99 |
| 4 | 144 | 160 | 11.11 | 128 | 148 | 13.51 | 128 | 153 | 16.34 | 168 | 180 | 6.67 |
| 5 | 128 | 133 | 3.91 | 96 | 119 | 19.33 | 105 | 120 | 12.50 | 141 | 147 | 4.08 |
| 6 | 188 | 188 | 0.00 | 181 | 181 | 0.00 | 182 | 182 | 0.00 | 195 | 195 | 0.00 |
| 7 | 160 | 183 | 14.38 | 146 | 170 | 14.12 | 132 | 173 | 23.70 | 176 | 193 | 8.81 |
| 8 | 268 | 272 | 1.49 | 266 | 270 | 1.48 | 265 | 269 | 1.49 | 268 | 281 | 4.63 |
| 9 | 186 | 245 | 31.72 | 180 | 246 | 26.83 | 181 | 245 | 26.12 | 200 | 248 | 19.35 |
| 10 | 262 | 303 | 15.65 | 249 | 293 | 15.02 | 252 | 302 | 16.56 | 273 | 310 | 11.94 |
| Job set number | case 3 | | | - | | | - | | | - | | |
| | LAOT 4 | | | - | | | - | | | - | | |
| | MSN of SMTTATWL NTC | MSN of SMTTATW ACT | % reducti on | | | | | | | | | |
| 2 | 241 | 275 | 12.36 | - | - | - | - | - | - | - | - | - |
| 3 | 241 | 277 | 13.00 | - | - | - | - | - | - | - | - | - |
| 4 | 208 | 225 | 7.56 | - | - | - | - | - | - | - | - | - |
| 5 | 177 | 188 | 5.85 | - | - | - | - | - | - | - | - | - |
| 7 | 234 | 261 | 10.34 | - | - | - | - | - | - | - | - | - |

## Conclusions

This paper introduces a nonlinear MIP model for machines, TT and tools simultaneous scheduling in MMFMS to minimize MSN with the lowest possible number of copies of every tool type without tool delay considering tool switch times between machines in MMFMS. This scheduling problem involves determining the lowest possible number of copies of every tool type for no tool delay, assigning of suitable tool copy for every job-operation, ordering and synchronization of those job-operations and associated trip operations of TT including the dead heading trip and loaded trip times of TT for minimum MSN. An algorithm for computation of MS and lowest possible number of copies of every variety of tools without tool delay is developed for a given schedule and Figure 2 shows its flow chart.  The proposed algorithm is tested on the job sets mentioned in section 2.4.3. From the tables 2, it is quite evident that CSA is robust and able to find many optimal alternatives for the problems. From tables 4 and 5, it is noticed that CSA is

outperforming Jaya algorithm. From Table 6, it is observed that impact of SMAATWLNTC on reduction in MSN over SMTTATWACT is significant.  In future work with machines and tool scheduling, subsystems such as robots and automated storage and retrieval systems (AS/RS) may be integrated.

## References

[1] Agnetis,Alessandro.Arianna Alfieri, Paolo, Brandimarte. Prinsecchi, Paolo. (1997). Joint Job/Tool Scheduling in a Flexible Manufacturing Cell with No On-Board Tool Magazine. Computer Integrated Manufacturing System, 10 (1), 61–68. https://doi.org/10.1016/S0951-5240(96)00023-7

[2] Saravanan, M., A,. Noorul Haq. (2008). Evaluation of scatter-search approach for scheduling optimization of flexible manufacturing systems. Int J Adv Manuf Technol, 38, 978–986. https://doi.org/10.1007/s00170-007-1134-5

[3] Chen, F. Frank. and Everett, E. AdamJr. (1991),The Impact of Flexible Manufacturing Systemson Productivity and Quality. IEEE Transactions on Engineering Management, 38(1)1, 33-45.

[4] Jyothi, S. D. (2012) Scheduling Flexible Manufacturing System Using Petri-nets and Genetic Algorithm. Project Report Indian Institute of Space Science and Technology, Thiruvananthapuram, https://www.semanticscholar.org › paper › SCHEDULING-FLEXIBLE-MAN...

[5] Shirazi, Rabia.& G. D. M. Frizelle. (2001). Minimizing the number of tool switches on a flexible machine: An empirical study. International Journal of Production Research, 39(15), 3547-3560, DOI: 10.1080/00207540110060888

[6] Tang, Christopher S. Eric V, Denardo. (1988). Models Arising from a Flexible Manufacturing Machine, Part I: Minimization of the Number of Tool Switches. Operations Research, 36(5), 767–777. https://doi.org/10.1287/opre.36.5.767

[7] Chandra, P. S. Li & M. Stan. (1993). Jobs and tool sequencing in an automated manufacturing environment. International Journal of Production Research, 31 (12), 2911-2925 .https://doi.org/ 10.1080/00207549308956907

[8] Song, Chang-Yong. Hark, Hwang. and Yeong-Daekim. (1995). Heuristic algorithm for the tool movment policy in Flexible Manufacturing systems. Journal of Manufacturing Systems, 14(3), 160-168. https://doi.org/10.1016/0278-6125(95)98884-9

[9] Roh, H.-K. and Y-D, Kim. (1997).Due-date based loading and scheduling methods for a flexible manufacturing system with an automatic tool transporter. International Journal of Production Research, 35 (11), 2989-3004, https:// doi.org/ 10.1080/ 002075497194255

[10] Tsukada,T.K. Kang. G. Shin. (1998). Distributed Tool Sharing in Flexible Manufacturing Systems. IEEE Transactions on Robotics and Automation, 14 (3), 379–389. DOI: 10.1109/70.678448

[11] Jun,Hong-Bae. Yeong-Dae, Kim. Hyo-Won, Suh. (1999). Heuristics for a Tool Provisioning Problem in a Flexible Manufacturing System with an Automatic Tool Transporter. IEEE Transactions on Robotics and Automation, 15(3), 488–496. DOI: 10.1109/70.768181

[12] Keung, K. W. W. H, Ip. and T. C. Lee. (2001). A genetic algorithm approach to the multiple machine tool selection problem. Journal of Intelligent Manufacturing, 12, 331–342. https://doi.org/10.1023/A:1011215416734

[13] Ecker, K.H. and J.N.D,Gupta. (2005). Scheduling tasks on a flexible manufacturing machine to minimize tool change delays. European Journal of Operational Research, 164, 627–638. https://doi.org/10.1016/j.ejor.2003.12.025

[14] Prabaharan,T. P. R,Nakkeeran, and N,Jawahar. (2006). Sequencing and Scheduling of Job and Tool in Flexible Manufacturing Cell. International Journal of Advanced Manufacturing Technology, 29 (3), 729–745. https://doi.org/10.1007/s00170-005-2567-3

[15] Karzan, Fatma KilinÇ. and Meral, Azizoğlu.(2008). The tool transporter movements problem in flexible manufacturing systems. International Journal of Production Research,46(11), 3059–3084. https://doi.org/10.1080/00207540601070135

[16] Sureshkumar, N., and R.Sridharan.(2009). Simulation Modeling and Analysis of Tool Flow Control Decisions in a Flexible Manufacturing System. Robotics and Computer Integrated Manufacturing, 25, 829–838. https:// doi.org/ 10.1016/ j.rcim. 2008.12.004

[17] Udhayakumar, P. and S, Kumanan. (2010). Sequencing and scheduling of job and tool in a flexible manufacturing system using ant colony optimization algorithm. Int J Adv Manuf Technol, 50, 1075–1084. https://doi.org/10.1007/s00170-010-2583-9

[18] Udhayakumar, P. and S, Kumanan. (2012). Some metaheuristic approaches for optimising tardiness of job and tool in a flexible manufacturing system. Int. J. Advanced Operations Management, 4(3) , 219-252.https://doi.org/10.1504/IJAOM.2012 .047683

[19] Aldrin Raj, J. Ravindran, D. Saravanan, M. and Prabaharan, T. (2014). Simultaneous scheduling of machines and tools in multimachine flexible manufacturing system using artificial immune system algorithm. International Journal of Computer Integrated Manufaturing, 27(5), 401–414. https://doi.org/10.1080/0951192X. 2013.834461

[20] Özpeynirci, Selin. (2015).A heuristic approach based on time-indexed modelling for scheduling and tool loading in flexibl manufacturing systems. Int J Adv Manuf Technol, 77, 1269–1274. https://doi.org/10.1007/s00170-014-6564-2

[21] Costa, A. F.A, Cappadonna, S, Fichera. (2016). Minimizing the total completion time on a parallel machine system with tool changes. Computers & Industrial Engineering, 91, 290–301.. https://doi.org/10.1016/j.cie.2015.11.015

[22] Sivarami Reddy, Narapu Reddy. Dwivedula, Venkata Ramamurthy. K, Prahlada Rao. M,Padma Lalitha. (2016). A Novel metaheuristic method for simultaneous scheduling of machines and tools in multi machine FMS. IET Digital Library International Conference on Recent Trends in Engineering, Science & Technology 2016, 1–6. ISBN-978-1-78561-785-0 DOI: 10.1049/cp.2016.1489

[23] Beezao, Andreza Cristina. Jean-Francüois, Cordeau. Gilbert Laporte,Horacio. Hidek, Yanasse. (2017).Scheduling identical parallel machines with tooling constraints. EuropeanJournal of Operational Research, 257(3), 834-844. doi: 10.1016/j.ejor.2 016.08.008

[24] Baykasoğlu, Adil. and Fehmi, Burcin Ozsoydan. (2017). Minimizing tool switching and indexing times with tool duplications in automatic machines. International Journal of Advanced Manufacturing Technology , 89,1775–1789.DOI 10.1007/s00170-016-9194-z

[25] Paiva Gustavo Silva. Marco Antonio M, Carvalho. (2017). Improved Heuristic Algorithms for the Job Sequencing and Tool Switching Problem. 88, 208-219. Computers and Operations Research, doi: 10.1016/j.cor.2017.07.013

[26] Gökgür, Burak.Brahim, Hnich. &Selin, Özpeynirci.(2018). Parallel machine scheduling with tool loading: a constraintprogramming approach. International Journal of Production Research. https://doi.org/10.1080/ 00207543. 2017. 1421781

[27] Sivarami Reddy, N. D.V,Ramamurthy. K, Prahlada Rao. (2018a).SimultaneousScheduling of Machines and Tools Considering Tool Transfer Times in Multimachine FMS Using CSA. International Conference on Intelligent Computing and Applications, Advances in Intelligent Systems and Computing 632, 421–432.

[28] Sivarami Reddy, N. D.V, Ramamurthy. and K, Prahlada Rao. (2018b). Simultaneous scheduling of jobs, machines and tools considering tool transfer times in multi-machine FMS using new nature-inspired algorithms. Int. J. Intelligent Systems Technologies and Applications, 17(1/2), , 70–88.

[29] Sivarami Reddy, N. D V, Ramamurthy. K, Prahlada Rao. & M. Padma Lalitha. (2019).Integrated scheduling of machines, AGVs and tools in multi-machine FMS using crow search algorithm, International Journal of Computer Integrated Manufacturing. DOI:10.1080/0951192X.2019.1686171 https://doi.org/10.1080/0951192X.2019.1686171

[30] Sivarami Reddy, N. D. V, Ramamurthy. K, Prahlada Rao.& M, Padma Lalitha. (2021).Practical simultaneous scheduling of machines, AGVs, tool transporter and tools in a multi machine FMS using symbiotic organisms search algorithm. International

Journal of Computer Integrated Manufacturing,  DOI: 10.1080/ 0951192X.2020.1858503    https://doi.org/10.1080/0951192X. 2020. 1858503

[31] Sivarami Reddy, N. D V,. Ramamurthy. M, Padma Lalitha.& K, Prahlada Rao.(2021b).Integrated simultaneous scheduling of machines, automated guided vehicles and tools in multi machine flexible manufacturing system using symbiotic organisms search algorithm.Journal of Industrial and Production Engineering.https://doi.org/10.1080/21681015.2021.1991014

[32] Sivarami Reddy N., Padma Lalitha M., S.P.Pandey, Venkatesh G.S.(2021c).  Simultaneous scheduling of machines and tools in a multi machine FMS with alternative routing using symbiotic organisms search algorithm. Journal of Engg. ResearchDOI : 10.36909/jer.10653

[33] Sivarami Reddy N., Padma Lalitha M., D V. Ramamurthy, K Prahlada Rao. (2022).  Simultaneous scheduling of machines and tools in a multi machine FMS with alternate machines using crow search algorithm., Journal of Advanced Manufacturing Systems  https://doi.org/10.1142/S0219686722500305

[34] Al-Refaie et al. (2017).Optimal Scheduling and Sequencing of Operating Room Under Emergency Cases. Jordan Journal of Mechanical and Industrial Engineering 11(1), 21-26.

[35] Abbas, Al-Refaie. and  Hala, Abedalqader. (2021). Optimal Quay Crane Assignment and Scheduling in Port's Container Terminals. Jordan Journal of Mechanical and Industrial Engineering, 15(2), 153-167.

[36] Lenstra, J.K.A.H.G,Rinnooy Kan. (1979).Computational complexity of discrete optimization problems. Ann. Discrete Math., vol. 4, 121–140.    https://doi.org/10.1016/S0167-5060(08)70821-5

[37] Lenstra, J.K. A.H.G,.Rinnooy Kan. (1981). Complexity of vehicle routing and scheduling problems. Networks, vol. 11, No. 2, 221–227. https://doi.org/10.1002/net.3230110211

[38] Askarzadeh,Alireza. (2016). A novel metaheuristic method for solving constrained engineering      optimization problems. Computers and Structures.169, 1– 12. https://doi.org/10.1016/j. compstruc.2016.03.001

[39] Oliva, Diego. , Salvador, Hinojosa. Erik, Cuevas. Gonzalo, Pajares. Omar, Avalos. Jorge, G«alvez. (2017). Cross entropy based thresholding for magnetic resonance brain images using Crow Search Algorithm. Expert Systems With Applications,79, 164-180. doi:10.1016/j.eswa.2017.02.042

[40] Sivarami Reddy, N. Dr.D.V,Ramamurthy. Dr. K, Prahlada Rao. and Dr. M, Padma Lalitha. (2017). Simultaneous Scheduling of Machines and Tools in Multi Machine FMS Using Crow Search Algorithm. International Journal of Engineering Science and Technology, 9(09S), 66–73.

[41] Sivarami Reddy,N. D.V,Ramamurthy. K,Prahlada Rao. (2018c). Simultaneous Scheduling of Machines and AGVs using Crow Search Algorithm. Manufacturing Technology Today, 17(09) ,12–22. ISSN: 0972-7396. www.i-scholar.in › index.php › MTT › search › authors › view › country=...

[42] Pankaj, Upadhyay. J.K, Chhabra.(2019). Kapur's entropy based optimal multilevel image segmentation using Crow Search Algorithm. Applied Soft Computing Journal105522, https://doi.org/10.1016/j.asoc.2019.105522.

[43] Anter Ahmed, M. Aboul Ella, Hassenian. Diego, Oliva.(2019).An improved fast fuzzy c-means using crow search optimization algorithm for crop identification in agricultural. Expert Systems With Applications, 118,340-354 doi: https://doi.org/10.1016/j.eswa.2018.10.009

[44] Spea Shaimaa, R. (2020).  Solving practical economic load dispatch problem using crow search algorithm. International Journal of Electrical and Computer Engineering (IJECE) , 10(4), 3431-3440

[45] Bilge,Ümit.Gündüz, Ulusoy.(1995).A time window approach to simultaneous scheduling of machines and material handling system in FMS. Operations Research, 43, 1058−1070. https://doi.org/10.1287/opre.43.6.1058

[46] Venkata Rao, R.(2016). Jaya: A simple and new optimization algorithm for solving constrained and unconstrained optimization problems. International Journal of Industrial Engineering Computations , 7, 19–34.

# Effect of Physical Parameters on the Outlet Temperature of the Shower Cooling Tower

## A. Asghari[1], N. Kordani [2*], A. Hallajisani[3]

*[1]Department of Mechanical Engineering Msc, Islamic Azad University, Nour Branch, Iran.*
*[2]Faculty of Mechanical Engineering, University of Mazandaran, Babolsar, Iran.*
*[3]Caspian Faculty of Engineering, College of engineering, University of Tehran, Tehran, Iran*

## Abstract

In the most industrial process and air conditioning systems, huge amount of heat are generated for better performance. The shower cooling tower (SCT) is used for heat transfer to the environment. In this study, mathematical modeling and tower behavior simulate based on the laws of heat and mass transfer. This is done after reviewing papers and rewriting governing differential equations using a computer program to solve numerical solution and then analyzing tower behavior. Also, the effect of physical parameters (the velocity of water droplet, inlet air velocity and water to air mass flow ratio) on reducing the outlet temperature of the water has been checked and compared with the results of the experiment, which has a great accuracy. Simulated data shows that, as the inlet air velocity increases, the corresponding heat and mass transfer coefficients increase, outlet temperature from tower decreases. Also due to the excessive increase in the droplet velocity, it does not have much effect on reducing the temperature of the outlet. By increasing the water to air mass flow ratio, decreasing of temperature is reduced.

## 1. Introduction

Free cooling techniques can be used to substantially reduce energy costs. During cold weather, the outside ambient temperature can help in saving energy in refrigeration systems (Al-Salaymeh and Abdelkader (2011)). Numerical simulation of time-dependent 2-dimensional forced convection flow over a pair of tandem circular cylinders in a rectangular channel has been carried out by Oyewola et al. (2019). This work suggests that in minimizing the vibration of the tubes and enhancing effective heat transfer by the heat exchangers, the aforementioned parameters and conditions should be taken into consideration.

Choosing the right cooling towers, requires complete recognition of the relevant parameters that will improve the thermal efficiency of the system. By knowing the exact performance of the tower in different conditions, investigating and providing operational conditions and optimal design, the cooling tower can save on water consumption, energy and maintenance costs. Investigating of SCT thermal performance is highly important. With rectification of the heat and mass transfer coefficients, and change in tower height, especially droplet diameter of the dots, one can increase the accuracy of the calculations relative to the other towers. The outlet temperature of water depends on the environmental conditions. By increasing environment temperature, the output temperature from the tower also increases. Therefore, changing the physical and geometric conditions can improve the outlet temperature of the tower.

At the beginnings of 19th century, lots of theories were devised to justify the transfer of heat and mass in evaporating water facility devices that have been invented, which are based on basic engineering rule. Cooling tower can be considered as a heat exchanger which water and air are in direct contact together. But no theoretical or experimental relation can precisely compute the total contact surface in a tower, to define a specific heat transfer coefficient for it. This problem becomes more complicated despite the phenomenon of mass transfer. Therefore, the design of the tower relies on a relationship that is confirmed by experiments and real examples. These relationships can be used to design or predict the tower's performance, if the design conditions change.

Over the past century, many researchers have studied the performance of cooling towers. The first practical step in solving the problem of direct current tower was taken by Merkel (1925). Merkel method was a combination of differential equations of mass transfer and air/water heat inside a tower.

A method was proposed by Suthedand (1997) in which an exact solution was used to solve the equations governing the cooling tower. Suthedand, in his model, considered the whole tower as a control volume, and

---

* Corresponding author e-mail: naser.kordani@umz.ac.ir.

adjusted its differential equations based on quantity changes from above to the bottom of the tower. In his model, he considered the effects of evapotranspiration of input water and assumed the factorial in the opposite tower. He solved the differential equations for his exact solution with the Tower A Program and the equations for the approximate computer solution, which was the same as the Merkel method with the program of Tower B solution was solved by Runge-Kutta (4th order) method. He also showed that neglecting the evaporation of water for the typical operating conditions of a sample in a tower could lead to further errors in higher ratios of water to air mass flow rates. For example, for water to air mass flow ratio equal to 2, it is 14%.

Wang and Nianping (2011) calculate mathematical equations of this type of Tower using of thermodynamic relations and examined the effect of various parameters on the thermal performance of these towers.

Asvapoositkul and Treeutok (2012) also investigated these towers operational in variable climate condition and obtain an accurate and simple equation compare to others.

SCT was first introduced and investigated by Givoni (1995). This tower consisted of a body (shell) with nozzles at the top and tank for collecting water at the end. In this tower, water from above was turned into fine droplets by spray nozzles, and along the path to the bottom of the tower. The Cooled air was also released from the top of the tower, Givoni and Al Hemiddi examined this tower in Riyadh, Saudi Arabia. with a maximum inlet air temperature 45 °c and relative humidity 50%, a drop in temperature of 16 °c. Satoshi and Givoni (1997) studied the thermal performance of SCT in japan. They measured inlet and outlet condition of air with respect to change in water flow in different time of the day in various heights. They showed that outlet air temperature depends on tower height, ambient condition, water flow, and distributer's types. He also investigated height and water flow effect on air temperature reduction of tower's used as air conditioner, and indicates that temperature reduces extremely in height less than 0.5 m. But with increase in height, outlet temperature reduction will decrease. Experimental investigations have been done to understanding these towers, but also they may not present a practical theory to study the system and predict result in mathematical equation [8]. Although by that time, no numerical analysis for the study of these systems was available, Xiaoni and his coworkers (2007) suggested one dimensional model, heat and mass Transfer (HMT) with experimental data and rules based on heat and mass conservation, to study water droplet displacement, so they study tower behavior.

Muangnoi and coworkers (2014) studied physical and geometrical parameter on the SCT and stated that the change in initial droplet diameter was the most, and that water velocity had the least effect.

In SCT (opposite current), sprayed water droplets exchange their thermal energy with cold water, so with increase area, heat exchange between the water droplets and air will increase, and increasing the height and exchange time as a result, the output temperature decreases.

Zunaid (2018a, b) investigated the effect of variation in air relative humidity and inlet water to air mass flow ratio on outlet temperature of SCT. The thermal efficiency of SCT increases with increasing the inlet air relative humidity and decreases with increasing the water to air mass flow ratio.

Anbazhaghan and his coworkers (2021) presented a two-dimensional model of water droplet collision to reduce errors in Xiaoni models.

Previous research conducted on the performance of a shower cooling tower has not considered the effect of physical parameters. So it is possible to improve outlet temperature and operation time with appropriate design (the velocity of water droplet, inlet air velocity and water to air mass flow ratio) depending on ambient condition.

## 2. Mathematical model and Governing Equations on SCT

Assumptions:
1. The Lewis factor is equal to one
2. Physical properties of the water are the same in hot and cold temperature
3. The water droplet moving in the tower act in the shapes of ball
4. The whole motion direction of the water droplet is vertical. It is assumed that the water droplet rises or falls vertically in one dimension.
5. The radiation heat transfer is ignored because of the small temperature difference.

For better checking of shower cooling tower performance, it is best to first study of heat and mass transfer at the surface of the drop of water. Movement acceleration, turbulence value, internal circulation and evaporation of water droplets have important effects on the performance of SCT.

### 2.1. Droplet velocity analysis during SCT

The droplets of water sprayed from the nozzle in a spherical and even form, eliminate droplet collisions, dispersal along the path, and non-uniformity of the flow. For a better understanding, consider a drop of water as shown in Figures 1 and 2.

The forces that enter the drop are: gravity, floating force, and air resistance

$$G_d = m_d g = \frac{\pi d_d^3 \rho_w g}{6} \tag{1}$$

$$F_d = \frac{\pi d_d^3 \rho_a g}{6} \tag{2}$$

$$R_d = \frac{\pi C_d \rho_a d_d^2 U^2}{8} \tag{3}$$

In equations 1-3, $C_d$ (drag coefficient) is equal to:
For laminar flow
$$C_d = \frac{18.5}{\text{Re}^{3/5}}$$
$$0.9169 \le \text{Re} < 508.3917$$
For turbulence flow
$$C_d = 0.44$$
$$\text{Re} \ge 508.3917$$

It was used Newton's second law definition (for the direction of power to be considered as positive):

$$a_d = \frac{\sum F}{m_w} = \frac{G_d - F_d - R_d}{m_w}$$

$$U_d = dz/dt \; ; \; a_d = \frac{du_d}{dt} = u_d \frac{du_d}{dz} \tag{4}$$

The equations given can be combined to obtain the kinetic equation for water droplets in the SCT:

$$\rho_w u_d \frac{du_d}{dz} = (\rho_w - \rho_a)g - 3C_d \rho_a (u_d - u_a)^2 / 4d_d \tag{5}$$

### 2.2. Analyses of enthalpy changes, temperature and humidity during SCT

The internal energy of a drop in the system changes with the loss of the amount of latent and tangible heat. For this purpose, that was considered a tower of height H and divide it into N equal to the thickness of dz. For a better understanding, a volumetric element was considered considering mass and heat transfer (Figure 2).

Total heat transfer at the common climate level, including heat transfer due to evaporation and transfer of heat.
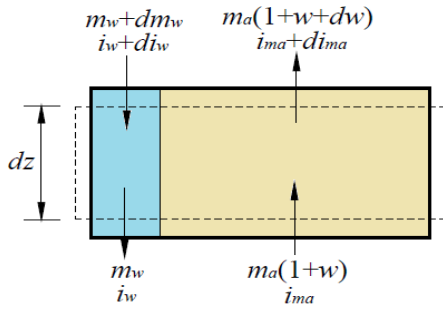


**Figure 1.** Volume control SCT (Xiaoni et. al (2008c))

Mass balance for the control volume is equal to:

$$dm_w = m_a dw \tag{6}$$

Energy balance for the control volume is equal to:

$$m_a di_{ma} = m_w di_w + i_w dm_w \tag{7}$$

In the above equation $i_w$ is air enthalpy and $i_{ma}$ is a enthalpy of the mixture of water and air.

The water flow that is directly in contact with the air involves a transient and tangible heat loss. The latent transmission is due to the evaporation of water and the transmission of tangential effects due to temperature differences.

$$dQ = dQ_c + dQ_e \tag{8}$$

The hidden and sensible heat is equal to:

$$dQ_c = h_c (T_w - T_a) dA$$

$$dQ_e = i_v h_d (w_{sw} - w_a) dA \tag{9}$$

The temperature difference in the equation can be replaced by enthalpy variations. The enthalpy of the saturated air at the local temperature is shown below:

$$i_{masw} = c_{pa} T_w + w i_v + (w_{sw} - w) i_v \tag{10}$$

The enthalpy of vapor mixtures for dry air units can be calculated as follows:

$$i_{ma} = c_{pa} T_a + w (i_{fgw0} + c_{pv} T_a) \tag{11}$$

$$T_w - T_a = \frac{(i_{masw} - i_{ma}) - (w_{sw} - w) i_v}{c_{pma}} \tag{12}$$

$$dQ = h_d \left[ \frac{h_c}{h_d c_{pma}} (i_{masw} - i_{ma}) + \left(1 - \frac{h_c}{h_d c_{pma}}\right) i_v (w_{sw} - w) \right] dA \tag{13}$$

With factorization from $h_d$ and Louis factor equal to one we have:

With replacing upon equations for enthalpy differences:

$$\frac{d_{ima}}{dz} = \frac{dQ}{m_a} = \left(\frac{m_w}{m_a}\right) \frac{6h_d}{\rho_w u_d d_d} (i_{masw} - i_{ma}) \tag{14}$$

The mass change of a drop is equal to the amount of mass transfer from the droplet to the air.

$$dm_d = h_d A_d (w_{Tw} - w_a) dA_d \tag{15}$$

By setting the mass of the droplet according to (1) and the area of the sphere $(A_d = \pi d_d^2)$ in the equation 15, the equation of moisture change is obtained which is equal to.

$$\frac{dw_a}{dz} = \left(\frac{m_w}{m_a}\right) \frac{6h_d}{\rho_w u_d d_d} (w_{Tw} - w_a) \tag{16}$$

$h_d$ is mass transfer coefficient in equation 16.

$$h_d = h_c / (cp_a + w_a cp_v) \tag{17}$$

$$h_c = \frac{k_a \times Nu_d}{d_d}$$

Internal energy differences is equal to summation of sensible heat due to temperature difference and latent heat due to water evaporation.
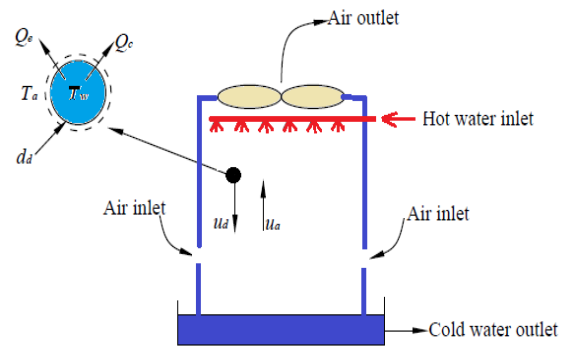


**Figure 2**. Energy transfer in droplet surface (Xiaoni et. al (2008c))

Sensible heat is equivalent to:

$$\frac{dU_d}{dt} = -(Q_{dc} + Q_{de}) \tag{18}$$

$$Q_{dc} = h_c A_d (T_w - T_a) \tag{19}$$

Latent heat is obtainable from following equation:

$$Q_{de} = h_d A_d (w_{Tw} - w_a) i_v \tag{20}$$

Internal energy is equal to:

$$dU_d = -\left[ h_c A_d (T_w - T_a) + h_d A_d (w_{Tw} - w_a) i_v \right] \tag{21}$$

$$m_d c_{pw} dT_w = -A_d h_d \left[ \frac{h_c}{h_d} (T_w - T_a) + i_v (w_{sw} - w_a) \right] \tag{22}$$

$$m_d c_{pw} dT_w = -A_d h_d (i_{masw} - i_{ma}) \tag{23}$$

Temperature difference equation is obtainable with replacing mass and droplet area:

$$\frac{dT_w}{dz} = \frac{-6h_d}{cp_w \rho_w u_d d_d} (i_{masw} - i_{ma}) \tag{24}$$

*2.3. Droplet diameter changes in the SCT*

Droplet mass variations in dz is:

$$m_d = h_d A_d \left( w_{Tw} - w_a \right)$$

$$dm_d \frac{u_d}{dz} = h_d \left( w_{Tw} - w_a \right) d_A \qquad (25)$$

With replacing mass equations and droplet cross section area in equation, change of droplet diameter has been obtained.

$$\frac{d\left( d_d \right)}{dz} = \frac{6h_d}{\rho_w u_d} \left( w_{Tw} - w_a \right) \qquad (26)$$

## 3. Analysis of the results

Physical parameters (drop velocity, inlet air velocity, and flow ratio) are investigated with changes in environmental conditions and assuming that the geometric parameters (droplet diameter and nozzle height) are constant, because the environmental parameters are different for different climates.

**Table 1.** Ambient and geometrical parameter range in SCT

| Nozzle height (m) | 10 |
|---|---|
| Droplet diameter (mm) | 0.8 |
| Dry bulb temperature (°C) | 25-35 |
| Relative humidity (%) | 20-80 |
| Water inlet temperature (°C) | 50 |

*3.1. Droplet initial velocity investigation in SCT*

The analysis of the graphs in Figures 3 and 4 shows that the effect of the initial velocity of droplet spray on the decrease in the outlet temperature is not significant, as it is obvious that the droplet reaches its limit velocity after a period of time and then moves at a constant velocity. So that the droplet velocity is high at the beginning of the nozzle and is constant from a height of 3 meter to the end, which is approximately the same for the different relative humilities.

Increasing the droplet velocity causes the droplet to reach the end of the tower faster. In this case, there is not enough time to exchange heat (water to air), or in other words, the droplet does not have enough time to transfer heat during the time of movement (first to the end of the tower). On the other hand, slowing down will cause a large amount of water droplets to drop out of the tower due to air velocity, which will increase the evaporation rate.
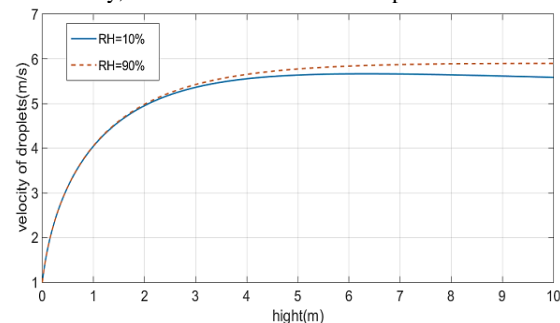


**Figure 3**. The droplet velocity related to height diagram with initial velocity 1m/s (tower height 10 m, water to air mass flow ratio 1.2, inlet air velocity 2 m/s, droplet diameter 0.8mm, inlet water temperature 50 °C and dry bulb temperature is 25 °C).
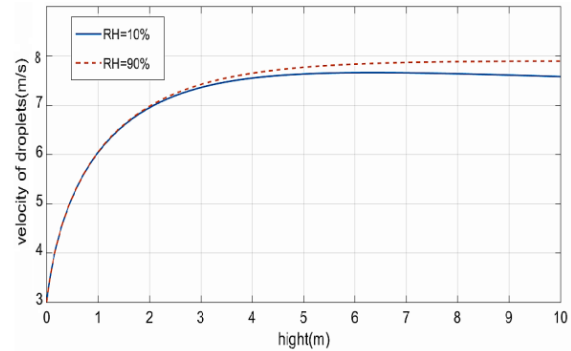


**Figure 4**. Droplet velocity-height diagram with initial velocity 3 m/s (nozzle height 10 m, water to air mass flow ratio 1.2, inlet air velocity 2m/s, droplet diameter 0.8 mm, inlet water temperature 50 °C and dry bulb temperature is 25 °C)

By comparing these diagrams, it is evident that with increasing initial velocity of the droplet, the temperature of the outlet of the water increases. As the input velocity increases, the durability time decreases and droplet exchange rate decreases along the tower. In this case, the output temperature is increased according to the diagram. Of course, the temperature increase is negligible. On the other hand, due to the increased durability of the droplet along the tower, the rate of evaporation increases. The values of water temperature output at various velocities are given in Table 2.

**Table 2.** Droplet velocity effect on outlet water temperature (°C)

| Droplet initial velocity (m/s) Relative humidity (%) | 1 | 2 | 3 | 4 | 5 |
|---|---|---|---|---|---|
| 25% | 33.3 | 33.5 | 33.7 | 33.9 | 34.2 |
| %50 | 34.3 | 34.5 | 34.7 | 34.9 | 35.3 |
| 80% | 35.6 | 35.8 | 36 | 36.1 | 36.4 |

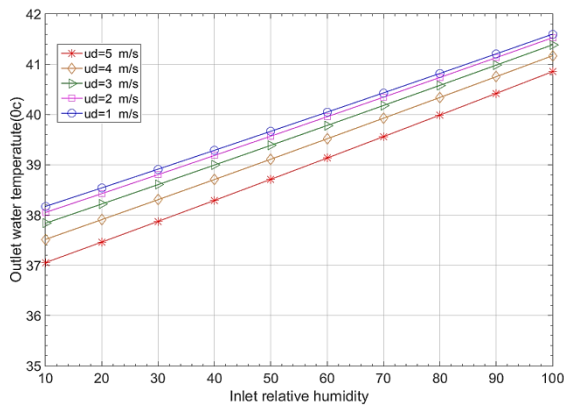*3.2. Effect of air velocity in SCT*

As the air velocity increases, the temperature of the air outlet from the tower decreases. Heat and mass transfer coefficients are directly related to the Reynolds number. Therefore, increasing the inlet air velocity, the coefficients of mass transfer and heat increase. Then the heat exchange rate increases and causes a decrease of the outlet temperature of the tower. In higher velocities, temperature drop rate is increasing.

By increasing the temperature of the dry bulb, the difference in temperature decreases (the temperature difference between the dry bulb and the inlet water). In this case, the tangible heat transfer is reduced, but the temperature difference between the dry bulb and the wet bulb is increased. As the relative humidity increases, in addition to the tangible heat transfer, the latent heat transfer is also increased. Therefore, the increase in the air flow rate will lose its effect on reducing the output temperature. As a result, by increasing of relative humidity, reducing the temperature of the outlet water from the SCT is less. In fact, the graphs of figure 6 have a greater slope than figure 5. If the temperature of the dry

bulb increases, so that the temperature of the dry bulb is equal to the inlet water temperature (50 °C), then the temperature drop rate in relative humidity above 95% is approximately zero.
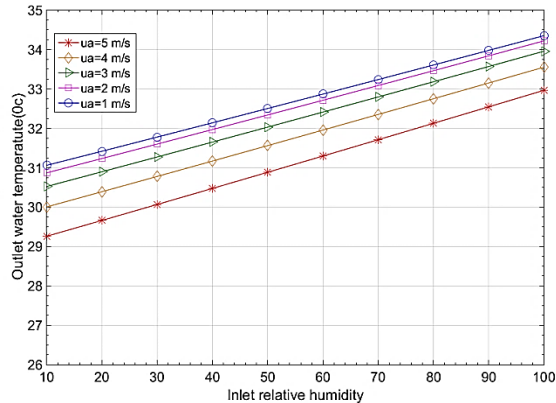


**Figure 5**. Effect of air velocity on outlet water temperature with dry bulb temperature 25 °C (nozzle height 10 m, water to air mass ratio 1.2, droplet velocity 2m/s, droplet diameter 0.8mm, inlet water temperature 50 °C)



**Figure 6**. Effect of air velocity on outlet water temperature with dry bulb temperature 35 °C (nozzle height 10 m, water to air mass ratio 1.2, droplet velocity 2 m/s, droplet diameter 0.8mm, inlet water temperature 50 °C)

Figure 8 shows that with increase of the inlet air temperature, reduction in tower outlet temperature is more. In fact, the decreasing rate of outlet temperature is more, when the inlet air velocity is increased from 4 to 5 m/s in compare with increasing of inlet air velocity from 1 to 2 m/s due to the square power of the velocity in the Reynolds number.

Considering that increasing of inlet air velocity causes decreasing of the outlet water temperature, but increasing of velocity increase evaporation rate.

Tables 3 and 4 shows decreasing rate of outlet temperature from the SCT in different droplet diameter and height. As nozzle height increase, the temperature reduction rate is increased. By increasing of droplet diameter, the temperature reduction rate is decreased. Also shows that by increasing of inlet air velocities, the temperature reduction rate is increased. This is more at the

higher velocities. The temperature difference is negligible for lower velocities.

### 3.3. The effect of mass flow ratio in SCT

As it is known, with the increase of the mass flow ratio, the temperature drop decreased. (The outlet water temperature of the SCT increases). The greater proportion of flow ratio causes decreasing of temperature drops. The role of air exchange between the droplets and the environment. So by increasing of flow ratio, the amount of water ratio increases, or the air ratio decreases. As a result, more droplets spray from nozzles. Therefore, the amount of air exchange with droplets decreases, so outlet temperatures will be increased more. By increasing of the relative humidity, the temperature reduction rate is decreased, or in the other word the temperature of the outlet water from the tower increases.
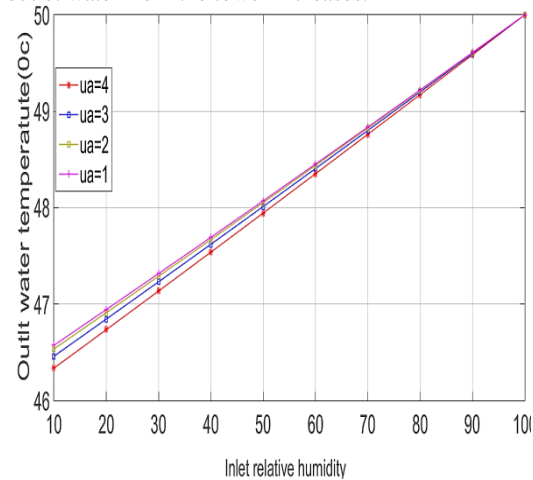


**Figure 7.** Effect of air velocity on outlet water temperature with dry bulb temperature 50 °C (tower height 10 m, water to air mass flow ratio 1.2, droplet velocity 2 m/s, droplet diameter 0.8 mm, inlet water temperature 50 °C).
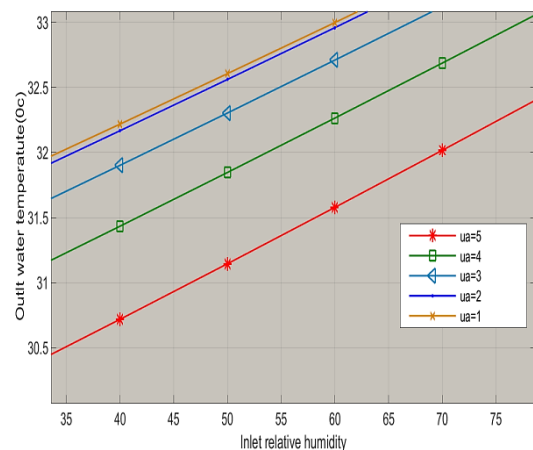


**Figure 8**. The effect of air velocity on the outlet water temperature with dry bulb temperature 25 °C
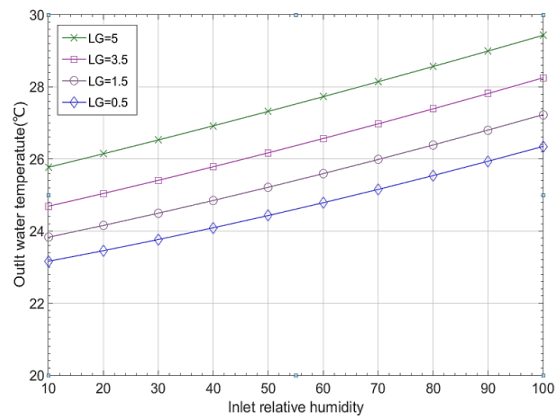
**Figure** 9. Effect of water to air mass flow ratio in the outlet temperature from the tower according to relative humidity (tower height 10 m, water to air mass flow ratio 1.2, droplet velocity 2 m/s, droplet diameter 0.8 mm, inlet water temperature 50 °C)

As shown in figure 9, with raise in mass flow ratio from 0.5 to 1.5, outlet temperature reduction is less than 0.6 °C and for mass flow ratio from 3.5 to 5 outlet temperature reduction is 1.2 °C. As a result, it's clear that in flow ratio more than 1.5, temperature reduction is more.

*3.4. Comparison between numerical and experimental results:*

Xiaoni and colleagues (2008a, b) have tried to study new methods that are capable of quick and easy estimation of the outlet temperature and are more accurate than the previous model. Therefore, attempts are made to assist the statistical relationships of the logical connection between the input and output variables (output water temperature) so that, with experimental data, we can estimate the temperature of the output water. This method is called

Projection Pursui Regression (PPR), which is very good accurate in comparison with the proposed model based on Heat and Mass Transfer (HMT) equations. However, this model is not an alternative model with HMT, because the accuracy of the output results in the PPR methods are related to the input data. The results of this study have been compared to 5 other samples that has been done by Xiaoni et. al (2008c), and the results are shown in Table 5 and Figure 10.

According to Table 5, the results obtained from this study are very close to experimental results and have a better accuracy than the numerical HMT method that has been done by Xiaoni et. al (2008c). With a slight change in inputs (changes in physical conditions), the accuracy of the results can be improved. As shown in Table 5 and Figures 10, it is clear that the results of this study, with the change in physical conditions than the PPR, are also more accurate, which can improve the results by decreasing of droplet velocity.
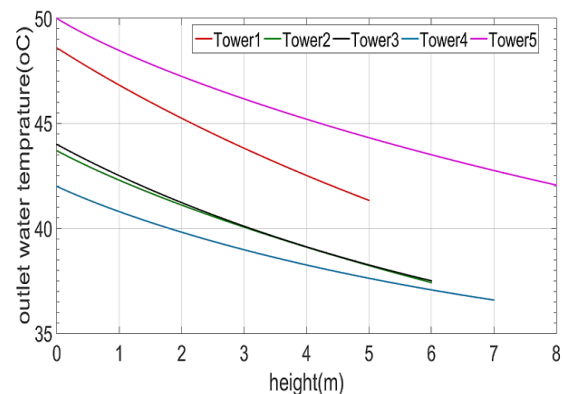


**Figure 10**. Outlet temperature diagrams from SCT according to height

**Table 3**. Outlet temperature from SCT for cold and dry climate (water to air mass flow ratio 1.2, droplet velocity 2 m/s, inlet water temperature 50 °C)

| Means of $T_{a(dry)}$ °C | Means of Relative Humidity (%) | Air velocity (m/s) | H=8(m) | | | H=10(m) | | |
|---|---|---|---|---|---|---|---|---|
| | | | d(mm) | | | d(mm) | | |
| | | | 0.7 | 0.8 | 1 | 0.7 | 0.8 | 1 |
| | | | $T_{w(out)}$ °C | | | | | |
| 35 | 38 | 1 | 35.5 | 36.8 | 39.4 | 34.5 | 35.6 | 38.1 |
| | | 2 | 36 | 37.3 | 39.9 | 35 | 36.1 | 38.7 |
| | | 3 | 36.3 | 37.7 | 40.1 | 35.3 | 36.4 | 39 |
| | | 4 | 36.5 | 37.8 | 40.2 | 35.5 | 36.6 | 39.2 |
| | | 5 | 36.5 | 37.8 | 40.2 | 35.6 | 36.7 | 39.3 |

**Table 4.** Outlet temperature from SCT for warm and dry district (water to air mass flow ratio 1.2, droplet velocity 2 m/s, inlet water temperature 50 °C)

| Means of $T_{a(dry)}$ °C | Means of Relative Humidity (%) | Air Velocity (m/s) | H=8(m) | | | H=10(m) | | |
|---|---|---|---|---|---|---|---|---|
| | | | d(mm) | | | d(mm) | | |
| | | | 0.7 | 0.8 | 1 | 0.7 | 0.8 | 1 |
| | | | $T_{w(out)}$ °C | | | | | |
| 29 | 63 | 1 | 31.7 | 33.4 | 37.1 | 30.4 | 32 | 35.4 |
| | | 2 | 32.4 | 34 | 37.7 | 31 | 32.6 | 35.9 |
| | | 3 | 32.8 | 34.4 | 37.9 | 31.4 | 33 | 36.2 |
| | | 4 | 33.1 | 34.6 | 38 | 31.6 | 33.3 | 36.4 |
| | | 5 | 33.1 | 34.6 | 38 | 31.7 | 33.4 | 36.5 |

427

**Table 5.** Comparison between numerical and experimental results of references and this research

|  | SCT 1 | SCT 2 | SCT 3 | SCT 4 | SCT 5 |
|---|---|---|---|---|---|
| Nozzle height (m) | 5 | 6 | 6 | 7 | 8 |
| Droplet diameter (mm) | 1 | 1.1 | 0.8 | 0.8 | 1.1 |
| Droplet initial velocity (m/s) | 2 | 2.4 | 2.5 | 2.3 | 2 |
| Inlet air velocity (m/s) | 6 | 5 | 6 | 5 | 4 |
| Air to water ratio | 0.8 | 1 | 0.9 | 0.9 | 0.8 |
| Relative humidity (%) | 69 | 74 | 70 | 68 | 78 |
| Dry bulb temperature (°C) | 48.6 | 43.7 | 44 | 42 | 69 |
| Testing results (°C) | 40.2 | 37.3 | 37.8 | 36.2 | 43.7 |
| Result with HMT method (°C) | 40.9 | 37.7 | 38.1 | 36.7 | 44.3 |
| Result with PPR method (°C) | 39.8 | 36.9 | 38 | 36.3 | 43.3 |
| This research result (°C) | 41 | 37.2 | 37.5 | 36.5 | 42.1 |

**Table 6.** Results of this research by change of droplet and inlet air velocity (other parameters according to table 5)

|  |  | SCT 1 | SCT 2 | SCT 3 | SCT 4 | SCT 5 |
|---|---|---|---|---|---|---|
| Physical parameter as table 5 | Droplet initial velocity (m/s) | 2.2 | 2.4 | 2.5 | 2.3 | 2 |
|  | Inlet air velocity (m/s) | 6 | 5 | 6 | 5 | 4 |
| New physical parameter | Droplet initial velocity (m/s) | 3.5 | 3 | 3.3 | 3 | 3.9 |
|  | Inlet air velocity (m/s) | 3.7 | 2.8 | 3.7 | 2.7 | 2.9 |
| This research results (°C) |  | 40.9 | 3.9 | 3.7 | 36.2 | 41.7 |
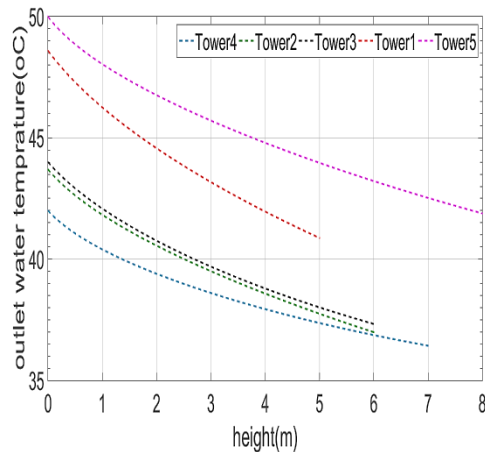


**Figure 11.** Outlet temperature diagrams from SCT according to height by applying changes in physical condition (table 6)
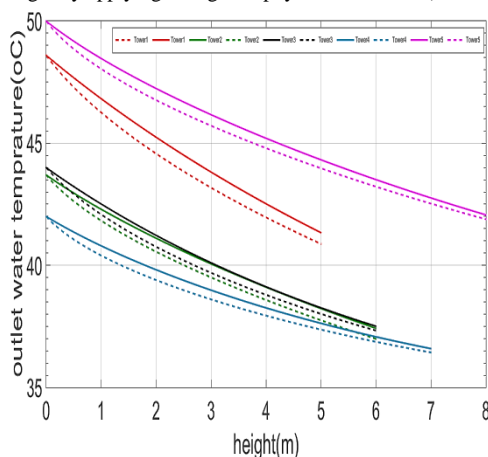


**Figure 12**. Outlet temperature diagrams from SCT according to height based on table 5 and by applying changes in physical condition

## 4. Conclusion

In this paper, mathematical models and computer program have been applied for physical parameter using HMT process. After analyzing and reviewing the results of the references, the findings of this research have been compared with the PPR statistical method that has fine precision. We find that the results can be improved by changing the physical conditions, because the high velocity of the droplet causes decreasing in droplet life time in the tower. In this case there is not enough time for heat transfer (water to air) or in other words, the droplet does not have enough opportunity to transmit heat during the movement time (first to the end of the tower), and the rise of the inlet air velocity causes an increase of evaporation rate. The overall conclusion is as follows:

1. Heat exchange from water evaporation increases with rising of flow ratio and causes increase of temperature reduction rate. By increasing of flow ratio (water flow increase or air flow decreases), temperature reduction rate increases.
2. With increasing of inlet air velocity, which corresponds to those heat and mass transfer coefficient increased, the output temperature of the tower decreases.
3. Whatever the velocity of the inlet air increases, the outlet temperature from the tower decreases.
4. In high relative humidity the latent heat transfer will reduce, and heat transfer mechanism will be tangible heat transfer. So the temperature drop will be less in comparison with lower relative humidity. As a result, with increasing of the relative humidity, the outlet water temperature increases.
5. With decreasing droplet velocity, the temperature reduction rate increases because the durability in the tower increases.
6. Droplet velocity is high at the beginning of the nozzle and is constant from heights of 3 m, which is the same for the different relative humidities.

## References

[1] Al-Salaymeh, A. and M.R. Abdelkader, (2011). Efficiency of Free Cooling Technique in Air Refrigeration Systems. Jordan Journal of Mechanical and Industrial Engineering, 5(4), 325-333.

[2] Asvapoositkul, W. and S. Treeutok (2012 May). A simplified method on thermal performance capacity evaluation of counter flow cooling tower. Applied Thermal Engineering 38, 160-167.

[3] Anbazhaghan, N. Karthikeyan, A. Jayaraman Jayaprabakar & Prabhu Appavu (2021): Assessment on effectiveness of a shower type cooling tower, International Journal of Ambient Energy, DOI: 10.1080/01430750.2021.1874520

[4] Givoni, B. and N. Al Hemiddi (1995). Applicability of a "Shower" Passive Cooling Tower in Hot Dry Climate. 20th National Passive Solar Conference, Minneapolis United State, 143-148.

[5] Merkel, F (1925). VerdunstungskfJhlung, VDI Forschungsarbeiten, No. 275, Berlin.

[6] Muangnoi, T., W. Asvapoostikul, and P. Hungspreugs (2014). Performance Charactrisics of A Downward Spray Water-Jet Cooling Tower. Applied Thermal Engineering, 69(1), 165-176.

[7] Oyewola, O.M., Ismail, O.S. and K. Abu, (2019). Numerical Simulation of Forced Convection Flows over a Pair of Circular Cylinders in Tandem Arrangement. Jordan Journal of Mechanical and Industrial Engineering, 13(4), 221-230.

[8] Parpanji, F (2016). Stimulation of Cooling Towers. MSC thesis. Tehran University, Tehran, Iran.

[9] Satoshi, Y., and B. Givoni (1997). EXPERIMENTAL PERFORMANCE OF THE SHOWER COOLING TOWER IN JAPAN. Renewable Energy IO (213), 179.-183.

[10] Suthedand, J. W. (1997). Analysis of mechanical draught counter flow air/water cooling towers. Trans ASME, J Heat Transfer 10(2-3), 179-183.

[11] Wang, Li. and Li. Nianping (2011). Exergry transfer and parametric study of counter flow wet cooling tower. Applied Thermal Engineering 31(5), 954-960.

[12] Xiaoni, Q., L. Yongqi and L. Zhenyan, (2008a). Numerical simulation of shower cooling tower baced on artificial network. Energy Conversion and Management 49 (4), 724-732.

[13] Xiaoni, Q. and L. Zhenyan (2008b). Further investigation on the performance of a shower cooling tower. Energy Conversion and Management 49, 570-577.

[14] Xiaoni, Q., L. Zhenyan, L. Dandan, (2008c). Prediction of the performance of a shower cooling tower based on projection pursuit regression. Applied Thermal Engineering 28(8-9), 1031-1038.

[15] Xiaoni, Q., L. Zhenyan, and L. Dandan (2007). Performance characteristics of a shower cooling tower. Energy Conversion and Management 40(1), 193-203.

[16] Zunaid, M., (2018). Energy and Second Law Analysis of Shower Cooling Tower Used for Air Cooling Application for Human Comfort with Variation in Water to Air Mass Flow Ratio. International Journal for Research in Applied Science & Engineering Technology, 6(3), 1302-1311.

[17] Zunaid, M., (2018) April - CFD Analysis of Shower Cooling Tower with Varying the Inlet Air Relative Humidity for Industrial Application, International Journal for Research in Applied Science & Engineering Technology, 6(4), 1523-1525

# Modeling of Natural and Hybrid Ventilation System in the Building of High Heat Gains

Sylwia Wciślik[*], Katarzyna Stokowiec

*Kielce University of Technology, Faculty of Environmental Engineering, Geomatics and Power Engineering, Kielce, Poland*

## Abstract

Hybrid ventilation systems present many advantages compared to the natural or mechanical ventilation systems. In the case of buildings with significant heat gains, they seem to be the proper solution, if correctly analyzed and designed. The paper presents the calculations and study of the natural ventilation parameters with the possibility of including roof fans in the model glasswork in Kielce, Poland. The calculations for the optimization process were conducted using Ventos software. The limitations of the method include maximal values of air temperature at the top of the building, air velocity at the inlets and outlets, and negative pressure. Conclusions for the summer season arise that the most optimal solution ensuring the minimum internal temperature and air velocity conditions for the glassworks building is the use of wall inlets located on two levels. On the other hand, in winter conditions not all wall intakes should be open. Further analyses and simulations were performed for hybrid ventilation. Assessments confirm the accuracy and efficiency of using natural ventilation in facilities with significant heat gains, including glassworks.

## 1. Introduction

Building ventilation is observed to have a growing interest as a crucial aspect in each building project. The essence of installing such a system depends on its purpose: control of indoor air quality or improving summer comfort. The optimization problem differs varying from its concept. In case of indoor air quality control, the challenge appears during heating periods. The cooling demand is to achieve an optimal balance between air comfort needs and energy use. Whereas ventilation as part of a strategy of energy efficient cooling requires maximization of the air flow rates without creating comfort problems.

High heat gains are often properly associated with industrial building, where the managed process involves adequate equipment as well as environment with temperatures above $35^0$C. Such working conditions are highly probable to cause both sudden as well as chronic health issues. Some of the existing buildings were constructed in order to support the technology, disregarding the systems that are supposed to provide thermal comfort for the employees. The visible discomfort may cause unwelcome physiological reactions such as heatstroke or fainting [1]. Not only the working conditions are of high importance. Buildings, especially with great heat gains, contribute to the energy consumption with Heating, Ventilations and Air Conditioning systems as elements that impact on anthropogenic climate change.

In case of high heat gains buildings, the solution to decrease the influence of high internal temperature appears to be hybrid ventilation, which may present a whole range of systems such as [2]:

- switching in time between natural ventilation and mechanical ventilation
- mainly a natural ventilation system (with support of mechanical ventilation if the pressure differences are not enough)
- mainly a mechanical ventilation system (with support of natural ventilation if the available natural forces are optimal).

The research conducted in the area of hybrid ventilation has increased [3]. But still, the number is relatively small, therefore the studies in this field seem to be a promising investigation. The trends discuss mostly thermal comfort internal air quality and numerical simulation.

The improvement of thermal parameters inside the building includes a well-designed ventilation system. The ventilation method that is widely applied [4] as well as easily employed in case of ventilation modernization is hybrid ventilation. This system creates a uniform air temperature as well as constant pollutant concentration by means of mixing flowing outdoor and indoor air. The hybrid ventilation system may work in two modes. The natural ventilation system is suitable when the outdoor air temperature is sufficient to obtain proper density differences. Therefore, this solution uses less energy than mechanical ventilation since the mechanical ventilation

---
* Corresponding author e-mail: sylwiazw@tu.kielce.pl.

mode in hybrid ventilation concept is applied only to compensate

for the shortcomings of natural ventilation by making the wind velocity adjustable. On the other hand, hybrid ventilation is less challenging than the natural one, since it relies on outdoor air conditions which need to be better than the indoor ones in terms of temperature, humidity and contaminants levels. Gravitational ventilation is subject to good wind speed and direction to enable an effective air flow through the building. The still pressure coefficient and normalized turbulent kinetic energy strongly influence natural ventilation [5].

The most appropriate for hybrid ventilation were discussed to be warm temperate climates [6]. They present a good alignment between buildings cooling needs and the mildness of the climate. An effective building operation is also obtained by means of well-managed methods for control of hybrid ventilation system that usually includes classical control methods. In case of temperate climates, the hybrid ventilation may save operational costs: even up to 60 (offices) -70% (schools), whereas in hot arid around 50% or warm humid only 28% [7]. In temperate climates, the strategy is generally achieved by maximizing natural ventilation. In dry tropical climates, potential savings are gained by implementing a cooling strategy.

Hybrid ventilation is widely researched in case of residential buildings. A possible solution suggested is a compilation of air intake through automatically regulated louvers in bedrooms and living rooms, both natural and mechanical exhaust: natural exhaust in bathrooms and fan exhaust systems in kitchens. The experiments in Portugal proved that such systems may provide adequate ventilation rates. PMV and PPD factors indicated that the operative temperatures satisfy the thermal requirements [8]. In multi-residential building, highly favorable are systems with the control strategy that maximizes the use of natural ventilation when outdoor conditions are optimal [9]. In Latvia hybrid ventilation system is proposed not only for new residential buildings but also during renovation processes [10].

The performance of a hybrid ventilation system with heat recovery for low-energy buildings with solar collectors and heat pump indicated many advantages of such a system [11]. In general, the system is based on natural ventilation with a fan utilization when natural driving forces are not sufficient. The heat of the exhaust air is recovered in an air-to-water heat exchanger and the heated water is applied to preheat the fresh air. Also, the system strongly reduces energy consumption due to the usage of sewage tank, where the sewage water from showers, sinks, washing machine etc. is stored temporarily. The heat recovered from the sewage system with solar energy is used to heat the ventilation air and preheat the cold water for domestic use. All the novel methods make the entire system more efficient than the traditional fan-assisted hybrid ventilation.

The solar adsorption refrigeration system was also evaluated experimentally and theoretically as a solar cooling system [12]. Analysis also includes determination of the duct layout, and the size of ducts in high-rise buildings [13]. The process was validated with network simulation performed in the 20-storey building.

Apart from residential buildings, the study also includes a comprehensive school in Helsinki [14]. Improvement of fan-assisted hybrid ventilation system allowed a decrease in concentration of indoor-generated pollutants. Innovative methods of hybrid ventilation may be also introduced in hospitals [15]. These solutions could be applied in most climate conditions and present high flexibility, and energy saving.

The experiments were also conducted for Chinese conditions for hybrid ventilation and proved thermal comfort for different outside conditions, since PMV index is between -0.5 and 0.5 [16].

In case of a multi-heat-source industrial plant a buoyancy-driven hybrid ventilation system was investigated and the effects of the above-floor inlet height and exhaust velocity were analyzed [17].The results of study indicated that properly increasing the above-floor inlet height can improve the working area thermal environment with the optimal above-floor inlet height was identified at 1.2 m.

Hybrid ventilation system may be equipped with a heat exchanger. The measurements results show the possibility to develop a ventilation system driven by natural forces including heat recovery [18]. The experiments include analysis of earth-to-air heat exchanger technology. They proved that new model are required for hybrid ventilation, since the existing ones are not appropriate to simulate such conditions [19]. The hybrid ventilation, with cold water circulating through the internal heat exchanger, managed to cool incoming air with temperatures of 25 to 35°C down to a comfortable 20°C [20]. It can be added that in such ventilation systems heat can be efficiently recovered using e.g. phase - change heat changers [21]. Another study develops a solar-driven hybrid ventilation system suitable for use in domestic buildings or classrooms with a wall-mounted convector unit that distributes fresh outside air heated or cooled with water circulating in a coil. This allows a constant supply of clean, filtered, conditioned air. The renewable energy sources are used to provide the cooling and heating of water [22].

An example of rooms with significant heat gains are bathrooms in glassworks, with bath and shift furnaces (glass melting tanks). Glass is made by melting, at a temperature of 1573°C, soda - sodium carbonate, $Na_2CO_3$, quartz sand $SiO_2$ and calcium carbonate $CaCO_3$, and then rapid cooling of the product. The general technological cycle related to the production of glass is presented in Figure 1. At each stage, there are different phases characterized by variable conditions of temperature, atmosphere and gas pressure.

In large-scale hall-type facilities - which include, among others glass and metal works, waste incineration plants and power plants - the burden of technological heat gains is often a significant problem, especially during the operation of plants in the summer. On one hand, we want to provide relatively optimal conditions for thermal comfort for employees, on the other hand, we should take into account the permissible operating temperature of the roof structure. If it is exceeded, it may cause material fatigue due to the deformation of nodes of light steel structures, which are very popular nowadays [23, 24]. As it turns out, the best and optimal solution to remove the air polluted with heat in such facilities is natural or hybrid

431

ventilation. This is the result of the required significant amount of air changes, in the order of 30÷40 l/h, and thermal draft, which eliminates the influence of horizontal air movements - wind - caused by the pressure difference and differences in the shape of the surface.

Literature studies rarely deal with the subject of ventilation in industrial buildings with significant dimensions and heat gains. Therefore, the article aims to mainly optimize the operation of natural ventilation in a model glassworks located in Kielce, 50.87°N / 20.63°E / 274 m above sea level (Poland) that belongs to the $II^{nd}$ climatic zone of the summer period, as shown in Figure 2. According to the PN-76/B-03420 standard [25] used to design ventilation systems in the given location, the following calculation parameters of the outside air are assumed: dry thermometer temperature: $\theta_e = 30°C$, relative humidity RH = 45%, moisture content x = 11.9 g/kg. Moreover, it is also shown how devices of hybrid ventilation may affect outgoing natural volumetric flow of air and temperature under the roof.

During summer, in the analyzed region, outside the dry bulb, temperature can reach even 36°C. It seems to be suitable to make also appropriate simulation for the conditions, which derives from the most actual meteorological data, which has also been calculated in the paper. Likewise, computational analysis for winter time shows and confirms that natural ventilation works more efficiently during cold days.
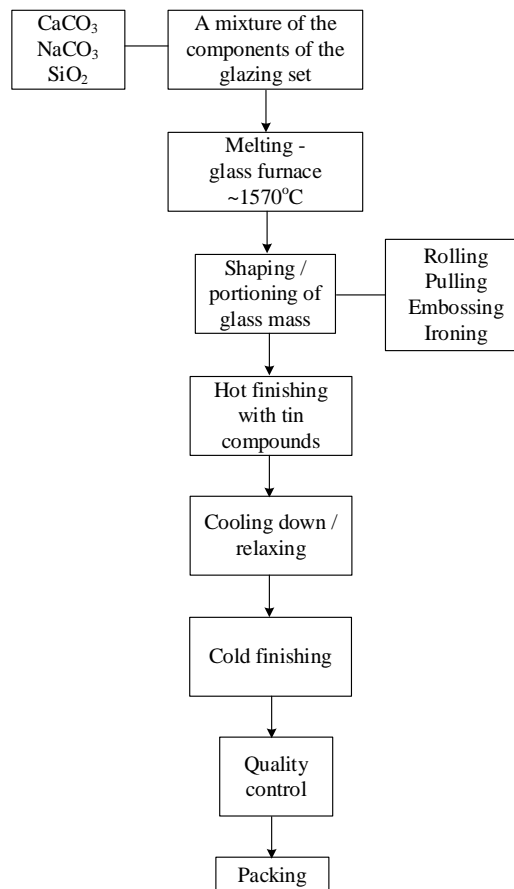


**Figure 1.** Technological process of glass production.



**Figure 2.**  The division of Poland into climatic zones for the design of ventilation and air conditioning systems [25].

## 2. Methodology

In the paper, the Ventos software [26] was used to calculate and analyze the parameters of natural ventilation with the possibility of including mechanical elements and taking into account the influence of wind. The model glassworks is built on a cuboid plan with an average height of $h_{av}=21$ m. Basic input data are given in Table 1. The calculations were made assuming that the building temperature is stable, i.e. the sum of heat gains in the room is equal to the sum of heat fluxes discharged by ventilation ($\Sigma\Phi_G=\Phi_{v,out}$). Heat gains through external walls were omitted due to their small share compared to heat gains from technology ($\Sigma\Phi_{G,ex.wall}<<\Phi_{G,tech}$). The parameter VB - degree of obstruction - appearing in Table 1 – indicates the share of technological devices in the total cubic capacity of the room; usually this parameter is in the range of $0.2\div0.6$. Recommended average wind speed around the building is set to 0 m/s, that is the worst possible option for natural ventilation. Inlet air temperature that is supplied to the building volume for the summer period (without air heating as it is for the winter time) is usually equal to external temperature. Total assumed heat gains from technology is set to 11.2 kW and derives mainly from operation of the blast furnace. Degree of room loading, depends mainly on the size, location or geometry of the heat source and the heat exchanger type; this parameter is usually adopted from the range of $\mu_T=0.2\div1.0$, and for glassworks it is 0.3. In addition, it is assumed that the maximum air temperature under roof at the $h_{max}$ height, due to the safety of structural members, should not exceed 70°C; the calculations also took into account radiation heat gains from technological systems and thermal devices. Another limitations are air velocity in the supply opening, $v_{in,max}=1.5$ m/s and negative pressure value not exceeding $\Delta p = 50$ Pa (which makes it possible to open the door easily). Limitations in modeling of the ventilation system in a glasswork are presented in Table 2.

**Table 1.** Basic input data for modeling of the ventilation system in a glasswork.

| Input data – description | Symbol, unit | Value |
|---|---|---|
| Room length | $a$, m | 50 |
| Room width | $b$, m | 50 |
| Maximum building height (roof ridge) | $h$, m | 22 |
| Mean room height | $h_{av}$, m | 21 |
| Degree of obstruction | VB | 0.4 |
| Mean wind speed | $U\infty$, m/s | 0.0 |
| Inlet air temperature | $\theta_{sup}$, °C | 30 |
| External temperature | $\theta_{ext}$, °C | 30 |
| Total thermal load from the processes | $\Phi_G$, kW | 11,200 |
| Degree of room loading | $\mu_T$, - | 0.3 |

**Table 2.** Limitation in modeling of the ventilation system in a glasswork.

| Input data – description | Symbol, unit | Value |
|---|---|---|
| Temperature under top | $t_{out}$, °C | 70 |
| Air velocity in opening | $v_{in}$, m/s | 1.5 |
| Air velocity in outlet | $v_{out}$, m/s | 10 |
| Negative pressure | $p$, Pa | 50 |

After determining the basic input data, the following parameters of air supply openings - wall air intakes - and roof exhaust - for the summer period (openings of natural ventilation - intakes and outlets) are assumed:

- total amount of the devices,
- the height of center of opening above the baseline/the ground,
- coefficient of the flow $C_v$ that depends on the device and its aerodynamic active surface; usually this parameter is set in the range of $C_v=0\div1$,
- the width and height or length of the inlet into a single device,
- coefficient of the wind resistance $C_w$ [-] that derives from the static and dynamic pressure ratio and wind parameters.
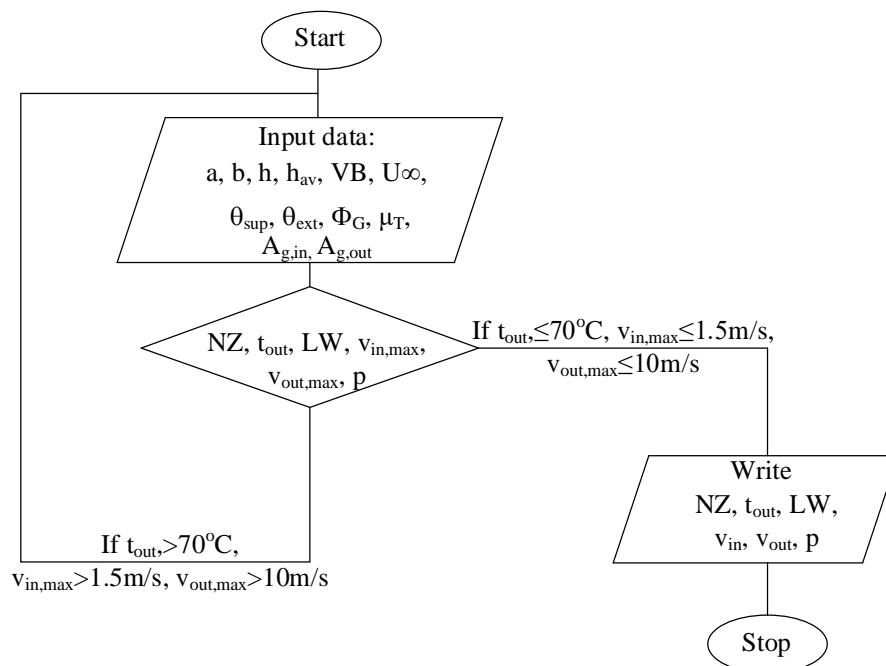


**Figure 3.** Block diagram of the calculation algorithm during simulation in Ventos.

### 3. Results

After defining the basic input data as well as geometric and aerodynamic parameters for the supply and exhaust openings, and after determining the accuracy of the next iteration of the calculation as 0.1, the following is calculated: inter alia, the maximum temperature under the roof, the amount and velocity of air flowing through each opening, the number of air changes, as well as the height of the pressure equalization zone in the building and the air pressure difference to the outside pressure. The calculations are made using the method of successive approximations so as not to exceed the limitations described in Table 2. The number of intakes and outlets and their total geometrically active surface are set in such a way as to achieve the minimum requirements specified therein.

In the first stage, the simulation was carried out with the assumption that the design external air temperature for Kielce, defined as standard, is $\theta_e = 30^\circ$C [25], and all

designed supply and exhaust openings are open. The results of this simulation are shown in Table 3.

### 4. Discussion

Based on the calculations, it is concluded that the most optimal solution is that numbered 7 (wall inlets are located on two levels – 2.9 and 4.9 m from the ground: 27 on each of them; the number of roof vents is also 27), where the total active area of the inlets is 77.76 m$^2$, and outlets of 71.08 m$^2$. The pressure equalization zone is located more or less in the middle of the hall (which is the most desirable case) and is 11.63 m (see Fig. 4), the supply velocities were not exceeded and amount to $v_{in}$=1.4 and 1.2 m/s, respectively, for air intakes located on two levels, and the maximum temperature under the roof of the hall is approx. 67$^\circ$C. Figures 5 and 6 show how the aerodynamic surface of the intakes and outlets affects the height of the pressure equalization zone. Air velocity in outlets does not exceed $v_{out}$ = 3.3 m/s in any case.

**Table 3.** Results of computer simulation of the natural ventilation system in a glasswork*s* for summer time and external temperature of $\theta_e$=30$^\circ$C.

| No. | 1 | 2 | 3 | 4 | 5 | 6 | 7 | 8 |
|---|---|---|---|---|---|---|---|---|
| Supply air intake, quantity | 10 | 15 | 30 | 30 | 30+30*) | 28+28*) | 27+27*) | 25+25*) |
| Exhaust air outlet, quantity | 10 | 15 | 15 | 25 | 28 | 27 | 27 | 27 |
| Unit geometric area of the inlet, m$^2$ | 2.0 x 1.8 | | | | | | | |
| Unit geometric area of the outlet, m$^2$ | 1.5 x 2.7 | | | | | | | |
| Opened for incoming air (geometric) $A_{g,in}$, m$^2$ | 36 | 54 | 108 | 108 | 216 | 201.60 | 194.40 | 180.00 |
| Opened for incoming air (aerodynamic) $A_{w,in}$, m$^2$ | 14.40 | 21.6 | 43.2 | 43.20 | 86.4 | 80.64 | 77.76 | 72.00 |
| Opened for outgoing air (geometric) $A_{g,out}$, m$^2$ | 40.50 | 60.75 | 60.75 | 101.25 | 113.40 | 109.35 | 109.35 | 109.35 |
| Opened for outgoing air (aerodynamic) $A_{w,out}$, m$^2$ | 26.33 | 39.49 | 39.49 | 65.81 | 73.71 | 71.08 | 71.08 | 71.08 |
| Incoming natural volumetric flow of air, $V_{in}$, m$^3$/h | 353 753 | 473 265 | 616 882 | 728 029 | 977 420 | 944 195 | 933 347 | 912 994 |
| Outgoing natural volumetric flow of air, $V_{out}$, m$^3$/h | 467953 | 587545 | 731296 | 841932 | 1091407 | 1058284 | 1048959 | 1025673 |
| Air displacement (per hour), LW, 1/h | 10.8 | 14.45 | 18.83 | 22.22 | 29.84 | 28.82 | 28.49 | 27.87 |
| Temperature under top, $t_{out}$, $^\circ$C | 127.9 | 103.1 | 86.1 | 77.6 | 65.4 | 66.7 | 67.1 | 68 |
| Air velocity in openings, $v_{in}$, m/s | 2.7 | 2.4 | 1.7 | 2 | 1.3 i 1.2 | 1.4 i 1.2 | 1.4 i 1.2 | 1.5 i 1.3 |
| Height of the neutral zone from ground NZ, m | 16.72 | 16.89 | 11.46 | 16.02 | 11.1 | 11.33 | 11.63 | 12.33 |

*) the inlets are located on two different levels
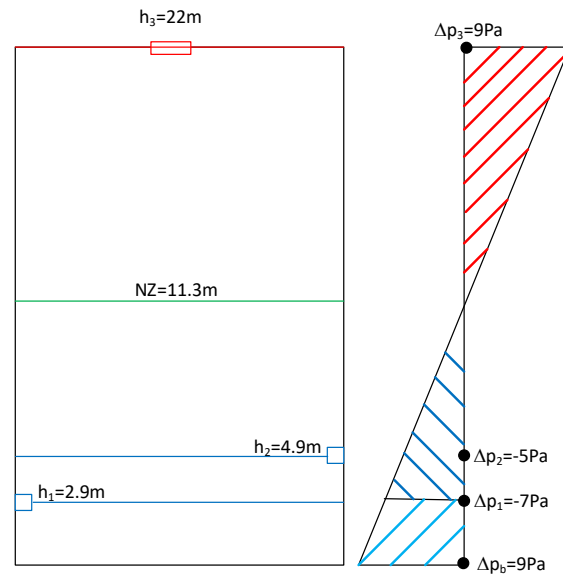
**Figure 4.** Height of the neutral zone from ground/pressure equalization zone, NZ for summer time.
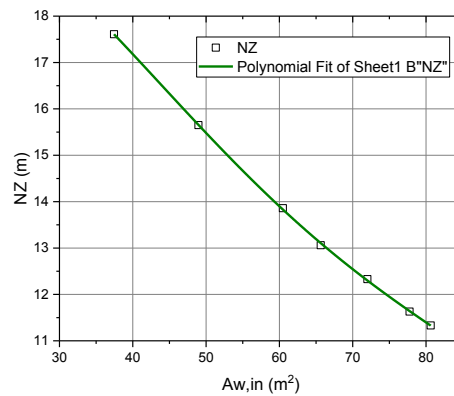


**Figure 5.** Height of the neutral zone from ground in the function of the air intakes aerodynamic area, NZ($A_{w,in}$).

However, the analysis of climatic conditions shows that the design temperature $\theta_e=30^oC$ is often exceeded, which may result in a significant decrease in the efficiency of ventilation systems, shutdown of production processes or, in extreme cases, even damage to structural elements. Based on the meteorological data [25], it can be noticed that the temperature of the dry bulb in the Kielce area, in the summer period, may be as high as $36^oC$ (data for July 2021). In such a case, the air temperature under the roof of the model glassworks would be exceeded and would be approx. $74^oC$. Therefore, it would be necessary to increase the aerodynamic intake area by 34.6 m² ($A_{w,in}=$ 106.56 m²), and the outlets by approx. 5.26 m² ($A_{w,out}=$ 76.34 m²); the temperature under the roof would then be $69.7^oC$, and NZ = 9.7 m; the total number of intakes on both levels is 38+36, and the number of outlets is 29.
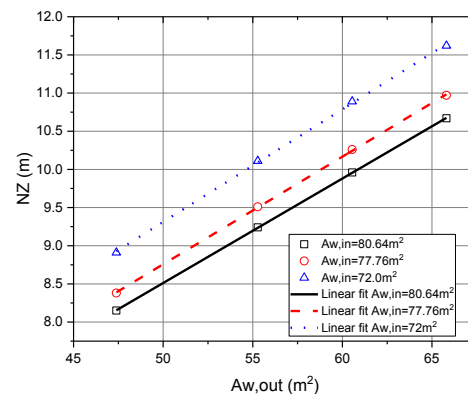


**Figure 6**. Height of the neutral zone from ground in the function of the exhaust air outlets aerodynamic area.

Figure 7 shows how the temperature under the roof of the building changes depending on the outside temperature for two cases of the active surface of the air intake/exhaust, respectively: 1) 77.76 m²/71.08 m²as well as 2) 106.56 m²/76.34 m².

The upper straight line in Figure 7 shows how the temperature under the roof of the building varies with changes in weather conditions and for all opened air supply and exhaust openings with a total active area of 77.76 and 71.08 m², respectively (27+27 air intakes and 27 exhaust vents); the areas have been set to meet the minimum requirements in Table 2 assuming that the design outside temperature is $\theta_e$=30°C. On the other hand, the lower straight line concerns the fulfillment of the minimum requirements in the case of exceeding the design temperature by $\Delta\theta_e$=6K (38+36 inlets and 29 outlets).

Ventilation system devices, both supply and exhaust, can be provided with appropriate sensors and controllers. This enables the amount of supply and exhaust air to be regulated by opening or closing the active ventilation surfaces so that the temperature under the roof of the building is similar throughout the year. Therefore, the next stage of the simulation consists of indicating the optimal opening area for winter period, in which the design outside temperature for Kielce is $\theta_e$=-20°C [24], and the heat losses amount to $\Phi_L$=450kW. After closing the lower lane of the intakes (0 openings/27 all) and reducing the intake openings on the higher level (20 open/27 all) and the exhaust vents to 7 open/27 all, the temperature under the roof is 54.4°C, and the pressure equalization zone is located at the level of NZ = 9.34 m (see Figure 8); the supply velocity has not been exceeded and is $v_{in}$ = 1.4 m/s.

What must also be analyzed is the impact of mechanical devices on natural convection in a model glasswork. In the Ventos software, in the 'Mechanical and hybrid ventilation devices' section, fans, air supply units and hybrid ventilation devices can be chosen. In our case, it is assumed that an exhaust fan with an output of 30,000 m³/h is placed at the same height as the roof vents, that is, 22 m. For each of the three outside air temperatures analyzed above ($i_e$= +30, +36, -20 °C) and the optimal configuration of the natural ventilation systems of the supply and the exhaust, the influence of the presence of a mechanical device was checked. It is a classic case of hybrid ventilation, where the gravity installation is

supported by an exhaust fan. Table 4 shows the results of this analysis.
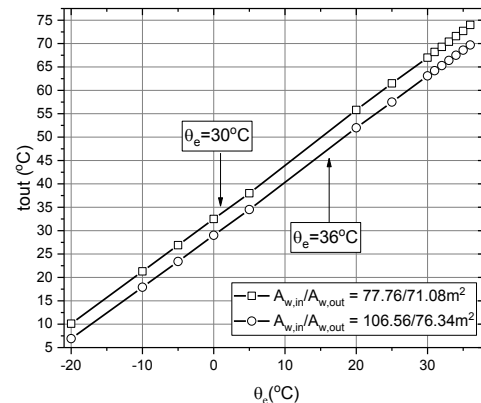


**Figure 7.** The temperature under the roof of the glassworks structure depends on the changing of external conditions, $t_{out}(\theta_e)$.
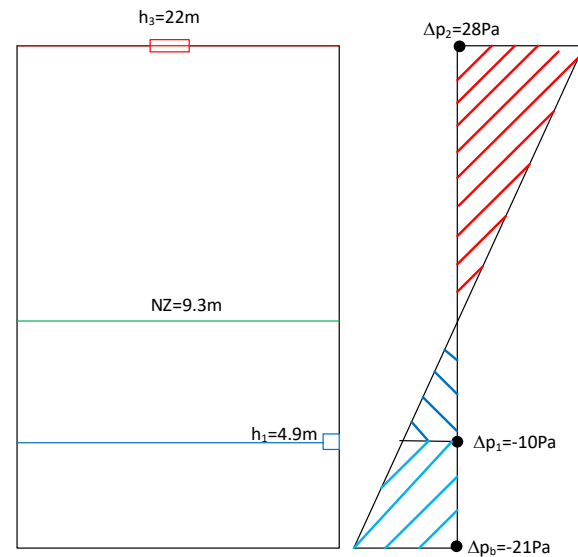


**Figure 8.** Height of the neutral zone from ground/pressure equalization zone, NZ for winter time.

**Table 4.**Results of computer simulation of the hybrid ventilation system in the glassworks for external temperatures of +30, +36 and -20°C, respectively.

| Case no. | 1 | 2 | 3 | 4 | 5 | 6 | 7 | 8 |
|---|---|---|---|---|---|---|---|---|
| $\theta_e$, °C | | +30 | | | | +36 | | -20 |
| Ventilation system | natural | hybrid | | | natural | hybrid | natural | hybrid |
| Opened for incoming air (aerodynamic) $A_{w,in}$, m² | | 77.76 | | | | 106.56 | | 28.80 |
| Opened for outgoing air (aerodynamic) $A_{w,out}$, m² | | 71.08 | | 0 | 76.34 | 0 | | 0 |
| Incoming natural volumetric flow of air, $V_{in}$, m³/h | 933,347 | 976,577 | 973,098 | 875,790 | 1,047,074 | 1,093,690 | 372,895 | 331,954 |
| Outgoing natural volumetric flow of air, $V_{out}$, m³/h | 1,048,959 | 970,560 | 977,094 | - | 1,159,868 | - | 482,514 | - |
| Exhaust fun of volumetric flow of air, $V_{out\_FUN}$, m³/h | - | 120,000 | 110,000 | 9x110,000 | - | 11x110,000 | - | 4x110,000 |
| Temperature under top, $t_{out}$, °C | 67.1 | 65.5 | 65.6 | 69.5 | 69.7 | 68.2 | 54.4 | 63.6 |
| Height of the neutral zone from ground NZ, m | 11.63 | 12.71 | 12.62 | 10.33 | 9.65 | 10.44 | 9.34 | 8.14 |

In the first case, the outgoing volumetric flow of air $V_{out}$ is slightly higher than that of $V_{in}$, which is normal due to differences in the air density in the supply and exhaust air. If we add an extraction device in the form of a roof fan with an output of 120,000 m³/h to this system, with gravity intake and exhaust vents, then $V_{out} < V_{in}$. This means that some of the air that should leave the building through the gravity vents is sucked in by the exhaust fan, which in this situation turns out to be ineffective (case no. 2). Only by reducing the efficiency of the mechanical device to 110,000 m³/h are the appropriate values of the air stream drawn from the building (case no. 3). If we wanted to completely replace the gravity ventilators with mechanical fans (case no. 4), their capacity would have to be 9 x 110,000 m³/h, which would ensure the correct temperature on the glassworks roof (69.5 <70ºC), and the pressure equalization zone would be at a reasonable level of 10.33 m. However, such a solution is much more expensive and does not ensure the maintenance of the design conditions for an outside temperature of + 36 °C (case no. 5). In this case, 11 exhaust fans are required (case no. 6).

In winter conditions, four fans are enough, but their presence lowers the pressure equalization zone to 8.14 m (cases 7 and 8).

These analyses and simulations confirm the accuracy and efficiency of using natural ventilation in facilities with significant heat gains, certainly include glassworks.

## 5. Conclusions

The paper concerns the optimization of natural ventilation in a model glassworks located in Kielce, where the total internal heat gains were determined as $\Phi_G = 11,200$ kW. The calculations were made using the Ventos software [26]. The basic conclusions of the analysis carried out are as follows:
- determining the maximum temperature of the ventilation air under the roof of the building is of key importance for the safety of the structure; here $t_{out}$=70ºC,
- at the outdoor temperature, for the summer period, amounting to θe=30ºC, the most optimal solution ensuring the minimum internal temperature and air velocity conditions for the glassworks building is the use of wall inlets located on two levels, 27 on each and 27 air exhausts on the roof of the building; the pressure equalization zone is NZ = 11.63 m and is located more or less in the middle of the room height; limiting the active surface of the air inlets $A_{w,in}$ shifts the pressure stabilization point towards higher values, which is an unfavorable phenomenon - reducing the $A_{w,in}$ area by half results in an increase of NZ to a value of over 17 m,
- if the outside temperature increased by 6K, the area of intakes, $A_{w,in}$ should be increased by about 44%, and the $A_{w,out}$ outlet by 7%; only in this way the temperature under the ceiling $t_{out}$ will not exceed the assumed value of 70ºC,
- in winter conditions, for the design outside temperature of θe=-20ºC, only 20 wall intakes on the upper level and 7 vents should be open; it ensures that the temperature under the roof of the building is kept at a similar level all year round,

- supply and exhaust elements should be mechanically controlled, depending on weather conditions,
- analyses and simulations made for hybrid ventilation confirm the accuracy and efficiency of using natural ventilation in facilities with significant heat gains, certainly include glassworks.

## References

[1] Y. Wang, L. Cao, Y. Huang, Y. Cao,"Lateral ventilation performance for removal of pulsating buoyant jet under the influence of high-temperature plume". IndoorBuilding Environment, Vol. 29, 2020, 543–557.

[2] P. Wouters, N. Heijmans, C. Delmotte, L. Vandaele,"Classifiaction of hybrid ventilation concepts". Proceedings of the 21st AIVC Conference, Den Haag, 2000.

[3] V. Soebiyan, "The trend of hybrid ventilation systems". 4th International Conference on Eco Engineering Development, 2020, IOP Conf. Series: Earth and Environmental Science Vol. 794, 2021, 012178.

[4] G. Cao, H. Awbi, R. Yao, Y. Fan, K. Sir´en, R. Kosonen, J. Jensen, Zhang, "A review of the performance of different ventilation and airflow distribution systems in buildings", Building Environment, Vol. 73, 2014, 171–186.

[5] L. K. Moeya, M. F. Kongb, V. C. Taia, T. F. Goc, N. M. Adam,"Effect of Gable Roof Angle on Natural Ventilation for an Isolated Building".Jordan Journal of Mechanical and Industrial Engineering, Vol. 15, No. 3, 2021, 291 – 300.

[6] L. L. Gomis, M. Fiorentini, D. Daly,"Potential and practical management of hybrid ventilation in buildings". Energy & Buildings, Vol 231, 2021, 110597.

[7] V. Soebiyan, "Hybrid ventilation systems on different climate". 4th International Conference on Eco Engineering Development 2020, IOP Conf. Series: Earth and Environmental Science Vol. 794, 2021, 012174.

[8] M. Pinto, V. Peixoto de Freitas, J. C. Viegas, L. Matias,"Residential Hybrid Ventilation Systems in Portugal: Experimental Characterization". Conference Paper, June 2006.

[9] Y. Lim, H. Yun, D. Song,"Indoor Environment Control and Energy Saving Performance of Hybrid Ventilation System for a Multi-residential Building". Energy Procedia, Vol. 78, 2015, 2863 – 2868.

[10] Borodiņecs, A. Krēsliņš, E. Dzelzītis, A. Krūmiņš, "Introduction of hybrid ventilation systems of dwelling buildings in Latvia".Proceedings of the Sixth International conference on indoor air quality, ventilation and energy conservation in buildings: sustainable built environment, Sendai, Japan, 2007.

[11] H. Davidsson, L. R. Bernardo, S.Larsson,"Design and Performance of a Hybrid Ventilation System with Heat Recovery for Low Energy Buildings". Journal of Environment and Engineering, 2011, Vol. 6, No. 2,469-477.

[12] R. Al-Rbaihat, A. Sakhriehb, J. Al-Asfar, A. Alahmer, O. Ayadi, A. Al-Salaymeh, Z.Al_hamamre, A. Al-bawwab, M. Hamdan,"Performance Assessment and Theoretical Simulation of Adsorption Refrigeration System Driven by Flat Plate Solar Collector". Jordan Journal of Mechanical and Industrial Engineering, Vol. 11, No. 1, 2017, 1 -11.

[13] S. Yoon, J. Seo, J. Lee, D. Song. A,"Study on Design Method for Hybrid Ventilation System in High-rise Residential Buildings". Conference Paper, May 2010.

[14] C.Vornanen-Winqvist, H.Salonen, Kati Järvi, M.A. Andersson, R.Mikkola, T.Marik, L. Kredics, J.Kurnitski, "Effects of Ventilation Improvement on Measured and Perceived Indoor Air Quality in a School Building with a Hybrid Ventilation System". International Journal of

Environmental Research and Public Health, Vol. 15, No. 7, 2018, 1414.

[15] E.Ramez, F. Habib,"Providing Design Strategies for Ventilation System in Treatment Environments (Proposed Sample: Hybrid Ventilation System in Hospitals)". International Journal of Architecture and Urban Development, Vol. 8, No.4, 2018,  1-4.

[16] X.Fua, D. Wu,"Comparison of the efficiency of building hybrid ventilation systems with different thermal comfort models". Energy Procedia, Vol. 78, 2015, 2820 – 2825, 6th International Building Physics Conference, IBPC 2015.

[17] X. Dou, D.Xie, Z. Wang, P. Xiao, H. Wang,"Improved buoyancy-driver hybrid ventilation system for multiple-heat-source industrial buildings. Case Studies". Thermal Engineering, Vol. 26, 2021, 101059.

[18] H. Davidsson, R. Bernardo, B.Hellström,"Theoretical and Experimental Investigation of a Heat Exchanger Suitable for a Hybrid Ventilation System". Buildings Vol. 3, 2013, 18-38.

[19] J. Zhang, F.Haghighat,"Simulation of earth-to-air heat exchangers in hybrid ventilation systems". Ninth International IBPSA Conference Montréal, Canada, 2005.

[20] W. Turner, H.Awbi,"Hybrid ventilation for cooling application".Conference paper, IAVEC 2007.

[21] R. Chatys, Ł. J. Orman, "Technology and properties of layered composites as coatings for heat transfer enhancement". Mechanics of Composite Materials, Vol. 53, No. 3, 351-360.

[22] W. J. N.Turnera,, H. B. Awbi, T. Payne,"Solar-driven hybrid ventilation system".The 9th World Renewable Energy Congress, Florence, Italy, 2006.

[23] Kontrymowicz, Ventosystem Natural ventilation in a glassworks - can it be controlled?,Cyrkulacje Vol. 20,2014, 45-47, www.cyrkulacje.pl

[24] W. Wciślik, R.Pała,"Some Microstructural Aspects of Ductile Fracture of Metals". Materials, Vol. 15, No 15, 2021, 4321.

[25] PN-B-03420:1976: Ventilation and air conditioning - Calculation parameters of the outside air.

[26] The VENTOS to calculate natural ventilation Copyright © 2022 VENTOSYSTEM Bohdan Kontrymowicz, www.ventosystem.pl

[27] www.meteoblue.com (access:14.02.2022).\

# Harvesting Human Being Energy to Charge Smartphone

## Elaf J. Majeed[1] , Amani J. Majeed[2*]

*[1]University of Basrah, College of Engineering, Electrical Engineering Department, Iraq*
*[2]University of Basrah, College of Engineering, Petroleum Engineering Department, Iraq*

## Abstract

Rapid development has occurred recently in the use of thermoelectric generators (TEGs), as they have been applied in numerous fields. Although TEGs can harvest the body's energy, the output voltages they yield are extremely small (a few hundred mV). Accordingly, the objective of this paper is to study the possibility of enlarging a voltage generated by the TEG to a level where it can be used.

In this paper, we provide a comprehensive simulation of the performance of TEGs system that harvests human energy by using one topology of the conversion circuit, the DC/DC step-up converter, that raises the external voltage so that portable mobile devices can be charged. In the proposed system ten pieces of the TEGs have been used, every system contains 35 TEG couples connected serially by legs. The methodology of the current study focuses on using the finite element method (FEM) to simulate the TEG system, where we used ANSYS Workbench software platform (Professional Version 18.1). Moreover, MATLAB and PSPICE Simulink have been used to simulate the energy conversion circuit. The outcomes of this study can be summarized in the following points: 1) the total voltage obtained from the ten pieces of the TEG system is about (2.165V). 2) Using the boost DC/DC converter system help to enlarge the total voltage of TEG to 5 Volt. 3) There is no signifying effect for the different shapes of TEG legs, where a comparison was made between two different shapes of TEG legs, one is rectangular and the other is equivalent cylindrical. 4) The results of TEG were also compared with the results of previous work, and a good agreement has been attained. 5) MATLAB - PSPICE simulation programs were used to design and implement the DC-to-DC boost converter circuit, and the results showed the output response of the overall system being in line with the study objectives.

## Nomenclature

| | |
|---|---|
| $A$ | Area [m$^2$] |
| $c$ | Heat capacity [J kg$^{-1}$ K$^{-1}$] |
| $C$ | Filter capacitance [F] |
| $D$ | The duty cycle [-] |
| $E$ | Electric field [V m$^{-1}$] |
| $F_s$ | Switching frequency [Hz] |
| $I_L$ | Inductor current [A] |
| $J$ | Electric current flux [A m$^{-2}$] |
| $k$ | Heat transfer coefficient [W m$^{-2}$ K$^{-1}$] |
| L | Inductance [Henry] |
| $P$ | Electric power [W] |
| $P'$ | Peltier coefficient [-] |
| $Q$ | Heat power [W] |
| $Q'$ | Density of Joule heating energy [W m$^{-3}$] |
| $q''$ | Heat flux [W m$^{-2}$] |
| $R$ | Electrical resistance [Ω] |
| $R_{DS}$ | Drain source ON-state resistance [Ω] |
| $R_L$ | Inductor resistance [Ω] |
| $S$ | Seebeck coefficient [V K$^{-1}$] |
| $T$ | Absolute temperature [K] |
| $T_s$ | Switching cycle [s] |
| $T_{ON}$ | ON state time [s] |
| $T_{OFF}$ | OFF state time [s] |
| $t$ | Time [s] |
| $V$ | Voltage [V] |
| $V_d$ | Forward voltage drop [V] |
| $V_L$ | Inductor voltage [V] |

**Greek letters**

| | |
|---|---|
| Δ | Difference |
| $\eta$ | Conversion efficiency |
| $\kappa$ | Thermal conductivity [W m$^{-1}$ K$^{-1}$] |
| $\rho$ | Density [kg m$^{-3}$] |
| $\rho_c$ | Charge density [C m$^{-3}$] |
| $\rho_e$ | Electrical resistivity [Ω m] |
| $\sigma$ | Electrical conductivity [S m] |
| $\tau$ | Time period [s] |

**Abbreviations**

| | |
|---|---|
| TEG | Thermoelectric generator |
| DC | Direct current |
| CCM | Continuous current mode |

## 1. Introduction

Globally, electric power generation is shifting to more environment-friendly methods, since the use of conventional sources of energy causes more environmental issues, including global warming, greenhouse gases, and air pollution. This makes the use of renewable energy resources crucial. Solar energy has been used in many applications, incling electric power generation and in water

\* Corresponding author e-mail: amani.majeed@uobasrah.edu.iq.

desalination processes, so a great deal of research has focused on developing it as a clean energy resource [1]–[5]. Moreover, wind energy has been growing rapidly as one of the cleanest sources of energy in recent years [6]–[10]. However, a new renewable energy sources must be found to counteract fossil energy's depletion by utilizing existing energy resources and seeking new ways of utilizing them. One of the latest renewable energy sources is thermoelectric generators (TEG) [11].

Science has strongly focused on the use of thermoelectric generators. Nevertheless, a difference in temperature between two semiconductor materials can reveal differences in voltage across these materials, according to Seebeck in 1822 [12]. TEGs have no moving parts and can generate electrical energy from geothermal and solar energy reliably and sustainably [13], [14]. Furthermore, it can be used at nuclear power plants for micro-power generation in the absence of severe accidents to ensure that sensors or indicators are functioning properly [15]. Mateu et al., 2007, used thermoelectric generator modules (TEGs) to harvest the body's energy and supply it to a wireless sensing module. Their hypothesis was that the TEG heat source comes from the human body and the ambient temperature can be represented by the TEG sink source [16]. Moreover, TEGs have been used for several decades to power space vehicles [17], [18]. In 2013, Hadjistassou et al., proposed a new design methodology based on a computational and analytical analysis, where a  segmented thermoelectric generator is proposed having a heat source temperature of 622.8 K  and a heat sink temperature of 298.2 K [19]. The study resulted in increased analytical accuracy. Considering its time-efficient framework, the hybrid computational-analytical modeling approach achieves a very good level of accuracy [19]. Elsheikh H. Mohamed, etal. (2014) introduced an in-depth review of thermoelectric materials and outlined parameters that contribute to the figure of merit thermoelectric efficiency (ZT). Furthermore, a discussion of the possibilities for optimizing thermoelectric materials was also discussed [20]. Kossyvakis D. N. et al., 2016 examined the performance of a tandem PV-TEG hybrid by using both poly-Si and dye-sensitized solar cells. Different thermoelectric devices with different thermoelement geometries were tested to determine their effect on performance. Additionally, the results of the experimental process have been utilized in order to evaluate the performance of the system under real-world operating conditions.  According to the results of the analysis conducted, when actual operating conditions are taken into account, TEGs with shorter thermoelements result in increased power output levels [21]. In 2018, Wang et al. developed a wearable TEG that can power electronic devices (such as a miniaturized accelerometer) by harnessing the energy of the human body. They used 52 pairs of N-type and P-type legs, which were cubic-shaped and made from powder materials derived from Bi2Te3. They demonstrated that their novel TEG generated 37.2 mV with only a 50 K temperature change for open circuit systems [22].

Moreover by using TEG, Proto et al., in 2018, analyzed the results of measuring the thermal energy harvested from human arms and legs. Four large areas from the skin (Biceps brachii, Flexor carpi radialis, Gracilis, and Gastrocnemius muscle) have been chosen as placement of TEG. Furthermore, users can perform daily activities such as walking, riding a bike, jogging, and sitting. The authors

concluded that the power generated took the range of (5-50 μW) and indicated that legs could be used as a placement for TEG due to the variety of biomechanical work generated by the gastrocnemius muscle [23]. In addition, TEG is used to recover waste heat, where Khalil and Hassan presented a 3D study in 2020 of how to enhance lost heat recovery by using TEG in chimneys via heat spreaders. In their study, the authors investigated how different sizes of heat spreaders affected the TEGs' performance that were used to recover heat from chimneys. As a result, the heat spreaders proved to be an effective way to recover waste heat from chimneys via TEGs while saving the initial fixed costs of the system. Where, TEGs' total power increased by 42% when 140 mm  heat spreaders were  used  [24]. Furthermore, Kanagaraj N. 2021, investigated the performance and the design of a hybrid photovoltaic–thermoelectric generator system using fractional-order fuzzy logic controllers-based maximum power point tracking. Where he studied the performance of the proposed maximum power point tracking (MPPT) technique under various thermal and electrical operating conditions by using a MATLAB simulation. According to the author results, the PV and TEG combined system provides higher energy efficiency than the PV module alone [25]. Al-Qadami et al. in 2022, presented a systematic review of the potentials of harvesting thermal energy from asphalt pavements and assesses the progress being made towards developing these technologies through bibliometric analysis. Moreover, they discussed the principles and basics of three main types of thermal energy harvesting technologies. Furthermore, they also described the system's configurations, efficiency, and materials [26].

It is noteworthy that the TEGs are small, lightweight, reliable energy converters since there are no mechanical parts to cause vibration or noise [27]. Despite TEG advantages, their applications are limited because of the high cost [28]. Therefore, in recent years many kinds of research have focused on TEG materials and geometry in order to get the optimum performance at low cost [29]–[32].

The previous studies focused exclusively on using energy directly from thermoelectric generators, which restricted their work to applications that required a low voltage, or used large numbers of TEGs to increase the output voltage level, which increased the overall cost of the system. Therefore, in this study, we intend to use only a few TEGs in order to achieve a relatively high voltage that is suitable for portable devices, such as mobile phones. Besides, an integrated simulation is conducted for a TEG system, as well as a boost DC/DC converter circuit for raising the TEG output voltage. The effect of different shapes on the output voltage was also examined by simulating two different TEG leg shapes, one with a rectangular shape and the other with a cylindrical shape.

## 2. Methodology

According to Fig. 1, the temperature of the human body is converted by the TEG into an electrical voltage, and this voltage is used as input for the DC/DC boost converter system to get an appropriate voltage which will be used for charging purpose. Therefore, the methodology contains two parts; the TEG part and the DC/DC boost converter system part.

## 2.1. Thermoelectric Generator (TEG)

The thermoelectric generator uses the difference in temperature between two sides to generate power. Therefore, one side needs to work as a heat source, while the other works as a sink source. The difference in temperature makes the electrons vibrate more intensely on the side with higher temperatures, which makes them move more slowly on the side with lower temperatures. As a result of this movement, the current appears, which can then be exploited as electrical energy. The TEG material used in this study is based on bismuth telluride ($Bi_2Te_3$). However, it consists of a ceramic plate (to enhance thermal conductivity), electrode solder material (to reduce thermal stress), and a pair of semiconductor legs; P-type and N-type, as shown in Fig. 2.

The behavior of the TEG materials are governed by the heat transfer equation coupled with the density continuity equation as follows [33], [34];

In thermoelectric analysis, the heat flow equation is:

$$\rho c \frac{\partial T}{\partial t} + \nabla . q'' = Q' \tag{1}$$

Where; T represents the temperature; t is the time; c represents the heat capacity; $q''$ represents a heat flux, and $Q'$ is the Joule heating energy.

The continuity equation for electric charge is;

$$\nabla . J = \frac{\partial \rho_c}{\partial t} \tag{2}$$

Where; J represents the flux of the electric current produced by the coupled Seebeck and Joule effects, and $\rho_c$ denotes to charge density.

The Joule heating energy and the heat flux are expressed as

$$q'' = -K \nabla T + P'J \tag{3}$$
$$Q' = J . E \tag{4}$$

Where;

$$P' = ST \tag{5}$$
$$J = -\sigma \nabla V - \sigma S \nabla T \tag{6}$$

By substituting Eq. (3-6) in Eq. (1) and Eq. (2), the governing equations will be written as follows:

$$\rho c \frac{\partial T}{\partial t} + \nabla . \left( -K \nabla T + \alpha T(-\sigma \nabla V - \sigma \alpha \nabla T) \right) = (-\sigma \nabla V - \sigma \alpha \nabla T)(-\nabla V) \tag{7}$$

$$-\sigma(\nabla^2 V + \alpha \nabla^2 T) = \frac{\partial \rho}{\partial t} \tag{8}$$

In Fig. 3, the geometric entries and dimensions have been explained for one piece of the studying system of rectangular and equivalent cylindrical TEG legs. Ten pieces of the TEG system have been used as demonstrated in Fig. 4. Every system contains 35 TEG couples connected serially by legs. The steady-state case has been assumed, and the human temperature represents a heat source for the TEG while the ambient temperature is used as a cold part of TEG.
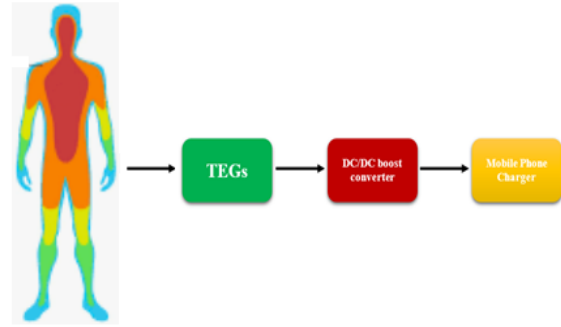


**Figure 1.** Block diagrams of the system
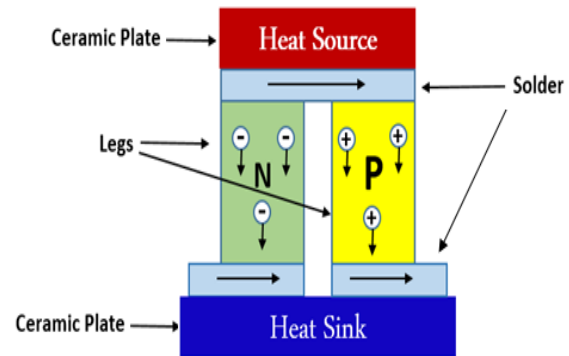


**Figure 2.** Thermoelectric Generator
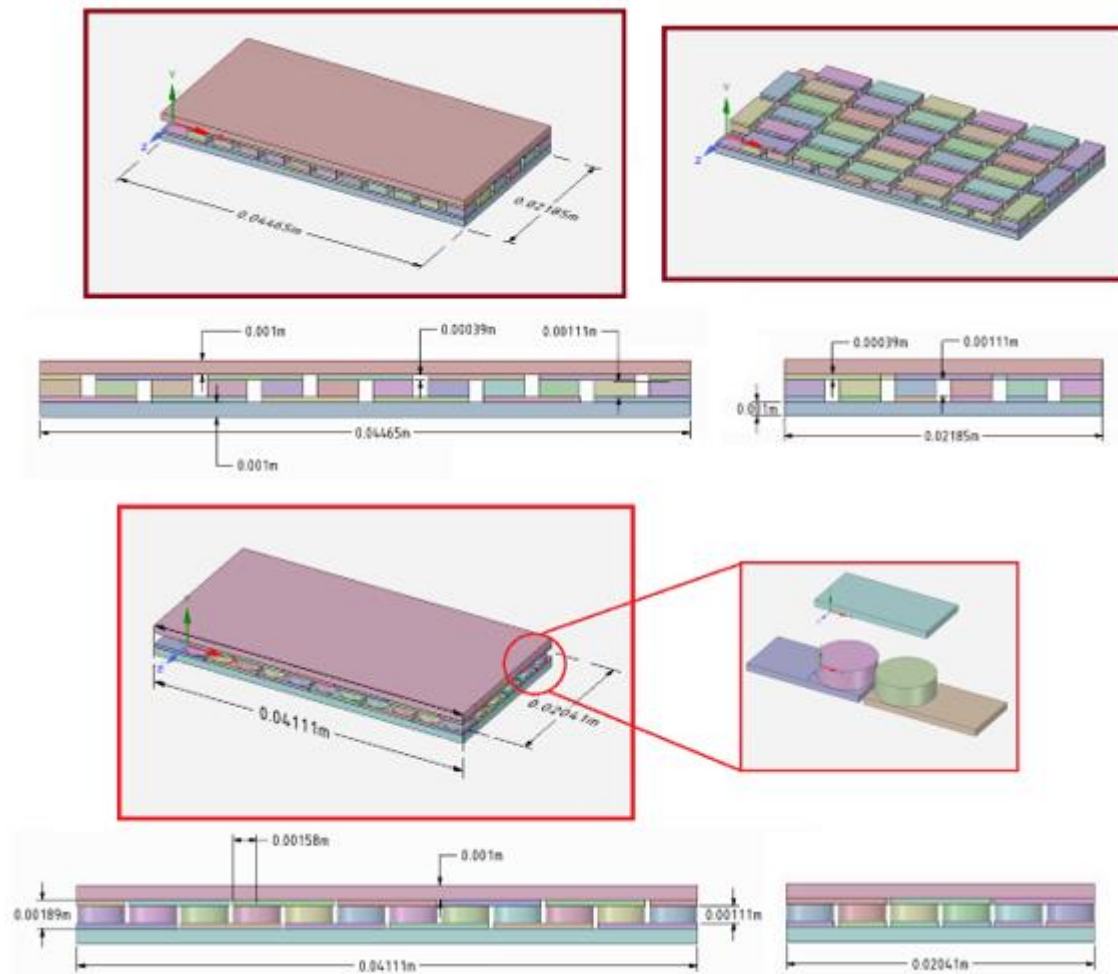
**Figure 3.** TEG geometry: (a) One piece of TEG with rectangular legs, (b) One piece of TEG with equivalents cylindrical legs
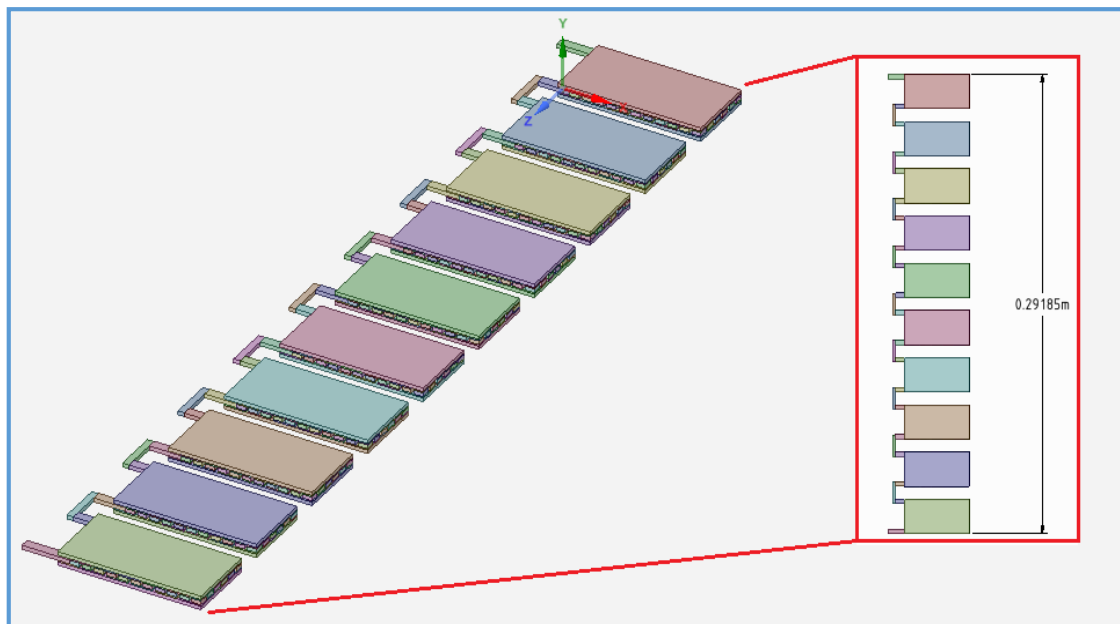


**Figure 4.** Ten pieces of TEG connected serially

Table 1 lists the parameters of the N-Type and P-Type components of the TEG part that were simulated with the ANSYS software package. Further, the ceramic plate has a thermal conductivity of 36.5 W m$^{-1}$ K$^{-1}$, while the resistivity and thermal conductivity of the solder layers are 1.68*10-8 Ω m and 390 W m$^{-1}$ K$^{-1}$, respectively.

**Table 1.** The parameters of the TEG materials used in this study [35].

| Components | Seebeck coefficient [V K$^{-1}$] | Resistivity [Ω m] | Thermal conductivity [W m$^{-1}$ K$^{-1}$] |
|---|---|---|---|
| P-Type | 0.0002 | 8.8*10$^{-6}$ | 1.55 |
| N-Type | -0.0002 | 1*10$^{-5}$ | 1.605 |

*2.2. DC-to-DC Boost converter circuit*

DC-DC power stage converters can be used in portable devices to generate the desired DC level. They can also be used to reduce ripples, and carry out a variety of other functions, such as modifying the voltage level (up or down steps), and regulating voltage.

Boost converter circuits provide greater output voltages than input voltages due to the equipment arrangement. By using the mentioned converter, the TEG output voltage increased to a much more suitable voltage for phone charging. The schematic diagram of the DC/DC asynchronous boost converter is shown in Fig. 5.
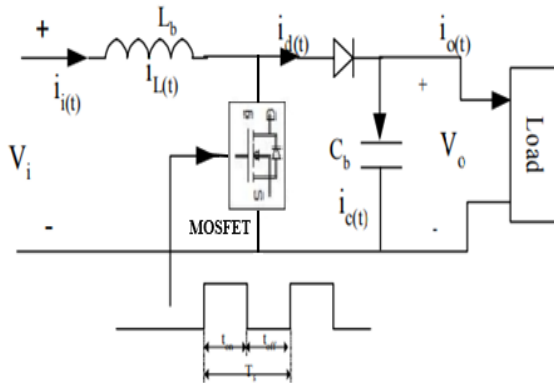


**Figure 5.** Asynchronous step-up DC/DC Converter Circuit Schematic.

Based on the continuous conduction mode (CCM) of the converter circuit, the inductor current flows continuously during the whole switching period. As a ramification, the boost power stage assumes two states per switching cycle. The ON state where the switch Q is on while diode D is blocked. During this stage, the current through the inductor L increase linearly and energy is stored in the inductor. The capacitor C supplies energy to the load R. The OFF state starts when the switch is off and the diode becomes conductive, the energy stored in the inductor L is returned to the capacitor and the load R. As shown in Fig. 6.

The duration of the ON stat $T_{on}$ is given by DTs, where D is the duty cycle curb by the control circuit, came across as a ratio of the switch ON time to the time of one complete switching cycle, $T_s$. The duration of the OFF state is $T_{off}$, and for continuous conduction mode, is equal to $(1 - D)T_s$ as there are only two states per switching cycle. These times are shown along with the waveforms in Fig.7.
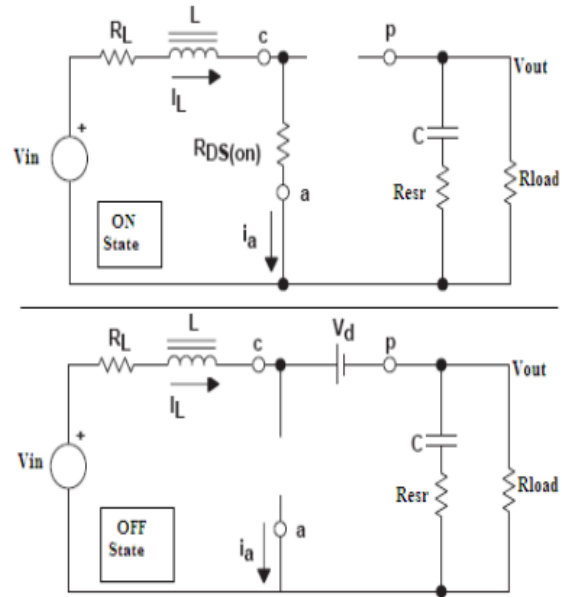


**Figure 6.** Boost Power Stage States [36]
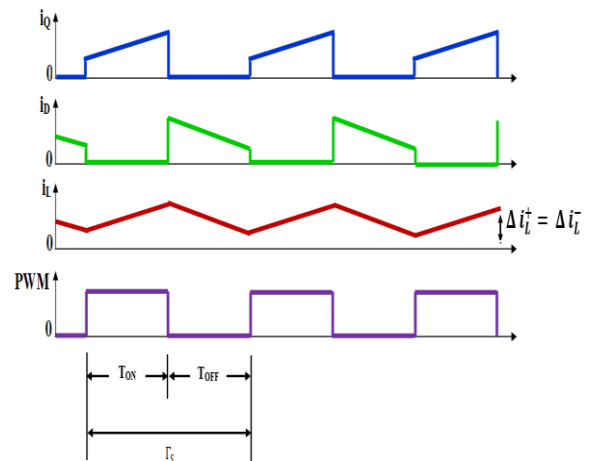


**Figure 7.** Waveforms of current and voltage in continuous inductor current mode (CCM)

Referring to Fig.6, Fig.7 and [36], the inductor-current increase is calculated by using the familiar relationship, when the circuit is ON;

$$V_L = L \times \frac{di_L}{dt} \rightarrow \Delta I_L = \frac{V_L}{L} \times \Delta T \qquad (9)$$

Therefore, the inductor current increases during the on state is:

$$\Delta I_L{}^{(+)} = \frac{V_{in} - (R_{DS} + R_L)I_L}{L} \times T_{ON} \qquad (10)$$

Where the $\Delta I_L{}^{(+)}$ represents the inductor ripple current. The output capacitor C provides all the output load current during this period.

Conversely, inductor current decreases during the OFF state as follows:

$$\Delta I_L{}^{(-)} = \frac{((V_{out} + V_d + I_L \times R_L) - V_{in})}{L} \times T_{OFF} \qquad (11)$$

Where the $\Delta I_L{}^{(-)}$ represents the inductor ripple current also.

Under steady-state conditions, the current increase during on-time $\Delta I_L{}^{(+)}$, and the current decrease during off-time, $\Delta I_L{}^{(-)}$, equalize. Alternatively, the inductor current would otherwise have a net increase or decrease from cycle to cycle, which would not constitute steady state.

Thus, by equalizing Eq. (10) and Eq. (11), the continuous conduction mode boost voltage conversion relationship can be obtained:

$$V_{out} = (V_{in} - I_L \times R_L) \times \left(1 + \frac{T_{ON}}{T_{OFF}}\right) - \quad V_d - $$
$$V_{DS} \times \left(\frac{T_{ON}}{T_{OFF}}\right) \qquad (12)$$

Let $T_s = T_{ON} + T_{OFF}$, $D = \left(\frac{T_{ON}}{T_s}\right)$, and $(1-D) = \frac{T_{OFF}}{T_s}$, then the steady-state equation for $V_{out}$ is:

$$V_{out} = \frac{V_{in} - I_L \times R_L}{1-D} - V_d - V_{DS} \times \frac{D}{1-D} \qquad (13)$$

Since the $R_L, V_d, and\ V_{DS}$ are insignificant enough to ignore, then Eq. (13) becomes:

$$V_{out} = \frac{V_{in}}{1-D} \qquad (14)$$

The boost inductance is defined as[37], [38]:

$$L = \frac{RD\ (1-D)}{2F_s} \qquad (15)$$

Moreover, the switching frequency, $F_s$ is presumed to be (25000 Hz).

For the boost output filter capacitor, Eq. 16 gives the required capacitance value (C) as a function of ripple voltage $(\Delta V_o)$, the duty cycle (D), the switching frequency $F_s$, and the output voltage [37], [38], and [39]:

$$C \geq \frac{V_o D}{F_s \Delta V_o R} \qquad (16)$$

The output voltage ripple is assumed to be 1%.

## 3. Results and Discussion

### 3.1. TEG simulation results

Ten pieces of the TEG system have been used. Each system consists of 35 TEGs connected serially by legs. Due to the difference in temperature between the cold and hot TEG legs sides and since these legs are serially connected, the electric voltage will be generated (which is already the Seebeck effect phenomenon). Fig. 8, shows the 3D voltage distribution for one piece of TEG when the TEG legs have a rectangular form.

Also, Fig. 9, shows the 3D electric voltage distribution but when the TEG legs have an equivalent cylindrical shape. Fig. 9-b, gives more visualization about the entries of the system, where the shape of TEG legs has been explicitly exposed.

Fig. 10 and Fig. 11 show the 3D TEGs temperature distribution for rectangular and cylindrical TEG legs form, respectively. The hot side of the TEG is represented by human body temperature (which is 37.8 C), while the cold TEG side is the ambient temperature. It is obvious that the difference is very little in the value of the electric voltage coming out of the two mentioned TEG shapes, where the percentage of the difference is about (0.2%). Moreover, the conformity of the results of the TEG part for the current work with the published work [35], can be seen in Fig. 12, which confirms the accuracy of the results obtained in this study, where a human body temperature of 37.8 degrees Celsius represents the hot side of the TEG, whereas the ambient temperature represents the cold side.
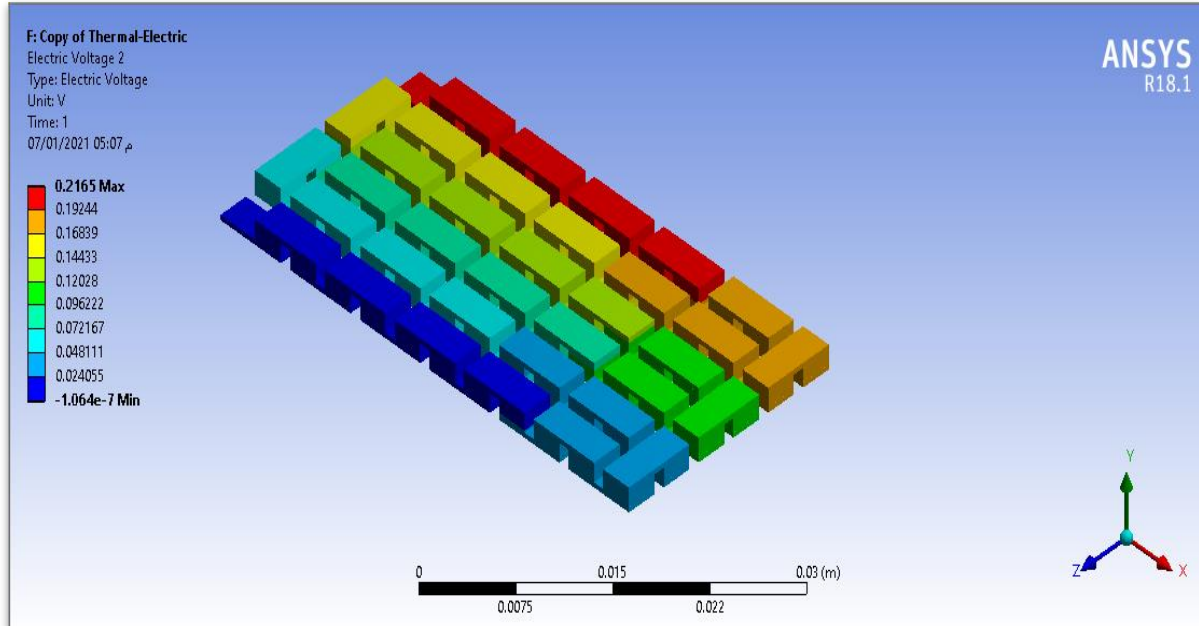


**Figure 8.** Volt distribution on one piece that contains 35 TEG couples with rectangular TEG legs shape.
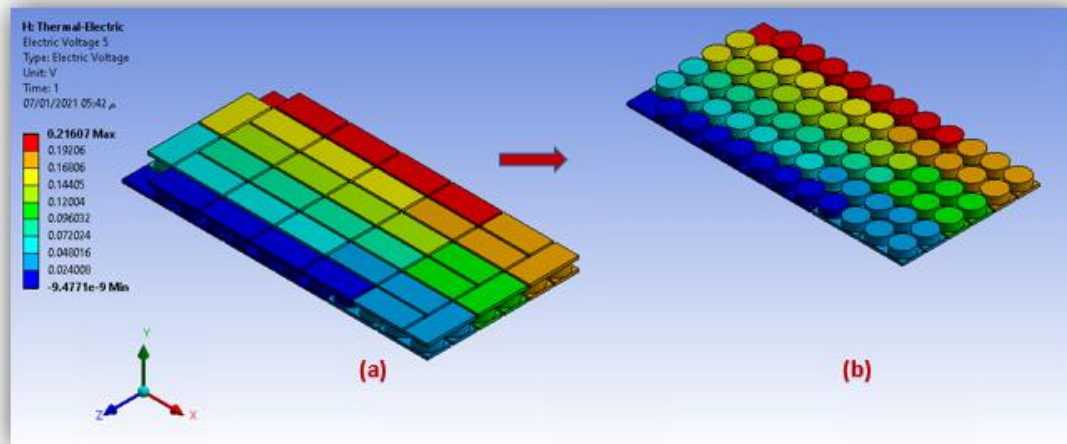
**Figure 9.** Volt distribution on one piece that contains 35 TEG couples with equivalent cylindrical TEG legs shape.
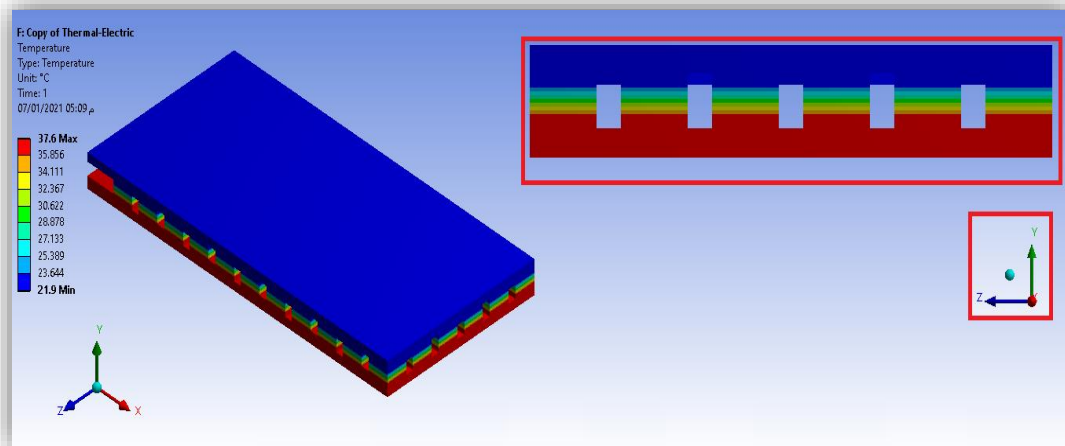


**Figure 10.** Temperature distributionon one piece that contains 35 TEG couples with rectangular TEG legs shape.
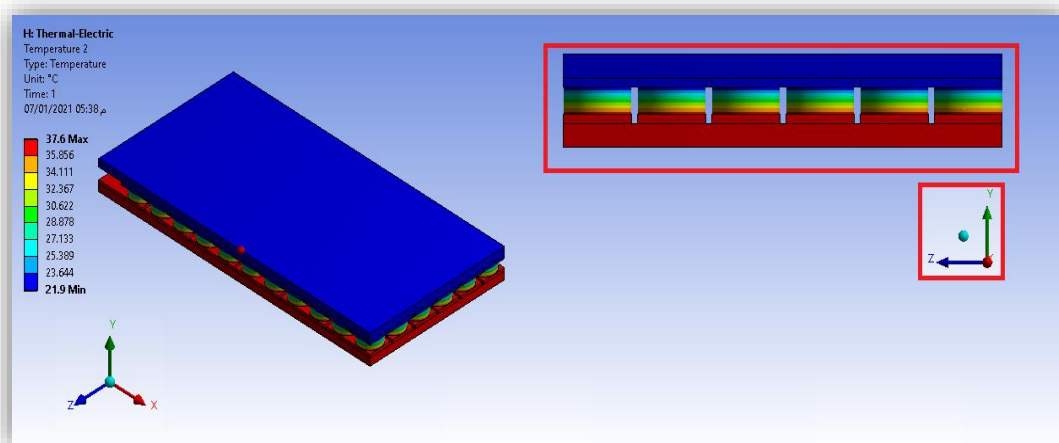


**Figure 11.** Temperature distribution on one piece that contains 35 TEG couples with equivalent cylindrical TEG legs shape.

### 3.2. Boost converter Simulation Results:

The boost converter, an asynchronous circuit, is modeled in Matlab/Simulink as shown in Fig. 13. The voltage input to this model comes from TEG systems (which is 2.165 V), with a switching frequency 25 kHz.

Fig. 14, reveals the output voltage of the converter concerning time obtained from Matlab simulation, which is (5V). While Fig. 15 shows the output current, which is 3000mA. The duty cycle is 0.567 for an operating frequency of 25 kHz.

The circuit diagram used for PSPICE / Simulink of the step-up converter is shown in Fig. 16. The purpose of this circuit is to measure output voltage across the resister R1, Moreover, Fig. 17 shows the output voltage across R1 which becomes stable after sometime, and remains at 5 V.
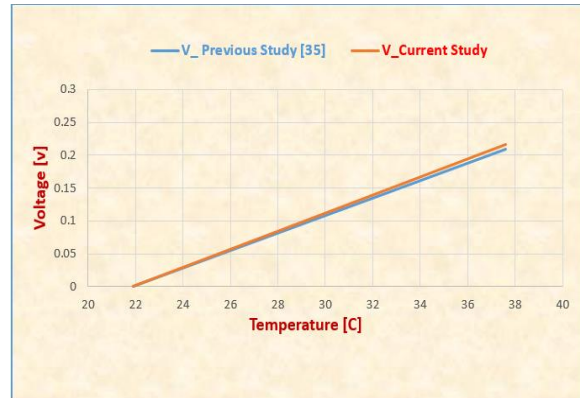


**Figure 12.** The output electrical voltage vs. temperature.
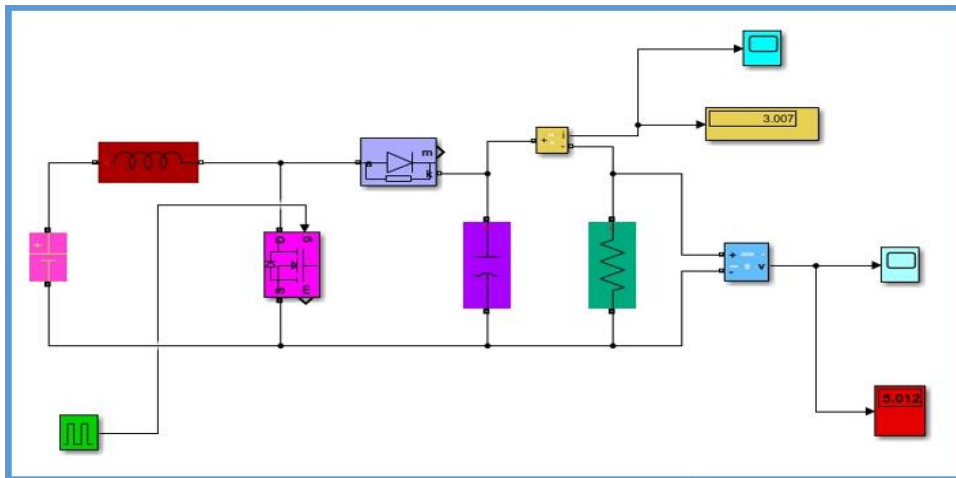


**Figure 13.** Circuit Diagramof the Boost DC/DC Converter used in MATLAB
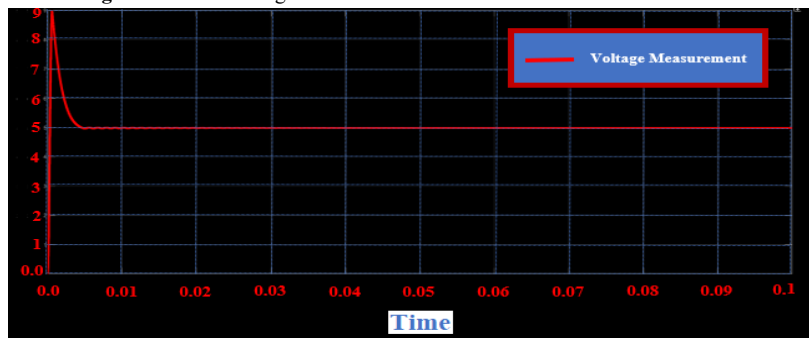


**Figure 14**. V$_o$ (Output Voltage) vs time in MATLAB
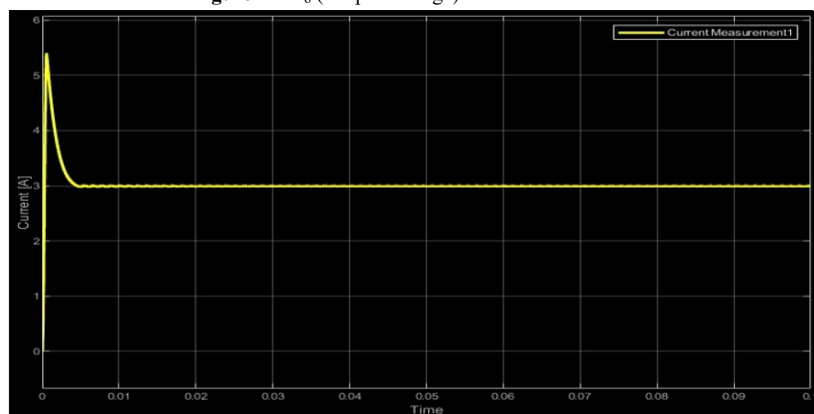


**Figure 15.** I$_O$(output current) vs Time in MATLAB.
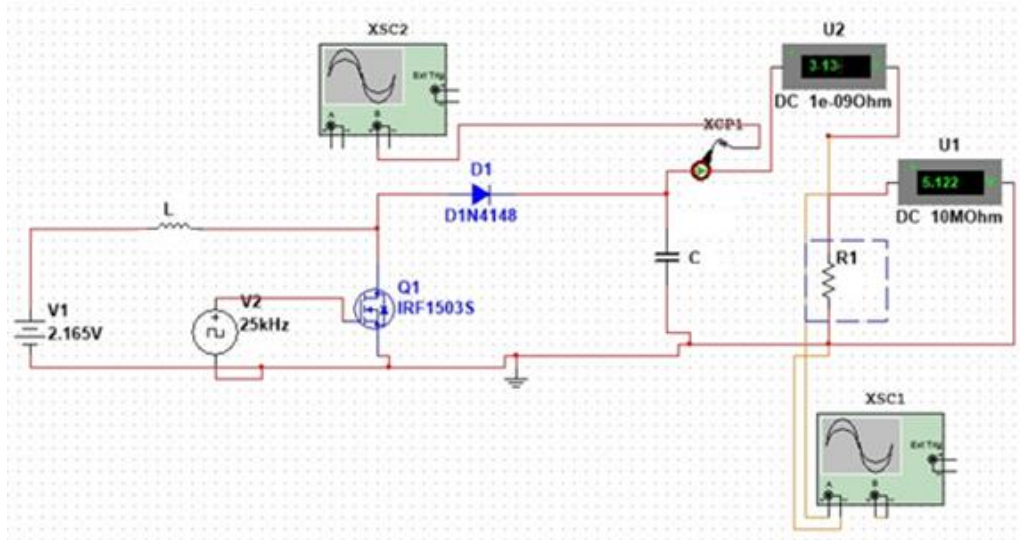
**Figure 16.** Circuit diagram of boost converter used in P PSPICE
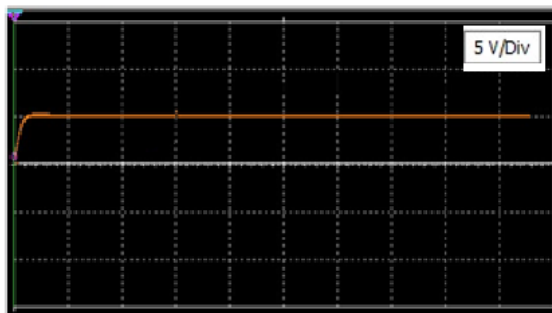


**Figure 17.** V$_{out}$ (Output Voltage) vs time in PESCPIC

## 4. Conclusion

A complete modeling and simulation of TEG system with a boost converter circuit was developed. The proposed TEG system consists of ten pieces of the TEGs with a total length of 0.29185 m. Each system that consists of 35 TEG couples connected serially by legs, has been simulated by using the finite element method. There is only a slight difference (0.2%) between the output response of the TEG electric voltage when two different leg shapes are used (the rectangular and equivalent cylindrical ones). In addition, an asynchronous DC to DC boost converter with continuous current mode was established. Simulations were conducted using MATLAB and PSPICE, and corresponding waveforms were obtained. The output voltage across the output capacitor is 5 V with a maximum output ripple of 1%. Based on the results from the simulation programs, we can see that the results obtained are somewhat similar and are also comparable to the desired result from the TEG system and power conversion circuit.

## References

[1] Majeed J. Amani, Najim E. Saleh, and Hammadi H. Salman, "Simulation Solar Electrical Generation Power Plant By Using Parabolic Trough In Basra City," Al-Qadisiya Journal For Engineering Sciences, vol. 7, no. 1, pp. 1–11, 2014.

[2] S. Kiwan, L. Venezia, F. M. Montagnino, F. Paredes, and R. Damseh, "Techno-Economic Analysis of a Concentrated Solar Polygeneration Plant in Jordan," Jordan Journal of Mechanical and Industrial Engineeringvol. 12, no.1, pp. 1 – 6, 2018.

[4] A. J. Majeed and G. J. Mohammed, "Sustainable Energy for Water Desalination System Relative to Basra Climate," Jordan Journal of Mechanical and Industrial Engineering, vol.9, no. 2, pp. 129 – 137, 2015.

[5] M. H. Nehrir et al., "A review of hybrid renewable/alternative energy systems for electric power generation: Configurations, control, and applications," IEEE Transactions on Sustainable Energy, vol. 2, no. 4. pp. 392–403, Oct. 2011. doi: 10.1109/TSTE.2011.2157540.

[6] M. Messaoud, B. Hadi, and D. Aissa, "Sensorless Control System Design of a Small Size Vertical Axis Wind Turbine," Jordan Journal of Mechanical and Industrial Engineering, vol.12, no. 2, pp. 93 – 98,2018.

[7] A. J. M. Al-Hussieni, "A Prognosis of Wind Energy Potential as a Power Generation Source in Basra City, Iraq State," European Scientific Journal, vol. 10, no. 36, 2014.

[8] K. al Bkoor Alrawashdeh, N. S. Gharaibeh, A. A. Alshorman, and M. H. Okour, "Magnus Wind Turbine Effect Vertical Axis Using Rotating Cylinder Blades," Jordan Journal of Mechanical and Industrial Engineering,vol.15, no. 2, pp. 233 – 241, 2021.

[9] E. A. Teshnizi et al., "Comprehensive Energy-Econo-Enviro (3E) Analysis of Grid-Connected Household Scale Wind Turbines in Qatar," Jordan Journal of Mechanical and Industrial Engineering,vol.15, no. 2, pp. 215 – 231,2021.

[10] C. Ghenai, T. Salameh, and I. Janajreh, "Modeling and Simulation of Shrouded Horizontal Axis Wind Turbine Using RANS Method," Jordan Journal of Mechanical and Industrial Engineering, vol.11, no. 4, pp. 235 -243,2017.

[11] C. Cekdin, Z. Nawawi, and M. Faizal, "The usage of thermoelectric generator as a renewable energy source," Telkomnika (Telecommunication Computing Electronics and Control), vol. 18, no. 4, pp. 2186–2192, 2020, doi: 10.12928/TELKOMNIKA.V18I4.13072.

[12] J. T. Seebeck, "Magnetic polarization of metals and minerals," Abhandlungen der Deutschen Akademie der Wissenschaften zu Berlin , vol. 265, pp. 1822–1823, 1822.

[13] C. Suter, Z. R. Jovanovic, and A. Steinfeld, "A 1kWe thermoelectric stack for geothermal power generation - Modeling and geometrical optimization," Applied Energy, vol. 99, pp. 379–385, 2012, doi: 10.1016/j.apenergy.2012.05.033.

[14] A. K. Trinh, I. González, L. Fournier, R. Pelletier, J. C. Sandoval V., and F. J. Lesage, "Solar thermal energy

conversion to electrical power," *Applied Thermal Engineering*, vol. 70, no. 1, pp. 675–686, Sep. 2014, doi: 10.1016/j.applthermaleng.2014.05.088.

[15] L. S. Chen, J. Y. Lee, and I. C. Bang, "Passive Micro Power Generation for Nuclear Safety with Thermoelectric Heat Pipe," 2013.

[16] L. Mateu, C. Codrea, N. Lucas, M. Pollak, P. Spies, and F. Iis, "Human Body Energy Harvesting Thermogenerator for Sensing Applications," 2007, doi: 10.1109/SENSORCOMM.2007.42.

[17] Rowe D. Michael, *Thermoelectrics Handbook Macro to Nano*, 1st ed. CRC Press, 2005.

[18] J.-P. Fleurial *et al.*, "2011 THERMOELECTRICS APPLICATIONS WORKSHOP Thermoelectrics: From Space Power Systems to Terrestrial Waste Heat Recovery Applications."

[19] C. Hadjistassou, E. Kyriakides, and J. Georgiou, "Designing high efficiency segmented thermoelectric generators," *Energy Conversion and Management*, vol. 66, pp. 165–172, 2013, doi: 10.1016/j.enconman.2012.07.030.

[20] M. Hamid Elsheikh *et al.*, "A review on thermoelectric renewable energy: Principle parameters that affect their performance," *Renewable and Sustainable Energy Reviews*, vol. 30. pp. 337–355, 2014. doi: 10.1016/j.rser.2013.10.027.

[21] D. N. Kossyvakis, G. D. Voutsinas, and E. v. Hristoforou, "Experimental analysis and performance evaluation of a tandem photovoltaic-thermoelectric hybrid system," *Energy Conversion and Management*, vol. 117, pp. 490–500, Jun. 2016, doi: 10.1016/j.enconman.2016.03.023.

[22] Y. Wang, Y. Shi, D. Mei, and Z. Chen, "Wearable thermoelectric generator to harvest body heat for powering a miniaturized accelerometer," *Applied Energy*, vol. 215, pp. 690–698, Apr. 2018, doi: 10.1016/j.apenergy.2018.02.062.

[23] A. Proto *et al.*, "Thermal energy harvesting on the bodily surfaces of arms and legs through a wearable thermo-electric generator," *Sensors (Switzerland)*, vol. 18, no. 6, Jun. 2018, doi: 10.3390/s18061927.

[24] H. Khalil and H. Hassan, "Enhancement of waste heat recovery from vertical chimney via thermoelectric generators by heat spreader," *Process Safety and Environmental Protection*, vol. 140, pp. 314–329, Aug. 2020, doi: 10.1016/j.psep.2020.05.023.

[25] N. Kanagaraj, "Photovoltaic and thermoelectric generator combined hybrid energy system with an enhanced maximum power point tracking technique for higher energy conversion efficiency," *Sustainability (Switzerland)*, vol. 13, no. 6, Mar. 2021, doi: 10.3390/su13063144.

[26] E. H. H. Al-Qadami, Z. Mustaffa, and M. E. Al-Atroush, "Evaluation of the Pavement Geothermal Energy Harvesting Technologies towards Sustainability and Renewable Energy," *Energies*, vol. 15, no. 3. MDPI, Feb. 01, 2022. doi: 10.3390/en15031201.

[27] D. Champier, "Thermoelectric generators: A review of applications," *Energy Conversion and Management*, vol. 140. Elsevier Ltd, pp. 167–181, 2017. doi: 10.1016/j.enconman.2017.02.070.

[28] J. Xiao, T. Yang, P. Li, P. Zhai, and Q. Zhang, "Thermal design and management for performance optimization of solar thermoelectric generator," *Applied Energy*, vol. 93, pp. 33–38, 2012, doi: 10.1016/j.apenergy.2011.06.006.

[29] S. Shittu, G. Li, X. Zhao, and X. Ma, "Series of detail comparison and optimization of thermoelectric element geometry considering the PV effect," *Renewable Energy*, vol. 130, pp. 930–942, Jan. 2019, doi: 10.1016/j.renene.2018.07.002.

[30] G. Li, S. Shittu, X. Ma, and X. Zhao, "Comparative analysis of thermoelectric elements optimum geometry between photovoltaic-thermoelectric and solar thermoelectric," *Energy*, vol. 171, pp. 599–610, Mar. 2019, doi: 10.1016/j.energy.2019.01.057.

[31] G. Li, X. Zhao, Y. Jin, X. Chen, J. Ji, and S. Shittu, "Performance Analysis and Discussion on the Thermoelectric Element Footprint for PV–TE Maximum Power Generation," *Journal of Electronic Materials*, vol. 47, no. 9, pp. 5344–5351, Sep. 2018, doi: 10.1007/s11664-018-6421-4.

[32] G. J. Snyder, "Application of the compatibility factor to the design of segmented and cascaded thermoelectric generators," *Applied Physics Letters*, vol. 84, no. 13, pp. 2436–2438, Mar. 2004, doi: 10.1063/1.1689396.

[33] S. Shittu, G. Li, X. Zhao, and X. Ma, "Thermoelectric generator performance enhancement by the application of pulsed heat power," 2019. doi: 10.11159/ffhmt19.146.

[34] L. Chen and J. Lee, "Effect of pulsed heat power on the thermal and electrical performances of a thermoelectric generator," *Applied Energy*, vol. 150, pp. 138–149, Jul. 2015, doi: 10.1016/j.apenergy.2015.04.009.

[35] A. Ferrario, S. Boldrini, A. Miozzo, and M. Fabrizio, "Temperature dependent iterative model of thermoelectric generator including thermal losses in passive elements," *Applied Thermal Engineering*, vol. 150, pp. 620–627, Mar. 2019, doi: 10.1016/j.applthermaleng.2019.01.031.

[36] B. Abdessamad, K. Salah-Ddine, and C. E. Mohamed, "Design and Modeling of DC/ DC Boost Converter for Mobile Device Applications," 2013.

[37] M. H. Rashid, *Power electronics: circuits, devices, and applications*. Pearson Education India, 2009.

[38] N. Mohan, T. M. Undeland, and W. P. Robbins, *Power electronics: converters,* applications, and design. John wiley & sons, 2003.

[39] Thejel, R. H., Ramzy S. Ali, and Elaf J. Majeed. "Novel Synthesis Methodology for Controlling Zero – Current Zero-Voltage Transition DC/DC Boost Converter.", Basrah Journal for Engineering Science 6, no. 1, 2006.

# Performance analysis of solar absorption ice maker driven by parabolic trough collector

## Mohamad H. Okour[*1], Hamza Al-Tahaineh[1], Wael Al-Kouz[2]

[1] *Mechanical Engineering Department - Al-Huson University College - Al-Balqa Applied University - P. O. Box 50, AlHuson 19117, Irbid, Jordan*

[2] *College of Engineering and Technology, American University of the Middle East, Kuwait*

## Abstract

The current research investigates the use of a two-stage ammonia-water double lift absorption cycle for residential house cooling. The main idea is to store the ice that is produced during the day so that it can be used to cool the building at night when the sun is not available. The Engineering Equation Solver (EES) program was used to simulate and investigate the relationships between different parameters in this cycle. The initial conditions such as the mass fraction difference between weak and strong solution, Mass fraction of ammonia in the evaporator, the temperature of the evaporator, and the ambient temperature.

The result showed that The heat transfer rate in absorber2 is 128.3 kW, the heat transfer rate in desorber2 is 195.4 kW, and the Evaporator heat transfer rate is 23.8 kW, indicating that 350 kg of ice is required to meet the cooling needs of the house at evaporator temperature 223 K and a COP of 0. 1216.

## Nomenclature

| Notation | Description | unit |
|---|---|---|
| $\dot{m}$ | Mass flow rate | (Kg/s) |
| h | Specific enthalpy | (Kj/Kg) |
| S | Specific entropy | (Kj/Kg-K) |
| Q | Quality | (Kg vapor/Kg) |
| X | Mass fraction of ammonia | (Kg ammonia/Kg) |
| $\dot{Q}$ | Rate of heat transfer | (Kw) |
| $\dot{W}$ | Mechanical power | (Kw) |
| COP | Coefficient of performance | |
| Cp | Specific heat capacity | (Kj/Kg-K) |
| E | Energy | (Kj) |
| η | Efficiency | |
| ε | Effectiveness | |
| G | Global radiation | (Kw/m2) |
| N | Number of solar collectors | |
| DX | mass fraction difference between weak and strong solution | (Kg ammonia/Kg) |

## 1. Introduction

Throughout the history of humankind, major advances in civilization have been accompanied by increased consumption of energy, which seems to be a major factor in the industrial power available and in the level of living of individuals. The existence of vast supplies of energy mostly leads to high rates of industrial growth. Furthermore, the availability of a low-cost energy source might lead to inefficient utilization of energy.

The world's hunger for energy has grown dramatically in the last few centuries, thus new sources of energy must be found and more efficient methods of utilizing them for different applications must be developed.

Fossil fuels, such as coal, gas, and oil, are the most common nonrenewable energy sources. These natural resources are a major source of energy for a wide range of industries; however, non-renewable energy has several drawbacks, including a negative environmental impact and a limited supply. Renewable energy, also known as clean energy, is derived from natural sources or processes that are replenished regularly. Sunlight and wind, for example, continue to shine and blow even though their availability is dependent on time and weather.

Solar energy could be utilized either by converting it to heat or to electricity, both of these forms have numerous applications like heating, cooling, food drying, and many more.

Sun's heat can be utilized to create cold by the usage of solar thermal cooling technologies like absorption and adsorption cycles.

In general, the ice demand increases for many fields requiring ice like food service, hospitals, industries,

---

\* Corresponding author e-mail: okour123@bau.edu.jo.

restaurants, hotels, laboratories, sports arenas, air conditioning, and various other places where large quantities of ice are needed continuously with different shapes and sizes. this incremental demand on ice makes it an attractive field for investment.

The requirement of a system that is fast and economically justified is necessary. Ice is used in this wide range of applications because it is safe for health, cheap handling equipment for chemical and physical properties, available everywhere and does not have bad side effects on foods or drinks.

A thermally driven adsorption chiller, integrated in a cooling tower, is used in the sun cooling project (water cooled system). Evacuated tube collectors provide heat to the chiller. Flat plate solar collectors were employed to deliver heat to the System of Solar Adsorption Refrigeration because the adsorption chillers demand a lower supply temperature to the generator, which can be easily produced by flat panel solar collectors [1].

For the use of medium-temperature solar energy, an adsorption ice maker with an energy storage system is proposed. The solar energy collected by the parabolic trough collector (PTC) was used to heat the adsorption ice maker in this system. The icemaker's performance was evaluated, and the highest coefficient of performance (COP) was found to be 0.15 experimentally [2].

The presented work investigates the use of a commercial freezer to efficiently produce ice using photovoltaic energy. The compressor's operation is adapted to the availability of solar energy using an innovative control unit. The proposed solar ice-maker was investigated using simulations and experiments. A design methodology for optimizing the solar energy supply system for a target ice production of 12 kilograms per day[3].

It was proposed to use a distributed photovoltaic energy system (DPES) to power an ice storage air conditioning system (ISACS). In addition, the optimization of system structure was investigated. The theoretical calculations and experimental tests were analyzed by the energy coupling and transferring characteristics in the light-electricity-cold conversion process. The system's energy utilization efficiency was found to be 4.64 percent [4].

An experiment using a working pair of activated carbon (AquaSorb 2000) and methanol for a solar adsorption ice maker system (SAIMS) [5].

### 1.1. The single-stage solar absorption cycle

A solar collector or concentrator, a hot fluid storage tank, an auxiliary heater, condenser, evaporator, expansion device, and thermal compressor make up a typical solar absorption cooling system. A generator, an absorber, and a mixture circulating pump, as well as a pressure reducing device (expansion device), make up the thermal compressor. The solution pump uses a small amount of energy compared to the mechanical compressor.

Absorption occurs when a substance in one state interpenetrates and combines with another substance in a different state. The two phases have a strong affinity for exothermically forming a solution or a mixture. This process can be reversed by heating the mixture and releasing the absorbed phase from the absorbent.

To power these systems, most absorption cooling systems use a single-stage absorption cycle with an H2O/LiBr working pair and either a solar flat plate collector or an evacuated tube collector with hot water. As shown in Figure 1, the single-stage solar absorption cooling system is based on the Basic absorption cycle, which has a single absorber and generator. The heat provided by the solar collector separates the refrigerant from the absorbent in the generator. The vapor-refrigerant condenses in the condenser, then expands in expansion valve 1, and evaporates in the evaporator at low pressure and temperature. A weak solution returns from the generator after passing through the expansion valve 2 and absorbs the cold refrigerant in the absorber. The rich mixture created in the absorber is pumped back to the generator by the pump. To improve the cycle efficiency, a typical solution heat exchanger can be used. The absorber is chilled by cooling water because the absorption is exothermic.

The aim of this study is to demonstrate that the two-stage ammonia-water double lift absorption cycle used in the solar absorption ice maker is thermally driven. Since absorption chillers based on double effect technology have the potential to convert solar energy more effectively while utilizing less primary energy produced by parabolic trough collectors. The Engineering Equation Solver (EES) program was used to simulate and investigate the relationships between different parameters in the cycle that was carried out for this purpose. The objective of our work is to conduct a thermal investigation of an ammonia-water two-stage double lift absorption cycle for solar ice makers and its application in air conditioning applications.
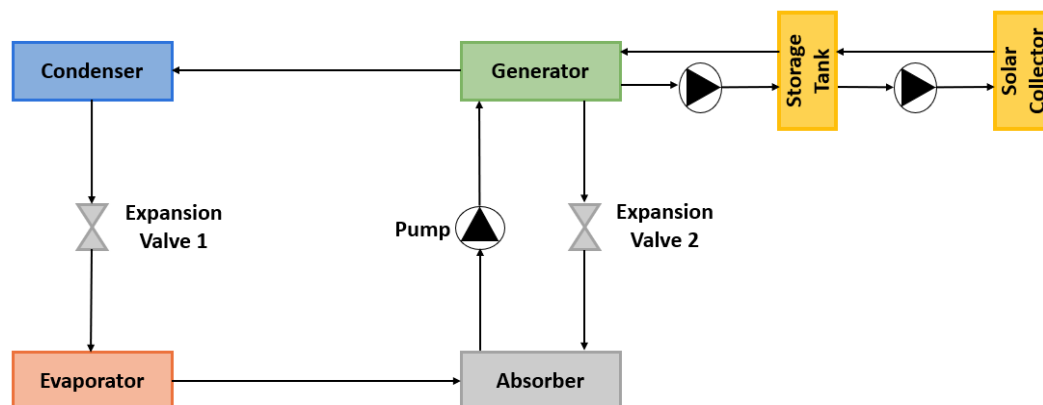


**Figure 1.** Single-effect solar absorption cycle

## 2. System Description:

### 2.1. Two-stage Solar Absorption Cycle

A double effect system can be achieved by adding an extra stage to the single effect cycle as a topping cycle. Absorption chillers based on the double effect technology have potential to convert solar energy more effectively while using less primary energy. They have a nearly double COP value when compared to single-effect systems (COP = 1.2). Their working liquids, on the other hand, must reach higher temperatures, exceeding 130ºC, which is outside the range for which most solar collectors are designed.

As shown in Figure (2), this absorption cycle, like water/LiBr two-stage cycles, uses the heat of the condenser to run desorber 1, and the flow in the intermediate solution circuit is reversed, reversing the function of these two component, as well as the pump and expansion valve.

The first law of thermodynamics is used to do an energy analysis. Where the first law of thermodynamics for an open system, or any component in an open system, is written as:

$$\frac{dE}{dt}\Big|_{cv} = \dot{Q} - \dot{W}_{cv} + \dot{m}_i \left( h_i + \frac{1}{2}V_i^2 + gz_i \right) - \dot{m}_o \left( h_o + \frac{1}{2}V_o^2 + gz_o \right) \qquad (1)$$

Each system component can be modeled as a control volume with inlet and outlet streams, heat transfer from or to the system, and/or work done on or by the system. Each component is taken as a single unit, the mass, and energy balance equations for the generator (G), condenser (C), evaporator (E), absorber (A), and auxiliary equipment like solution heat exchanger (SHX), rectifier (rec), and condensate precooler (Cprecooler) are established.

$$\sum \dot{m}_{in} - \sum \dot{m}_{out} = 0 \qquad (2)$$
$$\dot{Q} = \sum \dot{m}_{out} h_{out} - \sum \dot{m}_{in} h_{in} = 0 \qquad (3)$$

The COP of the system is an indication of how efficient the cooling or heating process is, the COP of any cooling cycle is given by equation (4).

$$COP_{actual} = \frac{Q_E}{Q_{Des2} + W_{pump1} + W_{pump2}} \qquad (4)$$

However, because $Q_E$ and $Q_{Des2}$ is too much larger than $W_{pump1}$ and $W_{pump2}$ so, the actual COP is given by:

$$COP_{actual} = \frac{Q_E}{Q_{Des2}} \qquad (5)$$

The actual COP of the refrigeration cycle should be compared to the Carnot COP (Maximum possible COP).

### 2.2. Ice calculation

A house in Amman Jordan was used to test the affordability of this method of cooling. The load of the house shown in figure (13), was calculated and the solar irradiation at the same place was calculated using PHOTOVOLTAIC GEOGRAPHICAL INFORMATION SYSTEM, then available $Q_{evap}$ was calculated by the following equation:

$$Q_{evaporator} = \eta_{collecter} \text{ N } A_{collecter} \text{ G COP} \qquad (6)$$

Where:
$Q_{evaporator}$: rate of heat absorbed by the evaporator (KW)
$\eta_{collecter}$: collector efficiency
N: number of collectors.
$A_{collector}$: the area of the collector (m²)
G: global radiation (KW/m²)
COP: coefficient of performance for the absorption cycle.

Figure (3), depicts the distribution of solar irradiation at Amman, Jordan during the day, with radiation values for beam, diffuse, and global radiation.
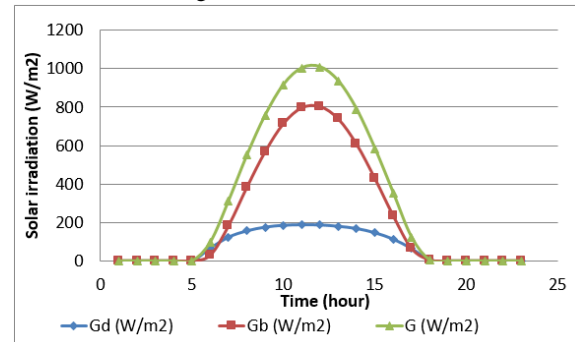


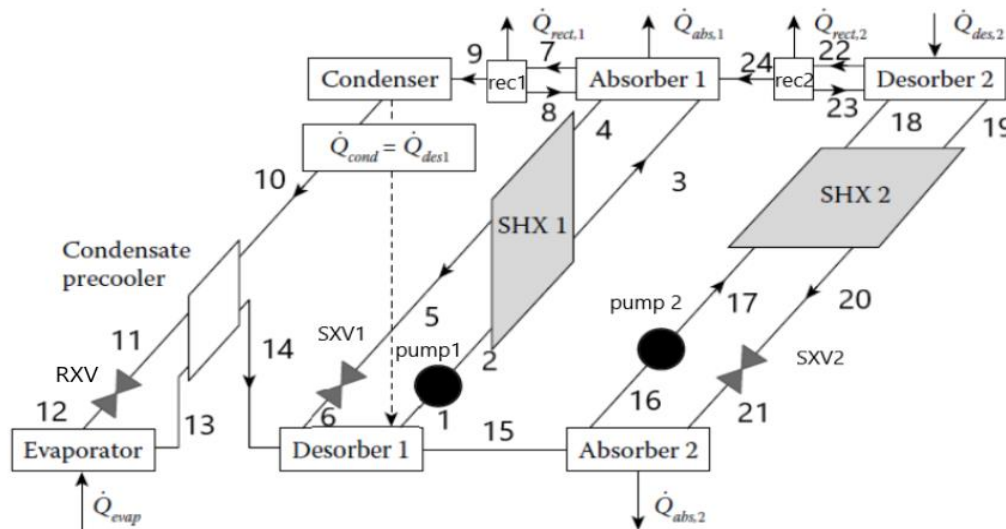**Figure 3.** the hourly distribution of solar irradiation in Amman Jordan



**Figure 2.** Two-stage double lift absorption refrigeration cycle

A parabolic trough collector is used in this simulation because of its relatively high efficiency, collector efficiency of 0.75, and collector Aperture area of 4 m$^2$ were assumed.

Next, an equation of conservation of energy is established to determine the energy available in the stored ice at any given time in the day given the $Q_{evaporator}$, $Ql_{load}$, and the amount of energy already stored in the ice.

$$E_{gen} + E_{in} - E_{out} = \Delta E_{system} \qquad (7)$$

Where:

$E_{gen}$: the energy generated inside the system (the system is considered to be the ice tank) (Kj)

$E_{in}$: the energy entering the system (Kj)

$E_{out}$: the energy leaving the system (Kj)

$\Delta E_{system}$: the energy accumulation inside the system. (Kj)

differentiating equation (7) with respect to time leads to:

$$\dot{Q}_{gen} + \dot{Q}_{in} - \dot{Q}_{out} = \dot{Q}_{system} \qquad (8)$$

Where:

$\dot{Q}_{gen}$: energy generation rate (KW)

$\dot{Q}_{in}$: the rate of energy entering the system (KW), in this case, it is $Q_{load}$

$\dot{Q}_{out}$: the rate of energy leaving the system (KW), in this case, it is $Q_{evaporator}$

$\dot{Q}_{system}$: energy accumulation rate inside the system (KW).

The following is the relationship between the amount of energy in the system and the rate of heat accumulation:

$$E_{system} = \int \dot{Q}_{system}\, dt + E_0 \qquad (9)$$

This can be written as considering $\dot{Q}_{gen}$ is none existed:

$$E_{system} = \int \left( \dot{Q}_{load} - \dot{Q}_{evaporator} \right) dt + E_0 \qquad (10)$$

Where:

$E_{system}$: the energy stored in ice (Kj) at a given time.

$E_0$: energy the ice possesses initially (Kj); at hour zero.

The model was built on EES, it was assumed that the cycle's COP is 0.1216 at evaporator temperature of 223 K, it was found that using this model, the number of solar collectors needed to cover building's cooling loads for the entire day was found to be 60, Figure (4) represents the energy stored in the ice throughout the day.

By knowing the maximum energy stored in ice (minimum energy value) and the minimum temperature, the mass of ice can be calculated by using equation (11) as follows:

$$M_{ice} = \frac{E_{system\, min}}{h_{ice}} \qquad (11)$$

Where:

$M_{ice}$: mass of stored ice (Kg)

$E_{system\, min}$: minimum energy stored in ice along the day (Kj)

$h_{ice}$: specific enthalpy of ice (Kj/Kg)

The mass of ice was found to be 352 Kg using equation (11). Ice temperature throughout the day can now be found as in Figure (5).
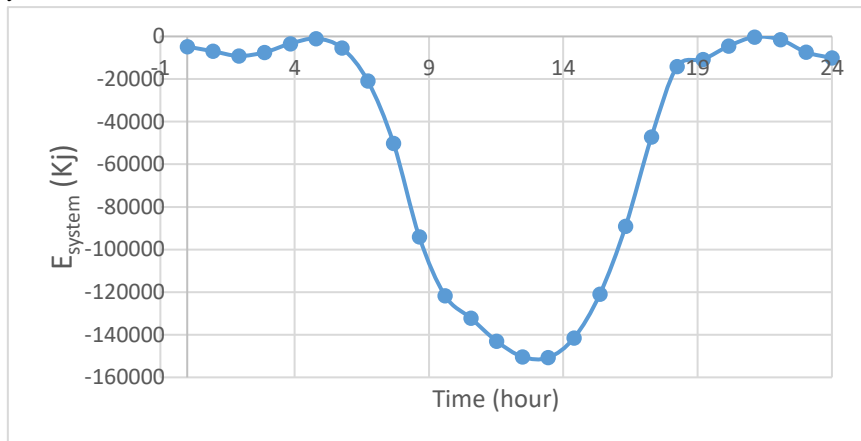


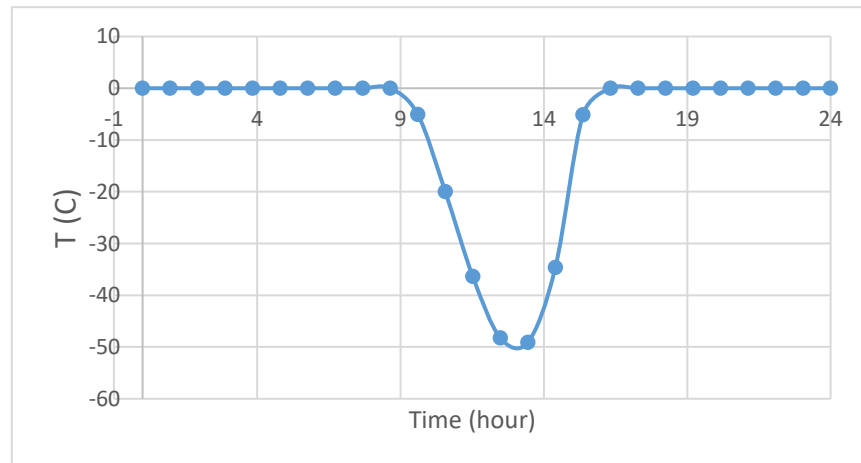**Figure 4.** energy stored in ice throughout the day



**Figure 5.** Ice temperature profile along the day

An overview of the ice maker used to make and store ice (and water) is made, the device should be able to store all the needed ice with acceptable heat transfer rates to both the ice and air, the device should also be able to transfer sensible heat only in which the humidity ration does not change along with it as shown in figure (6).

## 3. Results and Analysis

The simulation results are shown and discussed. For this aim, some parameters (Evaporator's Outlet Temperature, Evaporators Exit Quality, Refrigerant mass fraction, mass fraction difference between weak and strong solution (DX), Ambient Temperature) were compared.

Furthermore, a comparison between this cycle and the single-stage ammonia-water cycle was done.

Figure (7) shows the relation between the COP and evaporator's exit quality, the COP increases

to a certain point as the evaporator's exit quality increases, then falls as the evaporator's exit quality increases, the model can simulate for evaporator's exit quality values less than 0.98, however, a drop in COP occurs at high-quality values (higher than 0.93). This is due to the dramatic drop in pressure of the refrigerant at such high-quality values as in Figure (8), this drop in pressure causes the COP to drop as explained previously.
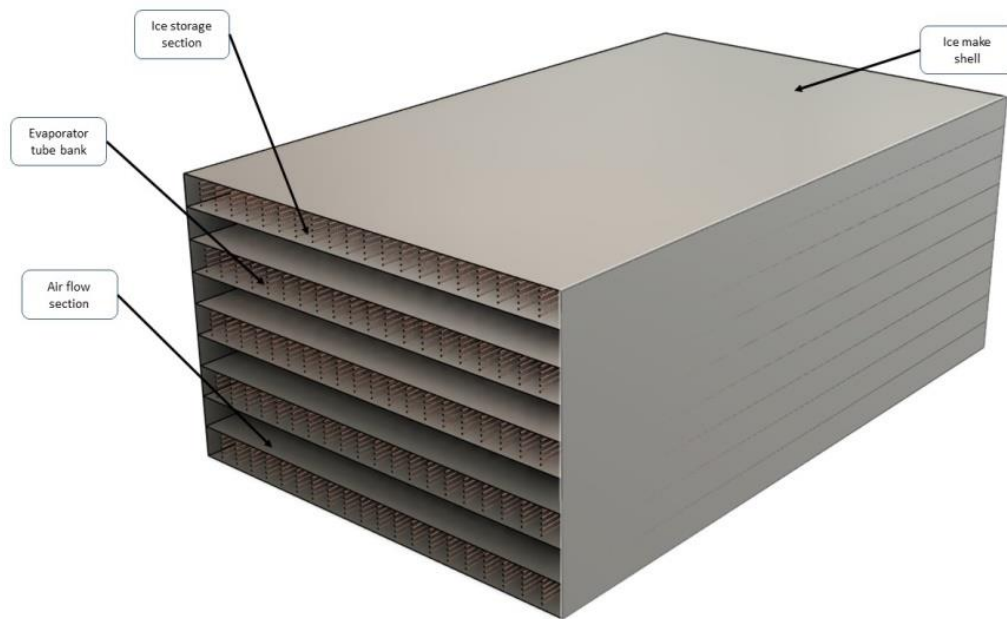


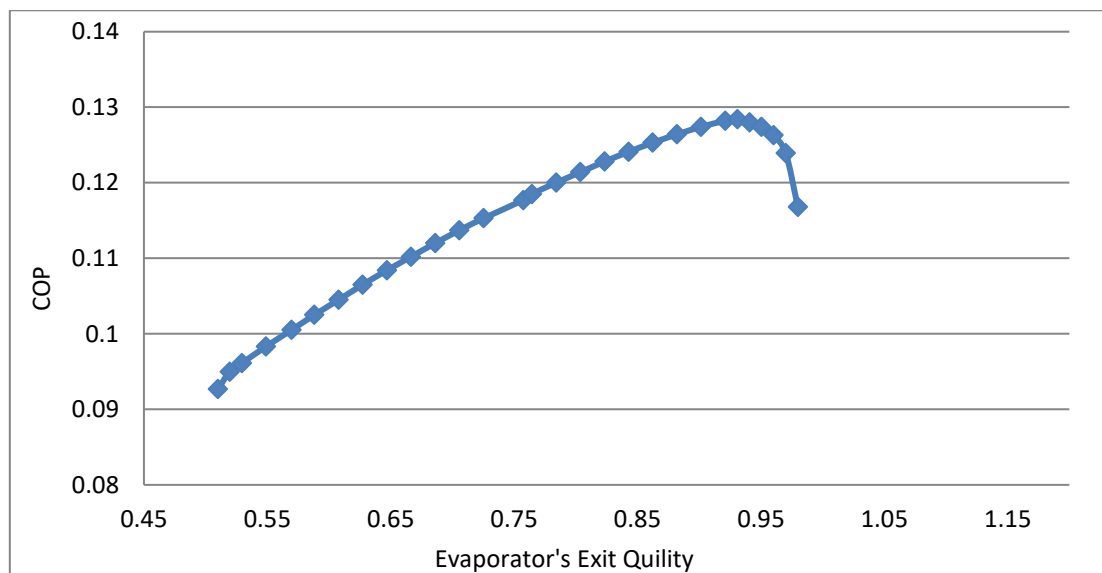**Figure 6.** view of an ice maker



**Figure 7.** COP relation to evaporators exit quality

Figure (9) shows the relation between the COP against refrigerant mass fraction, as expected; the COP increases as the refrigerant mass fraction increases due to the pressure increase, higher pressure leads to lower heat capacity at the desorber2 outlets, consequently to lower desorber2 heat. The simulation model is valid for values of refrigerant mass fraction lower than 0.9907.

Figure (10) illustrates the relationship between the COP and the mass fraction difference in the solution circuits (DX), the model can simulate DX values between 0.02 and 0.115, the results show that the COP is directly related to the DX value due to the decrease of the energy required at the desorber 2, however, this is due to the decrease in the mass fraction of point 19 (the weak solution line) which results in a decrease in the mass flow rates at points 18 (the strong solution line) and 19 while keeping the mass flow rates at point 22 (vapor line) and 23 (condensate line from rectifier) nearly constant.
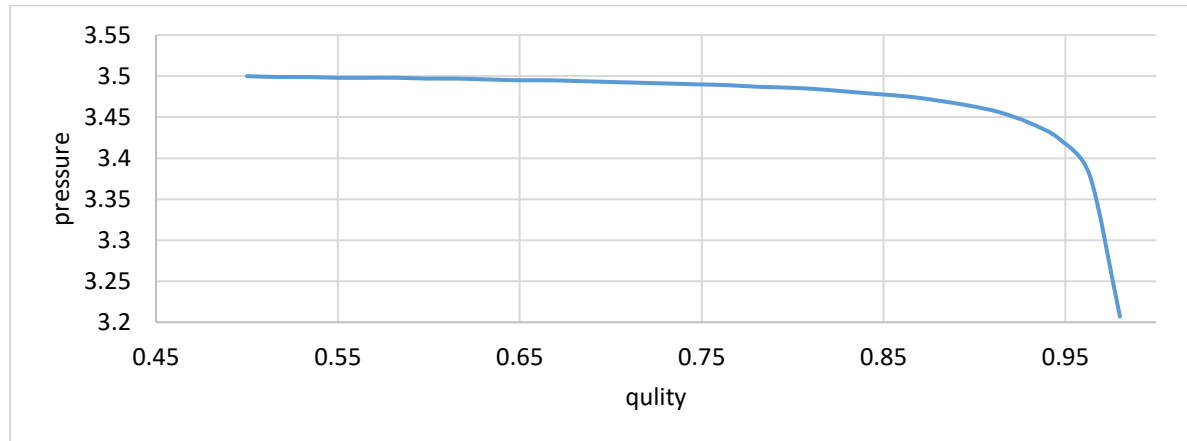


**Figure 8.** pressure and quality relationship of the ammonia-water mixture at a constant concentration
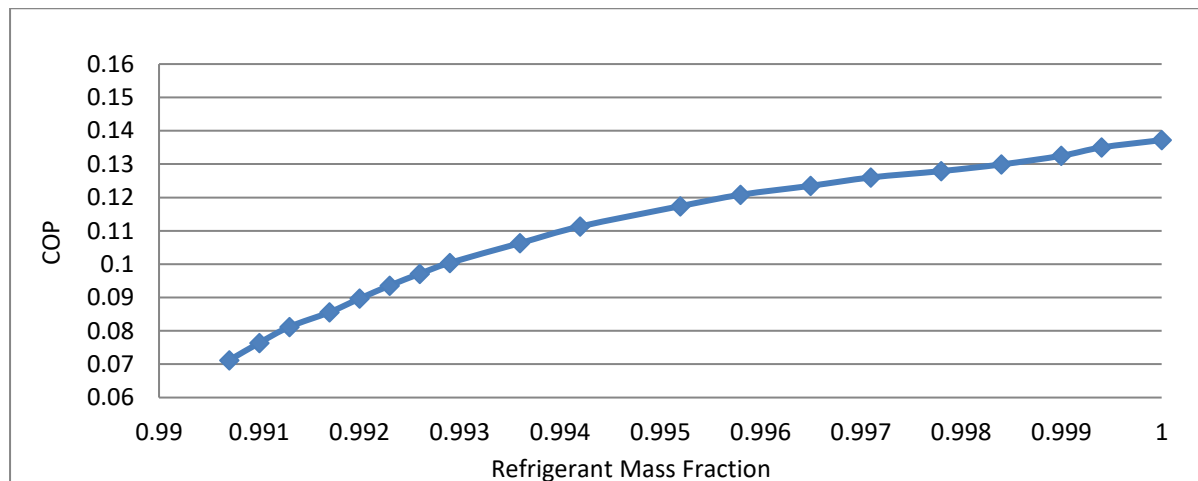


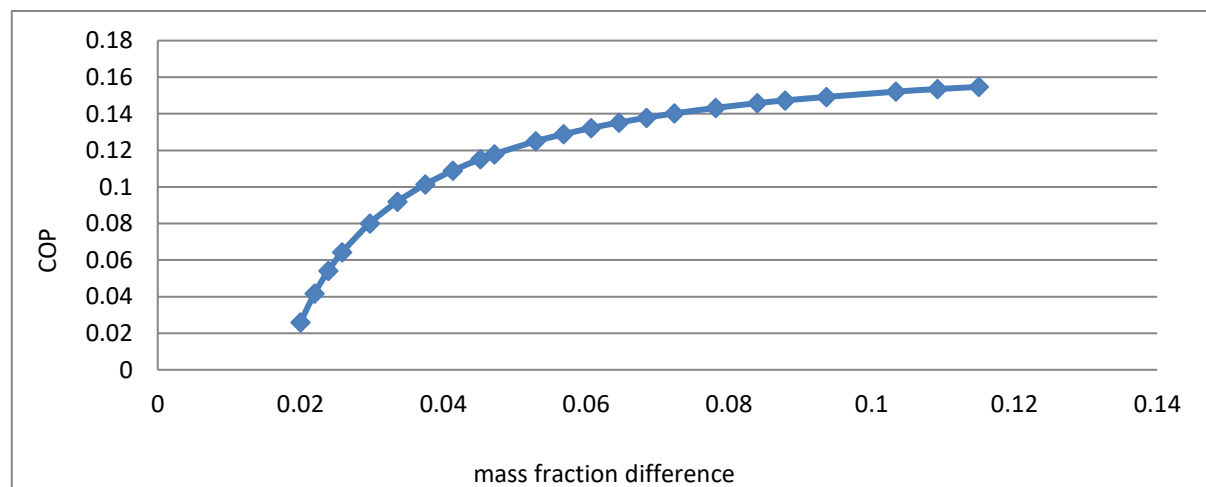**Figure 9.** COP relation to Refrigerant mass fraction



**Figure 10.** COP relation to mass fraction difference in the solution circuits

Figure (11) demonstrates that the higher the ambient temperature the lower the COP. This is mainly due to lower values of ammonia concentrations at the weak and strong solution lines at the desorber 2 which in turn results in an increase in the mass flow rates at these lines, thus increasing the desorber2 required heat. This result also follows the Carnot law of maximum efficiency.

A comparison between a single-stage ammonia absorption cycle and the two-stage double lift cycle is shown in Figure (12). despite the single-stage cycle has a higher COP value, it runs on a smaller range of evaporator temperatures and with a higher desorber temperature than the two-stage double lift cycle. The simulated data for the cycle illustrated in Figure 2 is provided in Tables 1 and 2.
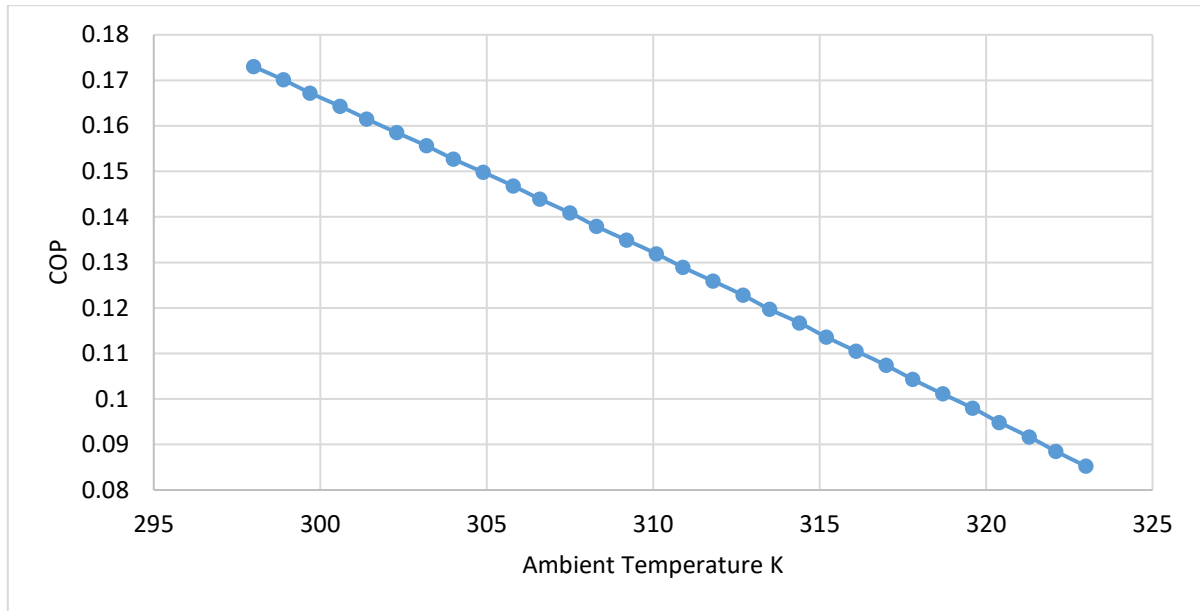


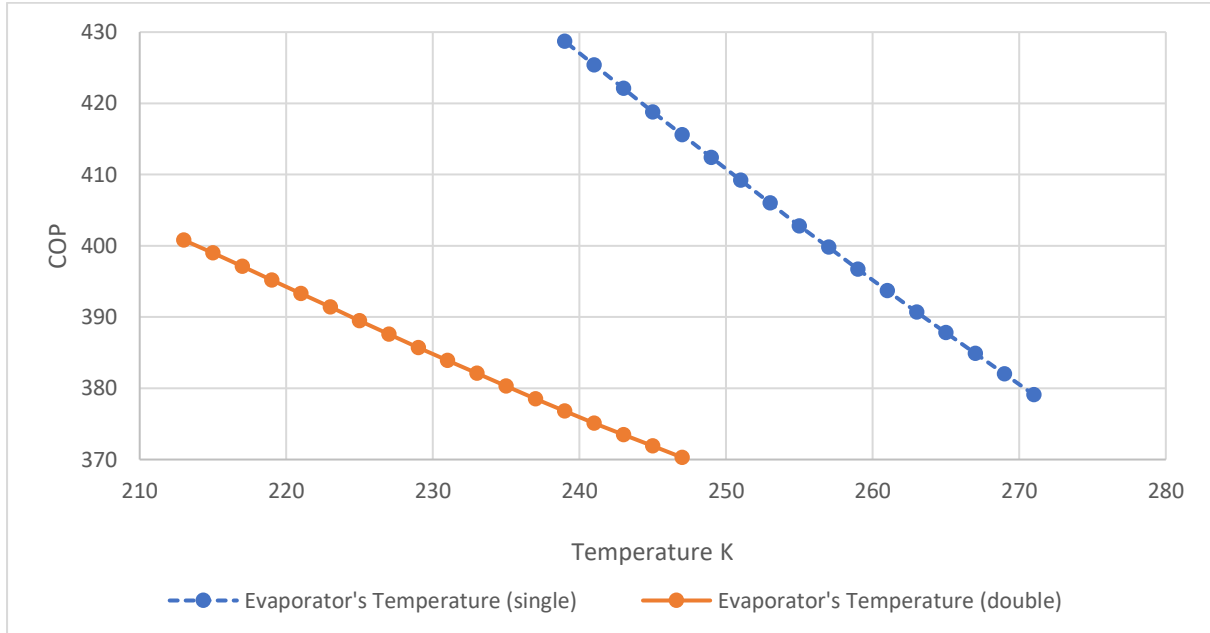**Figure 11.** COP relation to Ambient Temperature



**Figure 12.** A comparison between single-stage and two-stage double lift cycles with respect to evaporator and desorber operating temperatures.

**Table 1.** simulated data for the cycle

| State Points | m (kg/sec) | P (bar) | T (°C) | h (KJ/Kg) | x (kg/kg) | Vapor Quality |
|---|---|---|---|---|---|---|
| 1 | 0.2849 | 0.3428 | 266.4 | -250.1 | 0.3708 | 0 |
| 2 | 0.2849 | 3.296 | 266.4 | -249.7 | 0.3708 | -0.001 |
| 3 | 0.2849 | 3.296 | 303.6 | -85.01 | 0.3708 | -0.001 |
| 4 | 0.3097 | 3.296 | 313 | -55.14 | 0.4208 | 0 |
| 5 | 0.3097 | 3.296 | 278.9 | -206.7 | 0.4208 | -0.001 |
| 6 | 0.3097 | 0.3428 | 262.7 | -206.7 | 0.4208 | 0.04326 |
| 7 | 0.01846 | 3.296 | 313 | 1382 | 0.9908 | 1 |
| 8 | 0.000166 | 3.296 | 313 | -55.36 | 0.4208 | 0 |
| 9 | 0.01829 | 3.296 | 303 | 1352 | 0.996 | 1.001 |
| 10 | 0.01829 | 3.296 | 266.4 | -33.96 | 0.996 | 0 |
| 11 | 0.01829 | 3.296 | 242.4 | -141.8 | 0.996 | -0.001 |
| 12 | 0.01829 | 0.3428 | 220.3 | -141.8 | 0.996 | 0.06907 |
| 13 | 0.01829 | 0.3428 | 223 | 1159 | 0.996 | 0.975 |
| 14 | 0.01829 | 0.3428 | 258 | 1267 | 0.996 | 0.9958 |
| 15 | 0.04309 | 0.3428 | 266.4 | 1294 | 0.9956 | 1 |
| 16 | 0.8025 | 0.3428 | 313 | 89.88 | 0.1144 | 0 |
| 17 | 0.8025 | 3.296 | 313 | 90.19 | 0.1144 | -0.001 |
| 18 | 0.8025 | 3.296 | 372.4 | 340.3 | 0.1144 | -0.001 |
| 19 | 0.7594 | 3.296 | 391.4 | 454.7 | 0.06444 | 0 |
| 20 | 0.7594 | 3.296 | 328.8 | 190.4 | 0.06444 | -0.001 |
| 21 | 0.7594 | 0.3428 | 325.8 | 190.4 | 0.06444 | 0.006265 |
| 22 | 0.06964 | 3.296 | 378.2 | 1908 | 0.6597 | 1 |
| 23 | 0.02655 | 3.296 | 378.2 | 366.2 | 0.1144 | 0 |
| 24 | 0.04309 | 3.296 | 304.4 | 1353 | 0.9956 | 1 |

**Table 2.** simulated data for the cycle

| Summary of Energy Quantities | | |
|---|---|---|
| $\dot{w}p_1$ | Pump1 power | 0.09556kW |
| $\dot{w}p_2$ | Pump2 power | 0.2503kW |
| $\dot{Q}_{SHX1}$ | Heat transfer rate in solution SHX1 | 46.93kW |
| $\dot{Q}_{SHX2}$ | Heat transfer rate in solution SHX2 | 200.7kW |
| $\dot{Q}_{precooler}$ | Heat transfer rate in precooler | 1.973kW |
| $\dot{Q}_{abs1}$ | Heat transfer rate in absorber1 | 25.64kW |
| $\dot{Q}_{abs2}$ | Heat transfer rate in absorber2 | 128.3kW |
| $\dot{Q}_{rect1}$ | Heat transfer rate in rectifier1 | 0.7754kW |
| $\dot{Q}_{rect2}$ | Heat transfer rate in rectifier2 | 64.87kW |
| $\dot{Q}_{des1}$ | Heat transfer rate in desorber1 | 25.36kW |
| $\dot{Q}_{des2}$ | Heat transfer rate in desorber2 | 195.4kW |
| $\dot{Q}_{cond}$ | Condenser heat transfer rate | 25.36kW |
| $\dot{Q}_{evap}$ | Evaporator heat transfer rate | 23.8kW |
| COP | Cycle coefficient of performance | 0.1216 |

## 4. Discreet method

The available data of solar radiation is hourly based, thus the evaporator's capacity can be determined for each hour using eq. (6), Figure (13) shows the evaporator's capacity as well as building load along the day.

By using Microsoft Excel sheet, the data for the evaporator's capacity and building load were implemented, the hourly difference between both of these values was found as ($\Delta Q$), where:

$$\Delta Q = \dot{Q}_{load} - \dot{Q}_{evap} \qquad (12)$$
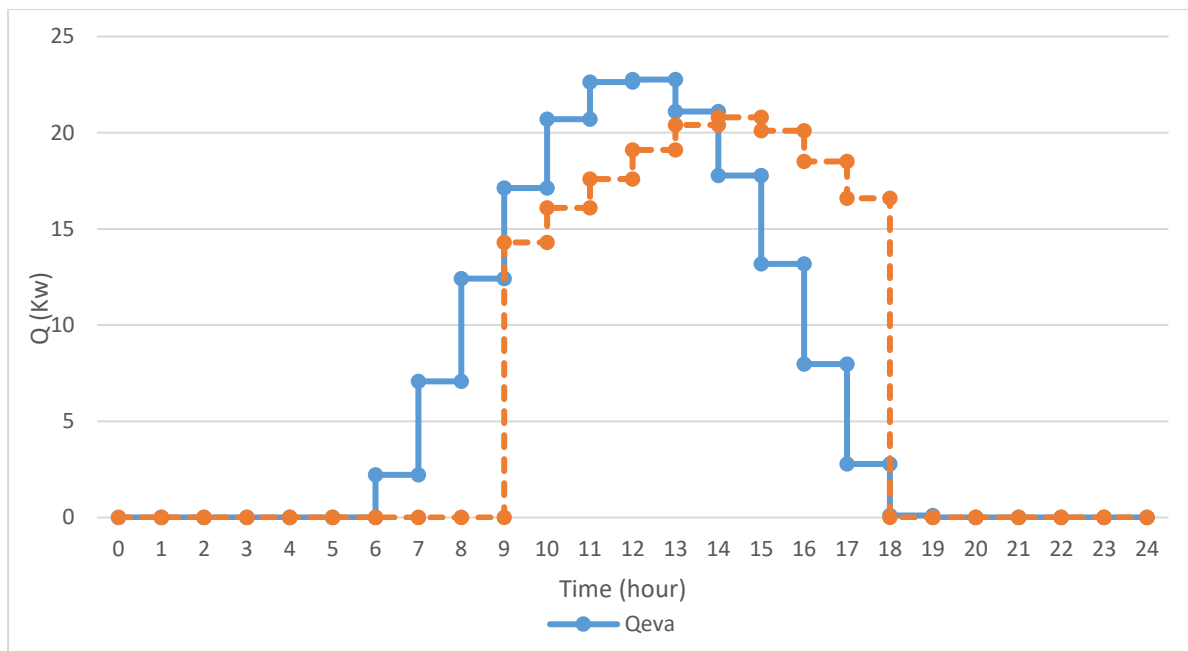
**Figure 13.** hourly evaporator's capacity and building load throughout the day.

Using this method, The number of solar collectors was found to be 61 and the mass of ice needed is found to be 350 Kg.

## 5. conclusions

The two-stage double lift ammonia-water absorption cycle model is limited by some of its parameters, going outside the limits would result in negative mass flow rates or unsatisfactory saturation properties.

This cycle operates at lower operating temperatures than the single-stage cycle, on the other hand, it has lower COP. Changing the cycle with one with higher COP while using the same evaporator design and ice storage principle might be more profitable.

This cycle can benefit from other sources of heat other than solar, it can be driven by a steam turbine condenser waste heat or geothermal heat since it runs on low generation temperatures.

The results obtained by the continuous method are very close to the results obtained using the discreet method. The result showed that the mass of ice needed to cover the house cooling needs is approximately 350 Kg at evaporator temperature of 223 K with a Cycle coefficient of performance COP of about 0.1216, while the Heat transfer rate in absorber2 is 128.3 kW, the Heat transfer rate in desorber2 is 195.4 kW, the Condenser heat transfer rate is 25.36 kW and the Evaporator heat transfer rate is 23.8 kW.

## References

[1] Al-Rbaihat R. ،Sakhrieh A., Al-Asfar J., Alahmer A., Ayadi O, Al-Salaymeh A., Al_hamamre Z., Al- bawwab A., Hamdan M., Performance Assessment and Theoretical Simulation of Adsorption Refrigeration System Driven by Flat Plate Solar Collector. Jordan Journal of Mechanical and Industrial Engineering JJmie,Vol. 11 (1), 2017, 1-11.

[2] Li, C., et al., Experimental study on an adsorption icemaker driven by parabolic trough solar collector. Renewable Energy, 57: p. 223-233,2013.

[3] Torres-Toledo, V., et al., Design and performance of a small-scale solar ice-maker based on a DC-freezer and an adaptive control unit. Solar Energy, 139: p. 433-443, 2016.

[4] Xu, Y., et al., Performance analysis of ice storage air conditioning system driven by distributed photovoltaic energy. Bulg Chem Commun, 48: p. 165-172, 2016.

[5] Attalla, M., et al., Experimental study of solar-powered ice maker using adsorption pair of activated carbon and methanol. Applied Thermal Engineering, 141: p. 877-886, 2018.

[6] Bataineh K. M., Gharaibeh A., Optimization Analyses of Parabolic Trough (CSP) Plants for the Desert Regions of the Middle East and North Africa (MENA). Jordan Journal of Mechanical and Industrial Engineering JJmie,Vol. 12 (1), 2018, 33-43.

[7] Ababneh A., Energy Conservation Using a Double-effect Absorption Cycle Driven by Solar Energy and Fossil Fuel. Jordan Journal of Mechanical and Industrial Engineering JJmie,Vol. 5 (3), 2011, 213-219.

[8] Moreno-Quintanar, G., W. Rivera, and R. Best. Development of a solar intermittent refrigeration system for ice production. in World Renewable Energy Congress-Sweden; 8-13 May; 2011; Linköping; Sweden. 2011. Linköping University Electronic Press.

[9] EESI Environmental and Energy Study Institute. 13/3/2020. Fossil Fuels. https://www.eesi.org/topics/fossilfuels/description?fbclid=IwAR0JcW2Iv3YrwCY4usR64FWHX52FXCm40aP4asBzXNfuVd6EPR5ch5-OayA

[10] Besagni, G., R. Mereu, and F. Inzoli, Ejector refrigeration: a comprehensive review. Renewable and Sustainable Energy Reviews, 53: p. 373-407, 2016.

[11] Zhang, X. and R. Wang, A new combined adsorption–ejector refrigeration and heating hybrid system powered by solar energy. Applied Thermal Engineering, 22(11): p. 1245-1258, 2002.

[12] Reddy, P.J.P. and S.S. Murthy, Studies on an Ejector-Absorption Refrigeration Cycle with New Working Fluid Pairs.

[13] Energy Developments: New Forms, Renewables, Conservation. Solar Furnace, 1984.

]14] Hamza Abdel-Latif Al-Tahaineh. Second Law Analysis of Solar Powered Absorption Refrigeration System, 2002.

[15] Photovoltaic geographical information system. 15/10/2019. Position information and standard conditions.

[16]Keith E.Herold Reinhard Radermacher Sanford A.Klein. Absorption Chillers and Heat Pumps. 2nd ed, 2016.

[17] Petros J. Axaopoulos, Michael P. Theodoridis, Design and experimental performance of a PV Ice-maker without battery. Solar Energy, 83(8):1360-1369, August 2009.

[18] Bu, X.B., Li, H.S., Wang, L.B., Performance analysis and working fluids selection of solar powered organic rankine-vapor compression ice maker. Sol. Energy 95, 271–278, 2013.

[19] M. Navidbakhsh, Ali Shirazi, S. Sanaye, Four E analysis and multi-objective optimization of an ice storage system incorporating PCM as the partial cold storage for air-conditioning applications.

Applied Thermal Engineering, Volume 58, Issues 1–2, Pages 30-41, 2013.

[20] M. Rosen, I. Dincer, Norman Pedinelli, Thermodynamic Performance of Ice Thermal Energy Storage Systems. Journal of Energy Resources Technology-transactions of The Asme, 122(4): 205-211 (7 pages), 2000.

[21] Beggs, C., The Economics of Ice Thermal Storage. Building Research and Information, 19 , No. 6 , pp. 342 – 355, 1991.

[22] Michel Pons , J. J. Guilleminot , Design of an Experimental Solar-Powered, Solid-Adsorption Ice Maker. Journal of Solar Energy Engineering, 108(4): 332-337, 1986.

[23] Z. F. Li And K. Sumathy, A Solar-Powered Ice-Maker with the Solid Adsorption Pair of Activated Carbon and Methanol. International Journal of Energy Research, 23, 517— 527, 1999.

# المجلة الأردنية

# للهندسة الميكانيكية والصناعية

# JJMIE

# المجلة الأردنية للهندسة الميكانيكية والصناعية